Structural Studies of Thallium Containing Germanate and Borate Glasses and Crystalline Phases

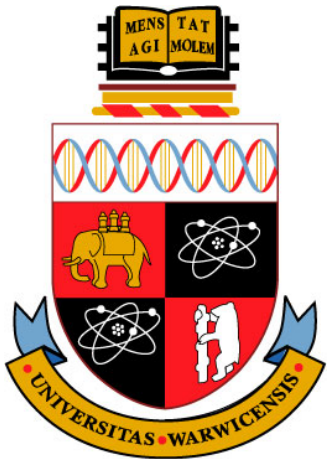

Nattapol Laorodphan

A thesis submitted to the University of Warwick in partial fulfilment of the requirement for the degree of Doctor of Philosophy

Department of Physics **September 2012**

Contents

Title **Page**

Acknowledgements

I would like to sincerely thank my supervisor, Dr. Diane Holland, for all help, guidance, encouragement and support she has given me throughout the course of my PhD. Without her this thesis would not be easily completed. I would also like to gratefully thank Professor Ray Dupree, for the knowledge of solid-state NMR, both theoretical and experimental, he has given me. Dr. Alex Hannon and Dr. Emma Barney are also thanked for their kind help with the neutron diffraction interpretation. Professor Steve Feller is thanked for the hospitality, which I received during my trip to Coe College.

I am grateful to Dr. Andrew Howes, Dr. John Hanna, Dr. Tom Kemp, Dr. Kevin Pike and Dr. Nathan Barrow for all their help with NMR experiments. I would like to thank Dr. David Walker for his kind help with XRD experiments. The Warwick Solid State NMR group is also thanked for their splendid facilities. The Warwick Diamond group and the Warwick Microscopy group are thanked for access to their Raman facilities and scanning electron microscopy (SEM) facilities, respectively. Mr. Dave Hammond, Mr. Steve York and Mr. Keith Briggs are thanked for their technical support.

I would like to express my thanks to the Department of Physics, University of Warwick; Department of Physics, Coe College; and Rutherford Appleton Laboratory for their research facilities that made this work possible. I also would like to express my thanks for all financial support from the Royal Thai Government and the Institute of Physics.

Ollie, Andy, Martin, Robin, Rabahh, Dan, Dean, Iain, Kaustav, Steve and Aoife are thanked for their help and their friendship during my time in the UK. My friends in Physics and the Thai community are also thanked for making me happy during my studies.

Finally, very special thanks to my family for their encouragement throughout my time in the UK. I would like to dedicate this thesis to my parents.

Declaration and published work

I declare that the work presented in this thesis is my own except where stated otherwise, and was carried out entirely at the University of Warwick, during the period of October 2008 to September 2012, under the supervision of Dr. Diane Holland. The research reported here has not been submitted, either wholly or in part, in this or any other academic institution for admission to higher degree.

Some parts of this thesis have been published, or are in preparation for publication as listed below. It is anticipated that further part of this work will be submitted for publication in due course.

Published

[1] ER Barney, AC Hannon, N Laorodphan, R Dupree, D Holland "A neutron diffraction and ^{205}Tl NMR study of the thallium germanate glass system" J. Non-Cryst. Solids **356** (2010) 2517-2523.

[2] ER Barney, AC Hannon, N Laorodphan, D Holland "The influence of lone-pair cations on the germanate anomaly in glass" J. Phys. Chem. C 2011, **115**, 14997–15007.

In preparation

[1] N.Laorodphan, E.Barney, A.Hannon, A.P.Howes, R.Dupree and D. Holland, "^{11}B and ^{205}Tl solid-state NMR, neutron diffraction and Raman spectroscopy study of thallium borate glasses".

[2] N.Laorodphan, E.Barney, A.P.Howes, J.V. Hanna, R.Dupree and D. Holland, "^{203}Tl and ^{205}Tl solid-state NMR study of thallium gernamate glasses".

Nattapol Laorodphan

September 2012

Abstract

The structure of glasses and devitrified phases, in $Tl_2O{\cdot}GeO_2$ and $Tl_2O{\cdot}B_2O_3$ systems, have been investigated using solid-state nuclear magnetic resonance (NMR), neutron diffraction and Raman spectroscopy. Gas pycnometry, thermal analysis and powder X-ray diffraction (XRD) have also been used to characterise and measure properties of glasses and devitrified phases.

The crystallisation study showed that metastable crystalline phases were obtained from low-temperature heat-treatment. X-ray diffraction of devitrification products, obtained at higher temperature, indicates crystallisation of the corresponding, more stable, stoichiometric compounds from the glass but with one or more second phases. Thallium NMR studies reveal that various chemical environments of thallium are present in the heat-treated samples. For the $Tl_2Ge_4O_9$ sample, whose crystal structure is known, magic angle spinning NMR reveals the presence of one thallium site, the $[Ge_3O_9]$ ring structure was observed using Raman spectroscopy.

A germanate anomaly is present in the thallium germanate glasses indicated by a minimum value of molar volume at x ~ 0.15. Neutron diffraction and Raman spectroscopy confirm the change in the coordination number of germanium from $[GeO_4]$ to $[GeO_{6\ or\ 5}]$. Tl solid-state NMR suggests that at least two thallium sites are also present in the glass, low and high coordinated thallium. Tl-NMR spectra are broad and shifted mainly due to the chemical shift dispersion and chemical shift anisotropy interaction, respectively. T_2 measurements confirmed that dipole-dipole and pseudodipole or exchange interactions are stronger in high thallium content glasses. A ^{203}Tl enrichment study determined that the broadening due to the exchange interaction is ~ 10 kHz.

Only three crystalline thallium borate phases were obtained, either singly or in combination with each other. Density data, X-ray diffraction patterns and solid-state NMR results of the three phases formed support what structural information exists in the literature. Chemical shift interaction and chemical shift dispersion contribute to the line broadening and lineshape of Tl NMR of TlB_5O_8 and TlB_3O_5 containing sample. Dipolar interaction and the Tl…Tl exchange interaction are stronger in the $Tl_2B_4O_7$ sample. The chemical shift anisotropy parameters of TlB_5O_8 and TlB_3O_5 are presented.

A borate anomaly is present in thallium borate glasses with a minimum value of molar volume at x ~ 0.28. Neutron diffraction and solid-state NMR spectroscopy confirm the change in the coordination number of boron to oxygen atoms from $[BO_3]$ to $[BO_4]$. N_4 values obtained from both techniques are very close and are larger than found for alkali borate glasses. Raman spectroscopy also reveals the changes in boron-oxygen superstructural units. ^{205}Tl solid-state NMR suggests that at least two thallium sites are present in the glass, low and high coordinated thallium. Tl-NMR spectra are broad and shifted mainly due to the chemical shift dispersion and chemical shift anisotropy interaction, respectively. T_2 measurement confirmed that dipole-dipole and exchange interactions occur in glasses throughout the range of studied compositions.

List of Figures

List of Tables

Glossary and Abbreviations

NBO	Non-bridging Oxygens
T_g	Glass transition temperature
T_c	Crystallisation temperature
DTA	Differential Thermal Analysis
NMR	Nuclear Magnetic Resonance
XRD	X-ray Diffraction
FID	Free Induction Decay
CSA	Chemical Shift Anisotropy
T_2	Transverse or Spin-spin Relaxation Time
T_1	Longitudinal or Spin-lattice Relaxation Time
M2	Second Moment
i(Q)	Neutron Distinct Scattering
T(r)	Total Correlation Function
MAS	Magic Angle Spinning
FWHM	Full Width at Half Maximum
r.f.	Radio frequency

Chapter 1
Introduction

1.1 Overview

Glass materials are involved in many aspects of daily life, for example: window glass, wine glass, car windscreen and the touch screen in a mobile phone. They are, without doubt, important to mankind. In glass science, there is extensive research to develop the glass properties necessary in order to fulfil the demands of their applications, for instance the need for very strong flat glass for mobile phone technology. The structure of glass has been widely studied because there is a relationship between glass properties and structure [1-7]. Oxide glasses are the main materials to be studied, as is the case in this thesis, which are thallium containing germanate (GeO_2) and borate (B_2O_3) glasses.

Thallium (Tl) containing glasses are of interest due to the presence of a large optical non-linearity response [8], due to the high polarisability of Tl^+ [9]. Thallium in its +1 oxidation state, i.e. Tl_2O, has a lone pair of electrons, which could be in a sterically active or inert environment and may also affect the glass structure, i.e. number and distribution of nearest neighbour oxygen atoms. Thallium has been found to be present in two different environments, a symmetric ionic environment at low thallium content (below 18 mole % for thallium borate glasses [10]) and an asymmetric covalent environment at high thallium content [11, 12], in which the lone pair of electrons are respectively sterically inert and active. The lone-pair of electrons occupy one of the s-p hybridised valence electron orbitals, which explains the distortion of the crystals containing post-transition metal or lone pair containing cation, e.g. Bi_2O_3 and PbO [13]. The exact hybridisation (plus possible contribution from higher energy d-orbital) can vary, resulting in changes in the O-M-O bond angles and the extent of the lone-pair in space.

Solid-state nuclear magnetic resonance (NMR) has been used to study the structure of thallium containing glasses, e.g. thallium borate [11, 12, 14], thallium germanate [11] and thallium silicate [11]. Nuclear magnetic interactions of thallium nuclei, such as chemical shift interaction and exchange interaction, have been investigated as a function of glass composition. Differences in the nuclear magnetic

interactions can be related to the changes in local thallium structure; for example, various size thallium clusters have been shown to occur in thallium silicate glass containing more than 20 mol % Tl_2O.

In addition to solid-state NMR studies, neutron [15, 16] and X-ray diffraction [17] have also been used to investigated the changes in thallium environment with glass composition, particularly thallium-thallium distances and thallium-oxygen coordination, inferred from the thallium-oxygen seperation. It has been reported that the thallium-oxygen coordination number in thallium germanate glasses reduced from 9 ($[TlO_9]$) to 3 ($[TlO_3]$) with increasing Tl_2O content [16]. A shortest thallium-thallium distance of about 4 Å was determined in thallium borate glasses using X-ray diffraction [17].

In this study, changes in thallium environments in thallium germanate and borate glasses were investigated using thallium (^{203}Tl and ^{205}Tl) solid-state NMR and neutron diffraction.

There is continuing debate on the structural nature of the anomalous changes (observation of a maximum of minimum) in properties of borate and germanate glass networks when a modifying oxide, e.g. alkali oxide, is added to the glass. For example, in germanate glasses, one proposed explanation is that higher coordination number germanate units $[GeO_n]$ are formed instead of the basic network $[GeO_4]$ units in GeO_2 glass [18]. An alternative explanation refers to the formation of $[GeO_4]$ ring structures and non-bridging oxygens (NBO) to explain the anomalies [19, 20]. In borate glasses, the anomalous behaviour can be explained by the changes in local boron environment from $[BO_3]$ units to $[BO_4]^-$ units when modifying oxide is added to the glasses [21-27]. This explanation is readily accepted because the two environments are easily distinguished by ^{11}B NMR. In addition to ^{10}B and ^{11}B solid-state NMR [23, 24], X-ray [28] and Neutron diffraction [28] have also been used to investigate these changes to the borate network.

In this study, ^{11}B solid-state NMR and neutron diffraction have been applied to investigate the changes in boron and germanium environments in thallium containing glasses. The differences in behaviour compared to alkali containing glasses have also been monitored. Moreover, Raman Spectroscopy has been used to investigate how the borate superstructural units present in the glasses, e.g. boroxol rings, pentaborate, triborate and diborate, change with increase in thallium oxide.

To understand the glass structure, it is sometimes useful to first understand the structure of the crystal phase at the same stoichiometric composition. This is due to the local structure in glass generally mimicking that in the crystal of the corresponding composition, although the distribution of bond angles and bond lengths might be different in glass. To this end, a structural study of the devitrified samples obtained by the heat-treatment of glass samples has been carried out in this thesis.

1.2 Aims of this study

This study has several aims which are listed below:

- To investigate the thallium local environment in thallium borate and thallium germanate glasses using ^{203}Tl and ^{205}Tl solid-state NMR and neutron diffraction. Thallium nuclear magnetic interactions, i.e. chemical shift interaction, dipolar interaction and exchange interaction, detected by Tl solid-state NMR study are sensitive to these changes in thallium. The Tl-O distances in the glasses, determined from the neutron diffraction data, could reflect the changes in thallium coordination number. Tl-Tl distances might be detectable by neutron diffraction technique.
- To investigate the germanate anomaly by determining the changes in germanium local structure in thallium germanate glasses using neutron diffraction and Raman spectroscopy. The densities and molar volumes of the glasses have also been monitored to confirm the relationship between the glass structure and properties.
- To investigate the borate anomaly by determining the changes in boron local structure in thallium borate glasses using ^{11}B solid-state NMR and neutron diffraction. The ability of ^{11}B magic angle spinning (MAS) NMR to distinguish and quantify $[BO_3]$ and $[BO_4]^-$ spectrum are well separated, would be useful to determine the effects of thallium oxide on the anomalous behaviour in borate glasses. Neutron diffraction will give information on the coordination number of boron and thallium in the glasses. Moreover, Raman spectroscopy can distinguish the various borate superstructural units present in the glasses.
- To investigate the effects of the lone pair of electrons of thallium oxide on the structure of borate and germanate glasses.

- To study the thallium environments in crystalline phases, formed by devitrification of thallium borate and thallium germanate glasses, using ^{205}Tl solid-state NMR spectroscopy. Understanding the nuclear magnetic interactions of thallium in crystalline phases will be helpful for recognising thallium environments present in the glasses. Investigation of the changes in thallium environment due to an increase of thallium content in the crystalline phases will be useful to identify possible clustering of thallium ions in the glass.
- To investigate the changes in germanium local structure in crystalline phases devitrified from thallium germanate glasses by Raman spectroscopy.
- To investigate the changes in boron local structure in crystalline phases devitrified from thallium borate glasses by ^{11}B solid-state NMR spectroscopy and Raman spectroscopy.

1.3 Thesis structure

The thesis will be divided into eight chapters, including the introduction chapter. The general points included in each chapter are mentioned below;

Chapter 2 reviews the definition of glass and glass structure and the literature on the structure of germanium oxide glass, boron oxide glass, alkali germanate glasses and alkali borate glasses. The structure of thallium containing glasses is also reviewed.

Chapter 3 briefly describes the theories behind the techniques used to investigate glass and crystal structure in this study including solid-state NMR, neutron scattering, X-ray diffraction (XRD) and Raman spectroscopy. The principles of thermal analysis and gas pycnometry are also mentioned.

Chapters 4 and 6 report and discuss the experimental results obtained from devitrified thallium germanate and borate samples, respectively. The results include thermal analysis of glasses, density and molar volume of crystalline samples. Identification of the phases present in the sample using XRD is described. Moreover, the structure of these crystalline phases will be explained using the data obtained from solid-state NMR and Raman scattering techniques.

Chapters 5 and 7 present the study of thallium germanate and borate glasses, respectively. This includes the density, molar volume, Raman spectra, neutron diffraction data and solid-state NMR results.

Chapter 8 will summarise all the main points obtained in this study along with suggested future work.

1.4 References

[1] W.A. Pisarski, J. Pisarska, M. Mączka, R. Lisiecki, Ł. Grobelny, T. Goryczka, G. Dominiak-Dzik, W. Ryba-Romanowski, *Spectrochimica Acta Part A: Molecular and Biomolecular Spectroscopy*, **79** (2011) 696.

[2] H.R. Fernandes, D.U. Tulyaganov, A. Goel, J.M.F. Ferreira, *Journal of the European Ceramic Society*, **32** (2012) 291.

[3] G. Calas, L. Cormier, L. Galoisy, P. Jollivet, *Comptes Rendus Chimie*, **5** (2002) 831.

[4] Q. Zheng, M. Potuzak, J.C. Mauro, M.M. Smedskjaer, R.E. Youngman, Y. Yue, *Journal of Non-Crystalline Solids*, **358** (2012) 993.

[5] V. Sundar, R. Yimnirun, B.G. Aitken, R.E. Newnham, *Materials Research Bulletin*, **33** (1998) 1307.

[6] F. Moreau, A. Durán, F. Muñoz, *Journal of the European Ceramic Society*, **29** (2009) 1895.

[7] E. Rysiakiewicz, Z. Słowiński, *Journal of Electrostatics*, **11** (1981) 107.

[8] J. Yumoto, S.G. Lee, B. Kippelen, N. Peyghambarian, B.G. Aitken, N.F. Borrelli, *Applied Physics Letters*, **63** (1993) 2630.

[9] J.R. Tressman, A.H. Kahn, W. Shockley, *Physical Review*, **92** (1953) 890.

[10] R.K. Momii, N.H. Nachtrieb, *Journal of Physical Chemistry*, **72** (1968) 3416.

[11] L.W. Panek, P.J. Bray, *Journal of Chemical Physics*, **66** (1977) 3822.

[12] J.F. Baugher, P.J. Bray, *Physics and Chemistry of Glasses*, **10** (1969) 77.

[13] D.J. Payne, R.G. Egdell, A. Walsh, G.W. Watson, J. Guo, P.A. Glans, T. Learmonth, K.E. Smith, *Physical Review Letters*, **96** (2006) 157403.

[14] H. Eckert, W. Müller-Warmuth, W. Hamann, B. Krebs, *Journal of Non-Crystalline Solids*, **65** (1984) 53.

[15] E.R. Barney, A.C. Hannon, N. Laorodphan, R. Dupree, D. Holland, *Journal of Non-Crystalline Solids*, **356** (2010) 2517.

[16] E.R. Barney, A.C. Hannon, N. Laorodphan, D. Holland, *Journal of Physical Chemistry C*, **115** (2011) 14997.

[17] K. Kamiya, S. Sakka, T. Mizuno, K. Matusita, *Physics and Chemistry of Glasses*, **22** (1981) 1.

[18] A. Hannon, D. Martino, L. Santos, R. Almeida, *The Journal of Physical Chemistry B*, **111** (2007) 3342.

[19] G.S. Henderson, *Journal of Non-Crystalline Solids*, **353** (2007) 1695.

[20] G.S. Henderson, L.G. Soltay, H.M. Wang, *Journal of Non-Crystalline Solids*, **356** (2010) 2480.

[21] P.J. Bray, S.A. Feller, G.E. Jellison Jr, Y.H. Yun, *Journal of Non-Crystalline Solids*, **38–39** (1980) 93.

[22] Y.H. Yun, P.J. Bray, *Journal of Non-Crystalline Solids*, **44** (1981) 227.

[23] S.A. Feller, W.J. Dell, P.J. Bray, *Journal of Non-Crystalline Solids*, **51** (1982) 21.

[24] G.E. Jellison Jr, P.J. Bray, *Journal of Non-Crystalline Solids*, **29** (1978) 187.

[25] J.R. Berryman, S.A. Feller, M. Affatigato, M. Kodama, B.M. Meyer, S.W. Martin, F. Borsa, S. Kroeker, *Journal of Non-Crystalline Solids*, **293** (2001) 483.

[26] R.E. Youngman, J.W. Zwanziger, *Journal of the American Chemical Society*, **117** (1995) 1397.

[27] R.E. Youngman, J.W. Zwanziger, *Journal of Physical Chemistry*, **100** (1996) 16720.

[28] I. Yasui, H. Hasegawa, Y. Saito, *Journal of Non-Crystalline Solids*, **106** (1988) 30.

Chapter 2

Introduction to Glass

2.1 Introduction

The structures of alkali germanate and borate glasses have been widely studied, although definite models of glass structure have not yet been confirmed because there are several factors that affect glass structure, for instance: glass composition, purity of glass and thermal history (both heating and cooling). Moreover, glass containing a monovalent lone-pair cation has a different glass structure compared to alkali glass at the same composition. In this thesis, germanate and borate glasses containing thallium, which is a lone-pair cation in its +1 oxidation state, are studied. Knowledge of the structure of glass would be useful for understanding the properties of thallium containing glasses. In addition, since few studies of the structure of thallium containing glasses have been published, the comparison between alkali-containing and thallium-containing glasses would be helpful.

In this chapter, glass and glass structure are defined and explained. Studies of the structures of germanium oxide, boron oxide, alkali germanate and alkali borate glasses are also reviewed. Brief reviews of the structures of thallium-containing germanate and borate glasses are given.

2.2 Definition of glass

Inorganic, organic and metallic materials can form glasses by several processes, such as cooling from melted liquid, vapour deposition [1, 2], sol-gel from liquid solution [3-6] or neutron irradiation of crystalline material [7]. However, some techniques might not be suitable for production scale. Glass is very useful and has many applications, for instance tableware, optic fibres, optical lenses, biomedical applications and devices in electronic equipment.

Glass can be defined in terms of its microstructure and physical properties: glass is an amorphous material, which has no long-range order, and exhibits glass transformation behaviour, which is a region of change in entropy or volume between a supercooled liquid and a “frozen liquid” or glass for both heating and cooling as

illustrated in **Figure 2.1** [8, 9]. The picture also shows differences between the frozen solid or crystalline material, the slow cooled glass and the fast cooled glass. The enthalpy or volume of crystalline material changes suddenly from liquid state to crystalline state under relatively slow cooling condition, the enthalpy or volume then slightly reduces as the temperature reduces, which is related to the heat capacity of the crystal. Thus, the structure of crystalline material certainly changes from that of the liquid due to the complete rearrangement of the atoms to give long-range order. For a glass former, the change of volume or enthalpy continuously reduces from the liquid state, under rapid cooling conditions, to produce a supercooled liquid. The structure of the supercooled liquid is also continuously but subtly rearranged on further cooling but without producing long-range order as in the crystalline material. On further cooling below the glass transition temperature, glass is formed and its entropy or volume deviates from that of the supercooled liquid; this also depends on the cooling rate. A slow cooling rate allows longer for structural rearrangement, the glass transformation region then occurs at a lower temperature. Glass transformation describes the temperature range of the change of enthalpy or volume of supercooled liquid to glass, not an exact temperature, thus the glass transition temperature (T_g), is experimentally taken as the intercept of the slopes of enthalpy or volume of the supercooled liquid and the glass. It is measured using various thermal analysis techniques [10], usually differential thermal analysis (DTA) or differential scanning calorimetry (DSC), which follow the change of sample temperature or enthalpy, respectively, while the sample is being heated or cooled.

2.3 Glass formation and crystallisation

As described above, glass and crystalline phase(s) may be formed from the liquid depending on a cooling condition. However, not only the quenching rate affects the glass formation, but structural aspects of glass forming material must also be considered. Therefore, in this section, the "*kinetic approach*" for glass formation, which relates to the cooling condition of glass forming, and the "*structural approach*" for glass formation will be presented.

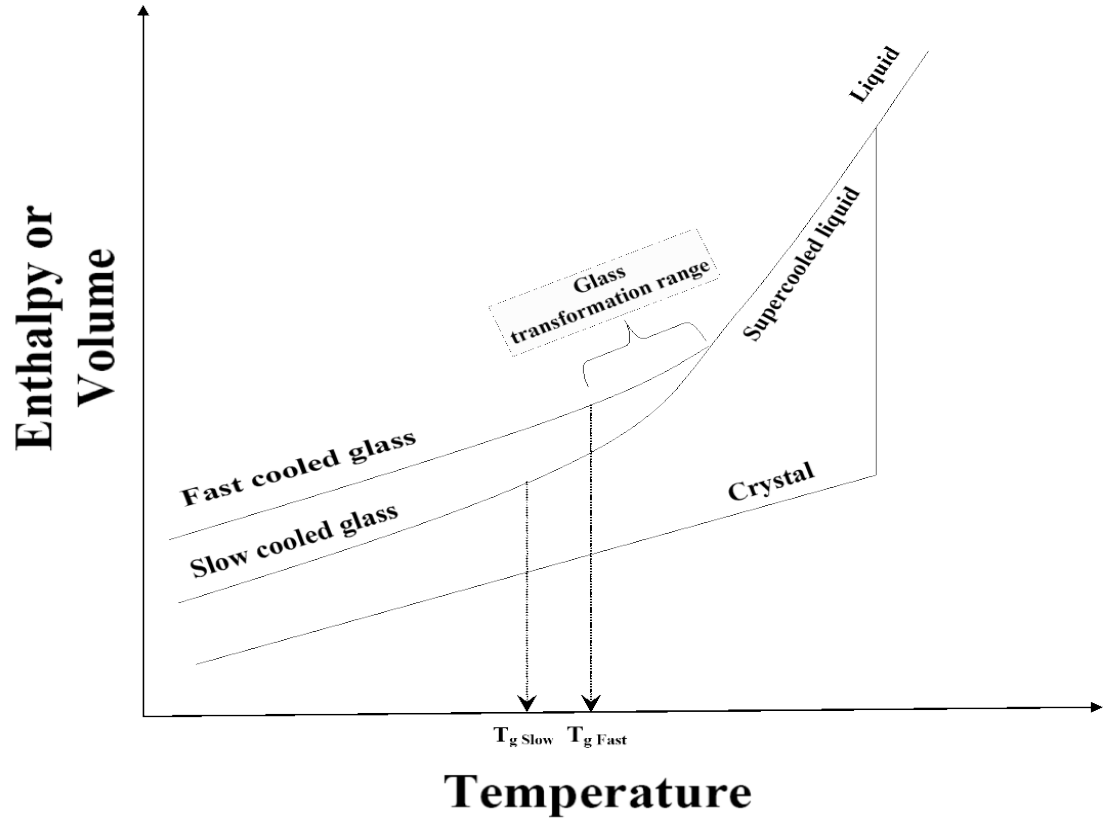

Figure 2.1 *Changes in entropy or volume of matter at various temperature (adapted from [8, 9])*

2.3.1 Kinetic approach

Crystallisation needs nuclei formation (i.e. nucleation) and growth of the crystalline phase(s). Thus, glass formation requires understanding the kinetics of nucleation and growth so as to avoid these processes during the glass forming process.

The kinetic barrier (ΔE_D), the activation energy for atoms to form nuclei, and the thermodynamic barrier (W^*), the free energy change of the system on nucleation, are two main factors that prevent glass from forming nuclei. The nucleation rate (I), usually in number of nuclei formed per unit volume per second, thus includes these two factors as shown in **Equation 2.1**.

$$I = nv \cdot e^{\left(-\frac{N_A W^*}{RT}\right)} \cdot e^{\left(-\frac{\Delta E_D}{RT}\right)} \qquad \textbf{(2.1)}$$

where *nv* is a Boltzmann probability factor to the total maximum rate, N_A is the Avogadro number, *R* is the gas constant and *T* is the absolute temperature.

Once nuclei of a critical size form in the glass, growth will be achieved by again considering the activation energy ($\Delta E'$) and free energy of crystallisation ($-\Delta G_x$). Atomic vibration frequency (v) takes into account atomic movement from liquid site to crystal site or vice versa. **Equations 2.2** and **2.3** express the magnitude of the atomic vibration frequency from the liquid to the crystal (v_{lx}) and from the crystal to the liquid (v_{xl}), respectively.

$$v_{lx} = ve^{\left(-\frac{\Delta E'}{RT}\right)} \quad \textbf{(2.2)}$$

$$v_{xl} = ve^{\left(-\frac{\left(\Delta E' - \Delta G_x\right)}{RT}\right)} \quad \textbf{(2.3)}$$

Thus to consider the rate of crystal growth, u, will be defined as $u = a(v_{lx} - v_{xl})$, where a is the distance between crystal site and liquid site. Substitute with the **Equations 2.2** and **2.3**,

$$u = ave^{\left(-\frac{\Delta E'}{RT}\right)} \cdot \left[1 - e^{\left(\frac{\Delta G_x}{RT}\right)}\right] \quad \textbf{(2.4)}$$

Thus, if the temperature *T* is greater than the melting temperature, T_m, the second term of the equation (with ΔG_x) becomes negative, thus u is negative, which means no crystal growth exists or no crystallisation. At temperature $T<T_m$, the second term is positive, so there is crystal growth. Nucleation (I) and crystal growth (u) can be presented as in **Figure 2.2** against temperature, where the schematic diagram shows that nucleation occurs at lower temperature. The crystallisation proceeds by first nucleation followed by crystal growth, thus an overlap area of both nucleation and growth leads to crystallisation in glass, where the smaller the area, the easier the glass formation.

2.3.2 Structural approach

Several theories concerning structural aspects of glass formation have been proposed in order to explain the structure of glass, which is somewhat challenging, due to the distortion of the structure in glass material. Goldschmidt observed that the radius ratio of a material that could form a glass as r_c/r_o must lie between 0.2-0.4, where r_c and r_o are cation and anion radius respectively. This work was then developed by Zachariasen [11], who considered oxide glass formation where the bonding is mainly ionic.

Zachariasen's rules of glass formation explain that, to form a glass, oxide A_mO_n must achieve;

(1) Oxygen atom will link to more than two A atoms.

(2) The coordination number of A to oxygen must be small.

(3) Only corner sharing is allowed by the oxygen polyhedra.

(4) Each polyhedron must at least share three corners.

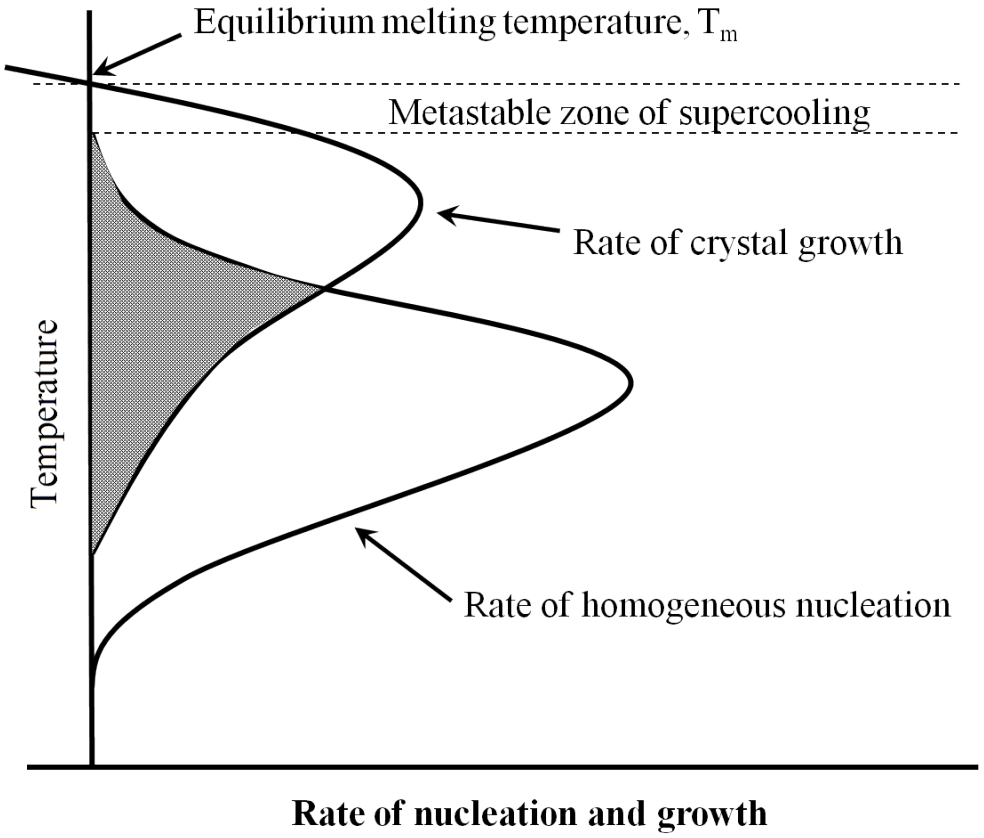

Figure 2.2 *Rate of nucleation and crystal growth at various temperatures below melting temperature (T_m)*

These mean that low coordination number polyhedra present both in crystalline and glassy state, have similar energy. High coulombic attraction in ionic oxide compounds, for example Al_2O_3, Li_2O and Na_2O, leads to edge and face sharing of polyhedra. This suggests that ionic oxide compounds are not good as "*glass formers*". However, more covalent oxides, i.e. B_2O_3, SiO_2 and GeO_2, follow the rules giving formation of triangular (3-coordinated) boron [BO_3] and tetrahedral (4-coordinated) silicon [SiO_4] and germanium [GeO_4], respectively. According to Zachariasen's rules and experimental evidence, [BO_3] triangular units and [SiO_4] or [GeO_4] tetrahedral units are

linked together via corner sharing to another three [BO_3], four [SiO_4] and four [GeO_4] units, respectively. Glass can more easily be produced by addition of "*network modifiers*", for example Li_2O, Na_2O and Cs_2O. The addition of these high ionic oxides causes creation of non bridging oxygen as the bridging oxygen (B-O-B or Si-O-Si or Ge-O-Ge) breaks to obtain balanced charge on the network modifier site. An example in Na_2O-SiO_2 glass is shown in **Figure 2.3**. The oxides, which have glass forming ability or act as network modifiers are listed in **Table 2.1**.

Dietzel [12] used the field strength around cation, F, to explain glass forming ability, expressed by **Equation 2.5.**

$$F = Z_c/a^2 \qquad \textbf{(2.5)}$$

where Z_c is the cation valency and a is a summation of cation and anion radii. The theory mentions that the F values for glass former and network modifier are 1.4 to 2 and 0.1 to 0.4, respectively. The values are also presented in **Table 2.1**.

Standworth [13] and Sun [14] classified oxides into three groups, glass former, glass modifier and intermediate. A good glass former has high electronegativity and could bond with oxygen by a bond of about 50% ionicity. On the other hand, low electronegativity cations form highly ionic bonds with oxygen and are called glass modifier. The intermediate then has character in between. Sun [14] also explained that the glass former should have higher bond strength so as to make crystallisation difficult, therefore the single bond strengths of cations were calculated and used to evaluate glass forming ability. A glass former should have a value higher than 80 kcal/mol and less than 60 kcal/mol for glass modifier (**Table 2.1**).

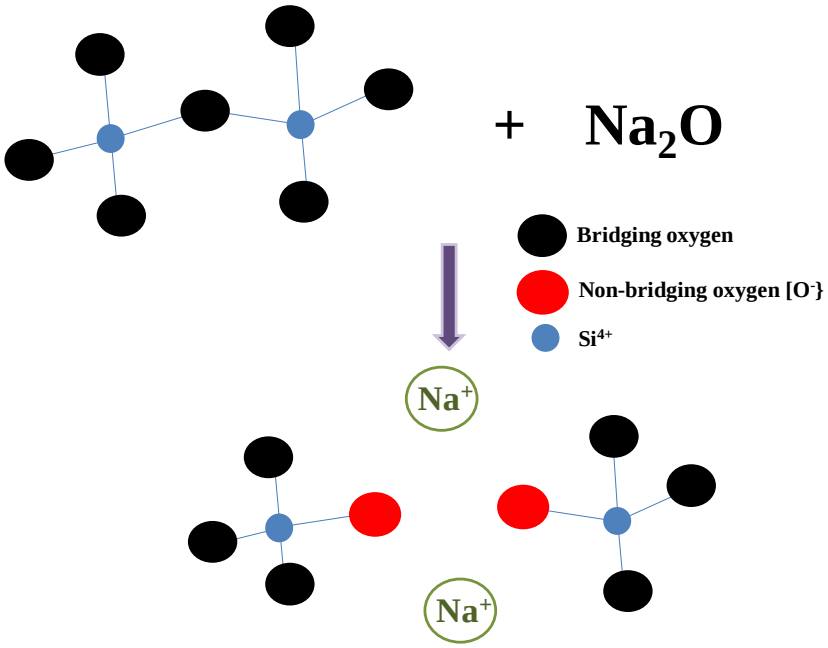

Figure 2.3 *Non-bridging oxygen formation due to the addition of Na_2O in $Na_2O{\cdot}SiO_2$ glass.*

Table 2.1 *Examples of glass former and modifier*

	Elements	Field Strength[12]	Single-Bond Strength (kcal/mol)
Glass Formers	B	1.63 (CN=3)	119 (CN=3)
	Si	1.57	106
	Ge	1.45	108
	P	2.10	111-88
Modifiers	Li	0.23	36
	Na	0.19	20
	K	0.13	13
	Ca	0.33	32
	Ba	0.24	33
	Pb	0.27	39

2.4 Structure of oxide glasses

2.4.1 Boron oxide and germanium oxide glasses

B_2O_3 and GeO_2 containing glasses are used in many applications. Thus, the glass structure was studied in order to understand the behaviour of the glasses. Base glasses B_2O_3 and GeO_2 were initially investigated in addition to the study of the modifier containing glasses.

Krogh-Moe [15] reviewed several models used to describe the structure of B_2O_3 glass, for example, random network model and molecular model. The model that is believed to best describe the B_2O_3 glass structure is the random network model that contains boroxol groups because there is supportive experimental and theoretical evidence [16], corresponding to the existence of the boroxol ring, which is a 6-member ring formed from three [BO_3] units as shown in **Figure 2.4**. The X-ray study by Mozzi and Warren [16] shows good agreement between experimental result and a calculation base on a randomly linked boroxol model. The results showed the pair distribution functions of the atoms, which revealed that three units of planar triangle boron [BO_3], with B-O distance ~1.37 Å, are bonded to form the boroxol group. The B-O-B bond angle is approximately 120° in the ring and approximately 130° for the linkage oxygen (B-O-B) between two boroxol groups. Moreover, Raman spectra revealed that the intense sharp peak at 808 cm^{-1} can be assigned to the localised vibration of the boroxol ring [B_3O_3] [17, 18]. This peak is independent of the boron isotope [19] but dependent on oxygen mass as the shift of the peak was observed in oxygen isotope substitution experiment [19]. The vibrational calculation of B_2O_3 glass structure [20] confirmed that the peak corresponds to the boroxol group vibration. Partial oxygen isotope substitution of $^{11}B_2{}^{16}O_{1.5}{}^{18}O_{1.5}$ glass has also been investigated and confirmed the presence of the boroxol ring by band splitting with ratio 1:3:3:1 [19]. The other broad band at around 1260 cm^{-1} is a delocalised band associated with B-O stretching in both ring and non-ring network [19]. As both boron isotopes have nuclear spin (I) $\geq$1 they experience the quadrupolar interaction in solid-state NMR. An early ^{11}B solid-state NMR study [21] reported only that the boron atom is bonded to three oxygen atoms to form trigonal [BO_3], though later ^{10}B and ^{11}B solid-state NMR studies showed that three [BO_3] trigonal units are bonded to form the boroxol ring [22]. Moreover, the ^{17}O solid-state NMR study of B_2O_3 glass by Jellison et al. [22] concluded that two distinct oxygen environments were in the glass, ring oxygen and non-ring oxygen with a small and large

distribution in asymmetry parameter, respectively. The ratio of ring to non-ring oxygen is approximately 1.2 which indicates that there are more boroxol units in the glass and the non-ring oxygen atoms are bonded mostly between one boroxol ring and one [BO_3] unit. The random network of B_2O_3 glass was then proposed to be a random distribution of [B_3O_3] rings (boroxol) and non-ring [BO_3] units. The B-O-B bond, involving non-ring oxygen, has also been calculated and found to be approximately either 134.6° or 128.1°, though the precise angle is difficult to calculate as it is difficult to assign the principal axes in the glass.

Germanium oxide is polymorphic [23] having rutile-like, α-quartz-like, β-quartz like and chalcedonic structures, although only two polymorphs exist at ambient temperature and pressure [24, 25], which are rutile-like structure [26] and α-quartz like [27]. X-ray and neutron diffraction [28, 29], and raman spectroscopy [24, 30] have been used in amorphous GeO_2 structure studies. X-ray scatting and neutron scattering [28, 29] showed similarity in the X-ray intensity function between the α-quartz structure and vitreous GeO_2 with a small deviation, which means that the structure of glassy GeO_2 is somewhat similar to the α-quartz structure as tetrahedral units ($[GeO_4]^-$) are the basic unit. The X-ray scattering study [29] reported a Ge-O pair correlation peak at about 1.74 Å, which is in agreement with other x-ray and neutron scattering studies. The Ge-O coordination number was also calculated using the K-approximation method giving a value of about 4.46, which differs from the value of 4 from the basic tetrahedral [GeO_4] unit. The experimental value was believed not to be significantly different from the true value of 4 as the calculation error is due to the approximation methods used for data analysis. The second pair correlation peak at about 3.18 Å, corresponds mainly to the distance of Ge-Ge pairs. This allows calculation of the intertetrahedral bond angle (Ge-O-Ge) as approximately 133°. Neutron diffraction [28, 31] showed that the first three peaks of the diffraction pattern correspond to the pair correlation of Ge-O, O-O and Ge-Ge at approximately 1.72, 2.85 and 3.45 Å, respectively. The former study [28] also reported a narrower Ge-O-Ge bond angle distribution compared with that of Si-O-Si in vitreous SiO_2. Absorption results obtained from Raman spectroscopy [24] reported that the peak positions from GeO_2 glass are similar to SiO_2 glass but shifted to lower frequencies due to the larger cation mass of Ge^{4+}. The Raman spectrum shows two peaks corresponding to the asymmetric stretching of Ge-O-Ge at approximately 860 and 998 cm^{-1} and symmetric bending of Ge-O-Ge between 500 and 620 cm^{-1}[24, 30].

The only NMR active isotope for germanium is ^{73}Ge at 7.73% natural abundance with spin, I = 9/2, quadrupole moment = -196 mb and ν_0 = 10.50 MHz at 7.05 T magnetic field (ν_0 is an experimental frequency relative to Larmor frequency of nuclei) [32]. It is very difficult to obtain a useful solid-state NMR spectrum with a low magnetic field instrument due to the large quadrupole moment. Thus, high fields (11.7 T - 21.1 T) have been applied to investigate ^{73}Ge nuclei in single crystals or solids [33-37]. ^{73}Ge solid-state NMR has also been investigated in amorphous material including GeO_2 glass [34, 37] and germanium selenide glass (GeSe) [38]. In GeO_2 glass, a broad resonance at ~ 630 ppm has been obtained from a spin-echo static experiment at 21.1 T. Because of the limited information from ^{73}Ge solid-state NMR due to the low sensitivity of the nucleus, ^{17}O solid-state NMR has been used [39] to estimate the Ge-O-Ge intertetrahedral angle. The results indicated that the angle is about 130°, which is slightly lower than quartz like GeO_2.

2.4.2 Binary oxide glasses

In this study, thallium borate and thallium germanate glasses are of interest. The oxidation state of thallium in glass is +1, like the alkali oxides, so that an understanding of the structure of alkali borate and alkali germanate glasses will be helpful to understand the structure of thallium borate and germanate glasses. Throughout this study, comparison of thallium containing with alkali containing glasses and crystalline phases are made in order to get a clear picture of both their similarities and their differences. Both borate and germanate glasses exhibit a so-called "*anomaly*", in which boron coordination and germanium coordination change with the glass composition. These are the changes from $[BO_3]$ to $[BO_4]^-$ to $[B_2O_2O^-]$ in alkali borate glasses and from $[GeO_4]$ to $[GeO_6]^{2-}$ to $[GeO_3O^-]$ in alkali gernanate glasses. The change in coordination effectively changes the cross-linking of the network (first increasing and then decreasing) such that there are "anomalous" changes in glasses properties manifest as minimum or maximum values as composition of alkali content increases [8]. For example a minimum in thermal expansion coefficient (α) is observed in lithium borate, sodium borate and potassium borate glasses [8] and maxima in density and refractive index are found in sodium germanate and potassium germanate glasses[23]. In this study, as the main purpose is to investigate the structure of glass, only densities and

molar volumes of thallium borate and thallium germanate glasses were determined to check for this anomalous behaviour.

On addition of alkali oxide modifier, for instance Li_2O [40-42], Na_2O [43], Cs_2O [44], K_2O [45] and Rb_2O [46], the borate structure changes due to the formation of tetrahedral boron ($[BO_4]^-$) and (or) non bridging oxygen (NBO). These structural changes are described by the N_4 value, which is the ratio of $[BO_4]^-$ to total boron present in the glass (**Equation 2.16**) and is usually plotted against the modifier oxide content.

$$N_4 = \frac{No.[BO_4]^-}{No.BO_3 + No.[BO_4]^-} \quad \textbf{(2.16)}$$

In binary alkali oxide borate glass, at alkali oxide contents lower than about 33 mol% [44, 47], the N_4 values follow the x/(1-x) relationship where x is described by **Equation 2.17**.

$$x = \frac{Number\ of\ moles R_2O}{Number\ of\ moles R_2O + number\ of\ mole B_2O_3} \quad \textbf{(2.17)}$$

The N_4 values of the higher alkali oxide content glasses decrease significantly due to the formation of non-bridging oxygen (NBO). This behaviour is the so-called borate anomaly. Physical properties, e.g. density and T_g, show anomalous behaviour [48]. Boron environment in binary borate glasses has been investigated using various techniques, i.e. ^{10}B and ^{11}B solid-state NMR [40, 41, 43, 47, 49], neutron scattering [50] and Raman spectroscopy [51]. Krogh-Moe [52] showed that alkali borate glass structure is composed of superstructural units, e.g. boroxol ring, tetraborate and diborate, forming a random network depending on the content of alkali oxide. **Figure 2.4** presents the reported superstructural units present in borate glasses [52, 53]. The existence of each superstructure unit has been reported both quantitatively [40, 42, 54] and qualitatively [53, 55]. Early NMR studies of lithium borate glass [40] showed the presence of for instance tetraborate, diborate, metaborate and so on, reflecting the stoichiometric crystalline phases at the corresponding composition. For example, at the composition of 25 mol% Li_2O, closes to lithium diborate: $Li_2O{\cdot}2B_2O_3$, the boron spectra show the presence of diborate units, but distortion is expected in glasses [42]. Quantitative analysis based on boron NMR results and the Krogh-Moe structural model of lithium borate glasses, showed glass structure could be divided into three regions depending on lithium oxide content [42]. First, at the composition $0 \leq$ mol% $Li_2O \leq 30$, glasses are composed of boroxol, tetraborate and diborate. Glasses at compositions between 30 and 50 mol% Li_2O contain a mixture of tetraborate, diborate, metaborate and loose $[BO_4]^-$.

Finally, beyond 50 mol% Li_2O glasses there are only loose $[BO_4]^-$, metaborate, pyroborate and orthoborate units found.

Raman spectroscopy has been applied extensively to the borate glass structure [56-59]. The peak positions corresponding to the vibrational modes of the superstructural units have been reported [53, 55] and used as guidelines in Raman studies of borate glass recently. Moreover, quantitative calculation of structural units has also been studied by Raman spectroscopy [54]. Raman study [57] showed that large $[BO_4]^-$ containing superstructural units are unfavourable with heavier alkali ions, thus the formation of non-bridging oxygens is predominant, causing a weaker B-O network leading to lower glass transition temperatures. Finally, neutron diffraction [50] gave information on bond distances of the short-range order in borate glasses containing the same fraction of Li_2O, Na_2O and Ag_2O. The effects of alkali oxide type on B-O, B-B and O-O distances were barely observable. The third peak, attributable mainly to O-O distance in boron superstructure units, may include the M-O distances leading to difficulty in M-O bond length determination (M is alkali metal). B-O bond lengths in $[BO_3]$ triangular units and $[BO_4]^-$ tetrahedral units have been indicated at about 1.37 and 1.47 Å, respectively. The M^+ distance and coordination number of oxygen atoms around M^+ ion depend on M^+. M-O distances were respectively reported to be about 2.0, 2.3 and 2.4 for Li-O, Na-O and Ag-O. Moreover, the coordination number is about 4 for Li^+ and Ag^+ and about 6 for Na^+.

Unlike silicate glass, change in germanium coordination to oxygen from 4 to higher was reported on addition of alkali oxide [60-63], while silicate glass shows only change in Q-species of $[SiO_4]$, which relate to the number of bridging or non-bridging oxygen atoms of tetrahedral units [64, 65]. Like alkali borate, alkali germanate glasses also show anomalous behaviour, again due to change in Ge-O coordination number [61, 62, 66-71]. Although, other model have been proposed which retain the $[GeO_4]$ environment but form ring structures [71, 72].

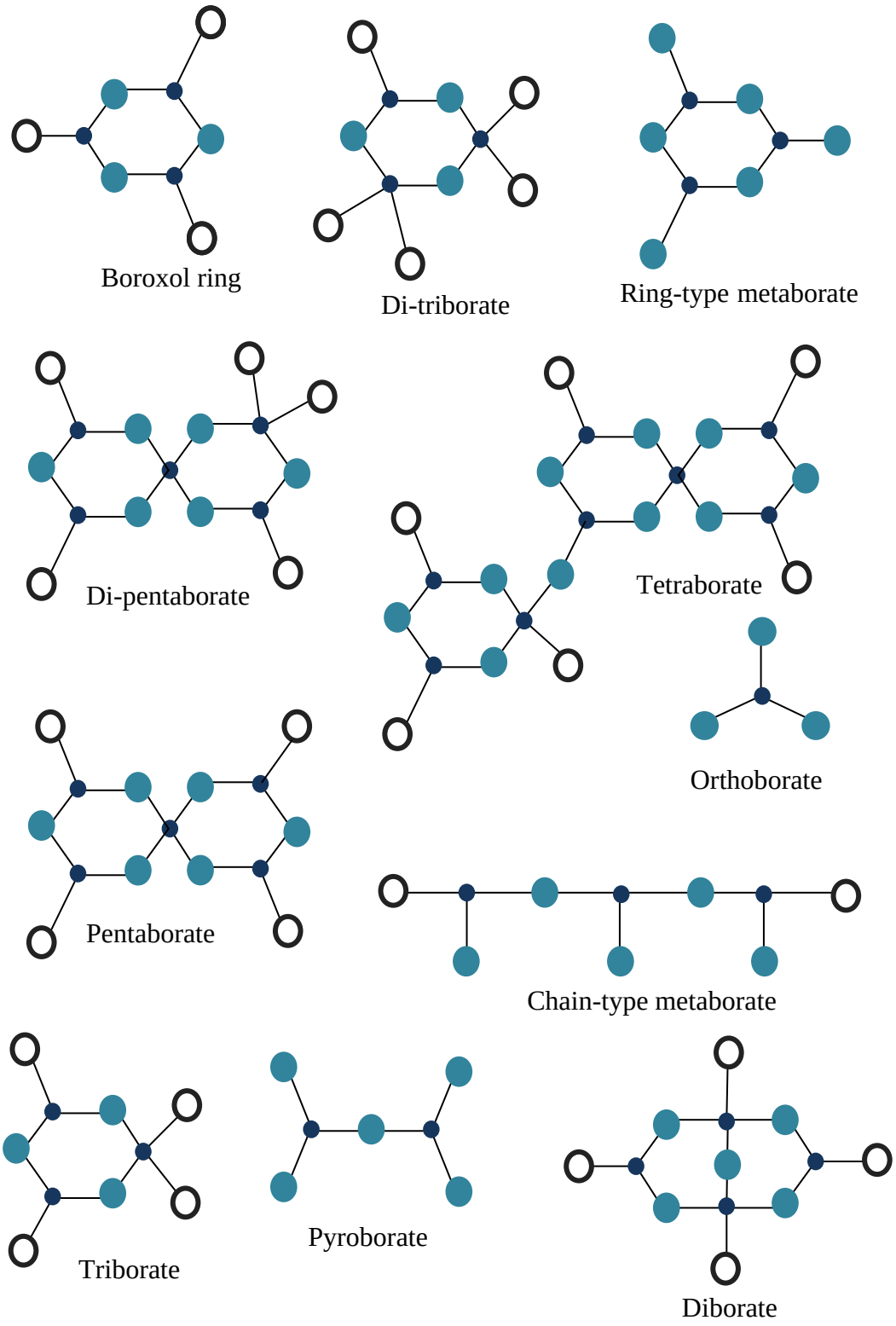

Figure 2.4 *Superstructural units found in binary borate glasses [53, 54].*

Several techniques e.g. neutron diffraction [61], electron paramagnetic resonance (EPR) [62], extended X-ray absorption fine structure (EXAF), X-ray diffraction [67] and Raman spectroscopy [68-71] have been applied to the structural study of germanate glasses. It has been reported that the [GeO_5] or [GeO_6] units have been formed as the alkali content increases. In addition, formation of non-bridging oxygen (NBO) was also detected [73], though not in low alkali content glasses (less than 20 mol%) [63, 66]. Thus, anomalous behaviour is explained by successive change in Ge-O coordination number and the formation of non-bridging oxygen atoms.

2.5 Example of lead containing glasses

Lead oxide (PbO) is an example of an oxide of a lone-pair cation, which is used extensively as a component in oxide glasses. Their structures are comparatively well-known compared to thallium containing glasses [74-83]. However, the oxidation state of Pb in PbO is +2, whereas it is +1 for thallium oxide (Tl_2O). In $PbO{\cdot}B_2O_3$ glasses, an X-ray diffraction study [83] showed that PbO acts as either network modifier or network former depending on the glass composition. At PbO content < 40 mol%, PbO is a network modifier, where the Pb-O coordination number is 6; [PbO_6]. Glasses with 40 – 70 mol% PbO contain [PbO_6] and [PbO_4] environments, which indicates a mixed role of network modifier and network former, respectively. In higher PbO content glass (70-80 mol%), PbO acts as the network former and [PbO_3] units are formed instead. ^{11}B NMR has also revealed that N_4 values increase as PbO enters the network up until the 50 mol% composition, where N_4 suddenly reduces. Takaishi et.al. [83] discussed that two $[BO_4]^-$ units are converted from [BO_3] units as one PbO is introduced into the network yielding the increase in N_4 values. However, N_4 is reportedly below the theoretical line, which is believed to be due to the formation of non-bridging oxygen containing [BO_2O^-] unit instead increase in coordination number. It is of interest to observe changes in coordination number and network-former or modifier role of lone-pair Tl^+.

2.6 Structure of thallium containing germanate and borate glasses in comparison with alkali containing glasses

Thallium (Tl) containing glasses are of interest due to the presence of a large optical non-linearity response [84], due to the high polarisability of Tl^+ [85]. Thallium in

its +1 oxidation state has a lone pair of electrons, which could be in a sterically active or inert environment and may also affect the glass structure, though the effect of the lone pair cation on overall glass structure has not yet been explained. The activity of the lone pair of electrons depends on the hybridisation of the electron orbitals of thallium. If only the lone pair of electrons occupies a purely s electron orbital, it is sterically inert. On the other hand, a sterically active lone pair of electrons occupies an sp^3 hybridised orbital or an sp3d hybridised orbital as in PbO crystal [86, 87]. This results in a distorted Pb environment where the 4 oxygen nearest neighbours are all located at one side of the Pb atom opposite the lone pair of electrons. In general summary, thallium has been found to be present in two different environments, a symmetric ionic environment at low thallium content (below 18 mole % for thallium borate glasses [88]) and an asymmetric covalent environment at high thallium content [89, 90]. Thallium pairs or clusters, with possible shortest 4.0 Å Tl-Tl distance in thallium borate glasses [91], have also been reported to occur in high thallium content glasses [89, 92, 93]**.** Thallium solid-state NMR studies [89, 93] showed a strong exchange interaction between thallium nuclei, which supports the presence of thallium pairs or clusters.

Thallium borate glasses have been studied structurally using various techniques, including ^{11}B, ^{203}Tl and ^{205}Tl solid-state NMR [89, 90, 93], X-ray diffraction [91, 94], neutron diffraction [94] and Raman spectroscopy [94]. Baugher and Bray [90] concluded, from a wide-line thallium solid-state NMR study, that a spherically symmetric ionic thallium unit is present in low thallium content glass, whereas the higher thallium content glass contains mainly non-spherically symmetric covalent units instead. Thallium thus behaves more like a glass modifier in low thallium content glasses and a glass former at high contents. Large chemical shift anisotropy and Tl-Tl exchange interactions were observed in the NMR study [89, 93]. Chemical shift interaction dominates at low thallium contents whilst, at high thallium contents glass, the exchange interaction dominates the spectrum suggesting there is a change in the thallium environment with thallium atoms located closer to each other. Panek and Bray [89] proposed that there are pairs of thallium (Tl-Tl) or clusters in high thallium content borate glasses. This is consistent with the study of thallium borate glass by X-ray diffraction [91] which showed pairs or large thallium clusters are formed in the glass with the shortest Tl-Tl distance at 4 Å as mentioned above. Eckert *et.al.* [95] studied thallium NMR in the $Tl_2S{\cdot}B_2S_3$ system showing that there are two thallium site in this

chalcogenide glass from the investigation of chemical shift anisotropy and Tl-Tl pseudoexchange interaction.

Changes in the boron environment in thallium borate glasses have also been investigated, mainly using solid-state NMR [90], which revealed that boron atoms are converted from three coordinated to four coordinated as Tl_2O content increases. At a molar fraction (x) of thallium oxide between 0 - 0.2, addition of one unit of Tl_2O causes the conversion of three $[BO_3]$ to $[BO_4]^-$, where as only two boron atoms are converted for $0.2 < x < 0.4$. Above this point, non bridging oxygen are formed. Two types of $[BO_4]^-$ units have been proposed, one with three-coordinated oxygen (one oxygen atom linked to 3 boron atoms) and one without [90]. It should be noted that it is hard to find an example of a glass or crystal that contains three-coordinated oxygen, which indicates that the presence of this type of $[BO_4]^-$ unit is doubtful. N_4 values obtained from the NMR study [90] are well above the predicted x/(1-x) value, which was explained by this formation of three-coordinated oxygen involving $[BO_4]^-$ units. A diffraction study of $Tl_2O{\cdot}B_2O_3$ glass [94] showed a much higher $[BO_4]^-$ concentration, which supports the high N_4 value compared to alkali borate glasses of the same composition. However, no three-coordinated oxygen was found in $Tl_2O{\cdot}2B_2O_3$ and $Tl_2O{\cdot}4B_2O_3$ glasses, since there was no peak at 3.1 Å, which corresponds to the B-O pairs in $[BO_4]^-$ tetrahedra linked by three-coordinated oxygen in $SrO{\cdot}2B_2O_3$ crystal. Raman spectroscopy also indicated that there was no three-coordinated oxygen present in thallium borate glasses [94].

In this thesis, ^{11}B solid-state NMR and neutron diffraction are combined to study the structure of thallium borate glass in order to identify the two types of thallium site and understand the abnormal variation of N_4 with x.

Thallium environments in thallium germanate glasses have been reported as very similar to the those in thallium borate glasses [89], the only difference being the composition of the glass where the pairs or clusters were formed. The pairs or clusters were formed; $x = 0.20$ in thallium germanate glasses, and $x = 0.30$ in thallium borate glasses. There are few reports of the germanium coordination changes in thallium germanate glasses. Riebling [96] reported a change from $[GeO_4]$ to $[GeO_6]^{2-}$ units as more thallium oxide was added.

This thesis reports the use of various techniques: ^{203}Tl and ^{205}Tl solid-state NMR, neutron diffraction and Raman spectroscopy, in order to investigate the changes in thallium and germanium environments in thallium germanate glasses.

2.7 References

[1] C. Boussardpledel, G. Fonteneau, J. Lucas, *Journal of Non-Crystalline Solids*, **188** (1995) 147.

[2] C. BoussardPledel, M. LeFloch, G. Fonteneau, J. Lucas, *Materials Research Bulletin*, **32** (1997) 805.

[3] Q. Xiang, Y. Zhou, Y.L. Lam, Y.C. Chan, C.H. Kam, B.S. Ooi, H.X. Zhang, S. Buddhudu, *Materials Research Bulletin*, **35** (2000) 1571.

[4] N. Olmo, A.I. Martin, A.J. Salinas, J. Turnay, M. Vallet-Regi, M.A. Lizarbe, *Biomaterials*, **24** (2003) 3383.

[5] H. Aguiar, J. Serra, P. Gonzalez, B. Leon, *Journal of Non-Crystalline Solids*, **355** (2009) 475.

[6] S. Rada, A. Dehelean, M. Stan, R. Chelcea, E. Culea, *Journal of Alloys and Compounds*, **509** (2011) 147.

[7] W. Jiang, Y. Zhang, W.J. Weber, *Physical Review B*, **70** (2004) 165208.

[8] W. Vogel, *Glass Chemistry*, Springer-Verlag (1994).

[9] J.E. Shelby, *Introduction to Glass Science and Technology*, The Royal Society of Chemistry (2005).

[10] M.E. Brown, *Introduction to Thermal Analysis- Techniques and Applications*, Chapman and Hall (1988).

[11] W.H. Zachariasen, *Journal of the American Ceramic Society*, **54** (1932) 3841.

[12] A. Dietzel, *Zeitschrift Fur Elektrochemie*, **48** (1942) 9.

[13] J.E. Standworth, *The Journal of the Society of Glass Technology*, **30** (1946) 54.

[14] K.H. Sun, *Journal of The American Ceramic Society*, **30** (1974) 277.

[15] J. Krogh-Moe, *Journal of Non-Crystalline Solids*, **1** (1969) 269.

[16] R.L. Mozzi, B.E. Warren, *Journal of Applied Crystallography*, **3** (1970) 251.

[17] L.A. Kilstiansen, J. Krogh-Moe, *Physics and Chemistry of Glasses*, **9** (1968) 96.

[18] F.L. Galeener, G. Lucovsky, J.C. Mikkelsen, *Physical Review B*, **22** (1980) 3983.

[19] C.F. Windisch Jr, W.M. Risen Jr, *Journal of Non-Crystalline Solids*, **48** (1982) 307.

[20] M.A. Kanehisa, R.J. Elliott, *Materials Science and Engineering B-Solid State Materials for Advanced Technology*, **3** (1989) 163.

[21] A.H. Silver, P.J. Bray, *Journal of Chemical Physics*, **29** (1958) 984.

[22] G.E. Jellison, L.W. Panek, P.J. Bray, G.B. Rouse, *Journal of Chemical Physics*, **66** (1977) 802.

[23] A. Margaryan, M.A. Piliavin, *Germanate Glasses – Structure, Spectroscopy and Properties*, Artech House (1993).

[24] M. Micoulaut, L. Cormier, G.S. Henderson, *Journal of Physics-Condensed Matter*, **18** (2006) R753.

[25] J.F. Scott, *Physical Review B*, **1** (1970) 3488.

[26] W.H. Baur, A.A. Khan, *Acta Crystallographica Section B - Structural Crystallography and Crystal Chemistry*, **27** (1971) 2133.

[27] G.S. Smith, P.B. Isaacs, *Acta Crystallographica*, **17** (1964) 842.

[28] J.A.E. Desa, A.C. Wright, R.N. Sinclair, *Journal of Non-Crystalline Solids*, **99** (1988) 276.

[29] A. Leadbetter, A. Wright, *Journal of Non-Crystalline Solids*, **7** (1972) 37.

[30] F.L. Galeener, G. Lucovsky, *Physical Review Letters*, **37** (1976) 1474.

[31] E. Lorch, *Journal of Physics Part C: Solid State Physics*, **2** (1969) 229.

[32] K.J.D. MacKenzie, M.E. Smith, *Multinuclear solid-state NMR of inorganic materials*, Pergamon (2002).

[33] S.V. Verkhovskii, A.Y. Yakubovskii, A. Trokiner, B.Z. Malkin, S.K. Saikin, V.I. Ozhogin, A.V. Tikhomirov, A.V. Ananyev, A.P. Gerashenko, Y.V. Piskunov, *Applied Magnetic Resonance*, **17** (1999) 557.

[34] J.F. Stebbins, L.S. Du, S. Kroeker, P. Neuhoff, D. Rice, J. Frye, H.J. Jakobsen, *Solid State Nuclear Magnetic Resonance*, **21** (2002) 105.

[35] S.V. Verkhovskii, A.Y. Yakubovsky, B.Z. Malkin, S.K. Saikin, M. Cardona, A. Trokiner, V.I. Ozhogin, *Physical Review B*, **68** (2003) 104201.

[36] Y. Takeuchi, M. Nishikawa, H. Yamamoto, *Magnetic Resonance in Chemistr*y, **42** (2004) 907.

[37] V.K. Michaelis, P.M. Aguiar, V.V. Terskikh, S. Kroeker, *Chemical Communications*, **31** (2009) 4660.

[38] S. Sen, Z. Gan, *Journal of Non-Crystalline Solid*s, **356** (2010) 1519.

[39] R. Hussin, R. Dupree, D. Holland, *Journal of Non-Crystalline Solids*, **246** (1999) 159.

[40] P.J. Bray, S.A. Feller, G.E. Jellison Jr, Y.H. Yun, *Journal of Non-Crystalline Solids*, **38–39** (1980) 93.

[41] Y.H. Yun, P.J. Bray, *Journal of Non-Crystalline Solids*, **44** (1981) 227.

[42] S.A. Feller, W.J. Dell, P.J. Bray, *Journal of Non-Crystalline Solids*, **51** (1982) 21.

[43] G.E. Jellison Jr, P.J. Bray, *Journal of Non-Crystalline Solids*, **29** (1978) 187.

[44] J.R. Berryman, S.A. Feller, M. Affatigato, M. Kodama, B.M. Meyer, S.W. Martin, F. Borsa, S. Kroeker, *Journal of Non-Crystalline Solids*, **293** (2001) 483.

[45] R.E. Youngman, J.W. Zwanziger, *Journal of Physical Chemistry*, **100** (1996) 16720.

[46] R.E. Youngman, J.W. Zwanziger, *Journal of the American Chemical Society*, **117** (1995) 1397.

[47] J.H. Zhong, P.J. Bray, *Journal of Non-Crystalline Solids*, **111** (1989) 67.

[48] M. Royle, J. MacKenzie, J. Taylor, M. Sharma, S. Feller, Densities, *Journal of Non-Crystalline Solids*, **177** (1994) 242.

[49] J. Banerjee, G. Ongie, J. Harder, T. Edwards, C. Larson, S. Sutton, A. Moeller, A. Basu, M. Affatigato, S. Feller, M. Kodama, P.M. Aguiar, S. Kroeker, *Journal of Non-Crystalline Solids*, **352** (2006) 674.

[50] J. Swenson, L. Borjesson, W.S. Howells, *Physical Review B*, **52** (1995) 9310.

[51] M. Irion, M. Couzi, A. Levasseur, J.M. Reau, J.C. Brethous, *Journal of Solid State Chemistry*, **31** (1980) 285.

[52] J. Krogh-Moe, *Physics and Chemistry of Glasses*, **6** (1965) 46.

[53] W.L. Konijnendijk, J.M. Stevels, *Journal of Non-Crystalline Solids*, **18** (1975) 307.

[54] T. Yano, N. Kunimine, S. Shibata, M. Yamane, *Journal of Non-Crystalline Solids*, **321** (2003) 137.

[55] B.P. Dwivedi, M.H. Rahman, Y. Kumar, B.N. Khanna, *Journal of Physics and Chemistry of Solids*, **54** (1993) 621.

[56] J. Lorösch, M. Couzi, J. Pelous, R. Vacher, A. Levasseur, *Journal of Non-Crystalline Solids*, **69** (1984) 1.

[57] B.P. Dwivedi, B.N. Khanna, *Journal of Physics and Chemistry of Solids*, **56** (1995) 39.

[58] B.N. Meera, J. Ramakrishna, *Journal of Non-Crystalline Solids*, **159** (1993) 1.

[59] E.I. Kamitsos, G.D. Chryssikos, *Journal of Molecular Structure*, **247** (1991) 1.

[60] D.G. Galimov, G.O. Karapetyan, V.K. Pavlovskii, Y. D.M., *Zhurnal Struktumoi Khimii*, **9** (1968) 883.

[61] A. Hannon, D. Martino, L. Santos, R. Almeida, *The Journal of Physical Chemistry B*, **111** (2007) 3342.

[62] U. Hoppe, R. Kranold, H.J. Weber, A.C. Hannon, *Journal of Non-Crystalline Solids*, **248** (1999) 1.

[63] M. Ueno, M. Misawa, K. Suzuki, *Physica B*, **120** (1983) 347.

[64] O. Gedeon, M. Liška, J. Macháček, *Journal of Non-Crystalline Solids*, **354** (2008) 1133.

[65] B.G. Parkinson, D. Holland, M.E. Smith, C. Larson, J. Doerr, M. Affatigato, S.A. Feller, A.P. Howes, C.R. Scales, *Journal of Non-Crystalline Solids*, **354** (2008) 1936.

[66] H. Jain, E.I. Kamitsos, Y.D. Yiannopoulos, G.D. Chryssikos, W.C. Huang, R. Kuchler, O. Kanert, *Journal of Non-Crystalline Solids*, **203** (1996) 320.

[67] S. Sakka, K. Kamiya, *Journal of Non-Crystalline Solids*, **49** (1982) 103.

[68] H. Verweij, J. Buster, *Journal of Non-Crystalline Solids*, **34** (1979) 81.

[69] E.I. Kamitsos, Y.D. Yiannopoulos, M.A. Karakassides, G.D. Chryssikos, H. Jain, *Journal of Physical Chemistry*, **100** (1996) 11755.

[70] T. Furukawa, W.B. White, *Journal of Materials Science*, **15** (1980) 1648.

[71] G.S. Henderson, M.E. Fleet, *Journal of Non-Crystalline Solids*, **134** (1991) 259.

[72] G.S. Henderson, *Journal of Non-Crystalline Solids*, **353** (2007) 1695.

[73] D.L. Price, A.J.G. Ellison, M.L. Saboungi, R.Z. Hu, T. Egami, W.S. Howells, *Physical Review B*, **55** (1997) 11249.

[74] A. Saini, A. Khanna, V.K. Michaelis, S. Kroeker, F. González, D. Hernández, *Journal of Non-Crystalline Solids*, **355** (2009) 2323.

[75] W.A. Pisarski, T. Goryczka, B. Wodecka-Duś, M. Płońska, J. Pisarska, *Materials Science and Engineering B*, **122** (2005) 94.

[76] J. Pisarska, L. Żur, T. Goryczka, W.A. Pisarski, *Journal of Rare Earths*, **29** (2011) 1157.

[77] W.A. Pisarski, J. Pisarska, M. Mączka, R. Lisiecki, Ł. Grobelny, T. Goryczka, G. Dominiak-Dzik, W. Ryba-Romanowski, *Spectrochimica Acta Part A: Molecular and Biomolecular Spectroscopy*, **79** (2011) 696.

[78] V. Martin, B. Wood, U. Werner-Zwanziger, J.W. Zwanziger, *Journal of Non-Crystalline Solids*, **357** (2011) 2120.

[79] V.N. Sigaev, I. Gregora, P. Pernice, B. Champagnon, E.N. Smelyanskaya, A. Aronne, P.D. Sarkisov, *Journal of Non-Crystalline Solids*, **279** (2001) 136.

[80] D. De Sousa Meneses, M. Malki, P. Echegut, *Journal of Non-Crystalline Solids*, **352** (2006) 769.

[81] H. Ushida, Y. Iwadate, T. Hattori, S. Nishiyama, K. Fukushima, Y. Ikeda, M. Yamaguchi, M. Misawa, T. Fukunaga, T. Nakazawa, S. Jitsukawa, *Journal of Alloys and Compounds*, **377** (2004) 167.

[82] N. Umesaki, T.M. Brunier, A.C. Wright, A.C. Hannon, R.N. Sinclair, *Physica B: Condensed Matter*, **213–214** (1995) 490.

[83] T. Takaishi, J. Jin, T. Uchino, T. Yoko, *Journal of the American Ceramic Society*, **83** (2000) 2543.

[84] J. Yumoto, S.G. Lee, B. Kippelen, N. Peyghambarian, B.G. Aitken, N.F. Borrelli, *Applied Physics Letters*, **63** (1993) 2630.

[85] J.R. Tressman, A.H. Kahn, W. Shockley, *Physical Review*, **92** (1953) 890.

[86] J. Leciejewicz, *Acta Crystallographica*, **14** (1961) 1304.

[87] J. Hill, *Acta Crystallographica*, **41** (1985) 1281.

[88] R.K. Momii, N.H. Nachtrieb, *Journal of Physical Chemistry*, **72** (1968) 3416.

[89] L.W. Panek, P.J. Bray, *Journal of Chemical Physics*, **66** (1977) 3822.

[90] J.F. Baugher, P.J. Bray, *Physics and Chemistry of Glasses*, **10** (1969) 77.

[91] K. Kamiya, S. Sakka, T. Mizuno, K. Matusita, *Physics and Chemistry of Glasses*, **22** (1981) 1.

[92] J. Krogh-Moe, H. Jürine, *Physics and Chemistry of Glasses*, **6** (1965) 30.

[93] L.W. Panek, *Nuclear Magnetic Resonance Studies of Tl^{203}, Tl^{205}, and O^{17} in Oxide Glasses*, Ph.D. thesis, Brown University (1977).

[94] I. Yasui, H. Hasegawa, Y. Saito, *Journal of Non-Crystalline Solids*, **106** (1988) 30.

[95] H. Eckert, W. Müller-Warmuth, W. Hamann, B. Krebs, *Journal of Non-Crystalline Solids*, **65** (1984) 53.

[96] F.F. Riebling, *Journal of Chemical Physics*, **55** (1971) 804.

Chapter 3

Experimental Techniques

3.1 Introduction

This chapter gives brief descriptions of the background theories of the techniques used in this study, namely solid-state nuclear magnetic resonance (NMR), neutron diffraction, Raman spectroscopy, X-ray diffraction (XRD), differential thermal analysis and gas pycnometry.

3.2 Solid-state nuclear magnetic resonance (Solid-state NMR) [1-6]

3.2.1 Basic principles

Solid-state NMR spectroscopy [7, 8] has greatly improved the understanding of glass structure, although it can only be applied to glass containing NMR active nuclei, which are nuclei with spin, I > 0 e.g. ^{11}B, ^{27}Al, ^{29}Si, ^{17}O, ^{203}Tl and ^{205}Tl. This is because NMR arises from the various interactions between the nuclear magnetic dipole moment ($\vec{\mu}$) of nuclei in the sample and internal and external magnetic fields. These interactions are for example the Zeeman interaction, dipolar interaction, quadrupolar interaction and chemical shift interaction. In general, the separation (ΔE) of the energy levels of a nucleus is dependent on the magnetic field strength (B) according to the relationship shown in **Equation 3.1**.

$$\Delta E = \gamma \cdot \hbar \mathrm{B} \qquad \textbf{(3.1)}$$

where γ is the gyromagnetic ratio of the nucleus and $\hbar$ is the reduced Planck constant which is equal to $h/2\pi$. In the NMR experiment, electromagnetic radiation of frequency ν_0 is applied to the system at the resonance condition ($h\nu_0 = \Delta E$), then the nuclei at lower energy level (spin aligned with the field if γ is positive) are excited to the higher energy level (spin opposed). The absorption peak detected is then sharp, though broadening can occur due to the presence of other interactions.

Assuming that the sample is in the static magnetic field, B_0, a small excess of nuclear spins in the sample will be preferentially oriented with the magnetic field, giving a net magnetisation M_0 parallel to the z-axis (defined as the field direction). In order to perform the pulse NMR experiment, the radio frequency (r.f.) pulse with the

Larmor frequency (ω_0), which is the frequency at which the nuclei are precessing about the magnetic field B ($\omega_0=\gamma B$), is applied to the sample along the x-axis, causing the net magnetisation to rotate towards the x-y plane. If this r.f. pulse is applied to the nuclei for a period of time τ, the magnetisation vector will rotate by the angle $\gamma H_1 \tau$ away from the z-axis as shown in **Figure 3.1**, where H_1 is the r.f. field perpendicular to the applied magnetic field B_0. Usually a 90° ($\pi/2$) r.f. pulse is applied to the nuclei in an NMR experiment, after which the net magnetisation will be in the x-y plane (transverse magnetisation, M_{XY0}). Immediately after the 90° r.f. pulse is completed, the magnetisation will decay in the x-y plane by two processes. The NMR signal, called the free-induction decay (FID), is the r.f. signal produced by the rotating transverse magnetisation and thus also decays after the pulse is completed. Since the magnetisation is inhomogeneous, due to the effect of nuclear interaction, e.g. chemical shift anisotropy, dipole-interaction and exchange interaction, the precession of the magnetisation of individual nuclei in the x-y plane occurs at different speeds and the spins dephase. The net transverse magnetisation of the system will thus decay to zero at the rate = $e^{\left(-t/T_2\right)}$ (**Figure 3.1)**, where T_2 is the transverse or spin-spin relaxation time.

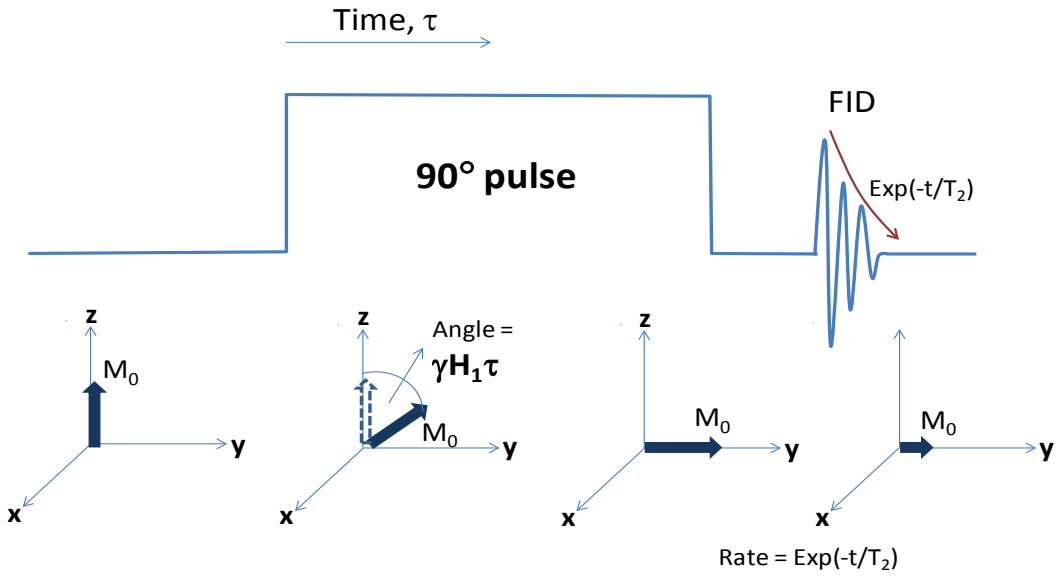

Figure 3.1 *Schematic diagram shows the T_2 relaxation time when 90° pulse applied.*

The signal also decays because the net magnetisation will eventually re-establish its equilibrium value with respect to the z-axis (i.e. the applied field) at a rate with time constant T_1 (the longitudinal or spin-lattice relaxation time) (**Figure 3.2**) producing a net magnetisation (Mz), at time t after the pulse, given by;

$$M_z = M_0\left(1 - e^{\left(-t/T_1\right)}\right) \qquad \textbf{(3.2)}$$

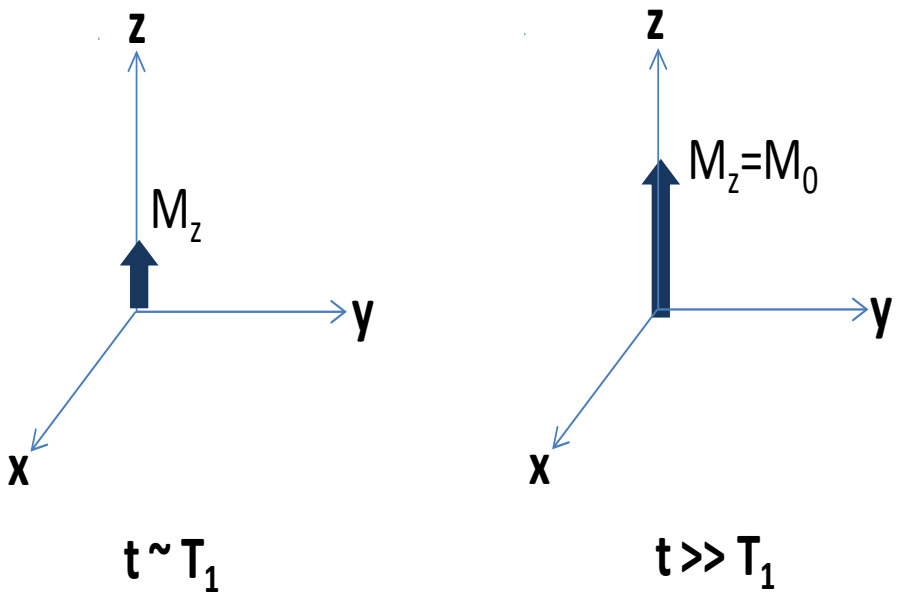

Figure 3.2 *Schematic diagram shows the recovery of net magnetisation dependent on T_1 [from [6]].*

The NMR spectrum is then obtained from the Fourier transformation of the FID, form the time domain to the frequency domain. In Fourier transform NMR, the rectangular 90° pulse is applied to the nuclei for the time τ (**Figure 3.1**). In case of a broad NMR spectrum, like that from thallium nuclei in this study, it is important to irradiate with the appropriate conditions. The Fourier transformation of a rectangular pulse in the time domain yields sinc function in the frequency domain. The amplitude A(ν) of the pulse is then given by

$$A(\nu) = \frac{\sin \pi\tau(\nu_0 - \nu)}{\pi(\nu_0 - \nu)\tau} \qquad \textbf{(3.3)}$$

as simply explained using **Figure 3.3**. Therefore, the wider NMR line, the shorter the pulse length should be in the NMR experiment.

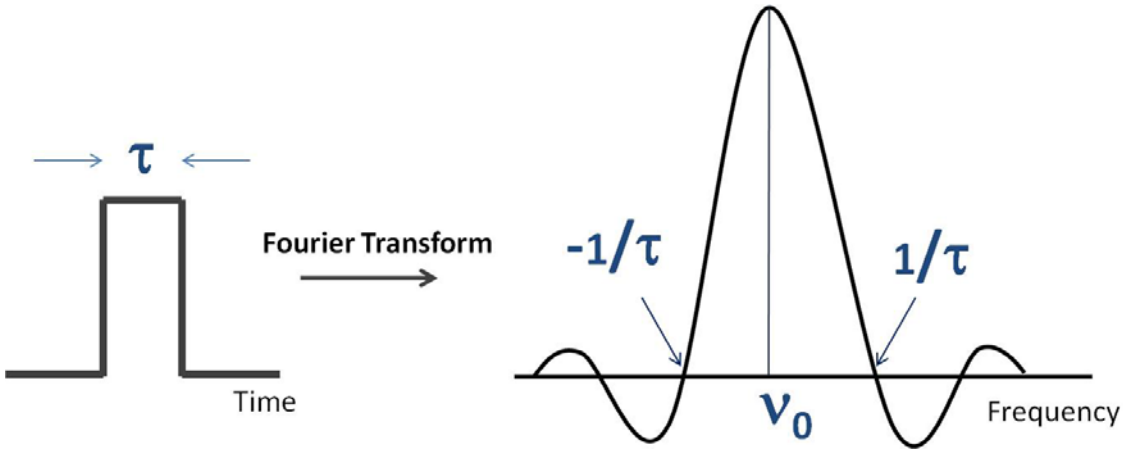

Figure 3.3 *Fourier relationship between rectangular pulse time* τ *and the amplitude of the frequency spectrum [from[1]].*

In NMR experiment an irradiation time (τ) need to be measured. For example, thallium chloride solution was used in thallium solid-state NMR study to determine the 90° pulse, in which the maximum intensity of the NMR spectrum appears.

3.2.2 NMR interactions

Hinton [9] has reviewed the NMR studies of thallium nuclei and concluded that several nuclear interactions are important in thallium solid-state NMR, including the chemical shift interaction, dipolar coupling, indirect (through-bond) coupling, all of which affect the NMR line broadening and relaxation of thallium study. In contrast, the quadrupole interaction dominates ^{11}B (I=3/2) NMR study.

This section describes only those interactions encountered in this study, which are chemical shift anisotropy, dipole-dipole interaction, indirect coupling and quadrupole interaction.

3.2.2.1 Chemical shift interaction

In a solid, a thallium nuclei in covalent environment is expected to produce a large chemical shift to lower field compared to one in ionic environment. This interaction originally comes from the shielding of the nucleus from an applied magnetic field by the surrounding electron clouds resulting in a change in the magnetic field local to the nucleus and a shift in resonance frequency ν, where $\nu = \nu_0(1 - \sigma_{zz})$ and σ_{zz} is the component of the chemical shift tensor in the direction of the applied field.

The chemical shift is proportional to the strength of the applied field. Thus the magnetic field, B_i, at nucleus *i*, would be;

$$B_i = (1 - \sigma)B_0 \quad \textbf{(3.4)}$$

where B_0 is the applied magnetic field and σ is the chemical shielding factor, which is the magnetic shielding parameter. As the chemical environment of the nucleus changes, e.g. due to change in bonding or coordination number, the local field can decrease (diamagnetic shift) or increase (paramagnetic shift). As the local field of the nucleus changes, the resonance frequency (ν) of the nucleus changes to;

$$\nu_i = \frac{\gamma}{2\pi}(1 - \sigma)B_0 \quad \textbf{(3.5)}$$

where γ is the gyromagnetic ratio of the nucleus.

The chemical shift (δ), with respect to a standard reference sample, is used instead of chemical shielding (σ). The chemical shift is reported in units of parts per million (ppm) defined as

$$\delta_{sample} = \frac{\nu_{sample} - \nu_{reference}}{\nu_{reference}}(\times 10^6) \quad \textbf{(3.6)}$$

Chemical shift also depends on the orientation of the nucleus with respect to the applied magnetic field. In powdered glass or polycrystalline materials, the nuclei are randomly oriented, giving a powder pattern, which is the summation of many resonance lines as shown in **Figure 3.4**.

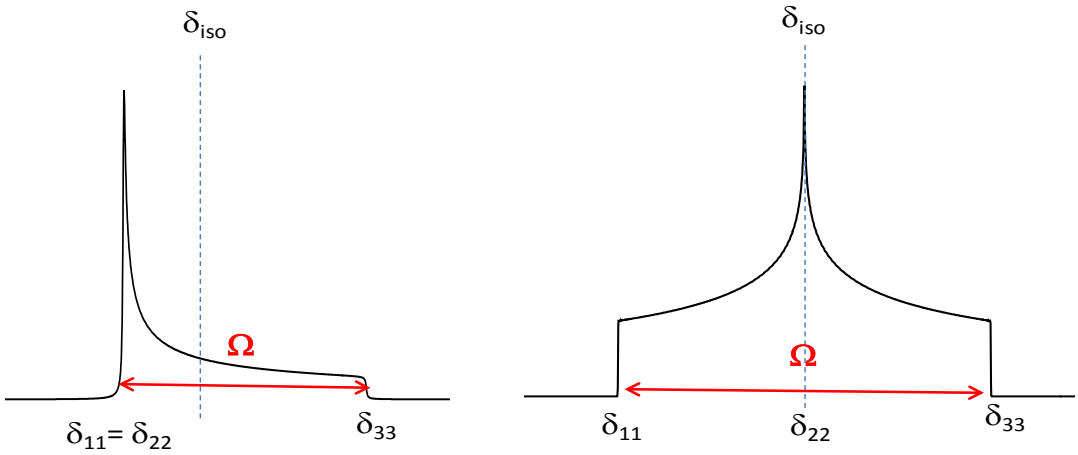

Figure 3.4 *Line shape of the powder patterns showing the chemical shift parameters.*

where δ_{11}, δ_{22}, δ_{33} are the chemical shift tensors.

Isotropic shift $(\delta_{iso}) = \frac{\delta_{11}+\delta_{22}+\delta_{33}}{3}$, gives the centre of gravity of the pattern.

Span $(\Omega) = \delta_{11} - \delta_{33}$, describes the maximum width of the powder pattern.

Skew $(\kappa) = \frac{3(\delta_{22}-\delta_{33})}{\Omega}$, describes the symmetry of the tensor, which can be used to infer the symmetry of the environment of the nucleus. For instance in the case of an axially symmetric tensor (e.g. in low-coordinated thallium with active lone pair of electrons), δ_{22} equals either δ_{11} or δ_{33}, and therefore skew is ±1. On the other hand if the tensor is spherically symmetric (e.g. in high-coordinated thallium), $\delta_{22}=\delta_{iso}$, and therefore skew is 0. The chemical shift parameters, in this study, were obtained by peak fitting/simulation using DM2010 software [10].

3.2.2.2 Dipole-dipole interaction [11]

In the case that the magnitude of the chemical shift anisotropy is small, other thallium nuclear magnetic interactions, for example dipolar interaction, are expected to be dominant. The dipole-dipole interaction is the through-space interaction between the magnetic moments of two nuclei, *i* and *j* (μ_i and μ_j) separated by distance r_{ij} for which the Hamiltonian (H_D) can be defined as;

$$H_D = \frac{\mu_0}{4\pi}\frac{\gamma_i\gamma_j\hbar^2}{r_{ij}^3}\left[I_i \cdot I_j - \frac{3(I_i \cdot r_{ij})(I_j \cdot r_{ij})}{r_{ij}^2}\right] \qquad \textbf{(3.7)}$$

where $\mu_i = \gamma_i \hbar I_i$ and $\mu_j = \gamma_j \hbar I_j$.

In general, the dipole interaction of like and unlike nuclei depends on the respective gyromagnetic ratios of the nuclei, the orientation of the nuclei and the inverse cube of the internuclear distance (r_{ij}). **Figure 3.5** shows the example of through-space dipole interaction between ^{203}Tl and ^{205}Tl, which might occur in thallium containing glasses. Dipolar interaction is independent of the magnetic field.

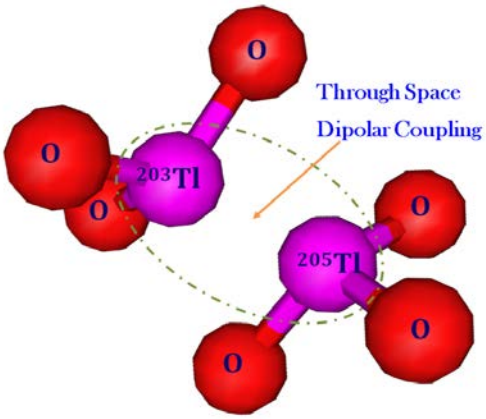

Figure 3.5 *schematic diagram shows the dipole interaction between unlike nuclei in thallium containing glasses.*

In this study, the dipolar contribution $\langle D_{ij} \rangle$ of the thallium borate crystalline phases is calculated from **Equation 3.8**;

$$\langle D_{ij} \rangle (in\ Hz) = \sqrt{\sum D_{ij}^2} \qquad \textbf{(3.8)}$$

where the dipolar constant;

$$D_{ij}(in\ Hz) = \left(\frac{\mu_0}{4\pi}\right) \frac{\gamma_{Tl}\gamma_{Tl}\hbar}{2\pi} \left(r_{ij}^{-3}\right)$$

[12].

3.2.2.3 Indirect coupling [11, 13]

Thallium solid state NMR spectra can be broadened by additional interaction mechanisms [9, 14, 15], one of these is the indirect spin-spin coupling exchange or exchange interaction [13] between non-identical isotopes, in this case between ^{203}Tl and ^{205}Tl, whereas the interaction between like nuclei, i.e. ^{203}Tl-^{203}Tl and ^{205}Tl-^{205}Tl, vanishes. Unlike the dipole interaction, this interaction is a through-bond interaction, because it occurs where there is overlap of the electronic wave functions of the thallium nuclei when the distance between ^{203}Tl and ^{205}Tl is sufficiently small as depicted in **Figure 3.6**. There are two types of this interaction [9]: the scalar exchange type, which is independent of orientation, and the psudodipolar type. The scalar exchange appears in the system where only s electron orbital of thallium atom is involved in bonding, whereas the pseudodipolar is present in the system where s and p electron orbitals are both involved. If only p electron orbitals involved, then both scalar exchange and psudodipolar interactions are present.

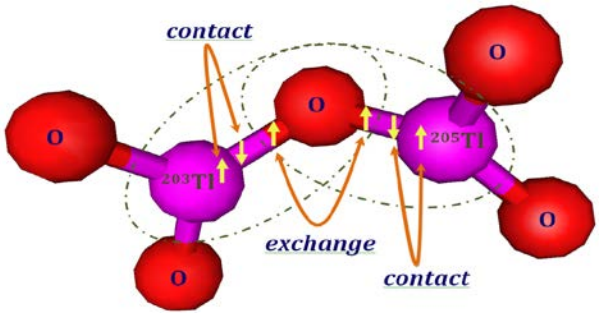

Figure 3.6 *schematic diagram shows the through-bond exchange interaction between unlike nuclei in thallium containing glasses.*

3.2.2.4 Quadrupole interaction

Nuclei with spin quantum number I ≥ 1 are known as quadrupolar nuclei, e.g. in this study ^{11}B has I=3/2, and they have a non-spherically symmetric charge distribution giving a non-zero nuclear electric quadrupole moment, *eQ*. This quadrupole moment can interact with the electric field gradient (EFG) in the sample, which arises from the electrons involved with the nuclei, e.g. bonding electrons or from a nearby ion. As in the case of the chemical shift and dipole interactions, the quadrupole interaction depends on the orientation of nuclei with respect to the applied field and the powder pattern is obtained as the envelope of many resonance lines. The broadening from this interaction and the spectrum shape depend on the quadrupolar coupling constant (C_q) which is expressed by;

$$C_q = \frac{e^2qQ}{h} \qquad \textbf{(3.9)}$$

and the asymmetry parameter (η_Q), which is defined by the EFG tensor in its principal axis system as $\eta_Q = \frac{V_{xx}-V_{yy}}{V_{zz}}$ where V_{ij} is the diagonalised tensor.

3.2.3 Spin-spin relaxation, T_2

In this study, T_2 was measured in order to investigate the presence of dipolar and exchange interactions in the sample. The Tl-NMR line shape is very broad and therefore very similar for different sites in glasses, whereas in crystals some difference in symmetry can be observed. In glasses, broad Gaussian-like spectra were obtained due to the distribution in environments (chemical shift dispersion) and also due to the increase in the number of interacting spins in the system as the amount of Tl_2O is increased.

Identifying the interactions that contribute to the line shape and line broadening is difficult. Thus, a spectrum with little characteristic feature, as in the case of thallium, can be described by the method of moments. The second moment can describe the intensity distribution as:

$$M_2 = \frac{3}{5}\left(\frac{\mu_0}{4\pi}\right)^2 \gamma_i^4 \hbar^2 I(I+1) \sum_j \frac{1}{r_{ij}^6} + \frac{4}{15}\left(\frac{\mu_0}{4\pi}\right)^2 \gamma_i^2 \gamma_j^2 \hbar^2 J(J+1) \sum_j \frac{1}{r_{ij}^6} + \frac{1}{3} J(J+1) \sum_j \bar{A}_{ij}^2 \quad \textbf{(3.10)}$$

where the first two terms correspond to the second moments due to dipolar interaction between like and unlike nuclei, respectively. In the third term, $\bar{A}_{ij}^2$ refers to the exchange interaction parameters.

T_2 is inversely proportion to the square root of M_2 as:

$$T_2 \propto \frac{1}{\sqrt{M_2}} \quad \textbf{(3.11)}$$

Thus, the T_2 is proportional to the cube of the internuclear distances (r_{ij}^3).

In the case of broad NMR spectra, much information is at the beginning of the FID and this can be distorted due to interference from probe circuitry, e.g. coil-ringing. This can be avoided by moving the FID away from the end of the pulse using an echo pulse sequence. In a pulse echo experiment, 90° and 180° pulses are applied to the sample with a time between these two pulses = τ as shown in **Figure 3.7**; the 180° pulse refocuses the dephased spins to in the x-y plane and the FID is then produced at time τ after the 180° pulse. This experiment is used to measure the spin-spin relaxation time (T_2), in which a series of experiments are run whilst changing the time τ between the two pulses. As a result, the strength of the signal, which is proportional to the net transverse magnetisation, reduces. This is because of the relaxation process of the net magnetisation in the x-y plane (**section 3.2.1)**, which produces a rate of decay = $e^{\left(-t/T_2\right)}$.

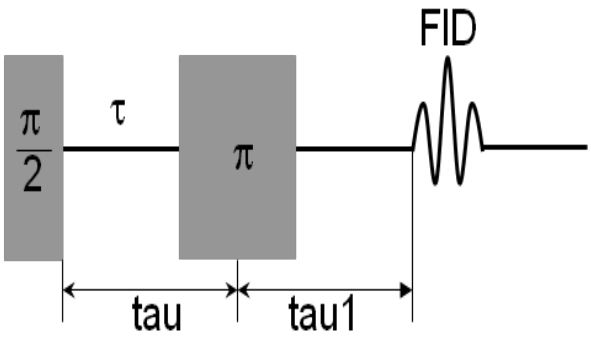

Figure 3.7 *Schematic diagram demonstrate the pulse echo experiment used in T_2 measurement and in thallium NMR experiment.*

In this study the intensity of the signal was obtained from the integration of the NMR spectrum, which is Fourier transformed from the free induction decay (FID). The values obtained are plotted against the time spacing between pulses (τ), T_2 relaxation time could then be obtained from the plot using an exponential decay function. **Figure 3.8** shows the change of the spectrum intensity as the time between pulses of the echo experiment increases.

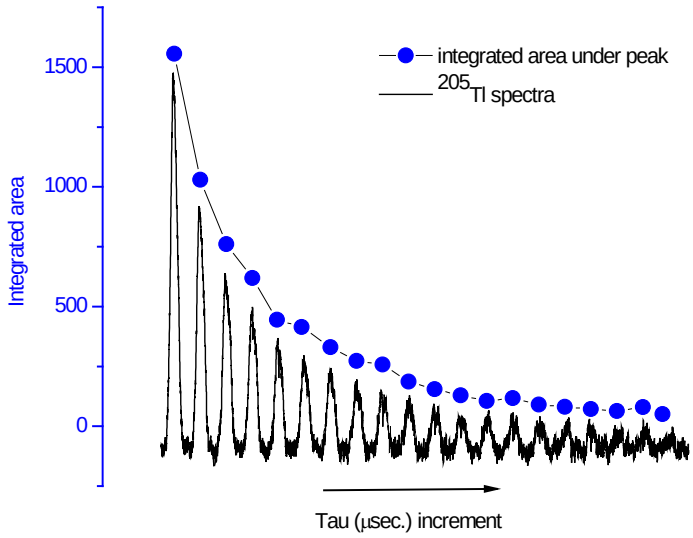

Figure 3.8 *An example of the T_2 measurement via the integration of the ^{205}Tl-NMR spectrum of glass.*

In thallium NMR, the FID signal is sometime incomplete, as shown in **Figure 3.9a**. The Fourier transform of the NMR spectrum into a frequency domain has to be started from the centre of the echo (as indicated by an arrow in **Figure 3.9**). In some cases, the complete FID is obtained (**Figure 3.9b**) and here the transform is done for the whole echo.

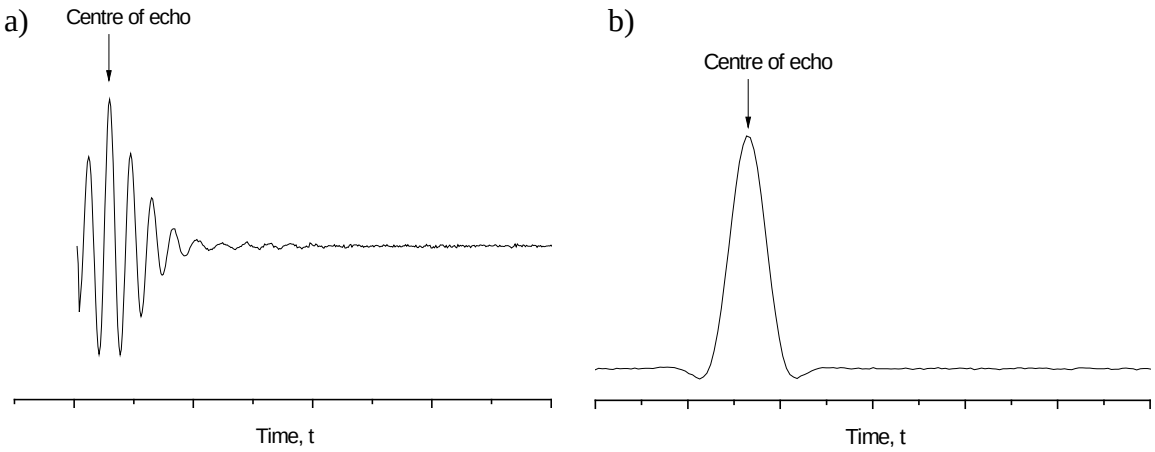

Figure 3.9 *Examples of free-induction decay signals obtained from* ***a)*** *high-temperature heat-treated 0.20Tl_2O·0.80GeO_2 and* ***b)*** *0.20Tl_2O·0.80GeO_2 glass, showing the incomplete and complete echo, respectively.*

3.3 Neutron diffraction [16-18]

Comprehensive glass structure cannot be determined as easily as crystal structure, which can employ Fourier analysis to obtain a unique structural model [3]. This is because of the lack of long-range periodic arrangement of atoms in glass, resulting in diversity in inter-atomic distances, bond angles and symmetry [4]. Neutron diffraction [19-22] has been used extensively to derive atomic separations in glasses and, less accurately, coordination numbers. In a neutron diffraction experiment, the differential cross section ($\frac{d\sigma}{d\Omega}$) is measured. This is defined by

$$\frac{d\sigma}{d\Omega} = I(Q) = I^s(Q) + i(Q) \quad \textbf{(3.12)}$$

where Q is the magnitude of the scattering vector for elastic scattering;

$$Q = \frac{4\pi}{\lambda}\sin\theta \quad \textbf{(3.13)}$$

$I^s(Q)$ is self scattering

$i(Q)$ is the distinct scattering

2θ is the scattering angle

The self-scattering can be calculated approximately by

$$I^s(Q) = \sum_l c_l \overline{b_l^2}\left(1 - P_l(\theta, \mu_l, \overline{K}, f, \varepsilon(E), \phi(E))\right) \quad \textbf{(3.14)}$$

where $\sum_l$ is calculated over the N elements in the sample. c_l is the atomic fraction and the total neutron scattering cross-section of element l is defined by $4\pi\overline{b_l^2}$. The Placzek inelasticity correction for pulsed neutron diffraction, P_l, is also applied. P_l is dependent on the scattering angle, ratio of the atomic mass of the atom l, μ_l, average kinetic energy per atom, $\overline{K}$, the ratio of scattered-to-total flight path, f, the detector efficiency, ε and the incident neutron flux, ϕ, where last two parameters are energy dependent terms.

More structural information is obtained by Fourier transform from the product of the subtraction between the data and self-scattering, which is the distinct scattering, $i(Q)$, giving the total correlation function

$$T(r) = T^0(r) + \frac{2}{\pi}\int_0^\infty Qi(Q)M(Q)\sin(rQ)dQ \quad \textbf{(3.15)}$$

where $T^0(r)$ is the average density contribution to $T(r)$ where $T^0(r) = 4\pi r g^0\left(\sum_l c_l \overline{b_l^2}\right)^2$, g^0 is the atomic number density, $\overline{b_l}$ is the coherent scattering length for element l and $M(Q)$ is a modification function to reduce the termination ripples arising from finite Q.

In the experiment, diffraction occurs for every element in the sample, thus, the correlation function is now a weighted sum of the partial correlation functions, $t_{ll'}(r)$ giving

$$T(r) = \sum_{ll'} c_l \overline{b_l}\,\overline{b_{l'}} t_{ll'}(r) \quad \textbf{(3.16)}$$

This summation gives a correlation function between each atom pair in the sample arising from the interatomic distances, which is simply illustrated in **Figure 3.10**.

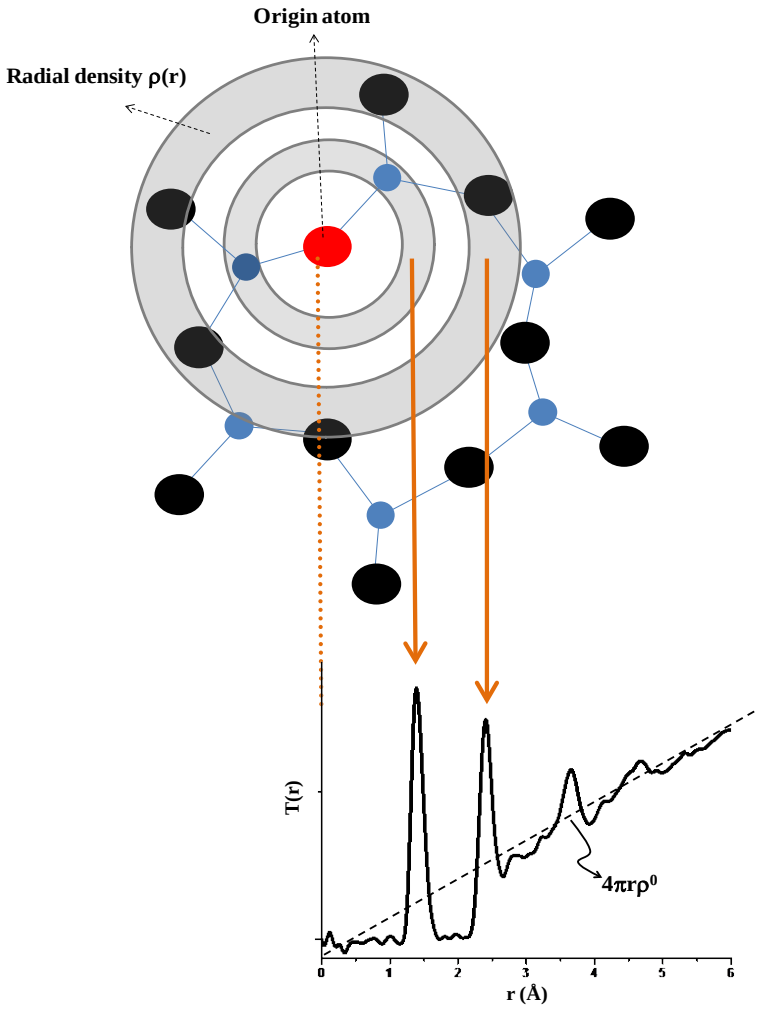

Figure 3.10 *schematic diagram of real space correlation arising from the interatomic distance.*

As each peak in *T(r)* plot arises from the correlation between two atoms of element l and l', thus the coordination number ($n_{ll'}$) can be calculated from:

$$n_{ll'} = \frac{r_{ll'} A_{ll'}}{(2-\delta_{ll'}) c_l \overline{b_l} \overline{b_{l'}}} \qquad \textbf{(3.17)}$$

where *r* is an average internuclear distance, which can be obtained from **Equation 3.18** and *A* is the area of the *T(r)* peak.

$$r_{ll'} = \frac{\int r \cdot T(r)}{\int T(r)} \qquad \textbf{(3.18)}$$

3.4 Raman Spectroscopy [4, 23]

Raman spectroscopy has been widely used to study glass structure [24-28]. It gives information on the amorphous structure by probing the excitations occurring in the sample, which correspond to vibrations involving the structural environment of a

particular atom or unit, on stimulation by electromagnetic radiation. A single laser light source, usually with a wavelength of visible light, e.g. ~514.5 nm or near infrared, e.g. ~785 nm, is used to excite the phonons in the sample, giving an inelastic scattered component, which contains the structural information. The frequency of the scattered light will be shifted both positively and negatively to an extent associated with the vibrational frequency of the phonon. In practice, a Raman scattering detector is at 90° to the incident beam, in order to avoid elastic scattering components that contain Rayleigh scattering information, which appear close to the Raman peak.

In general, a transition in a molecule between two quantised states can be achieved when Bohr's condition is satisfied, as

$$\Delta E = h\nu = h\frac{c}{\lambda} = hc\tilde{\nu} \qquad \textbf{(3.19)}$$

where ΔE is the difference of energy between two states or field

h is Planck's constant

ν is the vibration frequency

c is the velocity of light

$\tilde{\nu}$ is the wavenumber.

There are three processes involved in the sample after irradiation by incident laser light, which are *(1)* change in electronic polarisability of atom from ground state to virtual excited state, *(2)* creation (causing a negative shift of frequency) or annihilation (causing a positive shift) of phonons from electron-phonon interaction and *(3)* return of the electronic polarisability to the ground state (**Figure 3.11**).

In Raman spectroscopy, the scattered beam has frequencies $\nu_0 \pm \nu_m$ where ν_0 is the frequency of the incident laser radiation and ν_m is the vibrational frequency, in which $\nu_0 - \nu_m$ and $\nu_0 + \nu_m$ are called Stokes and anti-Stokes lines, respectively (**Figure 3.11**). The figure shows that the energy for Raman scattering is well below the first real excited state (E_1), so that the virtual state is assumed as the dashed line to distinguish it from the excited state. In the Raman experiment, ν_m is measured as a shift from the incident laser frequency. Applying the Maxwell-Boltzmann distribution law, the population of molecules resident in ν_0 are greater than in ν_1, so that the Stokes scattering line will be stronger than the anti-Stokes line.

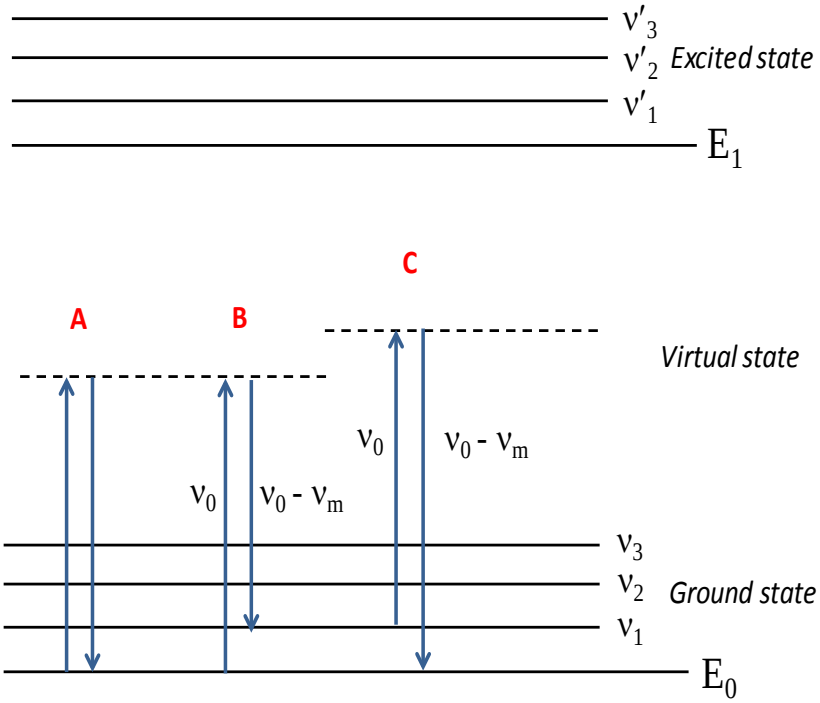

Figure 3.11 *Schematic diagram show the energy transitions for Rayleigh scattering, Stokes and anti-stokes Raman scattering, indicated by letters A, B and C, respectively.*

Raman scattering can be explained in terms of the electromagnetic wave fluctuation with time (t) using classical theory, as

$$E = E_0 \cos 2\pi\nu_0 t \qquad \textbf{(3.20)}$$

where E is the electric field strength, E_0 is the vibrational amplitude and ν_0 is the frequency of the electromagnetic wave, i.e. laser. Considering a diatomic molecule irradiated by laser light, an electric dipole moment occurs defined as

$$P = \alpha E = \alpha E_0 \cos 2\pi\nu_0 t \qquad \textbf{(3.21)}$$

where α is the polarisability, which is the proportionality constant. The vibration at ν_m introduces the nuclear displacement (q) with the vibrational amplitude q_0, which can be expressed as;

$$q = q_0 \cos 2\pi\nu_m t \qquad \textbf{(3.22)}$$

The displacement is a linear function at the small amplitude q_0, which could be written as;

$$\alpha = \alpha_0 + \left(\frac{\partial\alpha}{\partial q}\right)_0 q_0 + \cdots \qquad \textbf{(3.23)}$$

where α_0 is the polarisability at the equilibrium position and $\left(\frac{\partial\alpha}{\partial q}\right)_0$ is the rate change of polarisability with respect to the change in q at equilibrium position. Thus, for a laser

with frequency ν_0 and Raman frequency ν_m, the electric dipole moment could be written as;

$$P = \alpha E_0 \cos 2\pi\nu_0 t + \frac{1}{2}\left(\frac{\partial\alpha}{\partial q}\right)_0 q_0 E_0[\cos\{2\pi(\nu_0 + \nu_m)t\} + \cos\{2\pi(\nu_0 - \nu_m)t\}] \quad \textbf{(3.24)}$$

This equation corresponds to the oscillation of both Rayleigh (first term), and Raman scattering (second term).

3.5 X-ray diffraction [29]

X-Ray power diffraction has been applied in this study in order to check that an amorphous structure is achieved and also to identify the devitrified phases after heat-treatment (**Chapters 4 and 6**). **Figure 3.12** compares the X-ray diffraction patterns of amorphous and crystalline thallium germanate samples. Bragg diffraction peaks are obtained from the crystalline sample in **Figure 3.12b**.

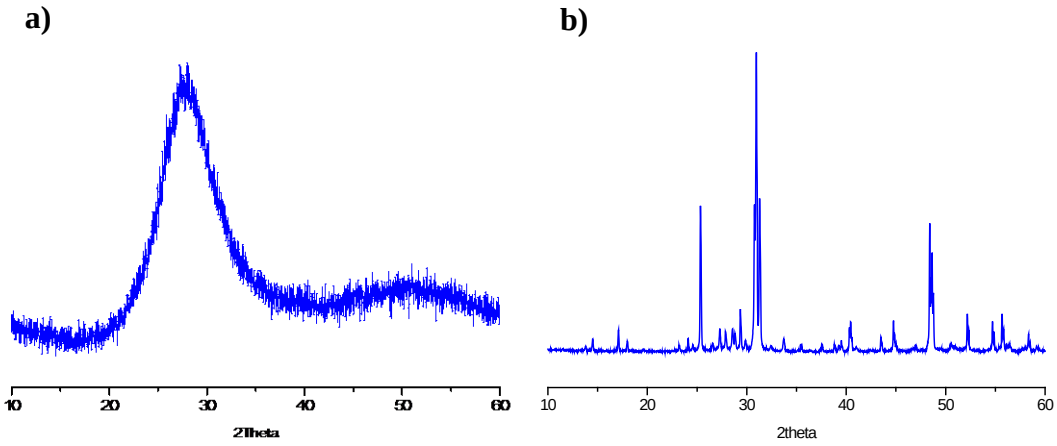

Figure 3.12 *Powder patterns obtained from XRD of* ***a)*** *$0.20Tl_2O{\cdot}0.80GeO_2$ glass and* ***b)*** *heat-treated $0.20Tl_2O{\cdot}0.80GeO_2$ sample (**Chapter 4**).*

Bragg's law is commonly used to explain X-ray diffraction from a crystal. In order to understand the Bragg law, **Figure 3.13** is helpful.

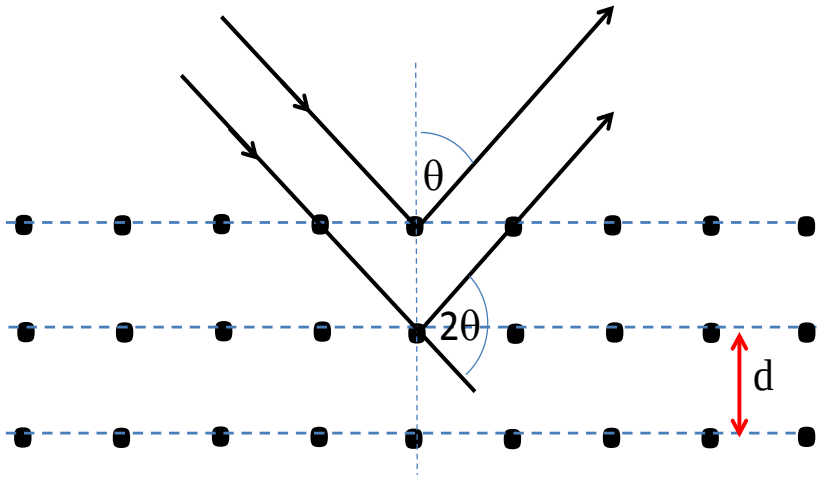

Figure 3.13 *Schematic diagram showing X-ray diffraction from a crystal at the Bragg condition*

The Bragg condition or Bragg's law is defined as

$$2d \sin\theta = n\lambda \qquad \textbf{(3.25)}$$

where d is the interplanar spacing of the crystal where atoms are periodically arranged

2θ is the angle between the diffracted beam and the transmitted beam, so called *diffraction angle*

λ is the wavelength of the incident X-ray

n is order of reflection

For X-ray powder diffraction, the diffracted beam that satisfies Bragg's law will be detected. Thus different crystal structures will give Bragg diffraction peaks at different angles as the plane-spacings (*d*) of each crystal structure are different. The intensity of the diffracted beam collected by the X-ray detector is plotted against the diffraction angle (2θ) to give a so called *diffraction pattern*. In order to compare crystal structures, not only the positions of the peaks in the diffraction angle are important but also their intensities. The diffraction patterns of devitrified samples in this study were compared to the reported patterns provided by the Daresbury ICSD database [30].

3.6 Thermal analysis [31]

Thermal analysis techniques are focused on the measurement of the exact value of a sample property, or the difference in that value between the sample and a reference standard material, or change of value of the sample property during temperature change, for example differential thermal analysis (DTA), differential scanning calorimetry (DSC) and thermodilatometry which record the temperature difference, enthalpy change and dimensional change of the materials, respectively. Examples of changes or reactions of material, which might occur with change in temperature, are decomposition, oxidation, change in crystal structure, sintering, melting, sublimation, formation of new compounds.

In DTA, the difference in temperature (ΔT), between sample (T_s) and reference material (T_r) i.e. $\Delta T = T_s - T_r$, which are subjected to the same heating profile, is measured and interpreted. The reactions, which may occur during heating or cooling of the materials, are either consuming (endothermic) or releasing (exothermic) energy from/to the environment. In a DTA experiment the increase of the sample's temperature is slower than that of the reference material when an endothermic reaction occurs during heating.

Theoretical approaches of DTA (and DSC – see below) are similar as follows;

After considering the heat flow equations and applying Newton's law, the final equation is:

$$dq_s/dt = (1/R)(T_h - T_{sm}) \text{ and } dq'_s/dt = (1/R')(T_{sm} - T_s) \quad \textbf{(3.26)}$$

For DTA, assuming that $T_{sm}=T_s$, $T_{rm}=T_r$ and $R' = 0$, the differential signal (ΔT) will be:

$$\Delta T = R(dT/dt)(Cs - Cr) \quad \textbf{(3.27)}$$

This means that the signal will only depend on the heat capacities of the sample and reference, thermal resistance and heating rate (dT/dt). It is also usual that thermal resistance can be ignored because it depends on DTA equipment and properties of sample and reference.

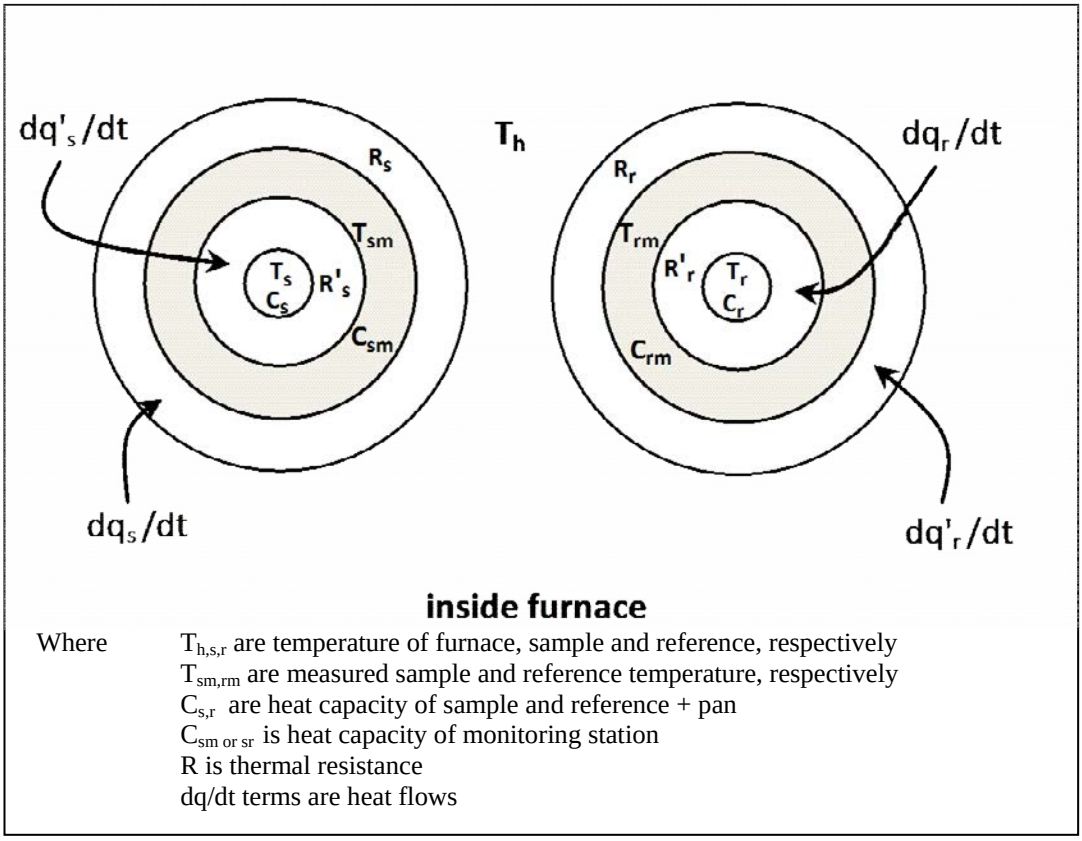

Figure 3.14 *Schematic diagram shows interior DTA or DSC (from [31])*

Other implementations of thermal analysis are two different techniques, power-compensated DSC and heat-flux DSC. For power-compensated DSC, the power applied to the sample side and reference side is different because it is necessary to equalise sample and reference temperature ($T_{sm}=T_{rm}=T_h$) and, assuming that all thermal resistance terms are zero, the signal of different heat or power input ($\Delta(dq/dt)$) is:

$$\Delta(dq/dt) = (dT/dt)(C_s-C_r) \quad \textbf{(3.28)}$$

Heat-flux DSC is more similar to DTA, except that instrument parameters such as thermal resistance (R) are dealt with by calibration at different temperatures.

DTA can be used to determine the phase equilibrium diagram, due to the changes in heat capacities, which relate to thermodynamic behaviour of any changes occurring during temperature change, for instance decomposition, crystallization, eutectic reaction and melting. The kinetics of material reactions can also be determined by thermal analysis.

3.7 Gas pycnometry

Density (ρ) of a sample is defined by the mass (m) per unit volume (V); $\rho=m/V$. The mass is measured using a laboratory balance and gas pycnometry is used to measure the volume of the sample, by measuring the amount of gas that is displaced by the sample. In this case, helium gas was used. However, the amount of gas or volume of gas is measure indirectly via the *ideal gas law*;

$$PV = nRT \tag{3.29}$$

where P = pressure, V = volume, n = number of moles, R = universal gas constant and T = absolute temperature.

In the gas pycnometer, the chambers of the reference cell and sample cell are isolated. The pressure of the sample chamber with sample present can be defined as:

$$P_a(V_{SC} - V_S) = n_a RT \tag{3.30}$$

where P_a = atmospheric pressure, V_{SC} and V_S are volumes of sample chamber and sample, respectively and n_a is number of moles of gas at ambient pressure. During the measurement, the reference chamber is filled with the gas to the exact pressure; P_1, giving:

$$P_1 V_{RC} = n_1 RT \tag{3.31}$$

where V_{RC} is volume of the reference chamber. When pressure P_1 is achieved, the valve between reference chamber and sample chamber is opened. After stabilising, a new pressure P_2 is achieved. **Equations 3.28** and **3.29** can be combined, giving;

$$P_2(V_{SC} - V_S + V_{RC}) = n_a RT + n_1 RT = P_a(V_{SC} - V_S) + P_1 V_{RC} \tag{3.32}$$

Defining P_a as zero, the volume of sample (V_S) can be simply written as;

$$V_S = V_{SC} - V_{RC}\left({}^{P_1}/_{P_2} - 1\right) \tag{3.33}$$

Thus, the volume of sample can be determined by measuring the ratio of the pressure P_1 and P_2 during the gas pycnometry measurement, whereas V_{SC} and V_{RC} are measured during cell calibration prior to the sample measurement using steel balls of known volume.

3.8 References

[1] K.J.D. MacKenzie, M.E. Smith, *Multinuclear solid-state NMR of inorganic materials*, Pergamon (2002).

[2] J.J. Fitzgerald, S.M. DePaul, *Solid-State NMR Spectroscopy of Inorganic Materials*, American Chemical Society (1999).

[3] W. Vogel, *Glass Chemistry*, Springer-Verlag (1994).

[4] K.J. Rao, *Structural Chemistry of Glasses*, Elsevier (2002).

[5] H. Eckert, *Progress in Nuclear Magnetic Resonance Spectroscopy*, **24** (1992) 159.

[6] E. Fukushima, S.B.W. Roeder, *Experimental Pulse NMR, A Nuts and Bolts Approach*, Westview Press (1981).

[7] A.H. Silver, P.J. Bray, *Journal of Chemical Physics*, **29** (1958) 984.

[8] G.E. Jellison, L.W. Panek, P.J. Bray, G.B. Rouse, *Journal of Chemical Physics*, **66** (1977) 802-812.

[9] J.F. Hinton, *Bulletin of Magnetic Resonance*, **13** (1992) 90.

[10] D. Massiot, F. Fayon, M. Capron, I. King, S. Le Calve, B. Alonso, J.O. Durand, B. Bujoli, Z.H. Gan, G. Hoatson, *Magnetic Resonance in Chemistry*, **40** (2002) 70.

[11] J.H. Van Vleck, *Physical Review*, **74** (1948) 1168.

[12] A. Wong, A.P. Howes, J.R. Yates, A. Watts, T. Anupold, J. Past, A. Samoson, R. Dupree, M.E. Smith, *Physical Chemistry Chemical Physics*, **13** (2011) 12213.

[13] N. Bloembergen, T.J. Rowland, *Physical Review*, **97** (1955) 1679.

[14] J.F. Hinton, K.R. Metz, R.W. Briggs, *Progress in Nuclear Magnetic Resonance Spectroscopy*, **20** (1988) 423.

[15] L.W. Panek, P.J. Bray, *Journal of Chemical Physics*, **66** (1977) 3822.

[16] A.C. Wright, *Journal of Non-Crystalline Solids*, **76** (1985) 187.

[17] A.C. Wright, A.G. Clare, D.I. Grimley, R.N. Sinclair, *Journal of Non-Crystalline Solids*, **112** (1989) 33.

[18] A.C. Hannon, *Nuclear Instruments and Methods in Physics Research Section A: Accelerators, Spectrometers, Detectors and Associated Equipment*, **551** (2005) 88.

[19] R.N. Sinclair, D.A.G. Johnson, J.C. Dore, J.H. Clarke, A.C. Wright, *Nuclear Instruments & Methods*, **117** (1974) 445.

[20] A.C. Wright, *Journal of Non-Crystalline Solids*, **40** (1980) 325.

[21] J.A.E. Desa, A.C. Wright, R.N. Sinclair, *Journal of Non-Crystalline Solids*, **99** (1988) 276.

[22] T. Sato, M. Misawa, O. Yamashita, K. Yoshida, H. Ebata, K. Maruyama, H. Iyetomi, *Journal of Non-Crystalline Solids*, **232–234** (1998) 574.

[23] J.R. Ferraro, K. Nakamoto, *Introductory Raman Spectroscopy*, Academic Press, (1994).

[24] L.A. Kilstiansen, J. Krogh-Moe, *Physics and Chemistry of Glasses*, **9** (1968) 96.

[25] F.L. Galeener, J.C. Mikkelsen, R.H. Geils, W.J. Mosby, *Applied Physics Letters*, **32** (1978) 34.

[26] F.L. Galeener, G. Lucovsky, J.C. Mikkelsen, *Physical Review B*, **22** (1980) 3983-3990.

[27] C.F. Windisch Jr, W.M. Risen Jr, *Journal of Non-Crystalline Solids*, **48** (1982) 307.

[28] C.F. Windisch Jr, W.M. Risen Jr, *Journal of Non-Crystalline Solids*, **48** (1982) 325.

[29] Y. Waseda, E. Matsubara, K. Shinoda, *X-ray Diffraction Crystallography*, Springer (2011).

[30] D.A. Fletcher, R.F. McMeeking, D. Parkin, *Journal of Chemical Information and Computer Sciences*, **36** (1996) 746.

[31] M.E. Brown, *Introduction to Thermal Analysis- Techniques and Applications*, Chapman and Hall (1988).

Chapter 4

Thallium Germanate Crystalline Phases

4.1 Introduction

Seven crystalline compounds are present in the Tl_2O-GeO_2 [1] phase diagram (**Figure 4.1)**. Unfortunately, few structural studies of these compounds have been published. Touboul and Feutelais [1] determined cell parameters for $Tl_2Ge_7O_{15}$, $Tl_2Ge_6O_{13}$ and $Tl_2Ge_4O_9$ and concluded that the germanium environments include both four and six coordination to oxygen atoms, i.e. [GeO_4] and [GeO_6]. They also concluded that the lone pair of electrons on Tl^+ in these compounds is stereochemically inert but is active in Tl_4GeO_4, $Tl_6Ge_2O_7$ and $Tl_2Ge_5O_{14}$, in which the germanate network is composed solely of [GeO_4] units. It can be concluded that the ratio of Ge:Tl affects the thallium and germanium environments. If Ge:Tl ≥ 2, the lone pair of electrons on Tl^+ will be inert and the germanium will be in both four and six coordination but if Ge:Tl < 1, the Tl^+ lone-pair will be stereochemically active and four-coordinated germanium only will be present [1]. It is anticipated that these environments are indicators of what to expect in the glass system. Nevertheless, the environment of thallium has not yet been confirmed in most of these compounds and little is known about $Tl_2Ge_2O_5$.

The only thallium germanate whose crystal structure has been published is $Tl_8Ge_5O_{14}$ [2], in which germanium is present as [GeO_4] and thallium as [TlO_3], where the lone pair of electrons is stereochemically active with the three oxygen atoms being located on the side of Tl^+ away from the oxygen atoms and with the shortest Tl-O distance at 2.52 Å [2].

Apart from $Tl_8Ge_5O_{14}$, which is not in the range of the compounds studied in this study (shaded in **Figure 4.1**), $Tl_2Ge_4O_9$ has been reported [1] to be isomorphous with $K_2Ge_4O_9$ [3] and $Rb_2Ge_4O_9$ [4], with the Tl^+ lone-pair being stereochemically inert. These tetragermanates contain [Ge_3O_9] rings consisting of three [GeO_4] tetrahedral units and linked by a [GeO_6] octahedral unit [1, 3, 4], although variation of Ge-O bond length and O-Ge-O angles is expected depending on the type of alkali ion [4]. In $K_2Ge_4O_9$

and $Rb_2Ge_4O_9$, the alkali ions (i.e. K^+ and Rb^+) are coordinated to seven oxygen atoms with K-O and Rb-O bond distances of between 2.72 to 3.44 Å [4].

XRD patterns of $Tl_2Ge_7O_{15}$, $Tl_2Ge_6O_{13}$ and $Tl_2Ge_2O_5$ do not indicate isomorphism with any alkali germanate structures yet determined [1] such as $Li_2Ge_7O_{15}$ [5, 6], $Li_2Ge_2O_5$ [7] and $Na_2Ge_2O_5$ [8].

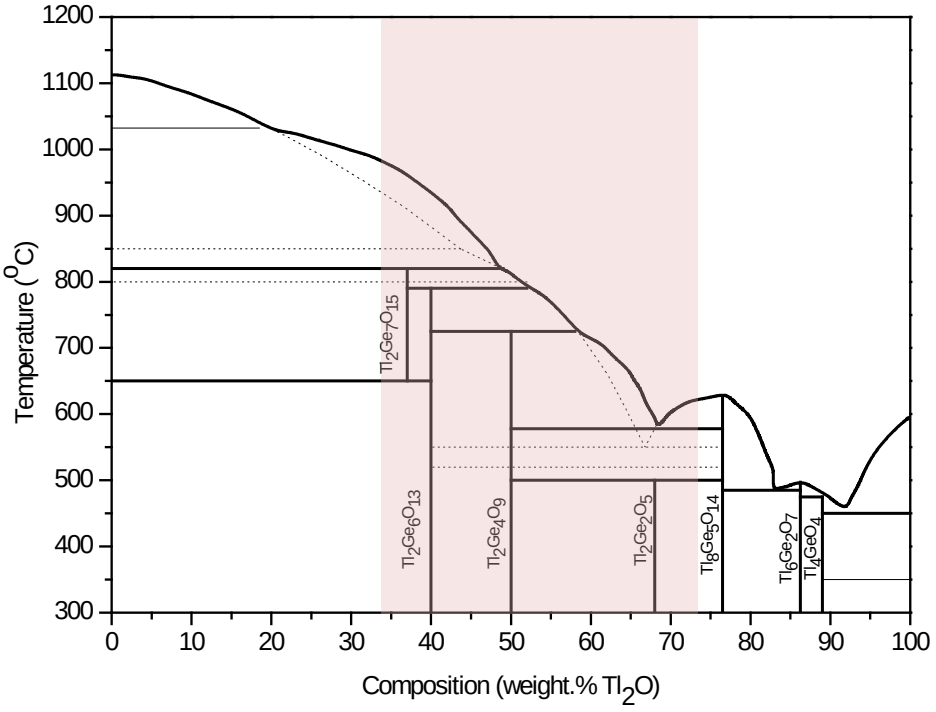

Figure 4.1 *Phase diagram of the $Tl_2O{\cdot}GeO_2$ system [1](the crystalline phases of interest; $Tl_2Ge_7O_{15}$, $Tl_2B_6O_{13}$, $Tl_2B_4O_9$ and $Tl_2B_2O_5$ are in the shaded region)*

In this chapter, heat-treated samples, whose composition correspond to $Tl_2Ge_7O_{15}$ (x=0.125), $Tl_2Ge_6O_{13}$ (x=0.143), $Tl_2Ge_4O_9$ (x=0.20) and $Tl_2Ge_2O_5$ (x=0.33) have been investigated using pycnometry, X-ray powder diffraction, solid-state NMR and Raman spectroscopy. Since the structures of these crystalline phases are not completely defined, the work reported in this chapter investigates the thallium environment in these crystalline phases which can then be used to explain the structure of thallium germanate glasses. Solid-state NMR is the main technique used in this study since structural details of the thallium environment can be inferred from the differences in the position, shape and size of the Tl-NMR spectra, which result from different magnetic interactions, e.g. the exchange interaction and chemical shift anisotropy. To identify phases obtained from heat-treatment in this study, X-ray diffraction patterns of

each sample are compared with ones from the literature. Moreover, the changes in germanium environment, i.e. coordination number, are monitored using Raman spectroscopy and comparing the spectra obtained in this study with the Raman spectroscopy studies of alkali germanate glasses.

4.2 Experimental detail

4.2.1 Sample preparation

Crystal phases were obtained by controlled crystallisation of the parent glasses. GeO_2 and Tl_2CO_3 were used as starting materials to make $xTl_2O{\cdot}(1\text{-}x)GeO_2$ glasses of the same stoichiometry as the crystals, i.e. x = 0.125, 0.143, 0.20, and 0.333 mole fraction Tl_2O for $Tl_2Ge_7O_{15}$, $Tl_2Ge_6O_{13}$, $Tl_2Ge_4O_9$ and $Tl_2Ge_2O_5$ respectively. Due to the possible loss of Tl_2O during the melting process, 2 mole % excess of Tl_2O was added to the samples. However, the nominal composition is used throughout this chapter. The melting and cooling processes were performed in the same manner as for thallium germanate glass [**Chapter 5**]. The glasses were then crystallised by heat-treatment at the crystallisation temperature (taken as the peak maximum) obtained from the DTA curves shown in **Figure 4.2**. There are two exothermic peaks in all of the glasses and therefore crystallisation was carried out at both temperatures (listed in **Table 4.1**). The powder samples were heated at 10 °C min^{-1} to the appropriate temperature and held at temperature for 15 hours followed by furnace cooling to room temperature. The samples were kept in a desiccator. Weight loss during crystallisation was also monitored.

^{203}Tl-enriched $Tl_2Ge_4O_9$ was prepared in order to investigate the thallium-thallium exchange interaction under NMR. 97.32 ± 0.3 % ^{203}Tl-enriched Tl_2O_3 and GeO_2 were used as the raw materials. The presence of Tl^{3+}, could not be detected by Tl solid-state NMR spectroscopy, indicating that the conversion of Tl^{3+} to Tl^{+} had completed.

Table 4.1 *heat-treatment temperatures obtained from DTA.*

composition	Expected crystalline compound	1st crystallisation peak (°C); metastable phase	2nd crystallisation peak °C); more stable phase
$0.125Tl_2O{\cdot}0.875GeO_2$	$Tl_2Ge_7O_{15}$	499	575
$0.143Tl_2O{\cdot}0.857GeO_2$	$Tl_2Ge_6O_{13}$	479	621
$0.20Tl_2O{\cdot}0.80GeO_2$	$Tl_2Ge_4O_9$	441	671
$0.333Tl_2O{\cdot}0.667GeO_2$	$Tl_2Ge_2O_5$	345	453

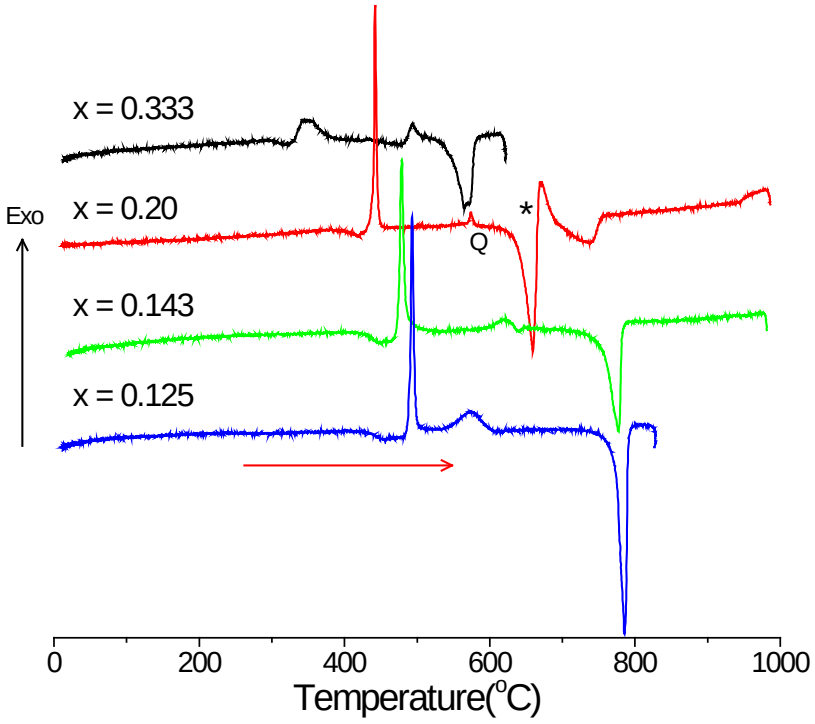

Figure 4.2(a) *DTA heating curves of glasses, showing two crystallisation events.*

(∗ *=metastable melting event; Q=α-β quartz (reference material) transition)*

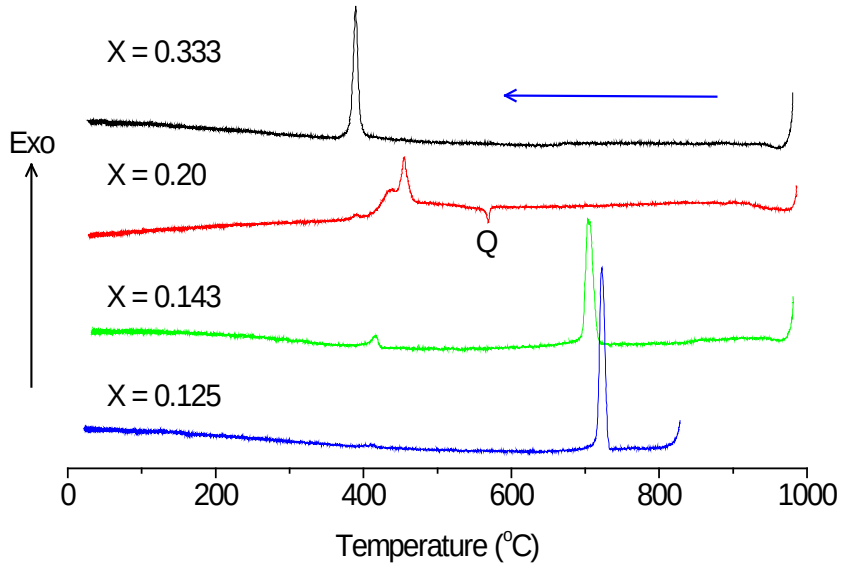

Figure 4.2(b) *DTA cooling curves of glasses, showing two crystallisation events. (Q=α-β quartz (reference material) transition)*

4.2.2 Density and Molar Volume

The density of each sample was measured using a Micrometritics AccuPyc 1330 gas pycnometer using helium. The molar volume of the samples was then calculated using the nominal compositions.

4.2.3 X-ray Diffraction

A Bruker D5005 CuKα X-ray diffractometer was used to characterise all crystallised samples. The patterns were acquired over 10 hours from 2θ = 10 to 100 degrees with an increment of 0.05 degree per step.

4.2.4 Thallium Solid-State Nuclear Magnetic Resonance

^{205}Tl and ^{203}Tl (for $Tl_2Ge_4O_9$ sample) static NMR was performed on a 4.7 T Chemagnetics Infinity 200 MHz spectrometer using a 6mm Varian probe tuned to 115.7 MHz and 114.3 MHz, respectively. A static echo pulse sequence was used with 1.5 μsec and 3 μsec pulse widths corresponding to 90° and 180° pulses, respectively with a pulse separation of 40 μsec, and 10 seconds pulse delay. Thallium nitrate ($TlNO_3$) solution

was used as the reference. Data have been processed for only half of the echo of the FID for the same reason as described in **Chapter 3**.

The crystallised ^{203}Tl-enriched $Tl_2Ge_4O_9$ sample was also used for an MAS experiment but was mixed with magnesium oxide (MgO) powder to reduce the mass inside the rotor, which could then be spun at 17.5 kHz. The experiment was performed on the same spectrometer as the static experiment but with a 2.5 mm Bruker probe. The same pulse echo sequence was applied except a pulse separation of 57 μsec was used instead for the MAS experiment, so that the echo delay (τ in **Figure 3.6**) was synchronised with the rotation speed (i.e. 1/17.5 kHz = 57 μsec).

4.2.5 Raman Spectroscopy

A Renishaw inVia Raman Microscope with a 514.5 nm Ar^+ laser was used to examine powder samples over the range 1800 cm^{-1} to 100 cm^{-1}. Several areas were examined in each case and various exposure times were used to ensure that the spectra were reproducible.

4.3 Results and discussion

4.3.1 Thermal analysis and crystallisation of glass

The results in **Figure 4.2(a)** show that two exothermic peaks were obtained in all thallium germanate glasses investigated in this study, consistent with the two crystallisation events previously observed in crystallisation studies of lithium germanate [9, 10] and lead germanate [11] glasses. It should be noted that, whilst the first exotherm is undoubtedly crystallisation, the second exotherm could either be crystallisation of a second phase or transformation of the first phase into a more stable form. A metastable phase is first crystallised at lower temperature, then transforms into the thermodynamically more stable phase at higher temperature, similar to events found in alkali germanate crystallisation studies [10, 12], The x = 0.20 sample (corresponding to $Tl_2Ge_4O_9$) possibly exhibits “metastable” melting of the metastable phase (at 659 °C) then followed by crystallisation of the more stable phase. The similarities of the melting points of the stable phases in the x = 0.125 and x = 0.143 samples may indicate that the same phase is present in both samples or may simply be the peritectic indicated by the phase diagram (**Figure 4.1** [1]). The DTA cooling curves **Figure 4.2(b)** give a better measure of this, since the onset temperatures are easier to determine. For x =

0.125, the onset of crystallisation is 733 ± 0.05 °C, and for x = 0.143 it is 721 ± 0.5°C. Touboul and Feutelais give a value of 725°C for the peritectic reaction: $Tl_2Ge_4O_9 \leftrightarrow Tl_2Ge_6O_{13}$ + liquid. Thus it can be assumed that the melting event (on heating) and the crystallisation event (on cooling) are in fact associated with the peritectic solidus and endo/exo between the solidus and liquidus are small for these compositions. According to the phase diagram (**Figure 4.1** [1]). The events in the cooling curves of the x = 0.2 and 0.333 samples are too low in temperature to be associated with crystallisation of any liquid phase therefore it is more likely that significant under-cooling has occurred resulting in crystallisation from a supercooled liquid.

4.3.2 Sample weight loss

Weight loss due to the crystallisation by heat treatment was very low in every sample (<1 wt%). Thus, the nominal composition is used in subsequent discussion of results. Density and molar volume values of samples can be compared with the values reported in the literature, (section **4.3.3**) but it should be noted that this is not an accurate method to determine sample composition, thus the nominal composition is used in all discussions. Since weight loss during crystallisation is very low, the composition of the crystalline sample should not be significantly different from the parent glasses whose density values consistent with the literature [13-15] (see section **5.3.2** and **Figure 5.1**).

4.3.3 Density and molar volume

Figure 4.3 shows the density of heat-treated samples in comparison with the parent glasses and also with the density values presented by Touboul and Feutelais [1]. The densities of samples heat-treated at the second exotherm are about 3 to 10 % higher than the values given in the literature [1] ($Tl_2Ge_7O_{15}$, $Tl_2Ge_6O_{13}$ and $Tl_2Ge_4O_9$). The densities of all heat-treated samples increase with thallium concentration, although XRD showed the samples to be multi-phase (see **4.3.4**). The densities of low temperature heat-treated samples usually lie in between the values for the parent glasses and the high temperature heat-treated samples.

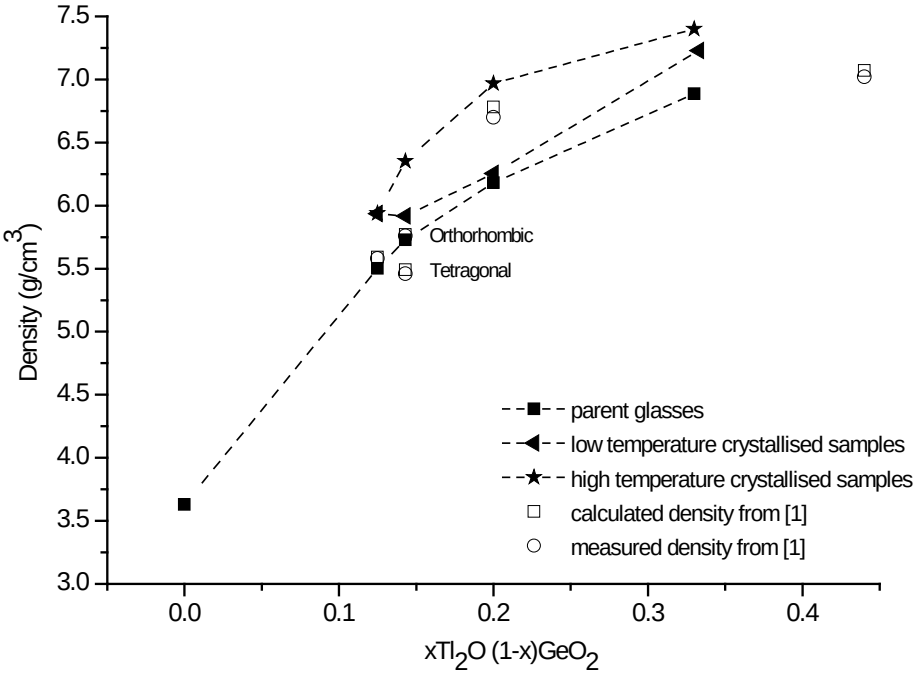

Figure 4.3 *Densities of low and high temperature heat-treated samples, parent glasses and crystalline compounds given in [1].*

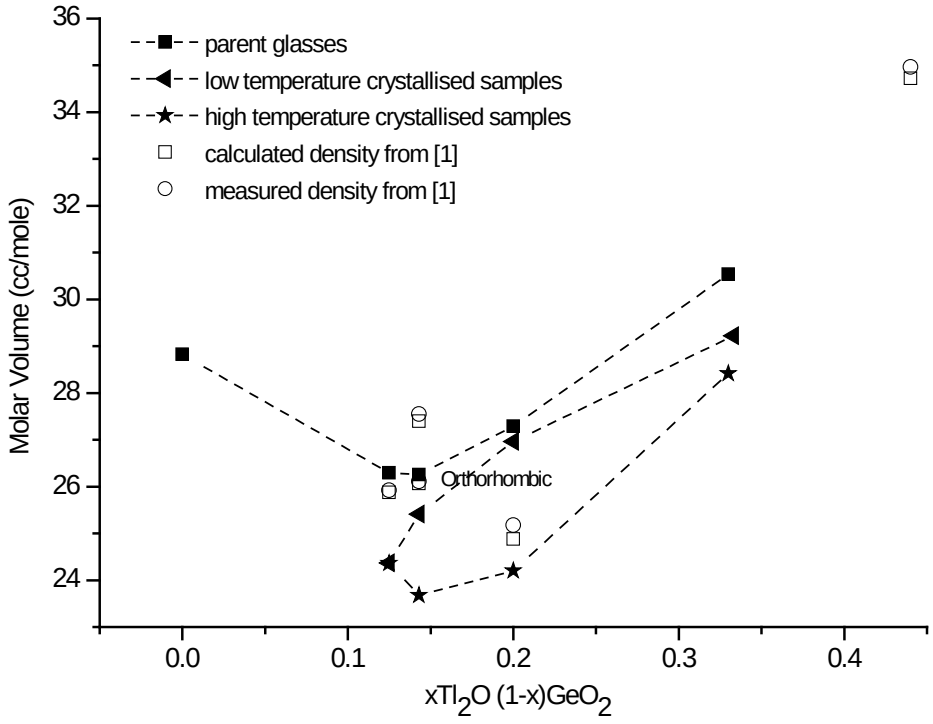

Figure 4.4 *Molar volume of low and high temperature heat-treated samples, parent glasses and crystalline compounds calculated from densities given in [1].*

The calculated molar volumes of the samples are compared with values calculated from literature density values in **Figure 4.4** [1]. The values are slightly below the calculated values from literature, which is consistent with the higher densities.

4.3.4 X-ray diffraction

X-ray diffraction patterns of heat-treated thallium germanate samples and data from [1] are compared in **Figure 4.5**. The intensities of the diffraction peaks obtained from the literature [1] were estimated as: very strong = 100%; strong = 80%; medium = 60%; weak = 40%; and very weak = 20%. Only the positions of the peaks were then compared and an asterisk indicates the matching peaks.

The pattern for orthorhombic $Tl_2Ge_6O_{13}$ is the best match not only for the high temperature phase from the x = 0.143 sample but also for both high and low temperature crystallised versions of the x = 0.125 sample (**Fig 4.6)**. Second phases are present in all three samples, particularly giving strong peaks at ~ 25.3^o and ~31.3^o which could be due to the presence of some $Tl_2Ge_2O_9$ although this is not the only impurity phase. It appears to be difficult to obtain the high temperature $Tl_2Ge_7O_{15}$ phase (stable between 650^{o}C and 820^{o}C [1]) by devitrification of the x = 0.125 glass at either 499^{o}C or 575^{o}C and nucleation of the low temperature (orthorhombic) phase of $Tl_2Ge_6O_{13}$ occurs more readily. The tetragonal to orthorhombic phase transition for this phase is reported to be irreversible [1].

The high temperature heat-treated $Tl_2Ge_4O_9$ sample is believed to be isomorphous with $Rb_2Ge_4O_9$ and $K_2Ge_4O_9$, according to their diffraction patterns which differ by slight shifts of the peak positions due to differences in the unit cell parameters consistent with the ionic radii of Tl^+, Rb^+ and K^+. However, not every alkali tetragermanate is isomorphous with thallium tetragermanate, as is the case of $Na_2Ge_4O_9$ where the Na^+ ion is significantly smaller (0.95 Å) than Tl^+, Rb^+ and K^+ (1.44, 1.48 and 1.33 Å respectively) [16]. **Figure 4.7** shows that the high temperature heat treated x = 0.20 sample does indeed match the pattern for $Tl_2Ge_4O_9$ [1]. It is unfortunate that there are no other crystal structure reports for Rb and K germanate compounds, in which the cation size would be closer to Tl^+. However, isomorphous structures are less likely where the thallium lone-pair becomes active.

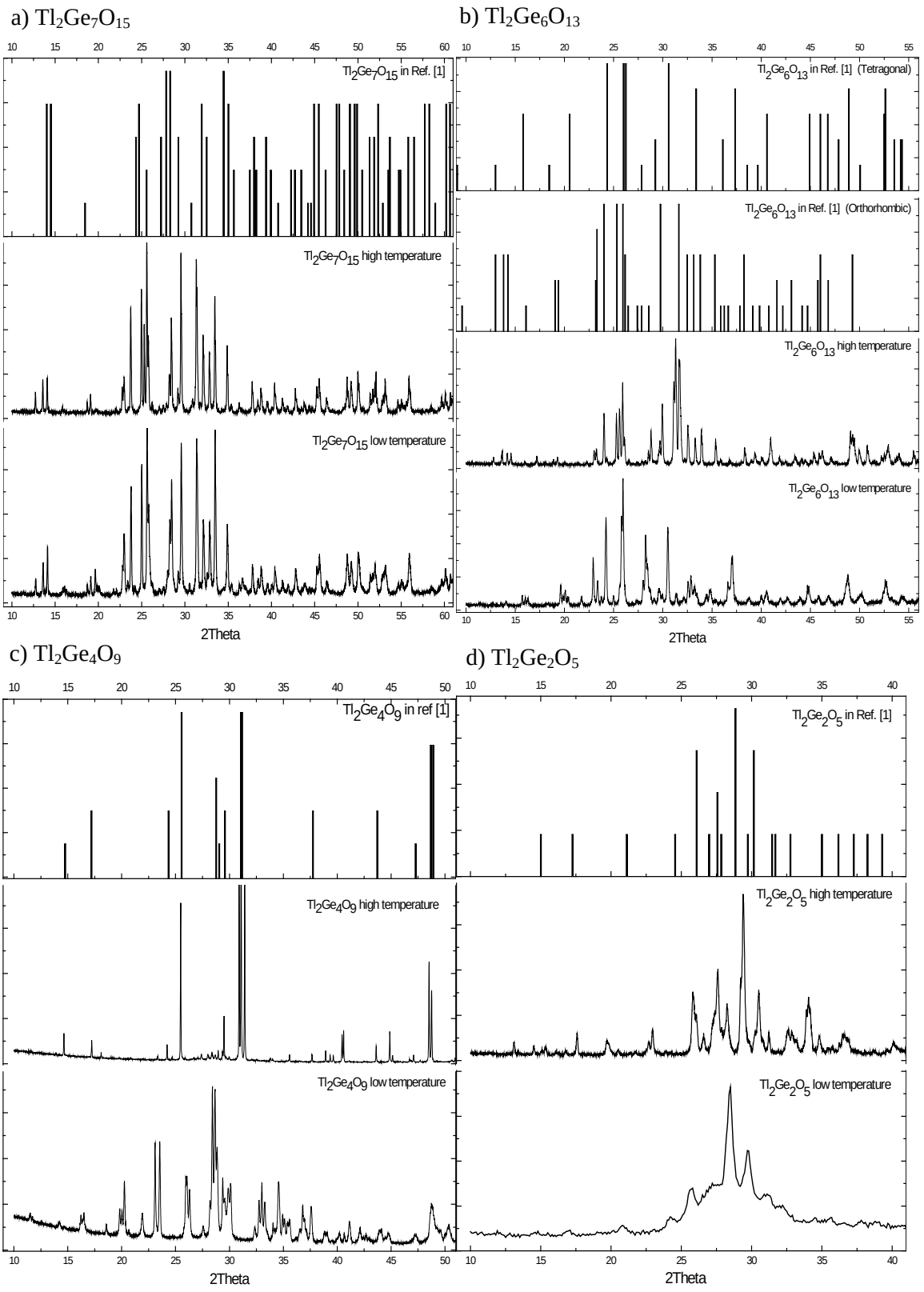

Figure 4.5 *X-ray diffraction patterns of low and high temperature heat-treated samples in comparison with one given in Ref. [1]*

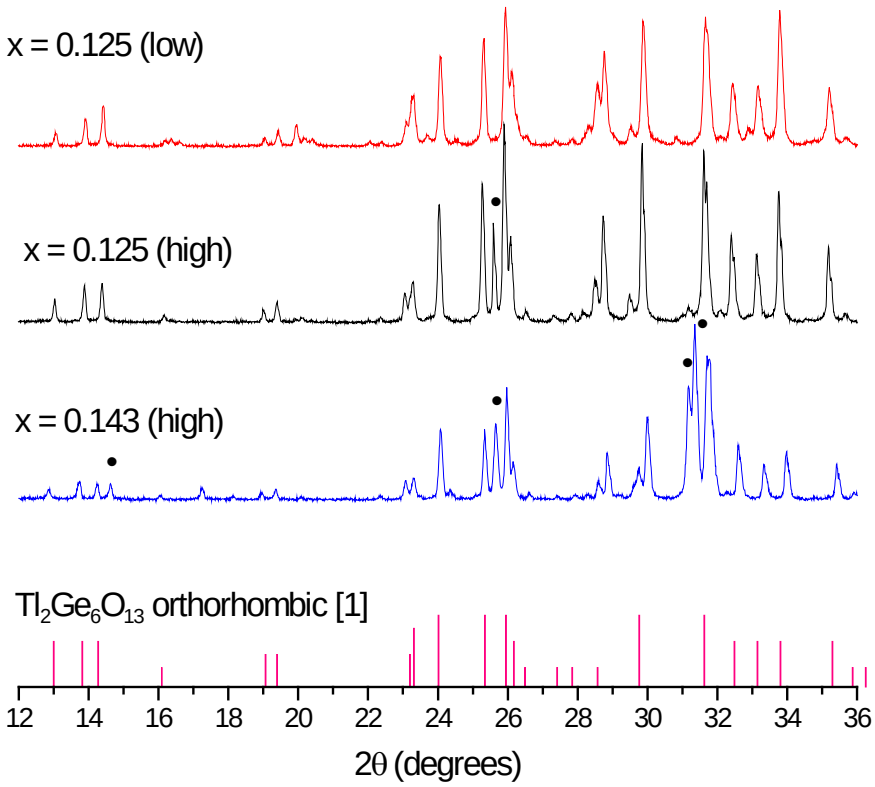

Figure 4.6 *X-ray diffraction patterns of heat-treated x = 0.125 and 0.143 compared with data for orthorhombic $Tl_2Ge_6O_{13}$[1]. (• - intense peaks from second phases, including $Tl_2Ge_4O_9$)*

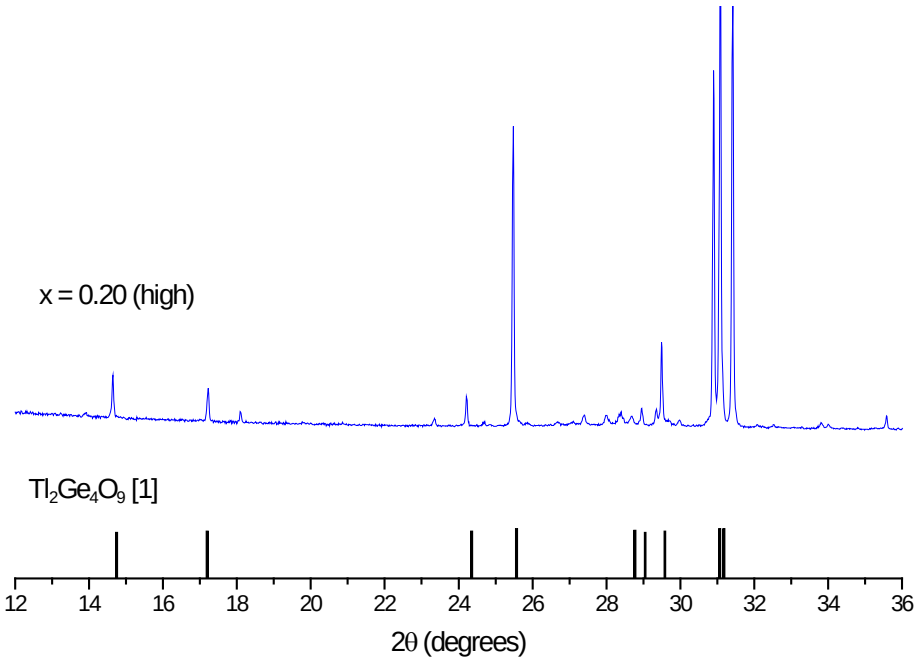

Figure 4.7 *X-ray diffraction pattern of x = 0.20 compared with data for $Tl_2Ge_4O_9$[1].*

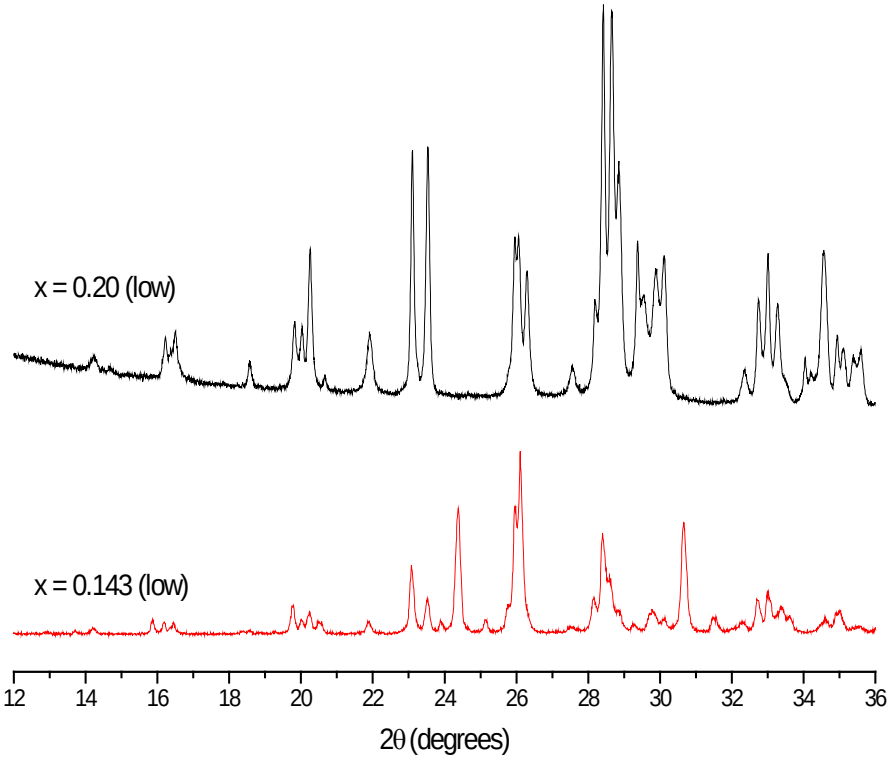

Figure 4.8 *X-ray diffraction patterns of low temperature heat treated x = 0.20 and 0.143 samples showing some similarities.*

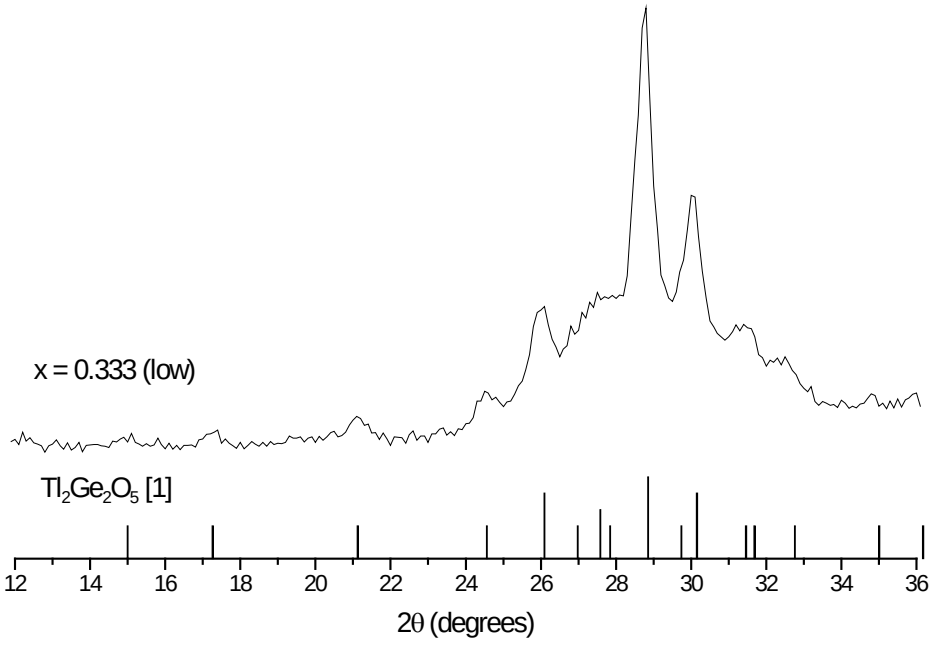

Figure 4.9 *X-ray diffraction pattern of low temperature heat treated x = 0.333 compared with data for $Tl_2Ge_2O_5$[1].*

The low temperature heat treated samples of x = 0.20 and x = 0.143 have some similarities (**Figure 4.8**) but neither correspond to any published patterns, either for thallium or for alkali metal germanate crystals. The X-ray diffraction pattern of low temperature heat-treated x = 0.333 is compared with data for $Tl_2Ge_2O_5$[1] in **Figure 4.9**. The amorphous peak in the pattern shows there is a large quantity of residual glass in this sample, so that the crystallisation process at low temperature is incomplete, and the peaks from the crystalline $Tl_2Ge_2O_5$ phase are also broad, indicating small crystallite size. The powder sample had been heated for 15 hours so both nucleation and crystallisation processes must be slow at this temperature.

Table 4.2 *Summary of crystal phases produced in heat-treated samples.*

x	$Tl_2Ge_7O_{15}$	$Tl_2Ge_6O_{13}$ orthorhombic	$Tl_2Ge_6O_{13}$ Tetragonal	$Tl_2Ge_4O_9$	$Tl_2Ge_2O_5$	Unknown phase(s)
0.125b(high)		✓ (*)				✓
0.125 (low)		✓ (*)				✓
0.143 (high)		✓ (*)		✓ (■)		✓
0.143 (low)						@, ✓
0.20 (high)				✓ (■)		✓
0.20 (low)						@, ✓
0.333 (high)						✓
0.333 (low)					✓	Glass

*, ■ and @ are the symbols used in NMR and Raman interpretation referring to the common phases found in the samples.

4.3.5 Thallium solid-state nuclear magnetic resonance

4.3.5.1 ^{205}Tl solid-state NMR study of heat-treated samples

^{205}Tl solid-solid state NMR spectra of crystallised samples are shown in **Figure 4.10**. and spectra fitted using DM2010 [17] are shown in **Figure 4.11** (x = 0.125 and x = 0.143 samples) and **Figure 4.12** (x = 0.20 and x = 0.333 samples). Fit parameters are summarised in **Table 4.3.** Lack of structural information for these phases makes the interpretation of the thallium environment using solid-state NMR very difficult. However, in conjunction with the XRD data, some information can be obtained e.g. number of thallium sites; multiphase crystallisation; or the presence of residual glass. In interpreting the spectra, it is assumed that Tl at low concentrations (Ge:Tl ≥ 2) will have

an inert lone-pair and therefore will be in a high-coordination, approximately symmetric environment so that the line shape may be approximated as Gaussian or a very broad CSA (as used to fit the $Tl_2Ge_6O_{13}$ phase). At high concentrations ($Tl_2Ge_2O_5$ in this study), the lone pair is expected to be active and therefore Tl^+ will be in a low-coordination, axially symmetric environment and the line shape will be CSA, though this will probably be masked by Tl…Tl dipole-dipole and exchange line broadening.

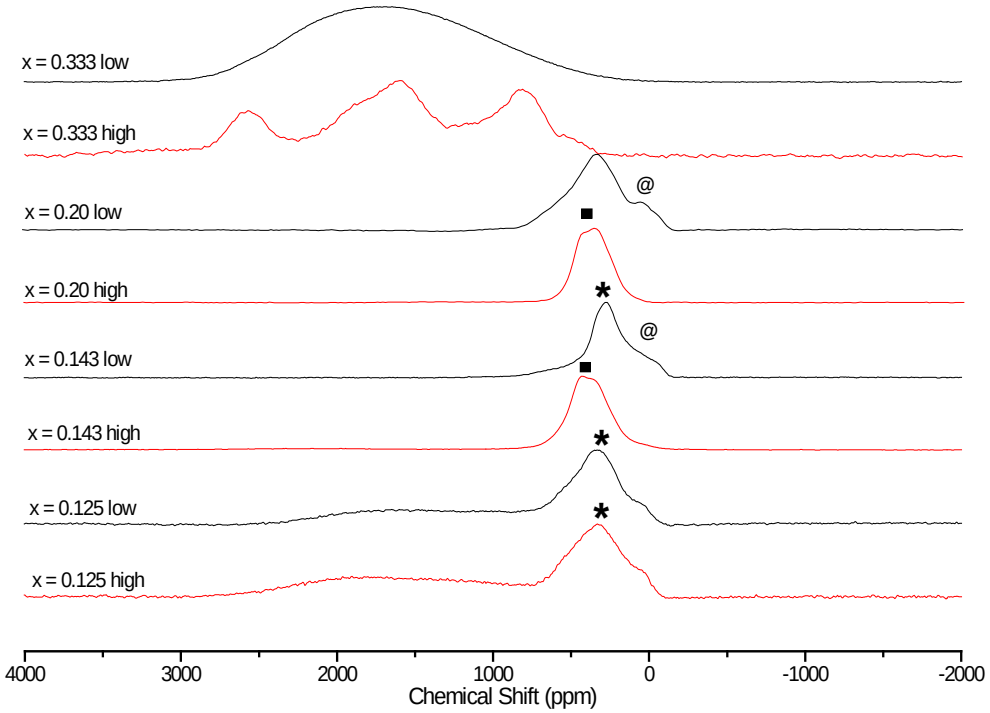

Figure 4.10 *^{205}Tl NMR spectra of heat-treated samples, where,* ■ *and @ are the common features found in the samples.*

From **Figure 4.10** and the X-ray diffraction pattern of the heat-treated samples, some samples might consist of the same thallium environment as the chemical shift positions of the spectra appear at similar values. The x = 0.125 (both low and high temperature) and x = 0.143 (high temperature) samples, which contain $Tl_2Ge_6O_{13}$ crystalline phase, have similar ^{205}Tl-NMR line shape at ~ 380 ppm. The fit of these samples has been carried out by first fitting the x = 0.143 (high temperature) sample using CSA line shape with line broadening. Similar CSA parameters were then applied to the x = 0.125 samples. The residual has been fitted with two Gaussian lines at ~ 2000 and ~1100 ppm to obtain a reasonable fit (**Figure 4.11**). Thus, there are at least three

different thallium sites in the x = 0.125 samples, consisting of the CSA line shape of $Tl_2Ge_6O_{13}$ phase and the Gaussian lines from the unknown phases.

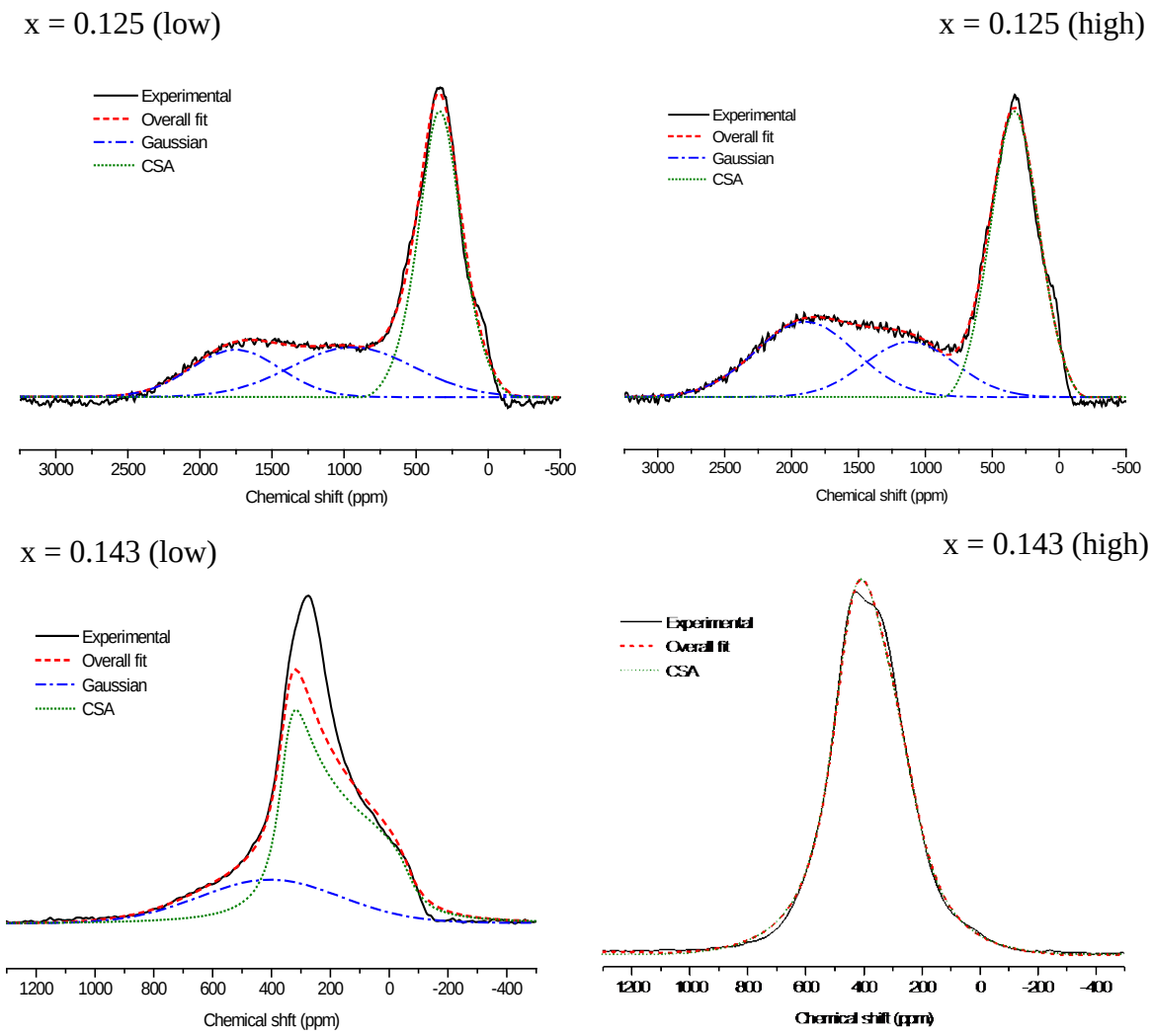

Figure 4.11 *^{205}Tl NMR spectra of low and high temperature heat-treated $Tl_2Ge_7O_{15}$ and $Tl_2Ge_6O_{13}$ samples, fitted with Gaussian and (or) broadened chemical shift anisotropy (CSA) contributions.*

The spectrum from the low temperature heat-treated x = 0.143 sample shows an axially symmetric CSA interaction. Thus, the spectrum was fitted with the CSA line shape with ~ 20 kHz line broadening. A Gaussian line shape was used to fit the broader contribution, which may arise from the glass residue (**Figure 4.11**). An extra Gaussian line shape at ~ 300 ppm, which appears at a similar position to $Tl_2Ge_4O_9$, could be added to the fit to minimise the difference between the experimental spectrum and the fit, but it has been omitted from the figure because there is no evidence from XRD that there is $Tl_2Ge_4O_9$ phase in this sample. The CSA line shape used to fit this sample was

also used in fitting the spectrum from the x = 0.20 sample heat-treated at low temperature as the ^{205}Tl NMR spectrum is similar (**Figure 4.12)**. The residual was fitted with a Gaussian line shape. The shoulder at ~ 50 to 100 ppm may arise from the unknown phase indicated by @ in **Table 4.2** and **Figure 4.10**. This phase may contain an active lone pair site, as found in high thallium content phases, and it has been fitted with a CSA line shape.

The high temperature heat-treated x = 0.20 sample spectrum can be fitted with two peaks: one dominant line (93 %) at ~400 ppm and one smaller (7 %) at ~518 ppm. This indicates that there is only one thallium site in the high temperature phase, consistent with $Tl_2Ge_4O_9$ being isomorphous with $Rb_2Ge_4O_9$ which has a single cation site. The smaller peak is from a thallium-containing impurity phase.

The low temperature $Tl_2Ge_2O_5$ crystalline sample may contain thallium-containing residual glass, according to the broad peak found in the X-ray diffraction pattern. A broad ^{205}Tl-NMR spectrum at around 1700 ppm was obtained. The spectrum is similar to that obtained from the glass samples (**Chapter 5**). Moreover, the position of the spectrum reasonably suggests that the thallium content in the residue is high (> 40 %mol), although the crystal phase which is present in the XRD pattern is the stoichiometric composition $Tl_2Ge_2O_5$. The spectrum could be fitted with two Gaussian contributions consistent with the fitting of glass spectra (**Chapter 5**) but the contribution from the crystal phase cannot be resolved. For a well ordered crystal, a significantly narrower line would be expected in the NMR spectrum. However, other factors must be taken into account: (a) the XRD peaks from the $Tl_2Ge_2O_5$ phase formed at low temperature are significantly broadened, indicating either small crystallite size or disorder in the crystal; (b) the Tl…Tl distances may now be sufficiently short that dipolar and exchange interaction broadening are occurring. In the high temperature $Tl_2Ge_2O_5$ crystalline sample, three peaks appear in the ^{205}Tl NMR spectrum at ~2700, 1680 and 700 ppm suggesting that there are three different thallium sites in this sample, although these three peaks may correspond to more than one crystalline phase. The parameters obtained from DM2010 [17] in all samples are reported in **Table 4.3**.

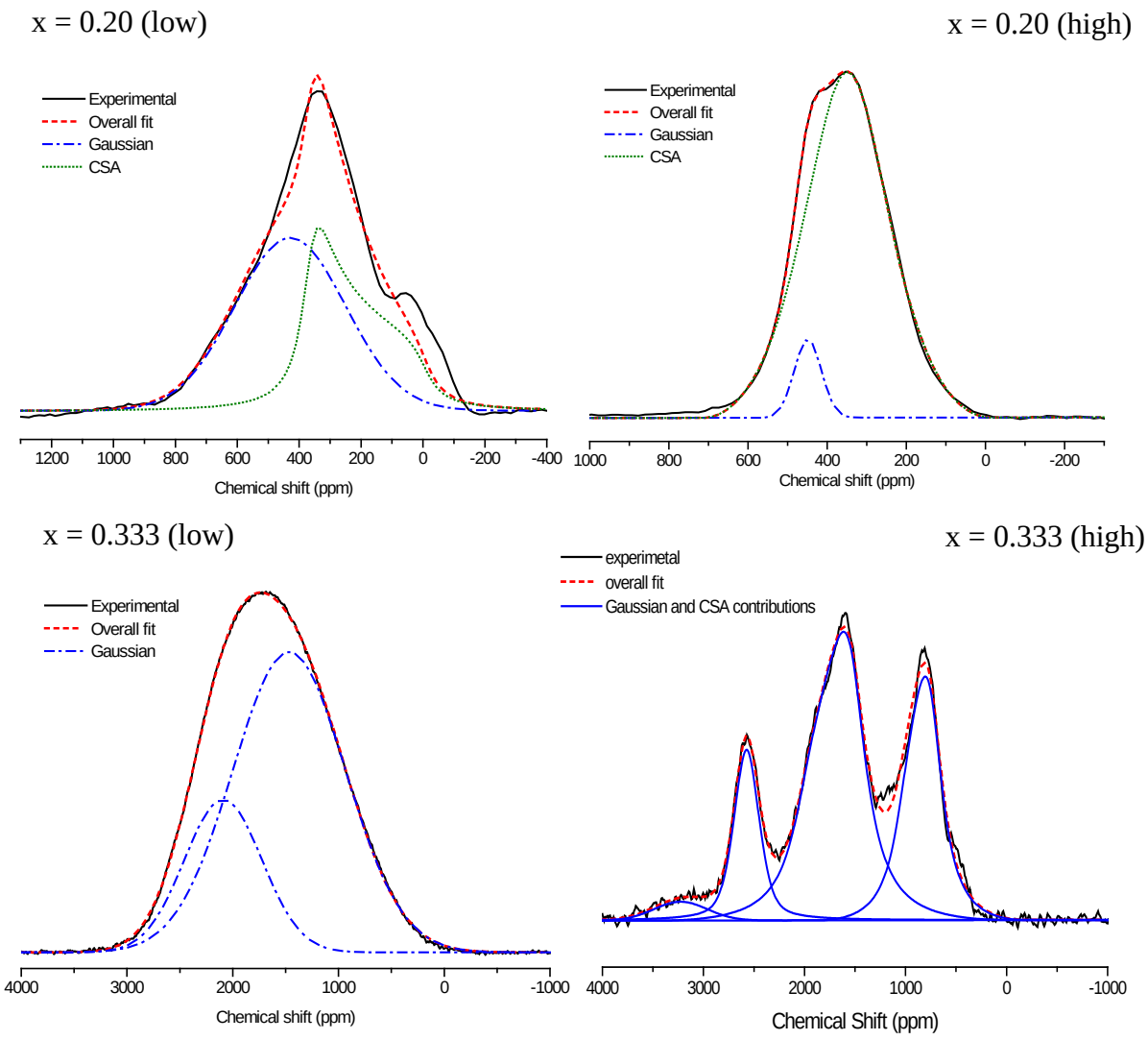

Figure 4.12 *^{205}Tl NMR spectra of low and high temperature heat-treated $Tl_2Ge_4O_9$ and $Tl_2Ge_2O_5$ samples, with the presence of Gaussian and (or) broaden chemical shift anisotropy (CSA) contributions.*

Table 4.3 *Fitting parameters obtained from DM2010 [17]*

Phase		%	CSA (static line shape)			Gaussian	
			δ_{iso} (ppm)	Span; Ω (ppm)	Skew; κ	position (ppm)	width (ppm)
X = 0.125 (low)	Gaussian	38				2000±10	840±10
	Gaussian	29				1100±10	1150±10
	CSA	33	380 ± 10	180 ± 10	1		
X = 0.125 (high)	Gaussian	51				2200±10	1000±10
	Gaussian	22				1300±10	900±10
	CSA	27	380 ± 10	180 ± 10	1		
X = 0.143 (low)	Gaussian	26				470±10	650±10
	CSA	74	240 ± 10	470 ± 10	1		
X = 0.143 (high)	CSA	100	440 ± 10	250 ± 10	1		
X = 0.20 (low)	Gaussian	58				500±10	490±10
	CSA	42	270 ± 10	420 ± 10	1		
X = 0.20 (high)	Gaussian	93			-1	520±10	90±10
	CSA	7	400 ± 10	120 ± 10	-1		
X = 0.333 (low)	Gaussian	26				2400±10	1000±10
	Gaussian	74				1700±10	1450±10
X = 0.333 (high)	Gaussian	18				2700±10	340±10
	CSA	52	1680 ± 10	600 ± 10	-1		
	CSA	30	700 ± 10	360 ± 10	-1		

4.3.5.2 Enrichment study

As described in the introduction, the only crystalline thallium germanate compound that has been proved to be isomorphous with the same stoichiometry alkali germanate compounds is $Tl_2Ge_4O_9$. It would be interesting to study the effect of isotope enrichment to obtain more structural information on the thallium environment in this compound. The nuclear magnetic interactions that are responsible for the line shape and line broadening in solid-state NMR spectra are chemical shift anisotropy, dipolar and exchange interaction [18, 19]. There are 29.5% of ^{203}Tl and 70.5% of ^{205}Tl in natural abundance thallium isotope, for which the gyromagnetic ratios (γ) are 15.5 $\times 10^7$ and 15.7 $\times 10^7$ rad·T^{-1}·s^{-1} respectively[20]. The major contribution to the line shape and line broadening in thallium solid-state NMR spectra is the chemical shift anisotropy. However, the high value of γ of these two isotopes may also broaden the NMR spectrum due to the dipolar interaction [18, 19].

Heat-treated ^{203}Tl enriched $Tl_2Ge_4O_9$ samples were also investigated. ^{203}Tl static NMR spectra obtained from natural isotope and enriched samples are compared in

Figure 4.13. As expected, narrower spectra are observed, which indicates that isotopic replacement could eliminate or reduce the effect of exchange interaction.

MAS NMR has also been carried out on heat-treated enriched samples (**Figure 4.14)**. The NMR spectrum of the low temperature heat-treated sample could not be narrowed by MAS at 17.5 kHz. Thus, only the high temperature heat-treated sample is shown in **Figure 4.14**. This could be considerably narrowed – sufficient to confirm the presence of a single peak and therefore single Tl site in $Tl_2Ge_4O_9$, in agreement with the structure [1].

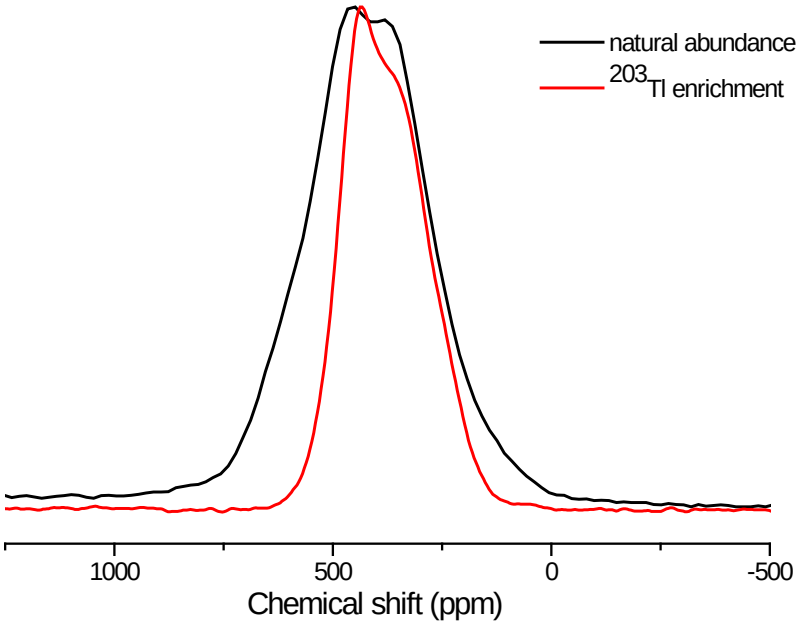

Figure 4.13 *^{203}Tl-NMR of natural abundance and enriched $Tl_2Ge_4O_9$ heat-treated samples at high temperature.*

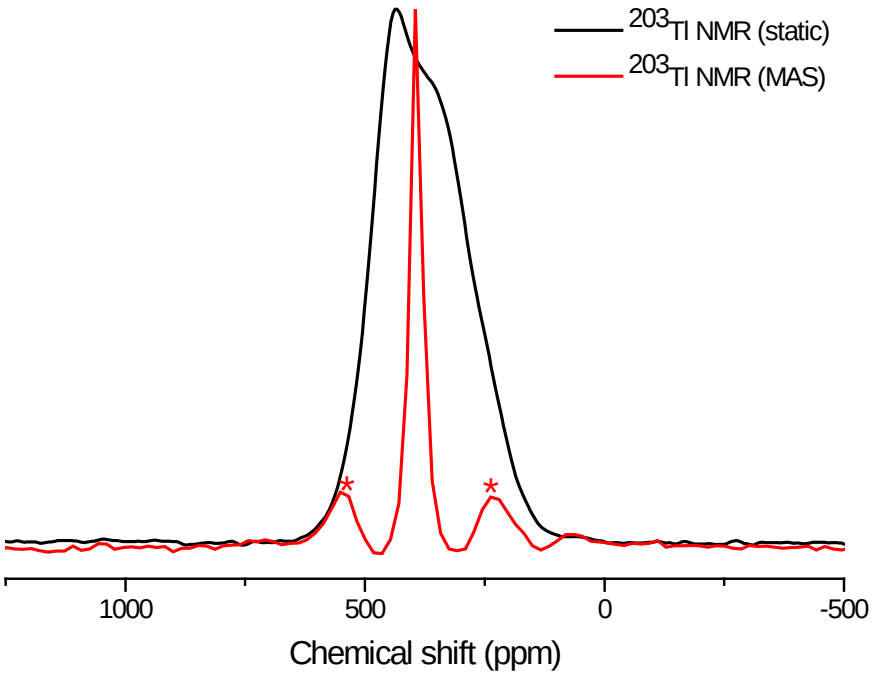

Figure 4.14 *Comparison of static and MAS ^{203}Tl NMR spectra from the ^{203}Tl enriched $Tl_2Ge_4O_9$ crystalline samples heat-treated at high temperature. (* indicates the spinning side band)*

4.3.6 Raman spectroscopy

^{73}Ge NMR is very difficult, for the reasons mentioned earlier. However, the local environment of germanium, in thallium germanate glass and crystals, could be inferred using Raman spectroscopy. Raman spectra of low- and high-temperature heat-treated thallium germanate samples are compared in **Figure 4.15**. The interpretation of the Raman spectra is done by comparison with data obtained from germanium oxide [21] and alkali germanate compounds [22-25]. According to Touboul and Feutelais [1], there are two different germanium environments, $[GeO_4]$ and $[GeO_6]$ in $Tl_2Ge_7O_{15}$, $Tl_2Ge_6O_{13}$ and $Tl_2Ge_4O_9$, which are also found in alkali germanate compounds [12]. The coordination number of oxygen atoms surrounding Ge^{4+} in $Tl_2Ge_2O_5$ remains unknown. The major Raman frequencies obtained from the thallium germanate heat-treated samples in this study are listed in **Table 4.4**.

The tetragonal polymorph of GeO_2 contains $[GeO_6]$ units whose vibrations give rise to Raman peaks at 680, 702 and 870 cm^{-1}. Quartz-like GeO_2 contains $[GeO_4]$ units and produces a characteristic Raman peak at 440 cm^{-1} due to rocking of the Ge-O bond of the GeO_4 unit.

Raman spectroscopy studies [12, 22, 24, 25] of alkali germanate crystalline compounds generally divide the spectra into four regions for discussion:

(1) Peaks observed at very low frequencies (<400 cm-1) - due to the alkali-oxygen vibration, deformation and lattice mode.

(2) Peaks observed between 450 – 550 cm^{-1} - due to the vibrations of the [Ge_3O_9] ring structure, which has been reported in $M_2Ge_4O_9$ compounds (where M=Li, Na and K). The peaks will be split if the rings are distorted[23].

(3) Peaks observed between 700 – 800 cm^{-1} - due to the asymmetrical vibrations of O-Ge-O (ν_{as}(O-Ge-O)). The presence of [GeO_4] and [GeO_6] units may result in differences of the peak position and the character of the peaks may be different.

(4) Peaks observed between 800 – 900 cm^{-1} (usually very strong and sharp) - due to the presence of non-bridging oxygens Ge-O^-.

From the Raman spectroscopy study of thallum germanate compounds systhesised in this study, only general statements can be made because the Raman peak positions are different from the ones observed in germanium oxide [21] or in alkali germanate compounds. Therefore, from the criteria mentioned above it could be summarised that;

1) Vibrations due to the [Ge_3O_9] ring structure are pronounced in high temperature heat-treated $Tl_2Ge_7O_{15}$, $Tl_2Ge_6O_{13}$ and $Tl_2Ge_4O_9$ samples, according to the peaks (marked as black square in **Figure 4.15**) present between 450-550 cm^{-1}.

2) There are no NBO in these heat-treated samples as evidenced by the absence of strong sharp peaks around 800 – 900 cm^{-1}.

3) The vibrations due to the germanate network in $Tl_2Ge_6O_{13}$ and $Tl_2Ge_4O_9$ are at ~ 533 cm^{-1} (asterisk in **Figure 4.15**) and ~ 219, 477 and 499 cm^{-1} (black square in **Figure 4.15**), respectively. The unknown phase in low temperature heat-treated x = 0.143 and x = 0.20 samples has common raman peaks at ~319, 575 and 644 cm^{-1}.

4.4 Conclusions

The structures of eight thallium germanate heat-treated samples were investigated using ^{205}Tl solid-state NMR, Raman spectroscopy and X-ray diffraction. Low temperature heat-treatment generally produces metastable phases, which will eventually transform to the more stable phases at high temperature or longer heat-treatment. Density values and calculated molar volumes of high-temperature phases

agree reasonably well with the values given in the literature. X-ray diffraction of these compounds indicates that high temperature heat-treatment provides crystallisation of the corresponding stoichiometric compounds from the glass but with one or more second phases. ^{205}Tl solid-state NMR studies reveal that various chemical environments of thallium are present in the heat-treated samples, according to the chemical shift of the peaks observed. In the samples with thallium oxide content less than 33 mol% ($x<0.33$), thallium seems to be in the high-coordinated environment, i.e. highly ionic, spherically symmetric. On the other hand, in high thallium content samples ($x\geq0.33$), thallium is in a low-coordinated environment, i.e. highly covalent, axially symmetric, as the Tl-NMR spectrum is very broad. ^{203}Tl NMR of an isotope enriched sample was also investigated for the $Tl_2Ge_4O_9$ sample, whose crystal structure is known. Raman spectroscopy and solid-state NMR confirms the $[Ge_3O_9]$ ring structure containing $[GeO_4]$ units with $[GeO_6]$ linkage, and one thallium environment exists in the high temperature heat-treated sample.

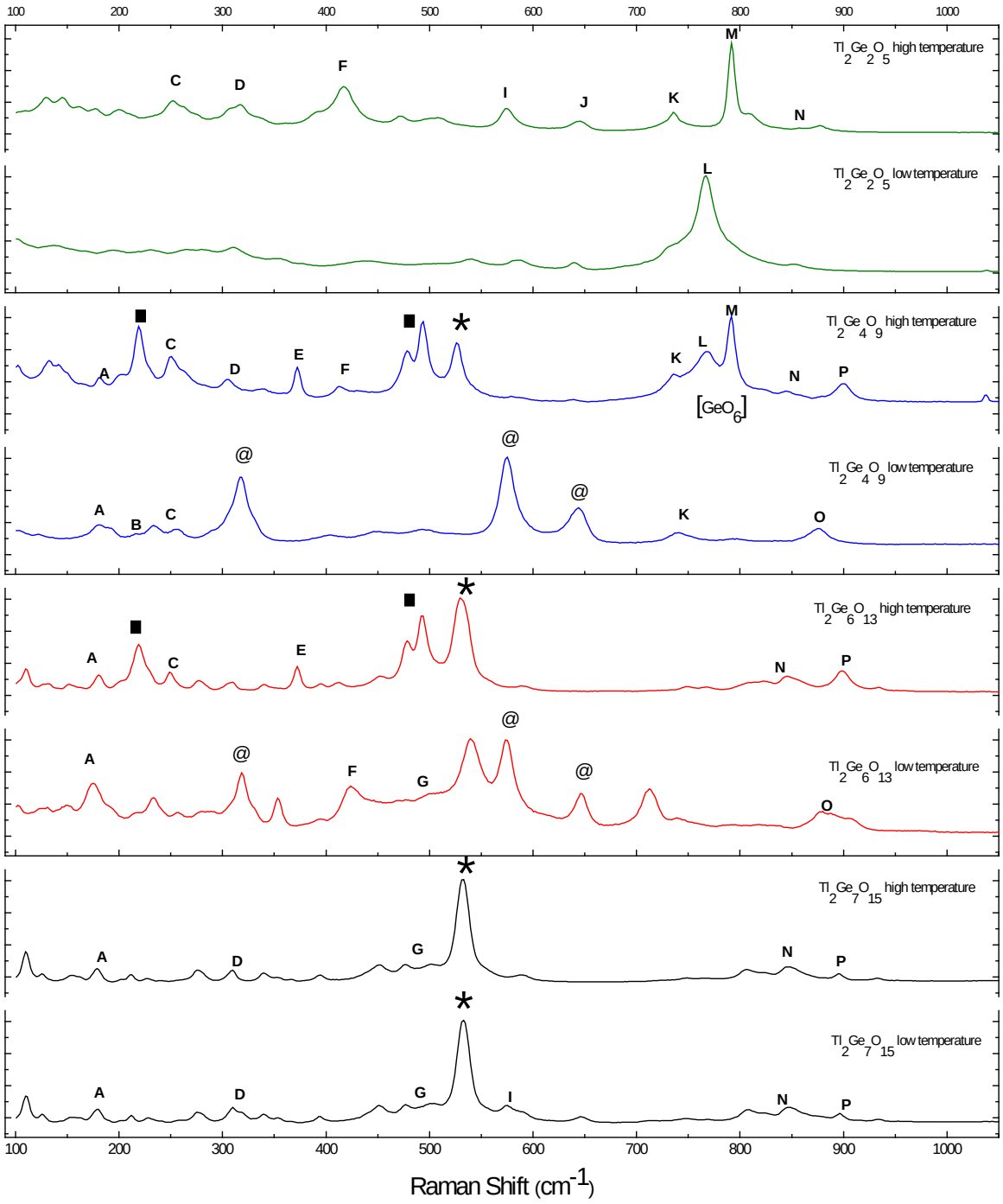

Figure 4.15 *Raman spectra of crystalline thallium germanate samples; $Tl_2Ge_7O_{15}$, $Tl_2Ge_6O_{13}$, $Tl_2Ge_4O_9$ and $Tl_2Ge_2O_5$.*

Table 4.4 *Observed Raman frequencies of heat-treated samples.*

Peak	Raman Shift (cm^{-1})							
	$Tl_2Ge_7O_{15}$		$Tl_2Ge_6O_{13}$		$Tl_2Ge_4O_9$		$Tl_2Ge_2O_5$	
	low T	**high T**	**low T**	**high T**	**low T**	**high T**	**low T**	**high T**
A	179	178	176	180	179	181	-	179
B	-	-	-	219	216	219	-	-
C	-	-	-	250	257	251	-	252
D	311	310	319	-	318	-	-	315
E	-	-	-	372	-	372	-	-
F	-	-	423	-	-	-	-	417
G	477	477	477	477	-	478	-	472
	501	501	499	493	-	494	-	508
H or *	533	532	540	531	-	527	540	-
I	576	-	575	-	575	-	586	575
J	-	-	647	-	644	-	640	645
K	-	-	-	-	740	736	-	736
L	-	-	-	-	-	767	767	-
M	-	-	-	-	-	792	-	792
N	808	806	-	814	-	825	-	811
	849	849	-	848	-	846	853	-
O	-	-	877	-	876	879	-	878
P	896	896	-	899	-	900	-	-

4.5 References

[1] M. Touboul, Y. Feutelais, *Journal of Solid State Chemistry*, **32** (1980) 167.

[2] M. Touboul, Y. Feutelais, *Acta Crystallographica Section B-Structural Science*, **35** (1979) 810.

[3] W.A. Vollenkl.H, *Monatshefte Fur Chemie*, **102** (1971) 1245.

[4] M. Goreaud, B. Raveau, *Acta Crystallographica Section B-Structural Science*, **32** (1976) 1536.

[5] Y. Iwata, I. Shibuya, M. Wada, A. Sawada, Y. Ishibashi, *Journal of the Physical Society of Japan*, **56** (1987) 2420.

[6] Vollenkl.H, A. Wittmann, H. Nowotny, *Monatshefte Fur Chemie*, **101** (1970) 46.

[7] W.A. Viillenkle.H, *Monatshefte Fur Chemie*, **99** (1968) 251.

[8] K. Kamiya, K. Matusita, H. Akiyama, S. Sakka, *Materials Research Bulletin*, **14** (1979) 641.

[9] V.N. Sigaev, S.V. Lotarev, E.N. Smelyanskaya, P.D. Sarkisov, A.A. Volkov, G.A. Komandin, V.V. Koltashev, V.G. Plotnichenko, *Glass Physics and Chemistry*, **32** (2006) 296.

[10] P. Pernice, A. Aronne, A. Marotta, *Thermochimica Acta*, **196** (1992) 1.

[11] V.N. Sigaev, I. Gregora, P. Pernice, B. Champagnon, E.N. Smelyanskaya, A. Aronne, P.D. Sarkisov, *Journal of Non-Crystalline Solids*, **279** (2001) 136.

[12] T. Furukawa, W.B. White, *Journal of Materials Science*, **15** (1980) 1648.

[13] F.F. Riebling, *Journal of Chemical Physics*, **55** (1971) 804.

[14] K. Nassau, D.L. Chadwick, *Materials Research Bulletin*, **17** (1982) 715.

[15] K. Nassau, D.L. Chadwick, *Journal of the American Ceramic Society*, **65** (1982) 197.

[16] G.V. Samsonov, *The Oxide handbook*, IFI/Plenum, (1982).

[17] D. Massiot, F. Fayon, M. Capron, I. King, S. Le Calve, B. Alonso, J.O. Durand, B. Bujoli, Z.H. Gan, G. Hoatson, *Magnetic Resonance in Chemistry*, **40** (2002) 70.

[18] J.F. Hinton, K.R. Metz, R.W. Briggs, *Progress in Nuclear Magnetic Resonance Spectroscopy*, **20** (1988) 423.

[19] J.F. Hinton, *Bulletin of Magnetic Resonance*, **13** (1992) 90.

[20] M.Winter (1993), *NMR Properties of Thallium*, available at http://www.webelements.com/thallium/nmr.html (Accessed: 5 November 2011).

[21] J.F. Scott, *Physical Review B*, **1** (1970) 3488.

[22] H. Verweij, J. Buster, *Journal of Non-Crystalline Solids*, **34** (1979) 81.

[23] J. Choisnet, A. Deschanvres, P. Tarte, *Spectrochimica Acta Part a-Molecular and Biomolecular Spectroscopy*, **31** (1975) 1023.

[24] H. Verweij, *Journal of Non-Crystalline Solids*, **33** (1979) 41.

[25] H. Verweij, *Journal of Non-Crystalline Solids*, **33** (1979) 55.

Chapter 5

Thallium Germanate Glasses

5.1 Introduction

High optical nonlinearity glasses are of interest, for instance in optical switching applications [1-3]. Heavy metals, like lead (Pb), bismuth (Bi), titanium (Ti) and tellurium (Te) were found to play an important role in the optical nonlinearity in oxide glasses, with germanate glass being of particular interest [1, 3]. Thallium germanate glasses have been selected to be structurally investigated because thallium has been shown to enhance nonlinear optical properties [2] and has the additional interest of the presence of a lone pair of electrons on the Tl^+ ion.

Alkali germanate glasses have been widely studied and their structures provide a good model to start to understand the effect of monovalent cation additions (R_2O) on the structure of germanate glass. In germanium oxide (GeO_2) glass, a network of [GeO_4] units is found [4-7] like that of [SiO_4] in silicon oxide (SiO_2) glass, but the structure of alkali germanate glasses differs from that of silicates. There is an increase in coordination number of germanium from 4 with addition of R^+ [8-10], while silicate glasses show only a change in Q-species $[SiO_4]^n$ ($0 \leq n \leq 4$; n = number of bridging oxygens) [11, 12]. Alkali germanate glasses also show anomalous changes in thermophysical properties due to the change in Ge coordination number, n_{GeO}, when alkali oxide content increases [8, 9], though there is some disagreement as to the actual higher coordination number. Hannon et al [8] investigated caesium germanate glasses using pulsed neutron diffraction and suggested that [GeO_5] units have been formed from [GeO_4] units. This was also reported in a potassium germanate study [9]. However, a neutron diffraction study of sodium germanate glasses [10] was interpreted in terms of the presence of [GeO_6] units, rather than [GeO_5]. A similar conclusion was reached using EXAFS (extended X-ray absorption fine structure) and X-ray diffraction studies of lithium, sodium and potassium germanate glasses [13]. In addition to the change of Ge environment, formation of non-bridging oxygens (NBO) was also detected and found to be related to the concentration of Rb_2O [14] in order to achieve a charge balance, although NBO have not been detected at a concentration of alkali oxide less

than 20 mol% in the case of sodium germanate glasses [10]. Neutron scattering data [4] showed the bond length of Ge-O to be 1.739 Å in [GeO_4], though the intratetrahedral bond angle of O-Ge-O was distorted. Jain et al [15] reported that [GeO_4] units are converted to [GeO_6] units at low Rb_2O concentration (about 15-20 mol%), with NBO present at higher Rb_2O concentration. Three Rb sites were found in this glass at various concentration of Rb_2O. Only one site (medium stability) was found in Rb_2O < 10 mol% glasses, with higher concentration containing two sites, high and low stability. Raman spectroscopy of these glasses has also been reported [16-19]. The anomalous behaviour could be explained by the change in n_{GeO} and the formation of non-bridging oxygen atoms, even though another model, proposing unchanged [GeO_4] environment but formation of rings, has also been published [19, 20].

Few structural studies have been published on thallium germanate $xTl_2O\cdot(1-x)GeO_2$ glasses [21, 22]. Riebling [23] observed a change in n_{GeO} from 4 to 6 as the concentration of Tl_2O increased. For $0.019 \leq x \leq 0.365$, the [GeO_4] units, which are parts of a corner-sharing network in GeO_2 glass, were transformed to [GeO_6]. The Tl-O bond was believed to change from ionic to covalent at x = 0.15; this was inferred from the colour change from colourless to yellowish at this composition which could be explained by the polarising power of Tl^+ in glasses [23]. Later in 1976, Panek and Bray [22] applied wide-line solid-state NMR to study the thallium environment in germanate glasses. The study confirmed the change from an ionic environment to a covalent environment around thallium when x increased, although the details of thallium coordination or thallium structure were not resolved [22].

As mentioned above, it is interesting to compare the changes in glass structure of thallium germanate glass with alkali germanate glasses in order to see the effect of the Tl^+ lone pair of electrons on the glass structure. Glass densities and molar volumes (calculated from density) are presented in order to observe the germanate anomaly in these glasses. Change in Ge-O coordination number, which is generally used to explain the germanate anomaly, was determined by means of neutron diffraction technique which also gave information on the Ge-O, Tl-O and Tl-Tl distances. These parameters are important to understand the change in glass structure with Tl_2O content. Thallium solid-state NMR was used to investigate the change in thallium environment in the glass in more details. In addition, Raman spectroscopy was used to tract the change in Ge-O

environment in comparison with the Raman studies of alkali and lead germanate glasses.

5.2 Experimental detail

5.2.1 Sample preparation

Thallium germanate glasses were prepared by traditional melting and quenching from a mixture of thallium carbonate (Tl_2CO_3) and germanium oxide (GeO_2). The batches, containing 5 to 50 mol% of thallium oxide (Tl_2O), were mixed and melted for 15 minutes in a Pt/Rh crucible at 100 °C above the liquidus obtained from the Tl_2O-GeO_2 phase diagram [24]. The melts were then cooled by splat-quenching between two cast iron plates. Weight change during the melting process was monitored to measure possible volatilisation of thallium oxides. Due to the slightly hygroscopic nature of the samples, they were then kept in desiccators until required for measurements.

In order to investigate the effect of the exchange interaction, which was observed in the thallium NMR study by Panek and Bray [22], 97.32 ± 0.3 % enriched Tl_2O_3 was used instead of Tl_2CO_3 in one sample at the composition x= 0.20. This composition was chosen to coincide with a known crystal structure (**Chapter 4**). The glass was prepared as above, but the melt was cooled in the crucible by dipping into water in order to increase the cooling rate.

5.2.2 Energy dispersive X-ray spectroscopy (EDS)

A Zeiss Supra55-VP Scanning Electron Microscope (SEM), operated at an accelerating voltage of 10 kV with an energy dispersive X-ray spectroscopy (EDS) and EDAX Genesis detector with thin window, was used to determine the thallium and germanium content of the glasses. A flat piece of glass was stuck to the sample holder with a carbon sticky pad and then coated with carbon. Several areas were examined in each case to ensure that the spectrum was reproducible.

5.2.3 Density and Molar Volume

The density of each sample was measured using a Micromeritics AccuPyc 1330 gas pycnometer using helium. The molar volume of the samples was then calculated using the nominal compositions.

5.2.4 Thallium Solid-State Nuclear Magnetic Resonance

^{205}Tl and ^{203}Tl (for 20 mol% sample) static NMR was performed on a 4.7 T Chemagnetics Infinity 200 MHz spectrometer using a 6mm Varian probe tuned to 115.7 MHz and 114.3 MHz, respectively. A static echo pulse sequence was used with 1.5 μsec and 3 μsec pulse widths corresponding to 90° and 180° pulses, respectively with a pulse separation, τ, of 40 μsec, and 10 seconds pulse delay. Thallium nitrate ($TlNO_3$) solution was used as the reference. Data have been processed for the whole echo of the FID as discussed in **Chapter 3**.

The spin-spin relaxation times (T_2) of the glass samples were measured by monitoring the changes in the area of the spectrum as the echo time, tau, was increased as described in **Chapter 3**.

5.2.5 Raman Spectroscopy

A Jasco NRS-3100 laser Raman Microscope (Coe College, Iowa, USA) with a 785 nm laser was used to examine powder samples of thallium germanate glasses over the range 1800 cm^{-1} to 100 cm^{-1}. Several areas were examined in each case and various exposure times were used to ensure that the spectrum was reproducible.

5.2.6 Neutron diffraction

Neutron diffraction data from the samples of composition x = 0.05 to 0.40 were obtained using the GEM diffractometer at the ISIS pulsed neutron source, Rutherford Appleton Laboratory, UK. Glass fragments were held in 8.3 mm diameter cylindrical cans made of 25 μm vanadium foil to minimise corrections due to the container. The differential cross-section $\frac{d\sigma}{d\Omega} = I(Q) = I^s(Q) + i(Q)$ was measured in order to obtain the distinct scattering $i(Q)$, where Q is the magnitude of the scattering vector.

The diffraction data were analysed and interpreted by Barney and are published in [25, 26]. Some of the relevant neutron diffraction results are used here in order to support the results obtained from other techniques.

5.3 Results and discussion

5.3.1 Glass composition and glass formation

Accurate knowledge of the glass composition is important for interpreting structural changes with composition. Differences from the nominal glass composition after sample preparation were obtained from (excess) weight loss measurements and EDS analysis. The % deviations from the nominal Tl2O composition, obtained from both methods are compared in **Figure 5.1**. Large difference are observed between these two methods. Errors which could arise in EDS measurements may be due to: (1) a rough sample surface (polishing was avoided due to the health and safety issues of high toxicity thallium and (2) non-calibrated EDS. The weight lost during the melting process was largely as expected from the decomposition of Tl_2CO_3, any excess is mainly due to the loss of thallium. This was < 1 mole % of Tl_2O for glasses with x = 0.05 to 0.50 [26]. Samples with x = 0.05 to 0.40 were clear and XRD confirmed that they were amorphous.

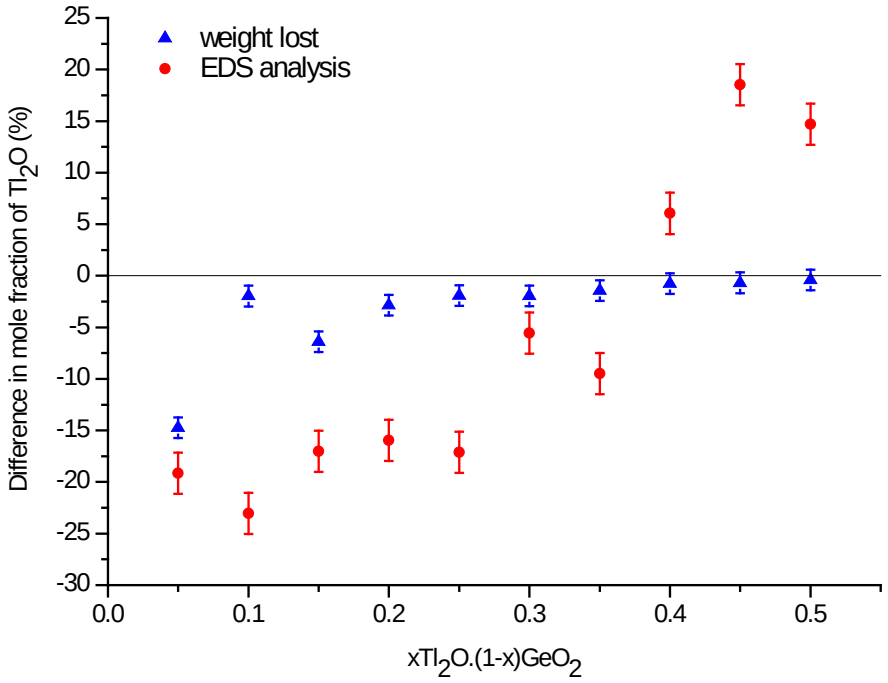

Figure 5.1 *% difference of measured mole fraction of Tl_2O in glasses from the nominal composition: obtained from weight loss (**blue triangle**) and EDS analysis (**red circle**).*

Although partial crystallisation of samples containing 0.45 and 0.50 mole fraction Tl_2O was observed, clear portions were selected for study (density, solid-state NMR and Raman spectroscopy) and assumed to be representative of the glass sample. Small dark particles were also found in glass samples with x = 0.45 and 0.50 which probably arise from disproportionation of Tl^+ to Tl^{3+} and Tl^0. As described above, the nominal composition is used throughout this chapter.

5.3.2 Density and molar volume

Glass densities and molar volumes, which were calculated using nominal compositions, are compared in **Figure 5.1** with values given in the literature [23, 27, 28] and with crystalline compounds described in [24]. The values obtained in this study are consistent with the literature, confirming that the Tl_2O content in the glasses is close to the nominal composition.

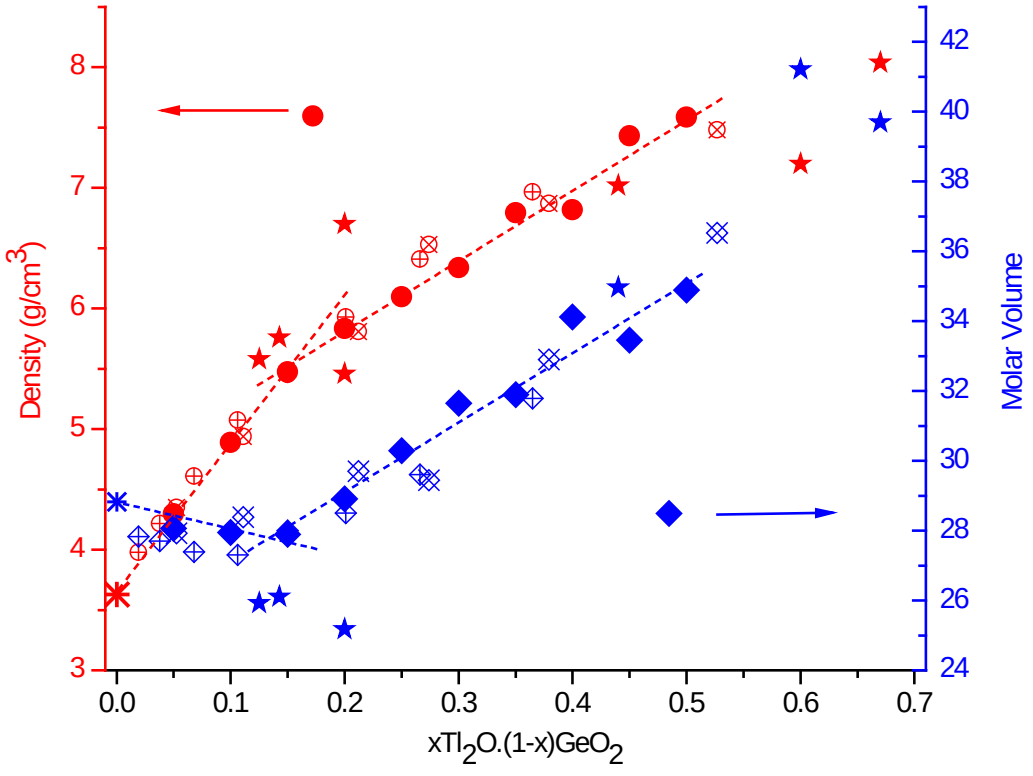

Figure 5.2 *Densities and molar volumes for glasses (**closed symbols** - measured in this study; **open symbols** - obtained from ref. [23, 27, 28], (**star**) - crystalline compounds obtained from ref. [24]; and **asterisks** at x = 0 are reported values for GeO_2 glass. Dotted lines are drawn to guide the eye.*

The germanate anomaly, observed in many alkali germanate glasses [8, 19, 20], is the existence of a maximum or minimum in the change of a given property with composition. In thallium germanate glass, this anomaly is observed as a change in slope in the density versus composition plot at about x = 0.15, where the minimum in molar volume is also observed. This reflects the change in local unit of germanium oxide network from [GeO_4] to [$GeO_{5\text{ or }6}$], previously reported for thallium germanate [23, 25, 26] and alkali germanate glasses [8, 9, 19, 20]. The densities and molar volumes of glasses are slightly different from the crystalline compounds [24] (stars in **Figure 5.2**) due to bond length and bond angle distortion in the glass which usually results in lower density.

5.3.3 Neutron Diffraction

The neutron diffraction study [25, 26] of these glasses is summarised here. The distinct scattering; *i(Q)* of the glasses of the composition x = 0.05 to 0.40 and of GeO_2 glass are shown in **Figure 5.3** and differences are clearly observed in the region Q < 15 $Å^{-1}$. The peak at ~0.84 $Å^{-1}$ increases in the intensity as more Tl_2O is introduced into the glasses and the peak at ~1.5 $Å^{-1}$, which is related to the Ge-O network, shifts to higher Q (to 2 $Å^{-1}$ at x = 0.40). A shoulder appears at ~ 3.9 $Å^{-1}$ in higher Tl_2O content glasses (x > 0.15).

The total correlation function in real space; *T(r)* of the glasses, which was obtained from the Fourier transform of the distinct scattering *i(Q)*, is shown in **Figure 5.4**. Peaks in T(r) correspond to the distances between pairs of atoms, i.e. the peaks at ~1.75, ~2.5 and 3.5-3.7 Å correspond to Ge-O, Tl-O and Tl-Tl distances, respectively. The relevant coordination number, n_{ij} can be calculated from the area A_{ij} of the peak at r_{ij} in *T(r)* from

$$n_{ij} = \frac{r_{ij} A_{ij}^{R} c_j \int_0^{Q_{\max}} \mathrm{d}Q}{(2-\delta_{ij}) \int_0^{Q_{\max}} w_{ij}^{R}(Q) \mathrm{d}Q} = \frac{c_j}{c_i} n_{ji}$$

where c_i and c_j are the concentrations of species i and j.

The result reveals that, as x increases, the peak at ~1.75 Å broadens and shifts to longer distance and the area decreases. This is presumed to be due change of coordination number of germanium to oxygen, n_{GeO} from 4 to 5 or 6 and possible formation of non-

bridging oxygen (NBO) atoms. The average Ge-O distance in thallium germanate glass increases as thallium content increases up to x = 0.30, then decreases at higher thallium content. This decrease happens at x ~ 0.19 in alkali germanates. n_{GeO} also reaches a higher value of 4.44 (compared with 4.36 in caesium germanates).i.e. the higher coordinated germanium site [$GeO_{5\ or\ 6}$] is stabilised in the presence of thallium [26].

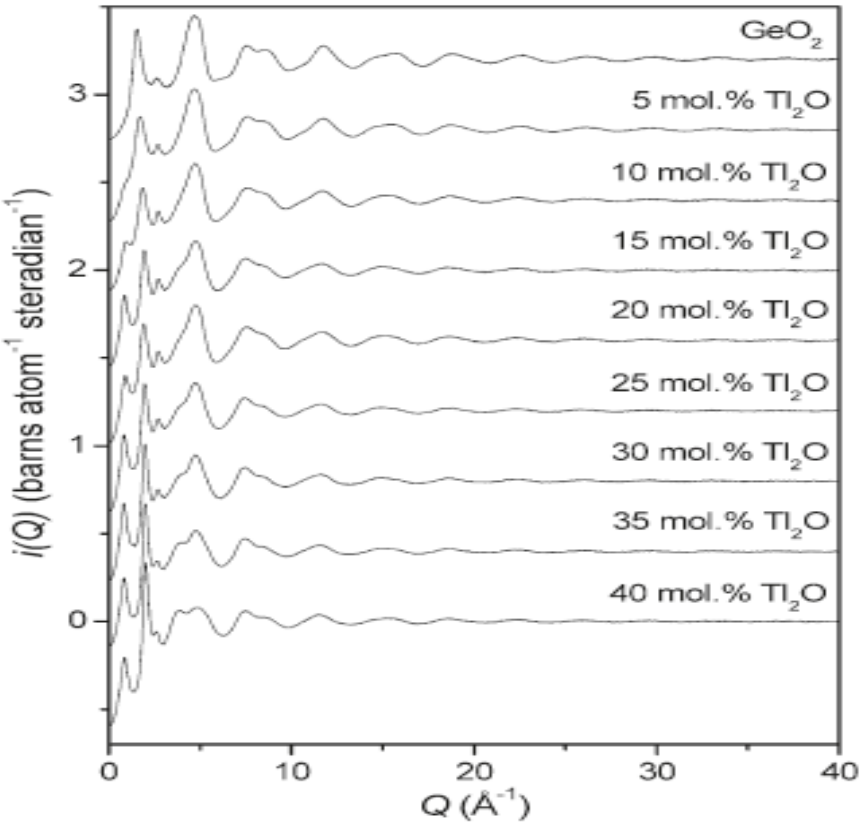

Figure 5.3 *Distinct scattering i(Q) of thallium germanate glasses and pure GeO_2 glass (taken from[26])* .

The coordination number of oxygen atoms around thallium, n_{TlO}, in low thallium content (x = 0.05 to 0.15) germanate glasses is somewhat similar to alkali germanate glass at the same composition, especially caesium germanate glass i.e. high and relatively symmetric. The Tl-O distance in the three coordinated thallium, [TlO_3], unit which is found in $Tl_8Ge_5O_{14}$ [29], is ~2.527 Å. A peak in T(r) at ~2.5 Å is readily visible for glasses containing more than 0.15 mole fraction of Tl_2O and increases in area

with x, indicating the growing dominance of [TlO_3] units. Higher Tl-O coordinations, expected at about 2.8 to 2.9 Å, are obscured by overlap with the O-O peak.

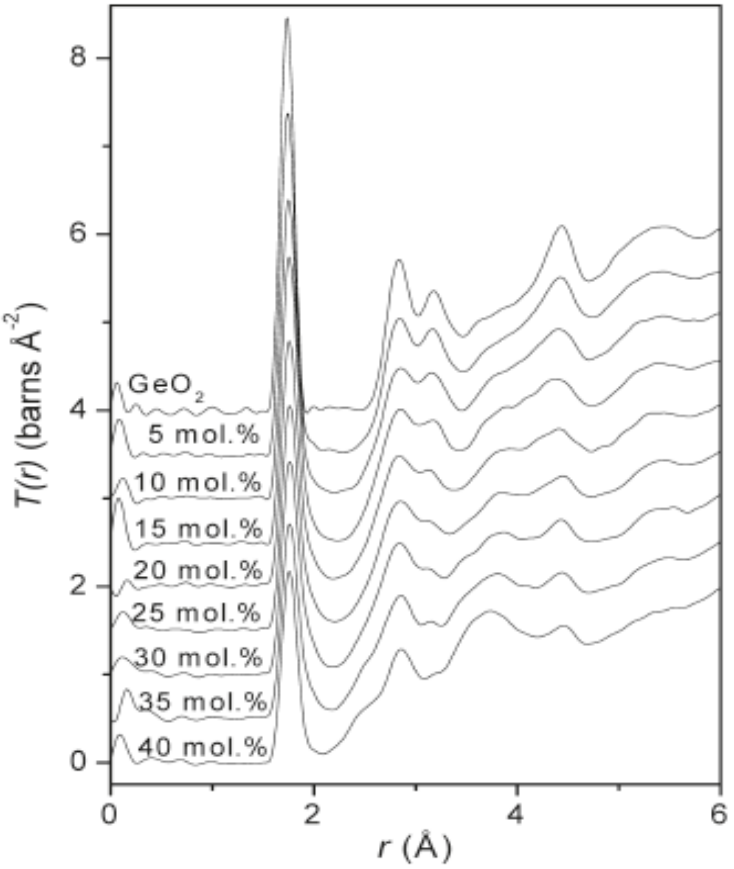

Figure 5.4 *Total correlation function; T(r) of thallium germanate glasses and vitreous GeO2.*

It is believed that the peak at about 3.3 to 4 Å is due to Tl-Tl distances. This peak is shifted to shorter distances as Tl_2O increases, and may be related to the presence of Tl-O-Tl or Tl-clusters in the glass.

5.3.4 Thallium solid-state nuclear magnetic resonance

5.3.4.1 ^{205}Tl solid-state NMR

^{205}Tl NMR spectra of glass samples are shown in **Figure 5.5**. Increasing thallium content, x, causes broadening of the spectrum from 750 ppm (85 kHz) to 1500 ppm (170 kHz). These widths are comparable with those observed in the thallium borate

glass spectra (**Chapter 7**), once allowance has been made for the greater dilution of Tl_2O by B_2O_3 than by GeO_2. The position of the spectra (peak centre at full width half maximum, FWHM) also shifts significantly downfield (to more positive values) from 200 ppm to 1770 ppm with x. Asymmetric line shape was obtained from the lower thallium concentrations ($0.05 \leq x \leq 0.15$). On the other hand more symmetric (Gaussian-like) spectra were obtained at higher thallium content, although there is a shoulder at the downfield edge (~2230 ppm) of the spectra (indicated by the arrow in **Figure 5.5**) for the x = 0.40, 0.45 and 0.50 samples. The spectrum of the x = 0.15 sample also shows a small feature (asterisk in **Figure 5.5**) at ~ 326 ppm.

As reviewed previously in **section 4.1**, the lone pair of electrons on Tl^+ may or may not be sterically active, which will affect n_{TlO}. If the lone pair of electrons is sterically active, an axially symmetric environment (usually lower coordinated to oxygen e.g. [TlO_3] [29] or [TlO_4] [30]) will be expected. On the other hand, if the lone pair of electrons is sterically inert, the thallium environment will have a higher oxygen coordination e.g. [TlO_7] or [TlO_9] [31]. In thallium germanate glasses, especially at low thallium content, the spectrum cannot be fitted with only a single contribution (chemical shift dispersion; CSA or dipolar interaction or exchange interaction), from which it can be inferred that there is more than one thallium site in the glass. So fitting employing DM2010 [32] used two Gaussian contributions to simulate the ^{205}Tl NMR spectra. Some examples (x = 0.05, 0.15, 0.25, 0.35, 0.40 and 0.50) of the fitting are given in **Figure 5.6**. The Gaussian contribution from the higher coordinated thallium environment is assumed to be at higher field (more negative shift) and *vice versa*. It has been reported that thallium in a covalent environment or in paramagnetic shielding has a chemical shift of several thousand ppm [33]. The strange peak and the shoulder in x = 0.15 and x = 0.40 to 0.50 samples, respectively, were also fitted by assuming the extra feature may be due to a small amount of crystalline phase present in x = 0.15 sample and to the existence of Tl^{3+} in x = 0.40 to 0.50 samples.

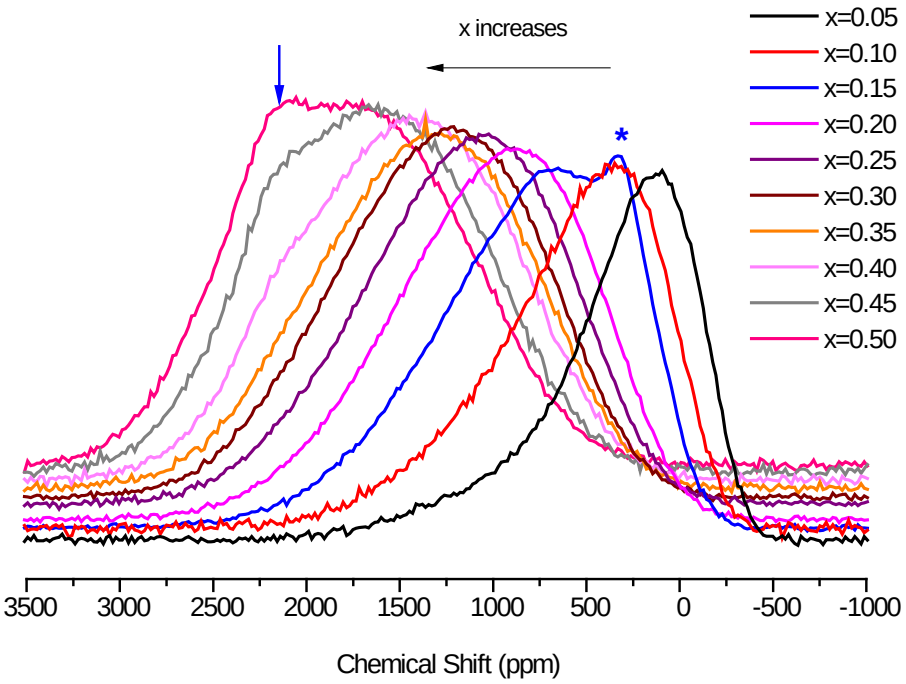

Figure 5.5 *^{205}Tl solid-state NMR of thallium germanate glasses; arrow indicates the position of Tl^{3+} and * indicates the presence of crystalline phase.*

The percentages of the high coordinated thallium site and the low coordinated (more positive shift) thallium site are plotted in **Figure 5.7**. These percentages were obtained by integration of the [TlO_{high}] and [TlO_{low}] peaks from the fit. The percentages of Tl^{+} present as crystalline phase in the x = 0.15 sample and as Tl^{3+} in the x = 0.40 – 0.50 samples are also reported. The width of the crystal peak at ~294 ppm in x = 0.15 sample, is ~420 ppm, which is narrower than the glass peak. It is consistent with the widths of some crystal peaks studied in the previous chapter. So it is believed that this contribution is from some devitrification during cooling, although it was not detectable by XRD. In x = 0.40 – 0.50 samples, it is believed that disproportionation occurs, during melting, from Tl^{+} to Tl^{3+} and Tl^{0} (metal). The metal phase was removed before the glasses were examined and Tl^{3+} remains in the glass phase. Therefore, for x = 0.40 – 0.50 samples, it was assumed that there is one Tl^{+} site and one Tl^{3+} site which was fixed at ~2570 ppm, where the shoulder appears. The parameters of the fit including positions and peak widths are listed in **Table 5.1**.

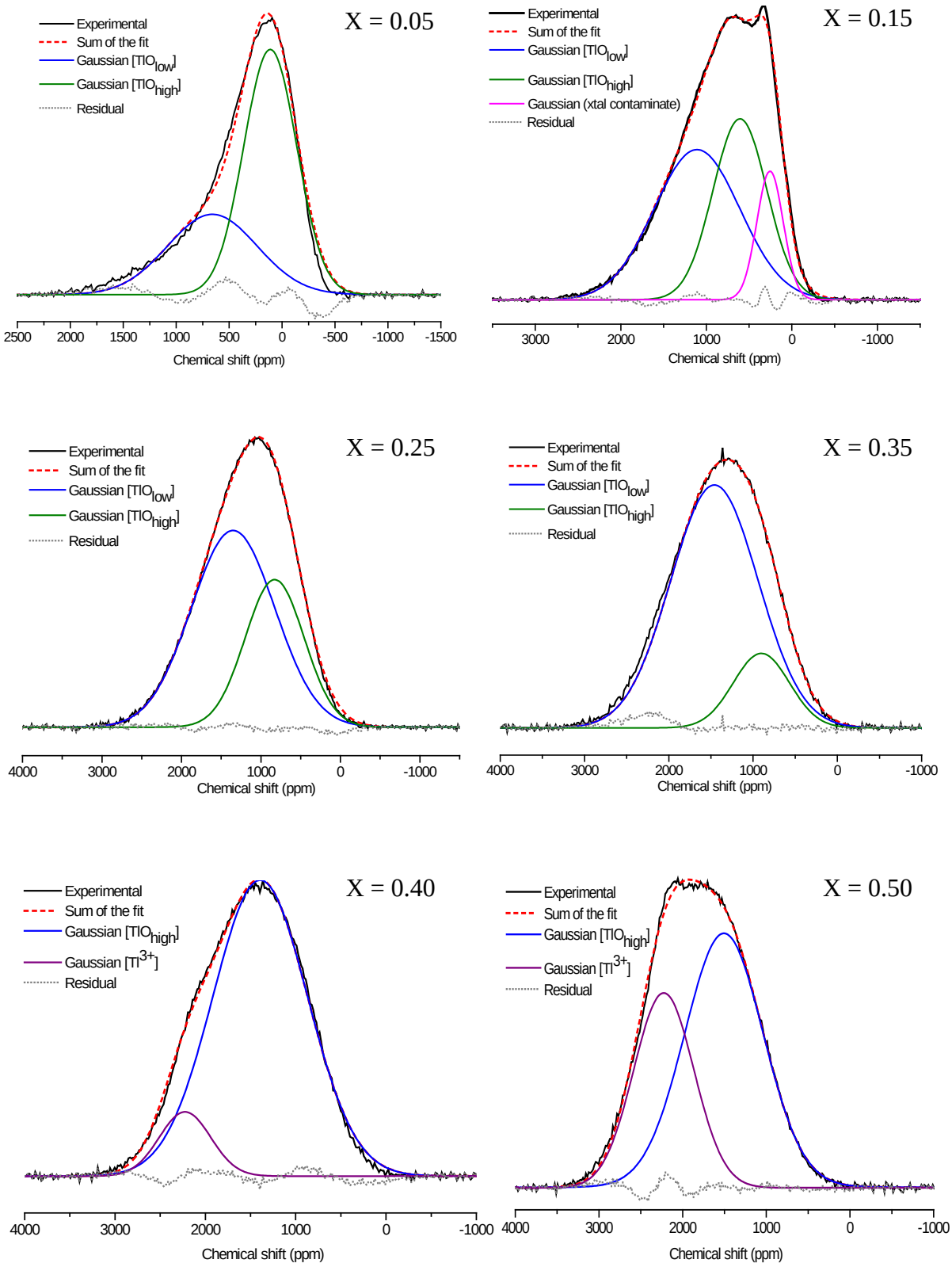

Figure 5.6 *Example of ^{205}Tl NMR spectra fitting using DM2010 [32]*

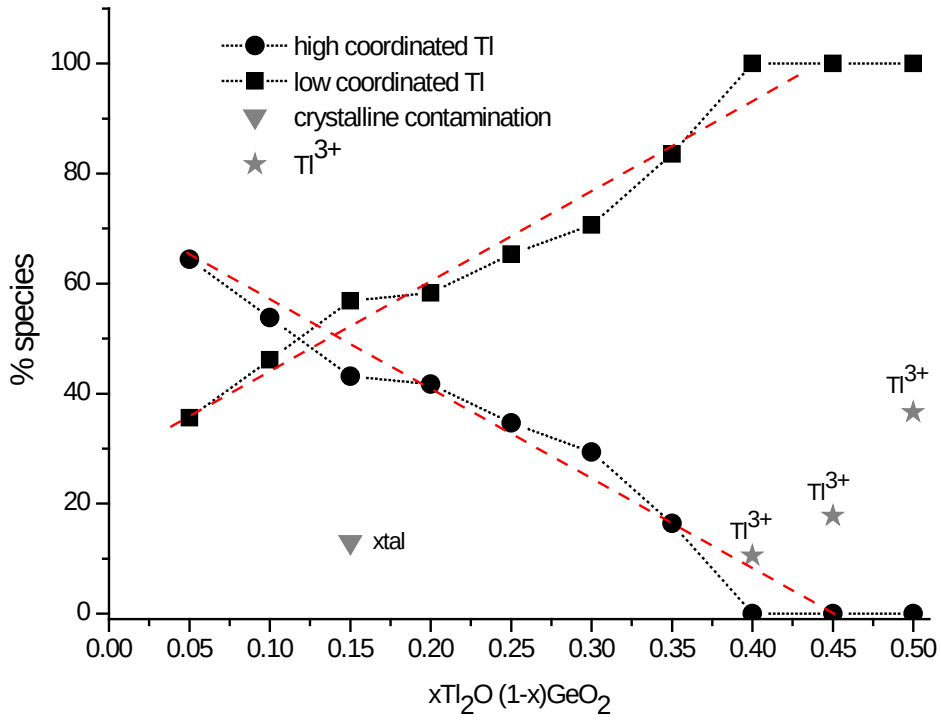

Figure 5.7 *percentage of each* ^{205}*Tl NMR spectrum obtained from the spectra fitting.*

From **Figure 5.7**, the [TlO_{low}] site gradually increases with x and reaches 100 % at x ~ 0.40, which is close to the composition of crystalline $Tl_8Ge_5O_{14}$ (x = 0.44) [29] whose structure contains [GeO_4] units and [TlO_3] units with sterically active lone pairs of electrons. The dashed line was drawn to estimate the linear relationship of these two thallium sites in glasses. It is interesting that these two lines intersect at about x = 0.15 composition, which is the composition where the density and molar volume curves of glass start to deviate (**Figure 5.2**). Thus, changes in dominant thallium environment from high coordinated to low coordinated could play an important role for the deviation of density at x = 0.15 as thallium is very heavy, compared to germanium. **Figure 5.7** also shows that there is ~ 13 % crystalline phase in x = 0.15 and ~ 10 to 40 % of Tl^{3+} in x = 0.40 to 0.50 samples.

Due to the large chemical shift range and very broad spectra, the presence of other thallium sites in the glass cannot be excluded. There is also a lack of crystal structure information and shift references of different thallium environments in oxide systems.

Table 5.1 *Fitting parameters of the glass samples obtained from Dm2010 [32]*

composition	Oxidation state	Thallium environment	%	Gaussian	
				position (ppm)	width (ppm)
X = 0.05	Tl^+ glass	TlO_{low}	35	760±10	1150±10
	Tl^+ glass	TlO_{high}	64	130±10	680±10
X = 0.10	Tl^+ glass	TlO_{low}	46	990±10	1200±10
	Tl^+ glass	TlO_{high}	54	330±10	770±10
X = 0.15	Tl^+ glass	TlO_{low}	57	1280±10	1360±10
	Tl^+ glass	TlO_{high}	43	700±10	860±10
	Tl^+ xtal		13% in sample	290±10	420±10
X = 0.20	Tl^+ glass	TlO_{low}	58	1440±10	1360±10
	Tl^+ glass	TlO_{high}	41	790±10	980±10
X = 0.25	Tl^+ glass	TlO_{low}	65	1560±10	1430±10
	Tl^+ glass	TlO_{high}	35	950±10	1010±10
X = 0.30	Tl^+ glass	TlO_{low}	71	1690±10	1420±10
	Tl^+ glass	TlO_{high}	29	1060±10	1010±10
X = 0.35	Tl^+ glass	TlO_{low}	84	1680±10	1410±10
	Tl^+ glass	TlO_{high}	16	1040±10	910±10
X = 0.40	Tl^+ glass	TlO_{low}	100	1610±10	1430±10
	Tl^{3+} ?		10% in sample	2570±10	770±10
X = 0.45	Tl^+ glass	TlO_{low}	100	1760±10	1410±10
	Tl^{3+} ?		18% in sample	2570±10	840±10
X = 0.50	Tl^+ glass	TlO_{low}	100	1740±10	1280±10
	Tl^{3+} ?		37% in sample	2570±10	980±10

From the values in **Table 5.1**, the positions and widths of the Gaussian contributions of the two thallium sites are plotted in **Figure 5.8**, showing that both increase as thallium content increases. The position of the Gaussian contributions relates to the chemical shift interaction, which arises from the chemical or electronic environment of the Tl nuclei [33-35]. The changes in the position of both contributions are large in the low x region, as the thallium lone-pair changes from sterically inert to sterically active. In high thallium content glasses (x > 0.30) the change is comparatively small.

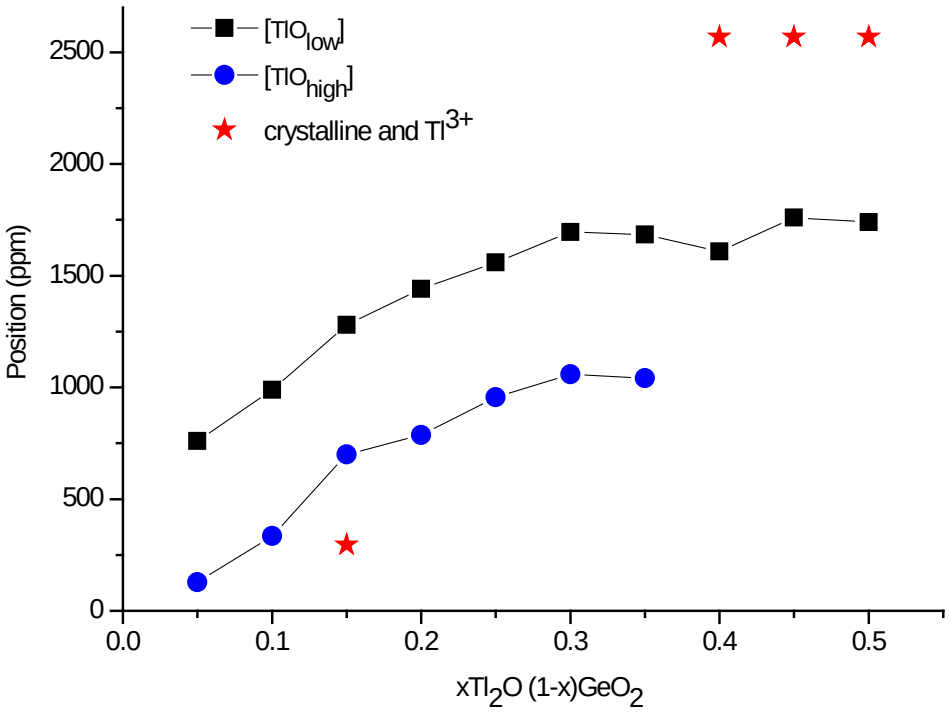

Figure 5.8a *Position of the Gaussian contributions obtained from DM2010 [32]*

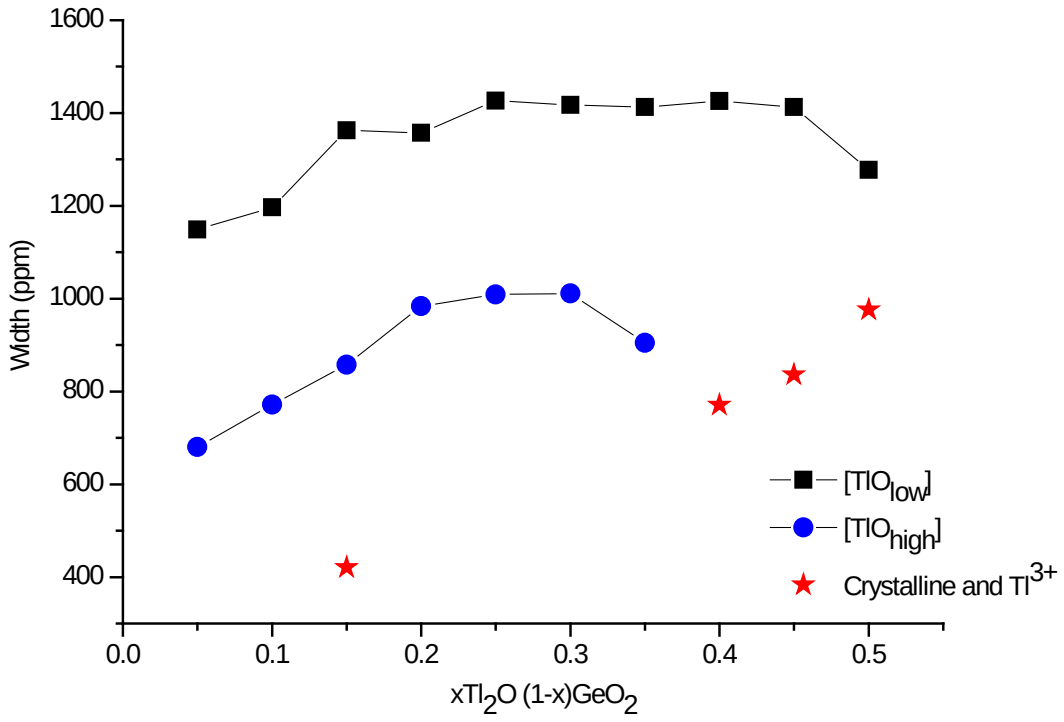

Figure 5.8b *Spectrum width of the Gaussian contributions obtained from DM2010 [32]*

Chemical shift dispersion is usually the main contribution to the line shape of Tl-spectra, though the line could be broadened due to other interactions, i.e. dipole-dipole interaction and pseudodipole interaction (exchange interaction) [22, 33, 36]. ^{205}Tl NMR spectra of these thallium germanate glasses have been broadened by direct and indirect dipole interaction**.** The very large FWHM value of x = 0.40 – 0.50 is believed to be due to the effect of Tl^{3+} contamination in the glass. It seems likely that the low coordinated thallium site plays an important role in the width of the NMR spectrum. The low coordinated thallium site is broader than the higher coordinated thallium site, which means that dipole-dipole interaction or exchange interaction of low coordinated thallium site is stronger. The dipolar interaction is a through space interaction between identical and nonidentical nuclei, whist the exchange interaction is a through-bond interaction via bonding electrons; both are controlled by the thallium-thallium distance [35]. It could be inferred from the broad ^{205}Tl-NMR spectra that the Tl…Tl (dipole interaction) or Tl-O-Tl (exchange interaction) exist in all compositions but is more significant at x > 15 mole %, which is consistent with the wide-line NMR study of Panek and Bray [22]. Thus, as Tl_2O increases, thallium tends to form a cluster or a Tl-rich phase with low-coordinated, highly covalent environment. Broadening due to the dipolar or exchange interaction is stronger than the chemical shift interaction hence the CSA parameters could not be obtained from the ^{205}Tl-NMR study.

A large distribution of chemical shifts, which is indicated by the change of the centre of the spectrum at FWHM, is due to the very different thallium environments, from high-coordinated, isolated thallium at low values of x, to low-coordinated, clustered thallium in high x glasses.

5.3.4.2 ^{203}Tl solid-state NMR

The exchange interaction has been described, using second moments, by Van Vleck [37] and Bloembergen and Rowland [38]. The only contribution from the exchange interaction to the second moment is from nonidentical nuclei, i.e. ^{203}Tl and ^{205}Tl. The way to reduce the line broadening due to the exchange interaction is to enrich the samples with one isotope, which in this study was ^{203}Tl. Static ^{203}Tl NMR of the ^{203}Tl-enriched sample is compared with that of the natural abundance sample in **Figure 5.9**. The FWHM of these spectra are 1344 and 1453 ppm (156 and 167 kHz) for ^{203}Tl-NMR spectra of the enriched sample and the natural abundance sample,

respectively. The enrichment reduces the broadening by ~100 ppm (~10 kHz), although the spectra are still very broad, which is due to shift dispersion. It can be inferred that the contribution from exchange interaction broadens the Tl-NMR spectrum by ~ 10 kHz in x = 0.20 sample. Broadening due to the dipolar interaction (but not chemical dispersion) can be eliminated by MAS, but to narrow the Tl-NMR spectrum in this sample would require an inaccessibly high speed.

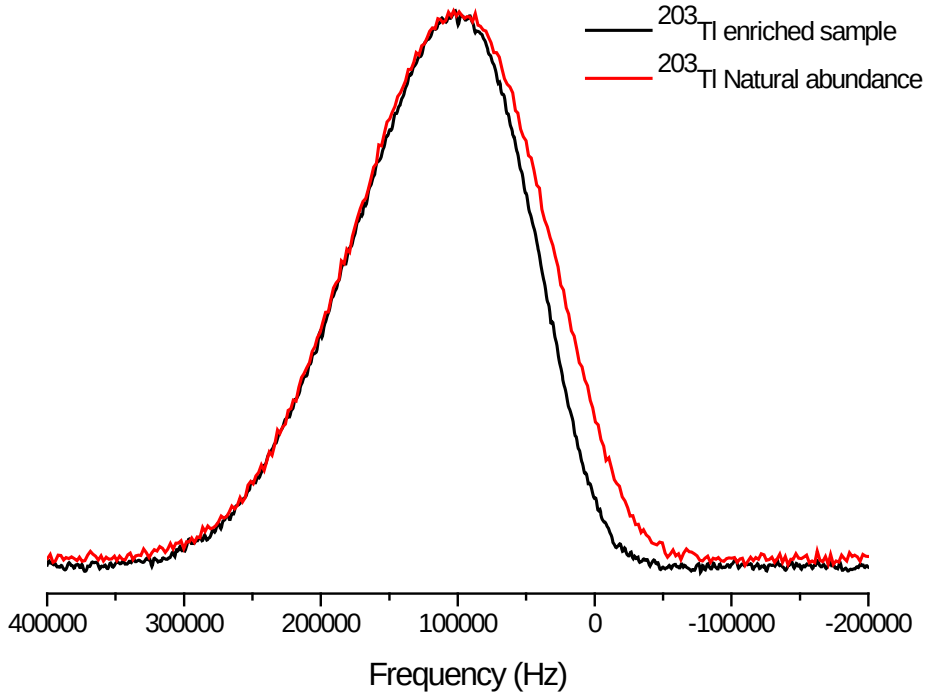

Figure 5.9 *^{203}Tl-NMR spectra of 0.20Tl_2O·0.80GeO_2 glass.*

5.3.4.3 Spin-spin relaxation time (T_2)

The transverse or spin-spin relaxation times, T_2, of glass samples were measured by a pulse-echo experiment as described in **section 5.2**. The T_2 times decrease as thallium content increases as shown in **Figures 5.10 and 5.11**. The rate of decrease is high at low Tl_2O concentrations (x = 0.05 to 0.25) but slow in higher thallium content glasses as shown by the change in the slope in **Figure 5.10**.

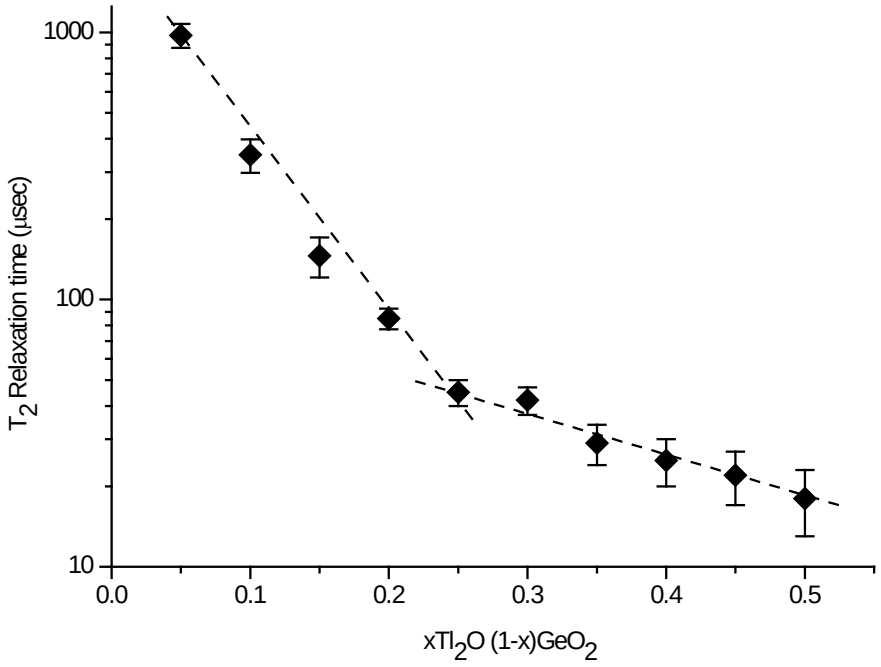

Figure 5.10 *Reduction of T_2 relaxation time of glasses as Tl_2O increases.*

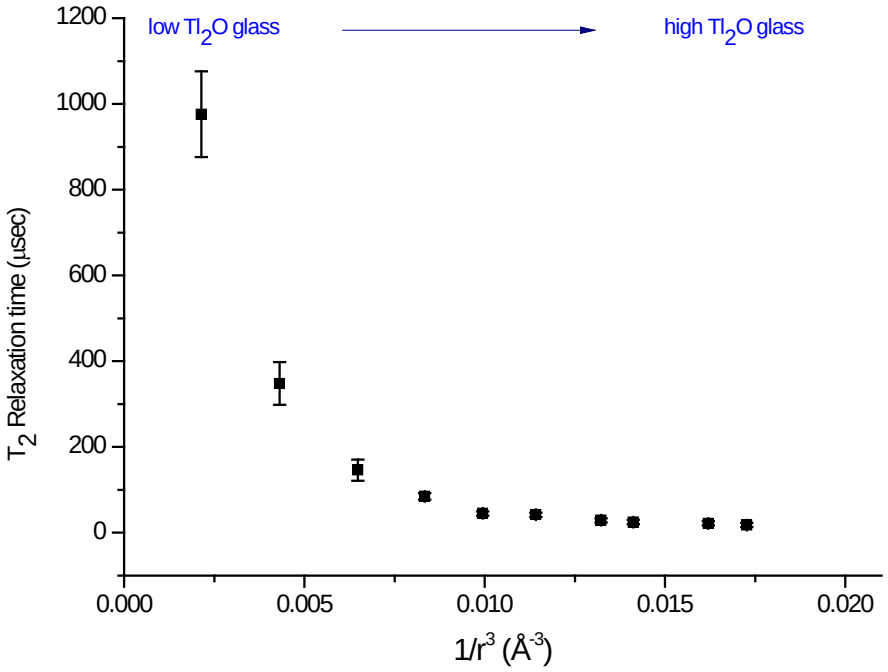

Figure 5.11 *Spin-spin relaxation time T_2 against $1/r^3$, where r is the Tl-Tl distance calculated assuming a homogeneous distribution of Tl in the glass.*

The spin-spin relaxation time is also inversely proportional to the square root of the second moment (M_2) (**Equation 3.9**), which is inversely proportional to the sixth power of internuclear distances (r_{ij}^6) (**Equation 3.8**). So that, where the nuclear magnetic interaction of thallium nuclei is dominated by dipole interaction and exchange interaction (**Equation 3.8**) between thallium nuclei, T_2 should be linearly relation to the Tl-Tl (r_{ij}) distance. In glasses with higher thallium oxide content, the thallium nuclei will be located closer together (shorter r_{ij}), the T_2 is then faster. In this study, Tl-Tl distances in the glasses have been calculated assuming a homogeneous distribution in the glass and using measured glass densities. The relationship between T_2 and $1/r^3$ is plotted in **Figure 5.10**. It is clear that there is no simple linear relation over the entire range. It seems likely that T_2 of high thallium content glasses ($0.25 \leq x \leq 0.50$) has a linear relationship $1/ (r_{ij})^3$, which agrees with the second moment equation given by Van Vleck [37] and Bloembergen and Rowland [38]. T_2, which is obtained from the method described in **Chapter 3** (**Figure 3.7**), is undoubtedly related to the broadening of Tl-NMR spectra. It could then be inferred that the line broadening mechanism in thallium germanate glass is dominated by other mechanisms i.e. chemical shift dispersion at low concentrations ($0.05 \leq x \leq 0.20$) and the dipolar or pseudodipolar or exchange interaction between Tl-Tl nuclei at high concentration. However, it is possible that the Tl-Tl distance does not correspond to homogeneous distribution, but there is clustering above $x \sim 0.2$.

5.3.5 Raman Spectroscopy

Raman spectra of thallium germanate glasses are shown in **Figure 5.12**. Peak positions are listed in **Table 5.2** with their assignments based on literature for alkali and lead germanate glasses [16, 19, 20, 39-41]; there is no information on the thallium germanate system. The low frequency region (100-250 cm^{-1}) is believed to be associated with the vibration of Tl-O units; similar peaks at low frequency in alkali [16] or lead germanate glass [41] have been assigned to the alkali-O or Pb-O stretching modes. There is an increase with x of the intensity of the region at ~150 cm^{-1}, which is partly obscured by the cut-off due to the notch filter. A peak emerges at ~250 cm^{-1} for high Tl_2O concentration ($x \geq 0.35$), possibly associated with the presence of Tl^{3+}.

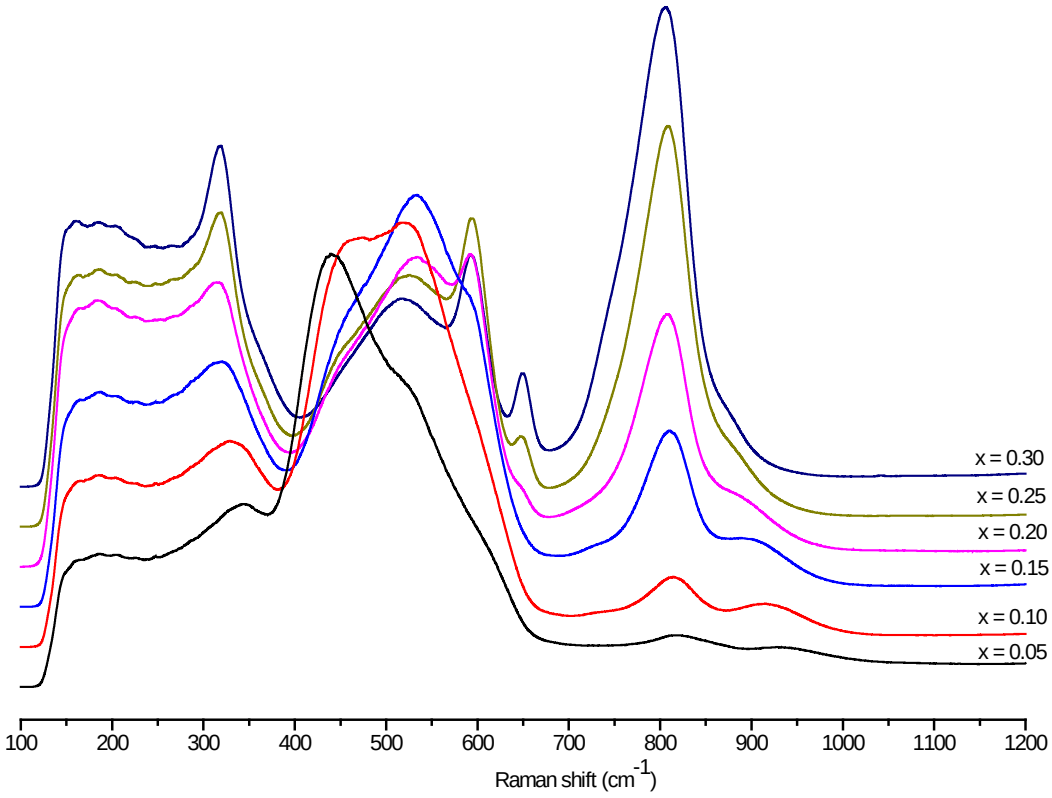

Figure 5.12a *Raman spectra of x = 0.05 – 0.30 thallium germanate glasses.*

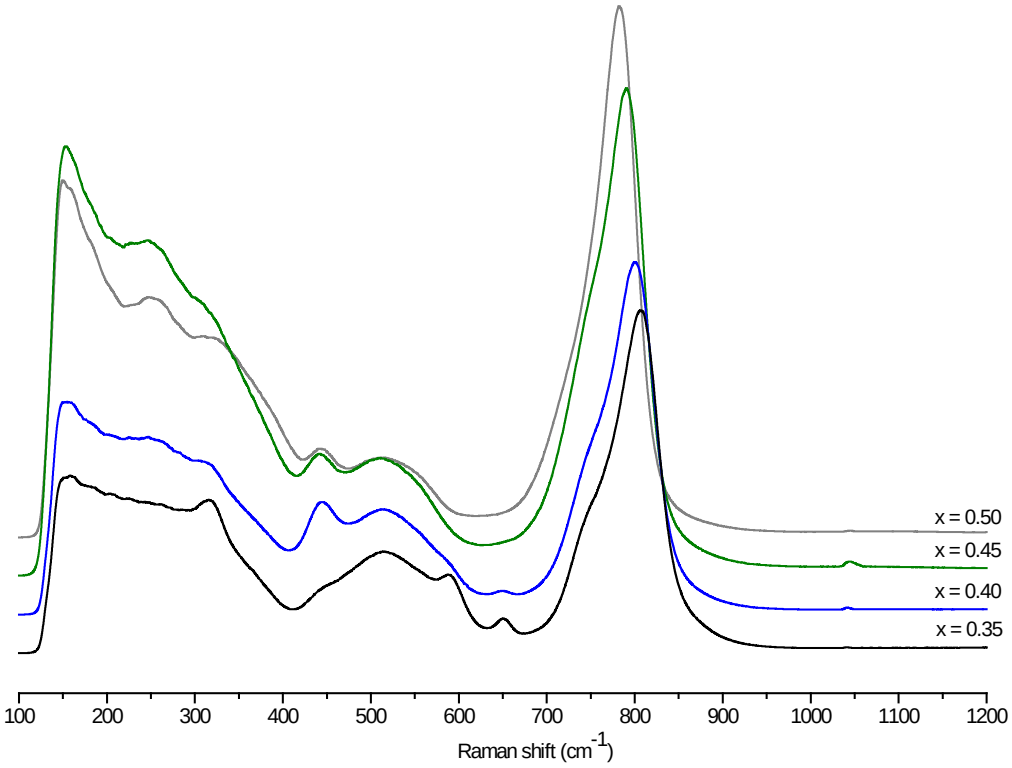

Figure 5.12b *Raman spectra of x = 0.35 – 0.50 thallium germanate glasses.*

Table 5.2 *Peaks list obtained from the Raman spectrum of thallium germanate glass with the assignments*

	Thallium content (x)										assignments
	0.05	**0.10**	**0.15**	**0.20**	**0.25**	**0.30**	**0.35**	**0.40**	**0.45**	**0.50**	
Raman Shift (cm^{-1})	148	149	160	180	171	160	150	155	153	154	Tl vibrational region
	-	-	-	-	-	-	250	250	250	250	
	344	330	320	315	320	319	321	320	320	320	Symmetrical [GeO_4] stretching
	440	460	450 (s)	452 (s)	450 (s)	450 (s)	445 (s)	443	441	443	
	529 (s)	520 (s)	539	534	525	515	515	515	510	510	
	-	-	600 (s)	596	596	595	592	595 (s)	560 (s)	560 (s)	High coordinated Ge; [$GeO_{5\ or\ 6}$]
	-	-	-	650 (s)	650	650	651	650	-	-	
	-	-	-	-	-	745 (s)	745 (s)	745 (s)	745 (s)	745 (s)	
	815	815	809	806	806	802	804	798	788	781	ν_{as}O-Ge-O, νGe-O^-
	928	915	912	900 (s)	880(s)	870(s)	-	-	-	-	

Error of the data is $\pm 5\ cm^{-1}$
(s) : shoulder feature

The region at ~300 to 1000 cm^{-1}, has previously been assigned to the Ge-O structure [16, 19, 20, 39, 41] with the peaks at 300 to 400 cm^{-1} and 400 to 500 cm^{-1} due to the bending and stretching vibrations of [GeO_4] respectively [41] and the peaks at 650 to 900 cm^{-1} associated with [GeO_6] units [19, 41] . Three peaks corresponding to [GeO_4] units are found at ~ 340, 440 and 529 cm^{-1}. The ones at 340 and 440 cm^{-1} are associated to the bending and stretching of [GeO_4], which is consistent with the lead germanate glasses [41].

With increasing x, the peak at ~340 cm^{-1} shifts to ~ 320 cm^{-1}, which may correlate with increased Ge-O bond length. The peak at about 529 cm^{-1} is believed to be due to the symmetric vibration of O-Ge-O and a deformation mode in GeO_2 and corresponds to a peak at 550 cm^{-1} in the alkali germanate study [16]. Vibrations at 600, 650 and 745 cm^{-1} are ascribed to [GeO_6] in thallium germanate glasses; their intensities increase with x, consistent with the neutron diffraction finding that the coordination number of Ge increases. The intensity of the peaks in the 800 to 930 cm^{-1} region, assigned to an asymmetric O-Ge-O vibration, could imply that higher symmetry Ge-O units exist in the glass.

It should be remembered that interpretation of Raman spectra in terms of the presence of Q-species, in which the number of bridging oxygen atoms around Ge atom changes as alkali increases, has been proposed [19, 20, 39] to describe the germanate anomaly, rather than the currently accepted changes in the coordination number of Ge.

5.3.6 Electrostatic bond strength calculation

Electrostatic bond strength (EBS) calculation [42] can be used to suggest a tentative glass structure in the thallium germanate system based on the experimental results above. **Figure 5.13** demonstrates the EBS of the oxygen atoms involving in the formation of the network structure and also non-bridging oxygens in thallium germanate glasses. The summation of the bond strengths connecting to the oxygen atoms should equal two (the valence of oxygen). The neutron diffraction study [26] revealed that Ge atoms change their coordination number from 4 to 5 or 6 as Tl_2O increases, up to about x = 0.30, then the coordination number decreases, which is believed to be due to the formation of non-bridging oxygens. The ^{205}Tl NMR and neutron diffraction studies show the presence of at least two different thallium environments. High coordinated thallium units, [TlO_6] (according to [26]), decrease in number as thallium content

increases and they convert to lower coordinated units, [TlO_3] (according to [26] and the $Tl_8Ge_5O_{14}$ crystal structure). In the case of low thallium content glasses ($0.05 \leq x \leq 0.15$), it is favourable for low and high coordinated germanium, i.e. [GeO_4] and [GeO_5] respectively according to the neutron diffraction study [26], to be bonded with the same oxygen atom, with high coordinated thallium providing the extra EBS contribution as shown in **Figure 5.13a**. The total bond strength is 1.966, which is very close to the ideal bond strength of 2. As x increases, there are more [GeO_5] units in the glass and the possibility of bridging between two high coordinated Ge. In this case, if the bridging oxygen is bonded to one high coordinated thallium, the EBS will be a lot less than 2 as shown in **Figure 5.13b**. Coordination to two high coordinated Tl atoms would bring the value closer to 2 but would be sterically hindered. In the case of alkali germanate glass, the more favourable solution is the formation of non-bridging oxygen. However, in thallium germanate, the change in thallium coordination number could stabilise the network link between [GeO_5] units. **Figure 5.13c** demonstrates this type of bond which provides an EBS of 1.933. As a result, high coordinated Ge continue to form until $x = 0.30$, although there is some evidence of non-bridging oxygens in the region, $0.15 \leq x \leq 0.30$. The favourable bond arrangement associated with the non-bridging oxygen is shown in **Figure 5.13d**. This also supports the evidence of Tl-O-Tl bonding, which gives the strong exchange interaction in the ^{205}Tl NMR study.

5.4 Conclusions

A germanate anomaly is present in thallium germanate glass with the minimum value of molar volume suggesting significant structural change due to the addition of thallium oxide modifier. Thallium oxide affects the glass structure in terms of both the germanate and thallium environments. Neutron diffraction and Raman spectroscopy confirm the change in the coordination number of germanium to oxygen atoms from [GeO_4] to [GeO_6] (or [GeO_5] from neutron diffraction). Tl solid-state NMR suggests that at least two thallium sites are present in the glass. A high coordinated thallium site with an inert lone pair of electrons is favourable in low thallium content glass. On the other hand, the amount of low coordinated thallium increases as Tl_2O increases. Tl-NMR spectra are broad and shifted mainly due to the chemical shift dispersion and chemical shift anisotropy interaction, respectively. T_2 measurement, which ignores the chemical shift mechanism, confirmed that dipole-dipole and pseudodipole or exchange

interactions are stronger in high thallium content glasses. ^{203}Tl enrichment shows ~ 10 kHz narrower spectra, which indicates that the broadening due to the exchange interaction is ~ 10 kHz. Raman spectroscopy also confirms the changes in Ge environment as Tl_2O increases, showing the presence of [GeO_4] and [GeO_6] in glasses. Electrostatic bond strength (EBS) calculation is used to suggest a tentative thallium germanate glass structure, where the change in thallium coordination number could stabilise high coordinated germanium, [$GeO_{5\ or\ 6}$]. Moreover, the Tl-O-Tl bond is explained using EBS calculation, supporting the presence of exchange interaction in the Tl NMR study of high thallium content glasses.

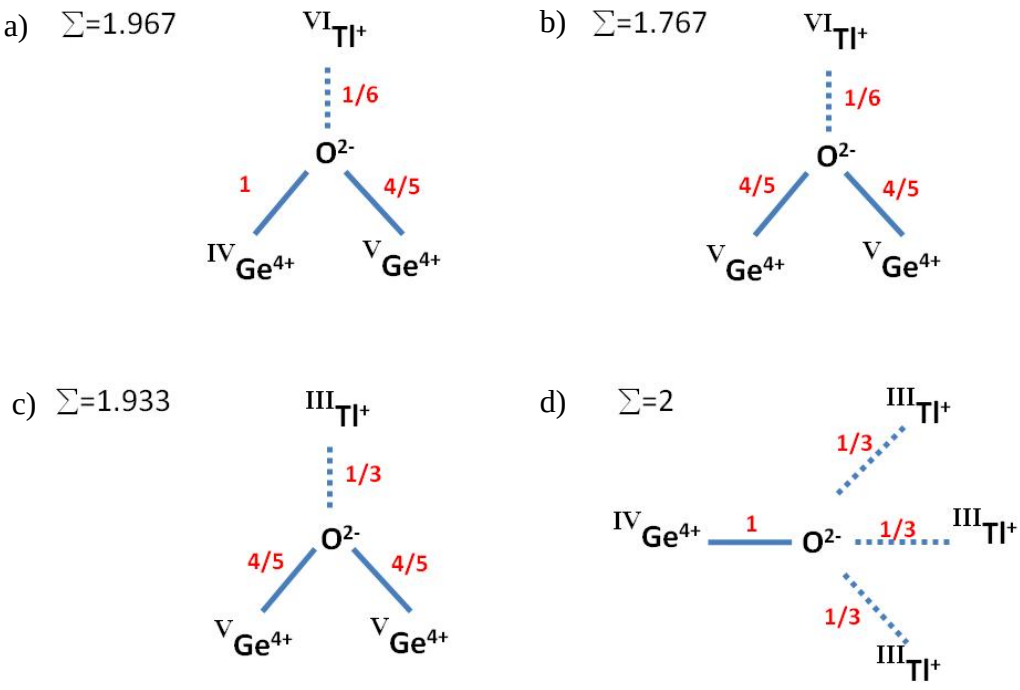

Figure 5.13 *Electrostatic bond strength (EBS) calculation describes the favoured glass structure in thallium germanate system.*

5.5 References

[1] D.W. Hall, M.A. Newhouse, N.F. Borrelli, W.H. Dumbaugh, D.L. Weidman, *Applied Physics Letters*, **54** (1989) 1293.

[2] J. Yumoto, S.G. Lee, B. Kippelen, N. Peyghambarian, B.G. Aitken, N.F. Borrelli, *Applied Physics Letters*, **63** (1993) 2630.

[3] E. Fargin, A. Berthereau, T. Cardinal, G. LeFlem, L. Ducasse, L. Canioni, P. Segonds, L. Sarger, A. Ducasse, J*ournal of Non-Crystalline Solids*, **203** (1996) 96.

[4] J.A.E. Desa, A.C. Wright, R.N. Sinclair, *Journal of Non-Crystalline Solids*, **99** (1988) 276.

5] E. Lorch, *Journal of Physics Part C Solid State Physics*, **2** (1969) 229.

[6] M. Micoulaut, L. Cormier, G.S. Henderson, *Journal of Physics-Condensed Matter*, **18** (2006) R753.

[7] A. Leadbetter, A. Wright, *Journal of Non-Crystalline Solids*, **7** (1972) 37.

[8] A. Hannon, D. Martino, L. Santos, R. Almeida, *The Journal of Physical Chemistry B*, **111** (2007) 3342.

[9] U. Hoppe, R. Kranold, H.J. Weber, A.C. Hannon, *Journal of Non-Crystalline Solids*, **248** (1999) 1.

[10] M. Ueno, M. Misawa, K. Suzuki, *Physica B*, **120** (1983) 347.

[11] O. Gedeon, M. Liska, J. Machacek, *Journal of Non-Crystalline Solids*, **354** (2008) 1133.

[12] B.G. Parkinson, D. Holland, M.E. Smith, C. Larson, J. Doerr, M. Affatigato, S.A. Feller, A.P. Howes, C.R. Scales, *Journal of Non-Crystalline Solids*, **354** (2008) 1936.

[13] S. Sakka, K. Kamiya, *Journal of Non-Crystalline Solids*, **49** (1982) 103.

[14] D.L. Price, A.J.G. Ellison, M.L. Saboungi, R.Z. Hu, T. Egami, W.S. Howells, *Physical Review B*, **55** (1997) 11249.

[15] H. Jain, E.I. Kamitsos, Y.D. Yiannopoulos, G.D. Chryssikos, W.C. Huang, R. Kuchler, O. Kanert, *Journal of Non-Crystalline Solids*, **203** (1996) 320.

[16] H. Verweij, J. Buster, *Journal of Non-Crystalline Solids*, **34** (1979) 81.

[17] E.I. Kamitsos, Y.D. Yiannopoulos, M.A. Karakassides, G.D. Chryssikos, H. Jain, *Journal of Physical Chemistry*, **100** (1996) 11755.

[18] T. Furukawa, W.B. White, *Journal of Materials Science*, **15** (1980) 1648.

[19] G.S. Henderson, M.E. Fleet, *Journal of Non-Crystalline Solids*, **134** (1991) 259.

[20] G.S. Henderson, *Journal of Non-Crystalline Solids*, **353** (2007) 1695.

[21] L.W. Panek, *Nuclear Magnetic Resonance Studies of Tl^{203}, Tl^{205}, and O^{17} in Oxide Glasses*, Ph.D. thesis, Brown University (1977).

[22] L.W. Panek, P.J. Bray, *Journal of Chemical Physics*, **66** (1977) 3822.

[23] F.F. Riebling, *Journal of Chemical Physics*, **55** (1971) 804.

[24] M. Touboul, Y. Feutelais, *Journal of Solid State Chemistry*, **32** (1980) 167.

[25] E.R. Barney, A.C. Hannon, N. Laorodphan, R. Dupree, D. Holland, *Journal of Non-Crystalline Solids*, **356** (2010) 2517.

[26] E.R. Barney, A.C. Hannon, N. Laorodphan, D. Holland, *Journal of Physical Chemistry C*, **115** (2011) 14997

[27] K. Nassau, D.L. Chadwick, *Materials Research Bulletin*, **17** (1982) 715.

[28] K. Nassau, D.L. Chadwick, *Journal of the American Ceramic Society*, **65** (1982) 197.

[29] M. Touboul, Y. Feutelais, *Acta Crystallographica Section B-Structural Science*, **35** (1979) 810.

[30] N. Penin, L. Seguin, B. Gerand, M. Touboul, G. Nowogrocki, *Journal of Solid State Chemistry*, **160** (2001) 139.

[31] M. Touboul, G. Nowogrocki, *Journal of Solid State Chemistry*, **136** (1998) 216.

[32] D. Massiot, F. Fayon, M. Capron, I. King, S. Le Calve, B. Alonso, J.O. Durand, B. Bujoli, Z.H. Gan, G. Hoatson, *Magnetic Resonance in Chemistry*, **40** (2002) 70.

[33] J.F. Hinton, *Bulletin of Magnetic Resonance*, **13** (1992) 90.

[34] J.J. Fitzgerald, S.M. DePaul, *Solid-State NMR Spectroscopy of Inorganic Materials*, American Chemical Society (1999).

[35] K.J.D. MacKenzie, M.E. Smith, *Multinuclear solid-state NMR of inorganic materials*, Pergamon (2002).

[36] J.F. Hinton, K.R. Metz, R.W. Briggs, *Progress in Nuclear Magnetic Resonance Spectroscopy*, **20** (1988) 423.

[37] J.H. Van Vleck, *Physical Review*, **74** (1948) 1168.

[38] N. Bloembergen, T.J. Rowland, *Physical Review*, **97** (1955) 1679.

[39] G.S. Henderson, L.G. Soltay, H.M. Wang, *Journal of Non-Crystalline Solids*, **356** (2010) 2480.

[40] K.E. Lipinskakalita, *Journal of Non-Crystalline Solids*, **119** (1990) 41.

[41] V.N. Sigaev, I. Gregora, P. Pernice, B. Champagnon, E.N. Smelyanskaya, A. Aronne, P.D. Sarkisov, *Journal of Non-Crystalline Solids*, **279** (2001) 136.
[42] L. Pauling, *Journal of the American Chemical Society*, **51** (1929) 1010.

Chapter 6

Thallium Borate Crystalline Phases

6.1 Introduction

Promising optical properties, such as non linear optical response [1], are found in several borate crystals; most of those studied being alkali and alkaline earth borates such as LiB_3O_5 [2], $Li_2B_4O_7$ [3], β-$Ba_3(B_3O_6)_2$ [1] and CsB_3O_5 [4]. Thallium borate crystals are expected to have similar properties and, as a result, several thallium borate crystals have been characterised and their crystal structures determined [5-10]. The phase diagram of the thallium borate system [5], shown in **Figure 6.1,** indicates that seven binary compounds can form. Crystal structures are known for Tl_3BO_3, $TlBO_2$, $Tl_2B_4O_7$, TlB_3O_5 and TlB_5O_8 [5, 7-11] and three of these are in the composition region of this study. The structures of TlB_9O_{14} and $Tl_2B_8O_{13}$ are not known. The similarity between the local environments in crystals and glasses means the NMR characteristics of the crystal phases are of interest in the study of thallium borate glasses.

Touboul and Nowogrocki [8] reported that the TlB_5O_8 crystal structure is very similar to that of β-potassium pentaborate (β-KB_5O_8), consisting of pentaborate units, $[B_5O_{10}]^-$ (**Figure 6.2a**), which contain four three-coordinated boron $[BO_3]$ units and one four-coordinated boron $[BO_4]^-$ unit (B2 in **Figure 6.2a**). Thallium ions coordinate to nine oxygen ions with the distances between Tl and O being 2.90 to 3.20 Å, slightly longer than the K-O bonds in β-KB_5O_8 crystal (longest distance 3.17 Å) [12]. B-O bond distances are almost identical to those in β-KB_5O_8 crystal.

The TlB_3O_5 crystal structure [7] contains $[B_3O_7]^-$ triborate rings (**Figure 6.2b**), which consist of two $[BO_3]$ units and one $[BO_4]^-$ unit (B3 in **Figure 6.2b**), with Tl^+ ions balancing the overall electronic charge of the molecule. Thallium is coordinated to four oxygen atoms with Tl-O distances between 2.662 and 2.895 Å. These oxygens lie to one side of the Tl^+ ion, opposite the lone pair. Another five oxygen atoms are found at distances between 3.195 and 3.484 Å though, since the nearest B is at 3.190Å, these can be disregarded as part of the coordination sphere. This crystal is analogous to the alkali triborate crystals, e.g. CsB_3O_5 (same space group $P2_12_12_1$) [13] and LiB_3O_5 (space

group $Pna2_1$) [14], although there is a difference in the oxygen coordination around the Cs ion, which has no lone-pair, with 7 atoms lying between 3.030 and 3.342 Å [13].

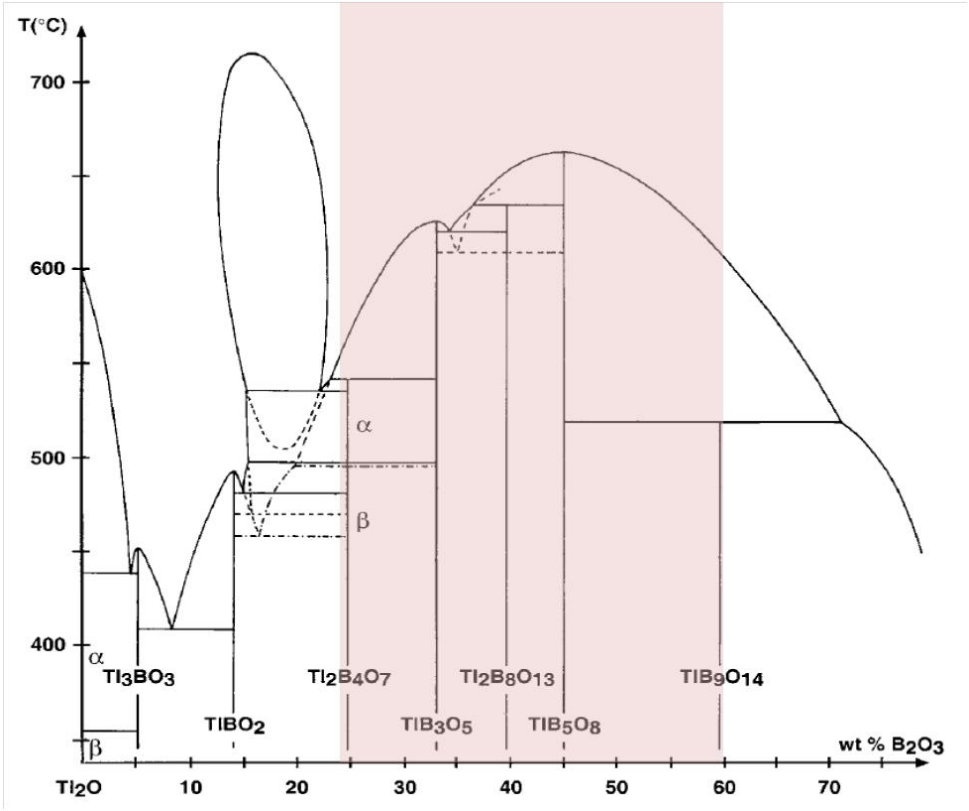

Figure 6.1 *Tl_2O-B_2O_3 phase diagram [5] (the crystalline phases of interest; TlB_9O_{14}, TlB_5O_8, $Tl_2B_8O_{13}$, TlB_3O_5 and $Tl_2B_4O_7$ are in the shaded region).*

The differences between thallium and alkali borate crystals are more significant for $Tl_2B_4O_7$, which has 3 formula units per unit cell ($Tl_6B_{12}O_{21}$) and 6 crystallographically non-equivalent Tl sites whilst the equivalent potassium or rubidium compounds have 2 formula units per unit cell (K or Rb)$_4B_8O_{14}$ [15, 16]. The two boron superstructural units in $Tl_2B_4O_7$ (**Figure 6.2c** and **d**) are $[B_5O_{12}]^{3-}$, consisting of two $[BO_3]$ units (B1 and B12 in **Figure 6.2c**) and three $[BO_4]^-$ units, and $[B_7O_{15}]^{3-}$, consisting of a group of four $[BO_3]$ units (B3, B5, B7 and B9 in **Figure 6.2d**) and three $[BO_4]^-$units. These superstructural units are unusual. The $[B_7O_{15}]^{3-}$ unit is found in only one other thallium borate crystal, hydrated $Tl_2B_4O_7$ ($Tl_2B_4O_7 \cdot H_2O$ or $Tl_4[B_8O_{12}(OH)_4] \cdot H_2O$), whose structure contains $[B_7O_{15}]^{3-}$ units plus one isolated $[BO_3]$ [17]. Thallium is coordinated to either 4 or 5 oxygen atoms in the six sites in

β-$Tl_2B_4O_7$, whilst K has 7 or 9 oxygen neighbours in α-$K_2B_4O_7$. As is the case for TlB_3O_5, the oxygen atoms lie on the same side of Tl^+, opposite to the stereochemically active lone pair of electrons. The shortest Tl-O bond is about 2.450 Å (the longest is about 3.036 Å) [5], which is not much different from $TlBO_2$ [6], $Tl_8Ge_5O_{14}$ [18] and Tl_3BO_3 [10] at 2.48, 2.46 and 2.45 Å, respectively. It was reported [5] that the glass former (B or Ge) to thallium ratio influences the activity of the lone pair of electrons which starts when this ratio is ≤ 3, i.e. TlB_3O_5 (3) [7], $Tl_2B_4O_7$ (2) [5], $TlBO_2$ (1) [6], $Tl_8Ge_5O_{14}$ (0.625) [18] and Tl_3BO_3 (0.33) [10]. Differences in crystal structure, compared with alkali borates, are also found for $TlBO_2$ [6] and Tl_3BO_3 [10] but these will not be discussed here.

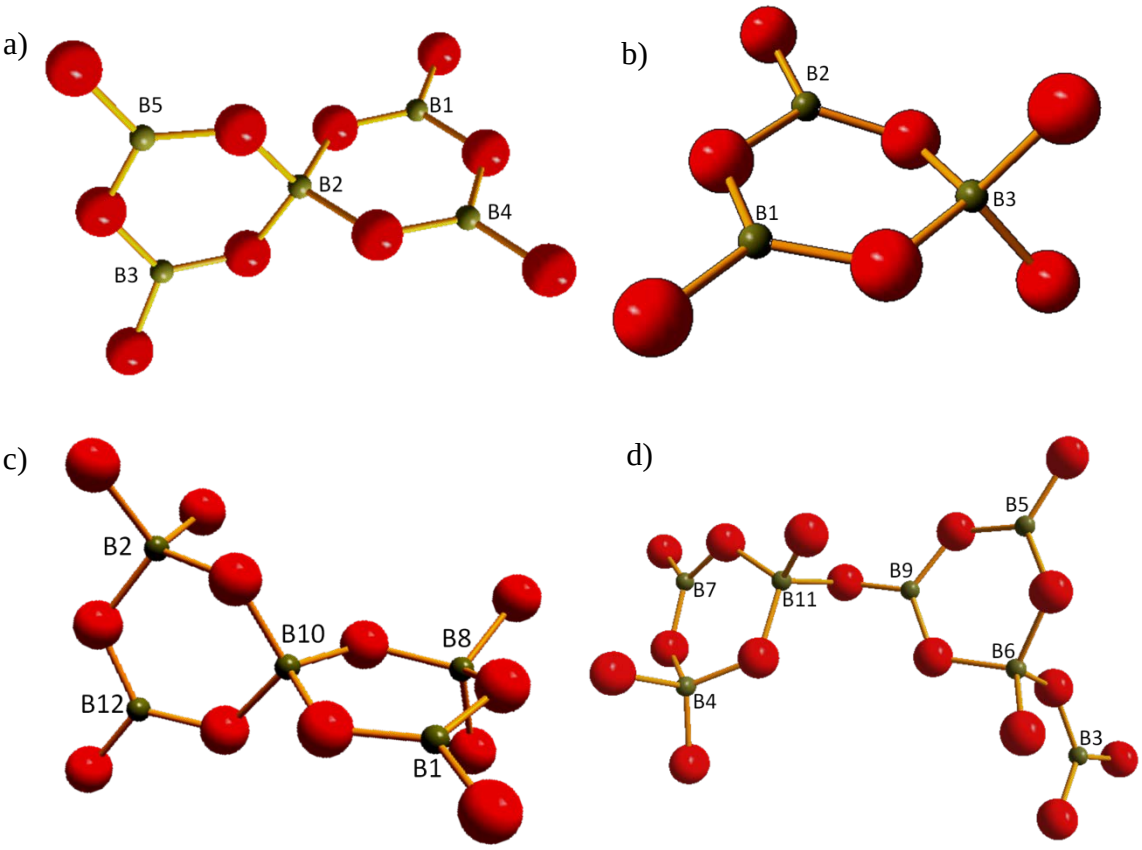

Figure 6.2 *Boron superstructural units in thallium borate compounds a)* $[B_5O_{10}]^-$*, b)* $[B_3O_7]^-$*, c)* $[B_5O_{12}]^{3-}$ *and d)* $[B_7O_{15}]^{3-}$.

The crystal structures of the other two thallium borate crystals (TlB_9O_{14} and $Tl_2B_8O_{13}$) which fall within the compositional range of this study have not yet been determined, which might relate to the difficulty in forming these crystal phases (see later).

X-ray diffraction, solid-state NMR, pycnometry and Raman spectroscopy were used to investigate the structure of these crystalline phases and their results are reported and discussed in this chapter.

6.2 Experimental details

6.2.1 Sample preparation

Crystal phases were obtained by controlled crystallisation of the parent glasses. Pre-melted boron oxide (B_2O_3) and Tl_2CO_3 were used as starting materials to make glasses of the same stoichiometry as the crystals, i.e. 10, 16.7, 20, 25, and 33.3 mol% Tl_2O glasses were made for TlB_9O_{14}, TlB_5O_8, $Tl_2B_8O_{13}$, TlB_3O_5 and $Tl_2B_4O_7$ crystalline phases, respectively. The melting and cooling processes were performed in the same manner as for thallium germanate glass [**Chapter 5**]. The glasses were then crystallised by heat treatment at the crystallisation temperature obtained from the DTA curves shown in **Figure 6.3**, i.e. 540, 525, 559, 496 and 435 °C for TlB_9O_{14}, TlB_5O_8, $Tl_2B_8O_{13}$, TlB_3O_5 and $Tl_2B_4O_7$ crystalline phases, respectively.

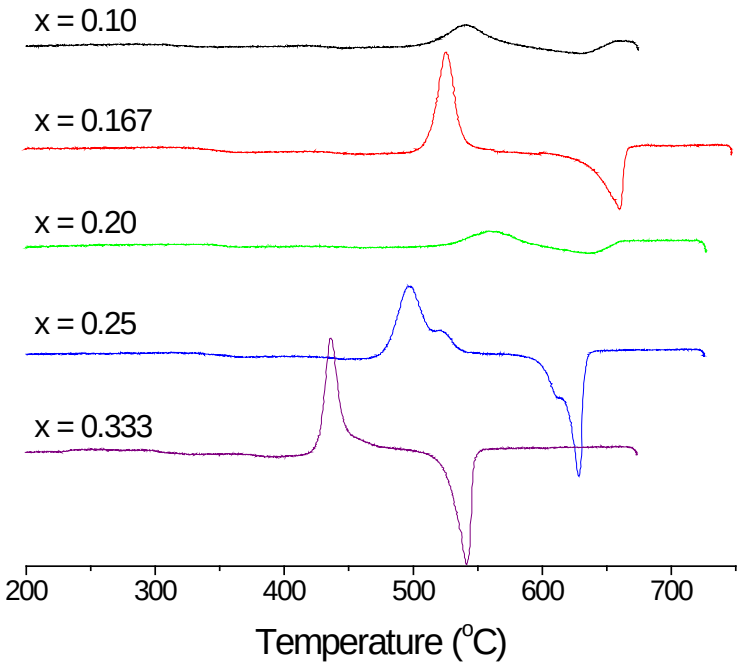

Figure 6.3 *DTA curves of glasses, showing the crystallisation events. Data were collected using a heating rate of 10 $^{o}C\ min^{-1}$.*

These temperatures were taken as the highest point of the exothermic crystallisation peak. Finely powdered glass was held at those temperatures for 15 hours then furnace cooled to room temperature and the samples were transferred to a desiccator. Weight loss during crystallisation was monitored.

6.2.2 Density measurement

The density of each sample was measured using a Micrometritics AccuPyc 1330 gas pycnometer using helium. The molar volume of the samples was then calculated using the nominal composition.

6.2.3 X-ray diffraction

A Bruker D5005 CuKα X-ray diffractometer was used to characterise all crystallised samples. The patterns were acquired over 10 hours from 2θ = 10 to 100 degrees with an increment of 0.05 degree per step.

6.2.4 Thallium solid-state nuclear magnetic resonance

^{205}Tl static NMR was performed on a 4.7 T Chemagnetics Infinity 200 MHz spectrometer using a 6mm Varian probe tuned to 115.7 MHz. A static echo pulse sequence was used with 1.5 μsec and 3 μsec pulse widths corresponding to 90° and 180° pulses, respectively with a pulse separation of 40 μsec, and 10 seconds pulse delay. Thallium nitrate ($TlNO_3$) solution was used as the reference. Data have been processed for only half of the echo of the FID for the reason described in **Chapter 3**.

The spin-spin relaxation times (T_2) of the samples containing pure crystalline phase were measured by monitoring the changes in the area of the spectrum as the echo time, tau, was increased as described in **Chapter 3**.

The TlB_5O_8 crystalline phase was also investigated using MAS NMR but was mixed with magnesium oxide (MgO) powder to reduce the mass inside the rotor, which could then be spun at 17.5 kHz during the spectrum acquisition. The experiment was performed on the same spectrometer as the static experiment but with a 2.5 mm Bruker probe. The same pulse echo sequence was applied except that the pulse separation was set at 57 μsec, so that it was synchronised with the rotation speed i.e. 1/17.5 kHz = 57 μsec.

6.2.5 Boron solid-state NMR

^{11}B NMR was performed on a 14.1T Bruker Avance II+ 600 MHz spectrometer using a 4mm Varian probe tuned to 192.5 MHz. The MAS frequency was 12.5 kHz and the samples were mixed with MgO powder to reduce the total mass of the packed rotor in order to safely achieve this spinning speed. A single pulse experiment was used with a 1.5 μsec pulse width and 8 seconds pulse delay. A very small r.f. tip angle of less than one-third of the solids 90° pulse length (determined using BPO_4) was selected, where the excitation of both $[BO_3]$ (large C_Q) and $[BO_4]^-$ (small C_Q) [19] are believed to be the same. BPO_4 was used as a secondary reference at -3.3 ppm with respect to the primary reference boron trifluoride ether ($BF_3{\cdot}Et_2O$).

The N_4 value, the fraction of boron present as $[BO_4]^-$ units, was obtained from the ^{11}B solid-state NMR spectrum. Topspin 2.1 software was used to integrate the areas of the $[BO_4]^-$ and $[BO_3]$ peaks [20-22]. **Figure 6.4** indicates how the areas are selected. The N_4 value was then calculated as $N_4 = \frac{area\ of\ [BO_4]^-}{area\ of\ [BO_3] + area\ of\ [BO_4]^-}$. The $[BO_3]$ area was first scaled by 1.04 in order to account for the area lost to the spinning sidebands.

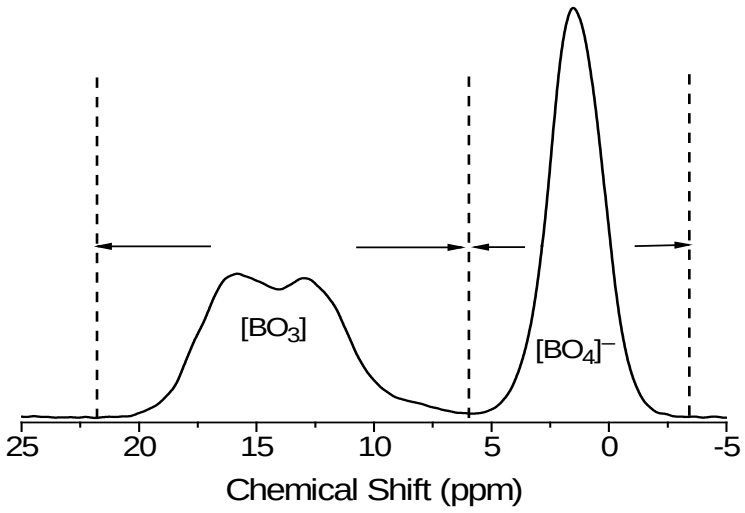

Figure 6.4 *An example ($Tl_2B_4O_7$) of the regions integrated to give the $[BO_3]$ and $[BO_4]^-$ areas used for N_4 calculation (after scaling $[BO_3]$ by 1.04).*

6.2.6 Raman spectroscopy

A Renishaw inVia Raman Microscope with a 514.5 nm Ar^+ laser was used to examine crystallised powder samples over the range 1800 cm^{-1} to 100 cm^{-1}. Several areas were examined in each case and various exposure times were used to ensure that the spectrum was reproducible.

6.3 Results and discussion

6.3.1 Sample weight loss

There is an expectation of some weight loss during the glass preparation process, although it is expected to be quite low as will be discuss in the following chapter on thallium borate glasses. However, weight loss during crystallisation was very low (< 0.5 wt%) as the temperature used for the devitrification of glass sample was not high (435 – 559 °C). The exception was the sample with x = 0.1 where the weight loss was about 2.5 wt%. This may be due to the removal of water which reacted with the glass powder prior to crystallisation, consistent with evidence of water contamination in low thallium content glasses, which will be discussed in **Chapter 7**. Thus, the concentrations of thallium and boron in the sample remain the same as in the precursor glass.

6.3.2 Density and molar volume

The measured densities and molar volumes of the crystallised samples are compared with the reported X-ray density values in **Figure 6.5**. Where single phase crystallised samples (x = 0.25 and 0.33) have been produced, their densities are in good agreement (and similarly for molar volumes calculated from density). Multiphase samples have densities which depend on the relative fractions of those phases. For example, the x = 0.1 sample should devitrify to give thallium enneaborate (TlB_9O_{14}) but in fact TlB_5O_8 is formed along with a residual glass phase which must be rich in B_2O_3 and this reduces the overall density of the sample to a value close to that expected for TlB_9O_{14}.

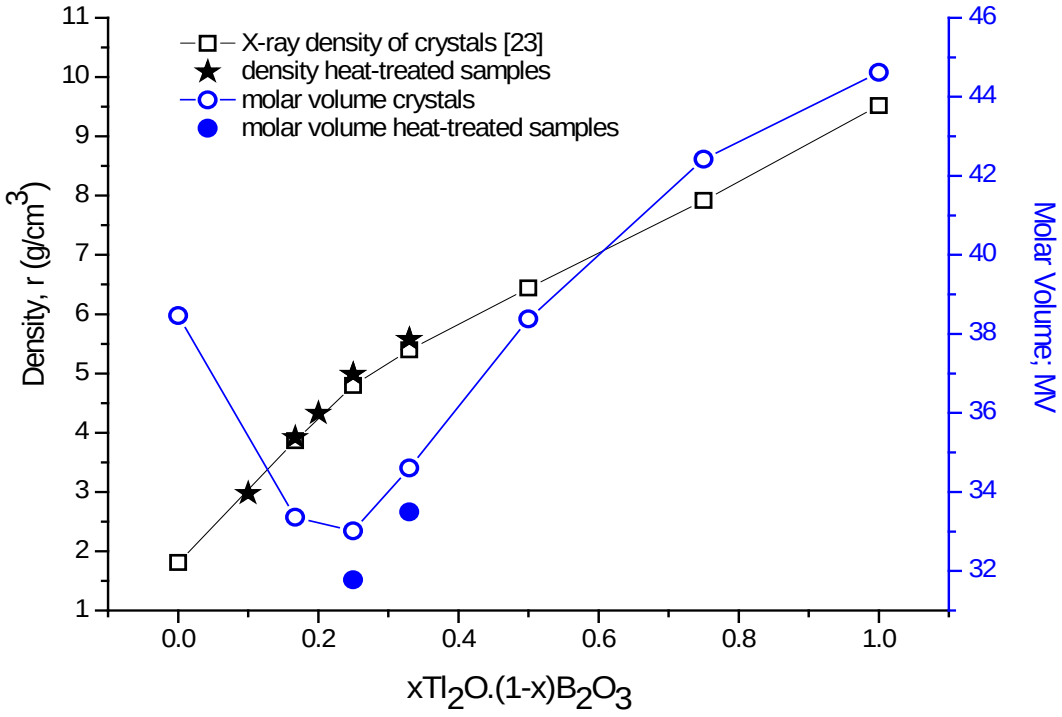

Figure 6.5 *Densities and molar volumes of the heat-treated samples (**closed symbols**) investigated in this study compared with values from the ICSD database[23] (**opened symbols**).*

6.3.3 Phase identification

The X-ray powder patterns of the crystallised samples are compared with the published diffraction patterns of the known crystals [23]. **Figure 6.6** reveals that only three samples have produced single crystalline phases, i.e. TlB_5O_8, TlB_3O_5 and $Tl_2B_4O_7$. Samples containing 0.17 and 0.20 fraction of Tl_2O contain at least two phases, TlB_5O_8 and TlB_3O_5, in different ratios as shown by the relative intensities of the characteristic peaks of those two crystals (square and asterisk in **Figure 6.6**, respectively).

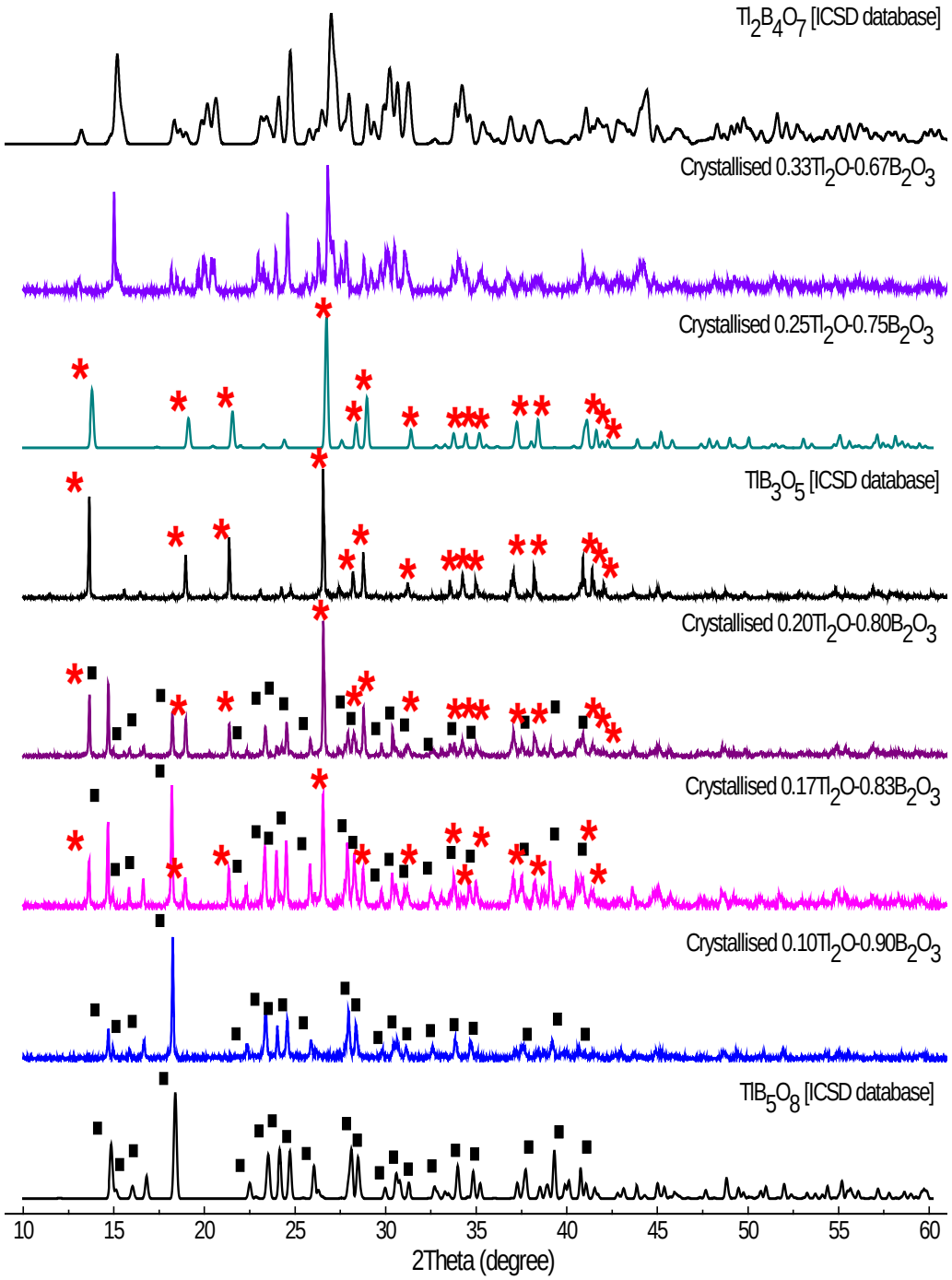

Figure 6.6 *Comparison of phases found in crystallised samples with the ICSD [23] database (characteristic X-ray peaks of :black square – TlB_5O_8; asterisk – TlB_3O_5 phase).*

Transformation of the glasses can be expressed by the equations:

1) $0.10Tl_2O{\cdot}0.90B_2O_3 \xrightarrow{540\ °C} xTlB_5O_8 + (0.1 - x/2)Tl_2O{\cdot}(0.9 - 5x/2)B_2O_3$

2) $0.17Tl_2O{\cdot}0.83B_2O_3 \xrightarrow{525\ °C} xTlB_5O_8 + yTlB_3O_5 + (0.17 - x/2 - y/2)Tl_2O{\cdot}(0.83 - 5x/2 - 3y/2)B_2O_3$

3) $0.20Tl_2O{\cdot}0.80B_2O_3 \xrightarrow{559\ °C} xTlB_5O_8 + yTlB_3O_5 + (0.20 - x/2 - y/2)Tl_2O{\cdot}(0.80 - 5x/2 - 3y/2)B_2O_3$

4) $0.25Tl_2O{\cdot}0.75B_2O_3 \xrightarrow{496\ °C} TlB_3O_5$

5) $0.33Tl_2O{\cdot}0.67B_2O_3 \xrightarrow{435\ °C} \beta\text{-}Tl_2B_4O_7$

Because the crystallised phases obtained from the samples containing 0.10, 0.17 and 0.20 mole fraction of Tl_2O do not correspond to the glass stoichiometry (e.g. TlB_5O_8 forms instead of TlB_9O_{14} from $0.10Tl_2O{\cdot}0.90B_2O_3$ glass) residual phase must also be present to balance the stoichiometry of the elements in these three samples. The residual phase in the sample must be vitreous as there are no extra Bragg peaks present in the XRD patterns. This assumption will be taken into account when calculating the amount of each phase in these samples **(Tables 6.1 and 6.2**):. The calculation will also use the density data and ^{205}Tl solid-state NMR data. Thus, expressions above contain terms to represent the presence of glass residue in the samples.

Table 6.1 *Relative molar fractions of crystal phases from NMR; Prediction of the composition of the residual phase in the crystallised samples.*

	x Mole fraction Tl_2O	molar ratio TlB_5O_8: TlB_3O_5	Oxide mole fractions in crystal phases				Residual		glass composition
			TlB_5O_8 (0.17 Tl_2O·0.83B_2O_3)		TlB_3O_5 (0.25 Tl_2O·0.75B_2O_3)		Tl_2O	B_2O_3	
			Tl_2O	B_2O_3	Tl_2O	B_2O_3			
case I	0.10	1	0.10	0.49	n/a	n/a	0.00	0.41	v-B2O3(41wt% in sample)
case II	0.10	1	0.09	0.44	n/a	n/a	0.01	0.46	$0.02Tl_2O·0.98B_2O_3$
case I	0.17	0.50:0.50	0.07	0.34	0.10	0.30	0.00	0.19	v-B2O3 (19wt% in sample)
case II	0.17	0.50:0.50	0.065	0.317	0.095	0.285	0.01	0.228	$0.04Tl_2O·0.96B_2O_3$
case I	0.20	0.26:0.74	0.04	0.195	0.16	0.48	0.00	0.125	v-B2O3 (12.5wt% in sample)
case II	0.20	0.26:0.74	0.036	0.175	0.154	0.46	0.01	0.165	$0.06Tl_2O·0.94B_2O_3$

* ratio of the area of the peaks from ^{205}Tl NMR study

Table 6.2 *Fraction of each phase in the sample calculated based on the density and ^{205}NMR data.*

	Mole fraction in glass		weight fraction of phases			Total density (g/cm^3)		
	Tl_2O	B_2O_3	TlB_5O_8[A]	TlB_3O_5[A]	glass	calculated[B]	experiment	Difference from calculation
case I	0.10	0.90	0.59	0	0.41	3.02	2.979 ± 0.002	-0.04
case II	0.10	0.90	0.53	0	0.47	2.99	2.979 ± 0.002	-0.01
case I	0.17	0.83	0.41	0.40	0.19	3.74	3.922 ± 0.002	+0.18
case II	0.17	0.83	0.382	0.38	0.238	3.82	3.922 ± 0.002	+0.10
case I	0.20	0.80	0.235	0.64	0.125	4.20	4.330 ± 0.001	+0.13
case II	0.20	0.80	0.211	0.614	0.175	4.19	4.330 ± 0.001	+0.14

[A] Calculated from the ratio of each crystalline phase present obtained from NMR data, i.e. fraction of TlB_5O_8 = fraction of total crystalline phase in the sample × fraction of TlB_5O_8 phase from ^{205}Tl NMR study.

[B] Density of B_2O_3 glass, $0.02Tl_2O.0.98B_2O_3$ glass, $0.04Tl_2O.0.96B_2O_3$ glass and $0.06Tl_2O.0.94B_2O_3$ glass are 1.81, 2.00, 2.22 and 2.42 g/cm^3, respectively (from density of glasses in **Chapter 7**).

6.3.4 ^{205}Tl solid-state NMR

^{205}Tl static NMR spectra of the crystallised samples are shown in **Figure 6.7**. The NMR results are consistent with the X-ray diffraction patterns and the peaks from each phase are sufficiently well resolved that their relative amounts can be measured (**Figure 6.8**) and these are presented in **Table 6.1**. The ^{205}Tl NMR spectra from samples where only a single crystal phase is present have been fitted using DM2010 [24] and Origin [25] (**Figure 6.9**) in order to obtain structural information on the thallium environment in TlB_5O_8, TlB_3O_5 and $Tl_2B_4O_7$. It was found that symmetrical chemical shift anisotropy (CSA) ($\kappa = 0$) controls the line shape from TlB_5O_8. This suggests that the chemical environment surrounding thallium is symmetric and the lone pair of electrons is sterically inert, $6s^2$ reflecting the [TlO_9] environment reported [8]. A small Gaussian line was also included to achieve a better fit, which could indicate that there is some thallium in the borate glass residue in this sample. In TlB_3O_5, an axially symmetric CSA ($\kappa = -1$) line shape was used with about 30 kHz broadening. The axial symmetry reflects the asymmetric thallium environment of [TlO_4], where all four oxygen atoms are located at the same side of thallium opposite the lone pair of electrons, which is sterically active, sp^3d [7]. The very broad spectrum of $Tl_2B_4O_7$ could be fitted using five Gaussian contributions in ratio 1:1:2:1:1 representing the six thallium sites in the crystal [5] and implying that two of them have very similar magnetic environments. The fit was constrained to give the expected intensity ratios. The quality of the fit obtained using Gaussian lineshapes in this ratio suggests that CSA parameters are not significant here compared with the broadening.

There is certainly insufficient information in the spectrum to attempt to fit CSA. The CSA and Gaussian parameters used in the fits described above are listed in **Table 6.3**. The peak position shifts to more paramagnetic shielding as Tl_2O content increases, which could also mean that the Tl-O bonding in the samples becomes more covalent [26, 27].

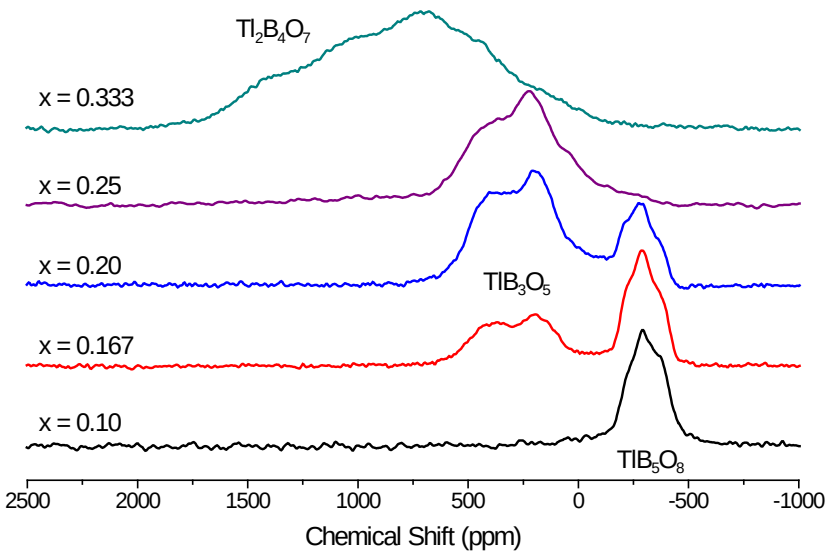

Figure 6.7 *^{205}Tl solid-state NMR spectra of crystallised samples*

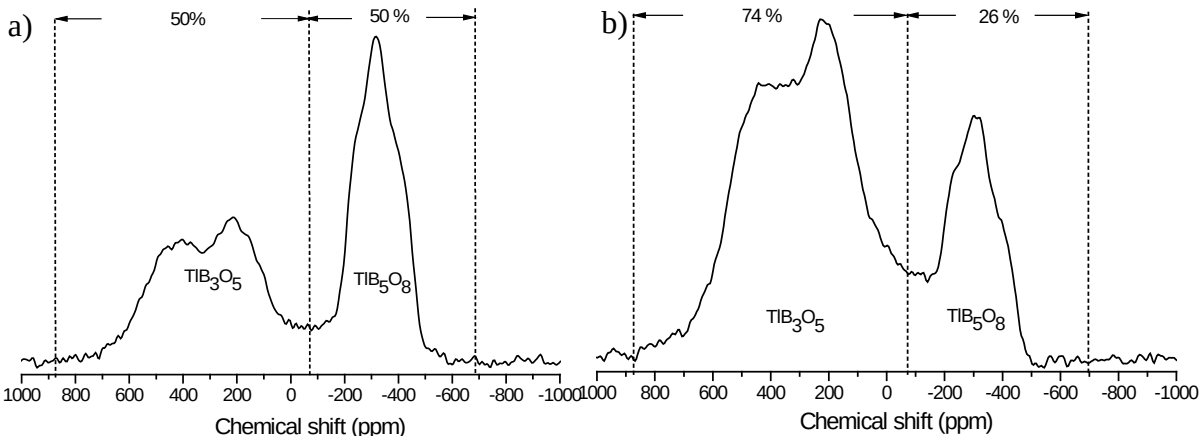

Figure 6.8 *Integration limit used and relative fractions of each phase in the heat-treated samples* ***a)*** *$0.17Tl_2O{\cdot}0.83B_2O_3$ and* ***b)*** *$0.20Tl_2O{\cdot}0.80B_2O_3$.*

The spectra become broader as Tl_2O content increases. The factors which determine the peak width, as described in **Chapter 3**, are: the CSA (related to site symmetry); the dipolar interaction, $\langle D_{ij} \rangle$, which is significant for both isotopes of Tl [26]; and the Tl...Tl exchange interaction [28]. Both of the latter depend on the separation of the thallium nuclei. The contribution from the dipolar interaction ($\langle D_{ij} \rangle$) to the NMR line width depends on $\frac{1}{r_{ij}^3}$, where r_{ij} is the separation of the two nuclei, and thus it increases with Tl_2O content and decreasing Tl…Tl separation [29]. The same is true for the Tl…Tl exchange interaction.

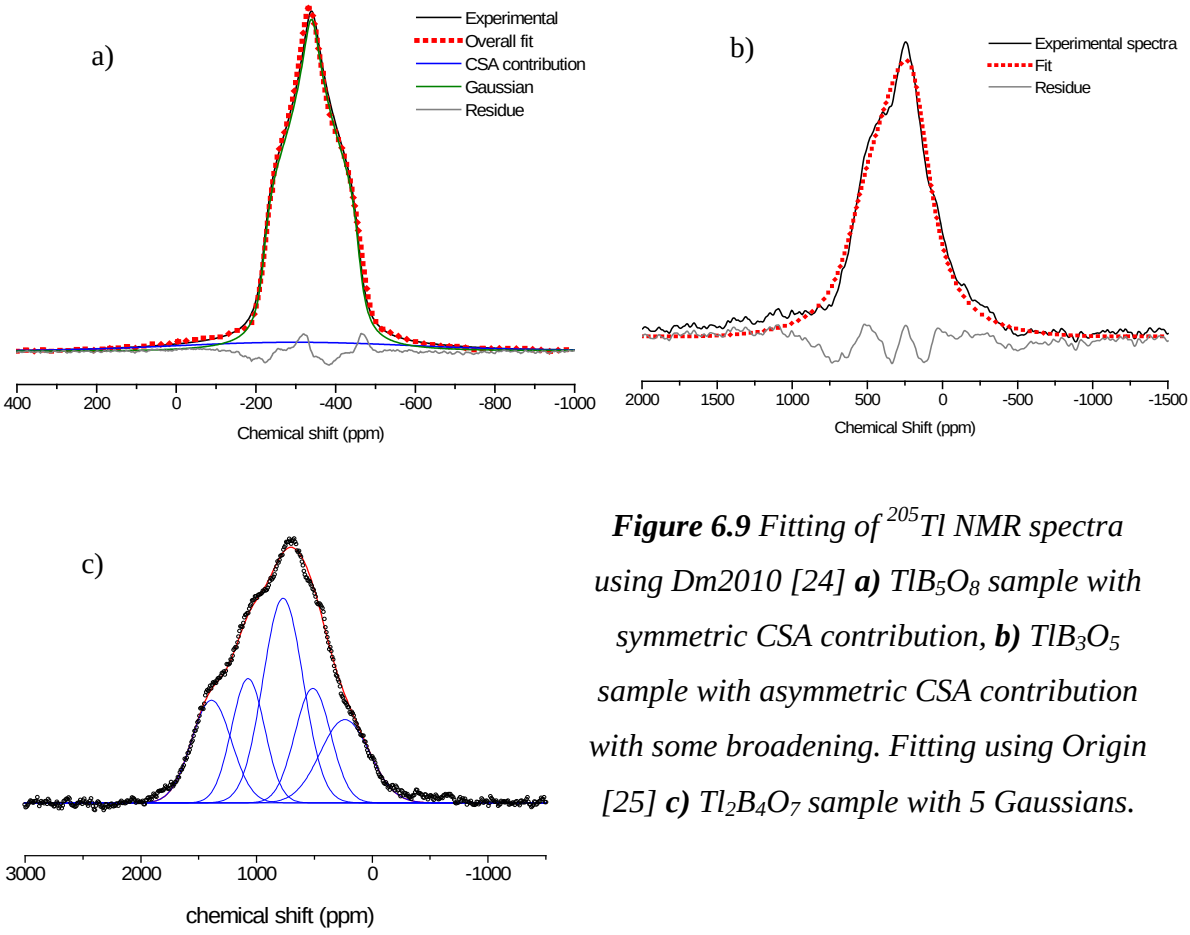

Figure 6.9 *Fitting of* ^{205}*Tl NMR spectra using Dm2010 [24]* ***a)*** *TlB_5O_8 sample with symmetric CSA contribution,* ***b)*** *TlB_3O_5 sample with asymmetric CSA contribution with some broadening. Fitting using Origin [25]* ***c)*** *$Tl_2B_4O_7$ sample with 5 Gaussians.*

The spin-spin relaxation time (T_2), the time taken for dephasing of the magnetisation, is controlled by nuclear magnetic interactions such as the dipolar and exchange interactions. The measured T_2 values shown in **Table 6.4** for the three crystal phases are not consistent with the calculated dipole interaction, since a longer T_2 was measured in TlB_3O_5, than in TlB_5O_8 which has the lower dipole interaction. However, the environments of thallium in TlB_5O_8 and TlB_3O_5 are very different, both in terms of coordination number, the activity of the lone pair of electrons as mentioned in **section 6.1** and Tl…Tl separation which will determine the extent of the exchange interaction broadening. The spectrum of $Tl_2B_4O_7$ is very broad (about twice the width of the TlB_3O_5 spectrum) due to the greater number of thallium sites (6 sites [5] compared to 1 [7, 8]). The dipole contribution in **Table 6.4** is averaged from the calculated dipole contribution $<D_{ij}>$ of an individual value obtained from each thallium sites (Tl1 to Tl6), reported in the database [23]. The individual dipole contributions of each thallium sites are 8016 Hz, 5806 Hz, 6129 Hz, 7043 Hz, 5823 Hz and 8513 Hz for Tl1 to Tl6 respectively.

For the samples containing a mixture of TlB_5O_8 and TlB_3O_5, the integrated areas of the peak from each phase (**Figure 6.8**), were measured and the percentage of each phase calculated (**Table 6.1)**.

From composition and ^{205}Tl NMR results, the fractions and compositions of residual glass in the samples with x=0.10, 0.17 and 0.20 have been calculated (**Table 6.1 and 6.2)**. Case I assumes that all Tl_2O is involved only in the crystalline phase(s). On the other hand in case II, 0.01 fraction of Tl_2O is assumed to be involved in the residual glass. Using the X-ray densities of TlB_5O_8 (3.865 g/cm^3[8]) TlB_3O_5 (4.798 g/cm^3[7]), and the measured densities of thallium borate glasses from **Chapter 7**, the densities of the heat-treated samples (x=0.10, 0.17 and 0.20) were calculated and compared to the experimental data in **Table 6.2**. The x = 0.25 and 0.33 samples were assumed to be single phase TlB_3O_5 and $Tl_2B_4O_7$ respectively, as supported by their measured densities.

CSA, dipolar and exchange interactions could be averaged by magic angle spinning (MAS) [26], thus an experiment was performed on the TlB_5O_8 sample to test this. Since the magnitude of the scalar coupling (J coupling) is very small in solids (whereas it is quite important in solution-state NMR), it is not considered in this study [30]. The static and MAS spectra are compared in **Figure 6.10** which shows a factor of 12 narrowing to give a single line ~ 15 ppm wide (with the centre of the peak at ~ -306 ppm). This confirms the presence of only one thallium site in the sample.

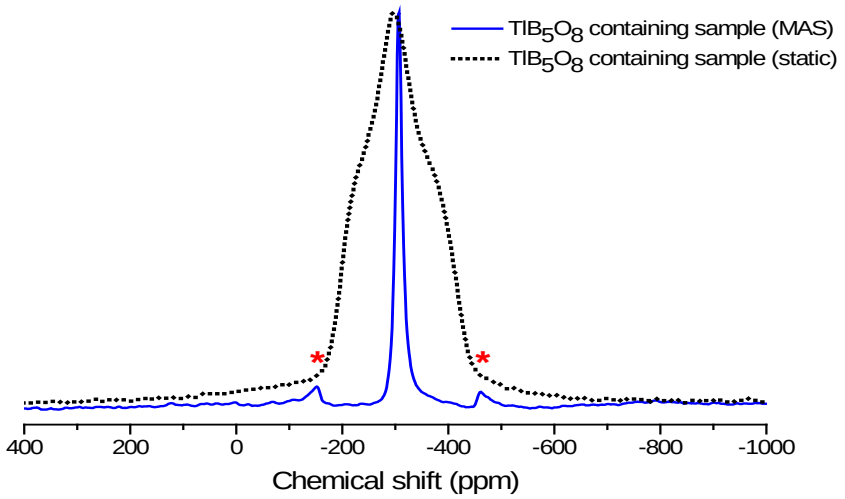

Figure 6.10 *Comparison of ^{205}Tl NMR spectra of TlB_5O_8 sample obtained by static experiment (dot line) and MAS experiment (solid line).*

6.3.5 ^{11}B solid-state NMR

^{11}B NMR spectra of samples containing only one crystalline phase (+ possible residual glass) are compared in **Figure 6.11**. The spectra have been normalised by the area of the [BO_3] peak. The intensity of the [BO_4]$^-$ peak, located around 2 ppm increases (TlB_5O_8 < TlB_3O_5 < $Tl_2B_4O_7$), as expected and the calculated N_4 values are shown in **Figure 6.12**. N_4 values of the TlB_3O_5 and $Tl_2B_4O_7$ containing samples were slightly above the expected value for the crystal structures and also the theoretical x/(1-x) line. The significance of this is discussed in the following chapter.

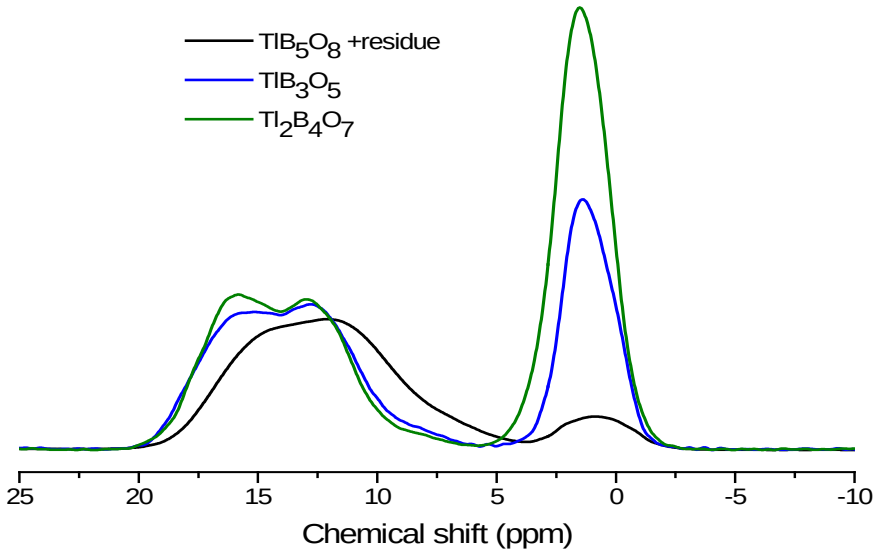

Figure 6.11 *^{11}B solid-state NMR spectra of crystallised samples (normalised to the area of the [BO_3] peak).*

Table 6.3 *Chemical Shift Anisotropy (CSA) parameters and Gaussian parameters from fitting of peaks due to TlB_5O_9, TlB_3O_5 and $Tl_2B_4O_7$. The relative proportions of the peaks for $Tl_2B_4O_7$ were fixed during fitting.*

Phase		%	CSA (static line shape)						Gaussian		
			δ_{11} (ppm)	δ_{22} (ppm)	δ_{33} (ppm)	δ_{iso} (ppm)	Span; Ω (ppm)	Skew; κ	position (ppm)	width (ppm)	Tl-Tl Min (Å)
TlB_5O_9	CSA	89	-220±10	-350±10	-470±10	-350±10	250±10	0			5.3161
	Gaussian	11.							-320±10	830±10	
TlB_3O_5	CSA	100	170±10	170±10	630±10	330±10	450±10	-1			3.7242
$Tl_2B_4O_7$	Gaussian	16.67							240±10	500±10	3.8315*
	Gaussian	16.67							510±10	360±10	3.5455*
	Gaussian	33.32							770±10	410±10	2 x 3.5544*
	Gaussian	16.67							1070±10	340±10	3.5422*
	Gaussian	16.67							1390±10	410±10	3.4642*

* the shortest Tl-Tl distances from each thallium site to its next nearest neighbour site obtained from ICSD [23] database

Table 6.4 *FWHM, peak position, dipolar contribution (<D_{ij}>) and relaxation time (T_2) of individual crystal phases*

Crystal phase	Tl-O coordination number (to 3.19 Å)	FWHM (ppm)	Position (ppm)	Shortest Tl-Tl distance (Å)	Dipolar contribution <D_{ij}> (Hz)	T_2 (μsec)
TlB_5O_8	9	230±10	-340±10	5.3200	3428	195
TlB_3O_5	4	500±10	310±10	3.7242	7804	298
$Tl_2B_4O_7$	4,5	av 400*	870±10	3.5544	av 6888**	67

* av = an average value from the line width of the Gaussian peaks of $Tl_2B_4O_7$ sample (listed in **Table 6.3**)

**av = an average value of <D_{ij}>, calculated from the individual thallium sites of Tl in the crystal structure parameter given in ICSD [23] database (see text)

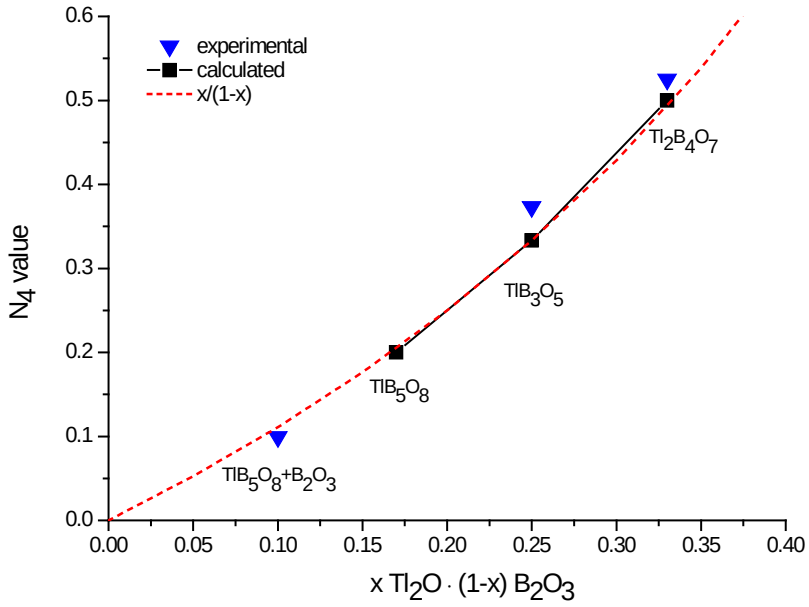

Figure 6.12 *N_4 values of crystallised samples obtained from ^{11}B NMR study compared to the calculated values from their crystal structure.*

6.3.6 Raman spectroscopy

Raman spectra of heat-treated thallium borate samples are compared with three related polycrystalline caesium borates [31] in **Figure 6.13**. Caesium and thallium spectra show some near identical peaks due to the presence of the same boron superstructural units, although the peaks observed in TlB_5O_8 and TlB_3O_5 are sharper and shifted to larger wavenumbers than for the corresponding caesium compounds. Pentaborate units produce characteristic peaks at 456, 769 and 881cm^{-1} (pentagons in **Figure 6.15**) and triborate units produce peaks at around 653, 753, 950 and 1340 cm^{-1} (triangles in **Figure 6.15**). The peak at 807 cm^{-1}, which is produced by the boroxol ring [32], is visible in the x = 0.1 spectrum, proving that there is residual B_2O_3 (or very low Tl_2O containing) glass in this sample. The feature observed at about 1520 cm^{-1} in TlB_5O_8 but 1480 cm^{-1} in CsB_5O_8. (marked as NBO? in **Figure 6.15**) has been ascribed to (B-O$^-$) bond stretching vibrations – i.e. (non-bridging oxygen (NBO) [33]. However, this argument should produce NBO-Tl vibrations at *lower* energies than NBO-Cs vibrations. This argument ignores the effects due to coordination number and bonding type. Peaks below 300 cm^{-1} are common in all thallium borate samples, due to the vibrations of the thallium oxide structure. The spectrum from $Tl_2B_4O_7$ has many overlapping peaks in this region because of the complexity of the medium range structure i.e. $(B_5O_{12})^{3-}$, $(B_7O_{15})^{3-}$ and also the presence of six Tl sites.

6.4 Conclusions

The structures of five thallium borate heat-treated samples were investigated using solid-state NMR (^{205}Tl and ^{11}B), Raman spectroscopy and X-ray diffraction. Only three crystalline phases were obtained, either singly or in combination with each other and/or residual glass where the stoichiometries of the crystal differed from the parent glass. The failure to produce $Tl_2B_8O_{13}$ and TlB_9O_{14} from their stoichiometric glasses may reflect problems with nucleation of these phases. A more extensive study of the compositions may be able to identify the correct sample state (bulk/powder) and nucleation/crystallisation sequence to produce these crystals. Density data, X-ray diffraction patterns and solid-state NMR results of the three phases formed support what structural information exists in the literature. As x increases, the lines are broadened not only by CSA and dipolar interactions but also by the Tl…Tl exchange interaction. The chemical shift anisotropy parameters of TlB_5O_8 and TlB_3O_5 are presented.

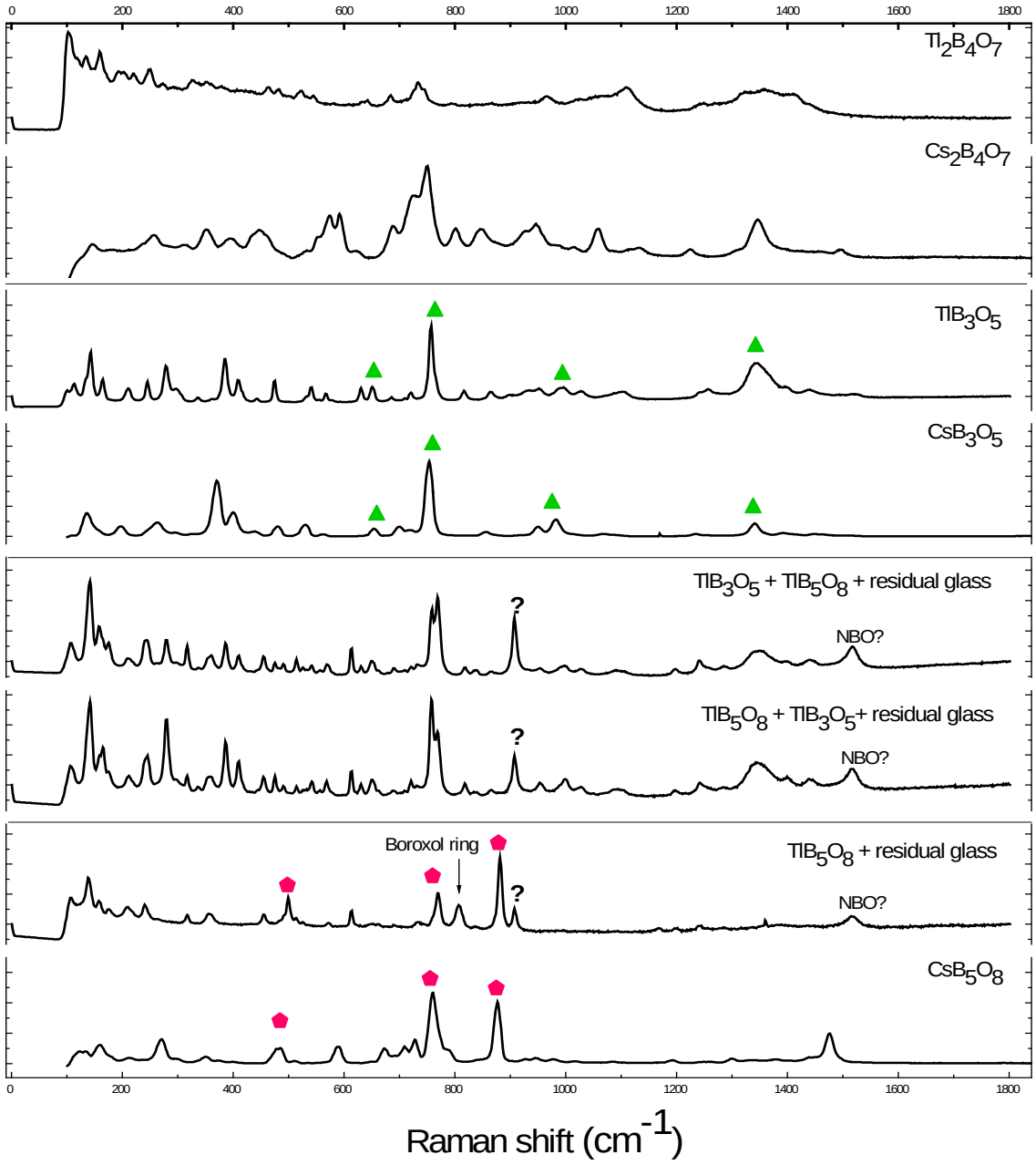

Figure 6.13 *Raman spectra of thallium borate crystalline phases compared with crystalline caesium borates from [31].*

6.5 References

[1] Y.N. Xia, C.T. Chen, D.Y. Tang, B.C. Wu, *Advanced Materials*, **7** (1995) 79.

[2] C.T. Chen, Y.C. Wu, A.D. Jiang, B.C. Wu, G.M. You, R.K. Li, S.J. Lin, *Journal of the Optical Society of America B-Optical Physics*, **6** (1989) 616.

[3] K. Byrappa, V. Rajeev, V.J. Hanumesh, A.R. Kulkarni, A.B. Kulkarni, *Journal of Materials Research*, **11** (1996) 2616.

[4] Y.C. Wu, T. Sasaki, S. Nakai, A. Yokotani, H.G. Tang, C.T. Chen, *Applied Physics Letters*, **62** (1993) 2614.

[5] N. Penin, L. Seguin, B. Gerand, M. Touboul, G. Nowogrocki, *Journal of Solid State Chemistry*, **160** (2001) 139.

[6] M. Touboul, D. Amoussou, *Revue De Chimie Minerale*, **15** (1978) 223.

[7] M. Touboul, E. Betourne, G. Nowogrocki, *Journal of Solid State Chemistry*, **131** (1997) 370.

[8] M. Touboul, G. Nowogrocki, *Journal of Solid State Chemistry*, **136** (1998) 216.

[9] R. Marchand, Y. Piffard, M. Tournoux, *Comptes Rendus Hebdomadaires Des Seances De L Academie Des Sciences Serie C*, **276** (1973) 177.

[10] Y. Piffard, R. Marchand, M. Tournoux, *Revue De Chimie Minerale*, **12** (1975) 210.

[11] A. Verbaere, R. Marchand, M. Tournoux, *Journal of Solid State Chemistry*, **23** (1978) 383.

[12] J. Krogh-Moe, *Acta Crystallographica*, **18** (1965) 1088.

[13] J. Krogh-Moe, *Acta Crystallographica Section B-Structural Science*, **30** (1974) 1178.

[14] S.F. Radaev, B.A. Maximov, V.I. Simonov, B.V. Andreev, V.A. Dyakov, *Acta Crystallographica Section B-Structural Science*, **48** (1992) 154.

[15] M.G. Krzhizhanovskaya, R.S. Bubnova, Bannova, II, S.K. Filatov, *Crystallography Reports*, **42** (1997) 226.

[16] J. Krogh-Moe, *Acta Crystallographica Section B-Structural Crystallography and Crystal Chemistry*, **28** (1972) 3089.

[17] M. Touboul, C. Bois, D. Amoussou, *Journal of Solid State Chemistry*, **48** (1983) 412.

[18] M. Touboul, Y. Feutelais, *Journal of Solid State Chemistry*, **32** (1980) 167.

[19] S. Kroeker, J.F. Stebbins, *Inorganic Chemistry*, **40** (2001) 6239.

[20] L. Vanwullen, W. Mullerwarmuth, *Solid State Nuclear Magnetic Resonance*, **2** (1993) 279.

[21] S. Sen, Z. Xu, J.F. Stebbins, *Journal of Non-Crystalline Solids*, **226** (1998) 29.

[22] C. Jager, K. Herzog, B. Thomas, M. Feike, G. Kunathfandrei, *Solid State Nuclear Magnetic Resonance*, **5** (1995) 51.

[23] D.A. Fletcher, R.F. McMeeking, D. Parkin, *Journal of Chemical Information and Computer Sciences*, **36** (1996) 746.

[24] D. Massiot, F. Fayon, M. Capron, I. King, S. Le Calve, B. Alonso, J.O. Durand, B. Bujoli, Z.H. Gan, G. Hoatson, *Magnetic Resonance in Chemistry*, **40** (2002) 70.

[25] OriginLab Corporation, *Computer program: OriginPro 8.5* (1991).

[26] J.F. Hinton, Bulletin of Magnetic Resonance, **13** (1992) 90.

[27] J.F. Hinton, K.R. Metz, R.W. Briggs, *Progress in Nuclear Magnetic Resonance Spectroscopy*, **20** (1988) 423.

[28] N. Bloembergen, T.J. Rowland, *Physical Review*, **97** (1955) 1679.

[29] A. Wong, A.P. Howes, J.R. Yates, A. Watts, T. Anupold, J. Past, A. Samoson, R. Dupree, M.E. Smith, *Physical Chemistry Chemical Physics*, **13** (2011) 12213.

[30] D.C. Apperley, R.K. Harris, P. Hodgkinson, *Solid State NMR: Basic Principles & Practice*, Momentum Press (2012).

[31] R.N. Sinclair, R. Haworth, A.C. Wright, B.G. Parkinson, D. Holland, J.W. Taylor, N.M. Vedishcheva, I.G. Polyakova, B.A. Shakhmatkin, S.A. Feller, B. Rijal, T. Edwards, *Physics and Chemistry of Glasses-European Journal of Glass Science and Technology Part B*, **47** (2006) 405.

[32] E.I. Kamitsos, M.A. Karakassides, *Physics and Chemistry of Glasses*, **30** (1989) 19.

[33] G.D. Chryssikos, J.A. Kapoutsis, A.P. Patsis, E.I. Kamitsos, *Spectrochimica Acta Part A: Molecular Spectroscopy*, **47** (1991) 1117.

Chapter 7

Thallium Borate Glasses

7.1 Introduction

As previously mentioned in **Chapter 5**, thallium germanate glass is of interest due to its distinct optical nonlinearity properties. Thallium and silver borate glasses may also possess interesting optical nonlinearity [1]. Extensive studies of the structure of alkali borate glasses have been published. Thallium borate glass on the other hand has not much been investigated. Thus, in terms of the structure of glass, it is a very interesting system to investigate, not only because of its optical properties but also the effect of the lone-pair electrons of Tl^{+}, which make the structure somehow different from alkali borate systems. The lone pair of electrons could potentially be sterically active or inert depending on the environment surrounding thallium. In **Chapter 5**, the lone pair of electrons was found to be sterically active on thallium in low coordination to oxygens [TlO_3], which is more favoured in high thallium content glass. On the other hand, the [TlO_7] unit, in which the lone pair of electrons is sterically inert, is more favoured in low thallium content glass [2, 3]. This phenomenon could also be present in the thallium borate system. The change in boron structure from 3- to 4-coordinated in the presence of a lone-pair cation could be also interesting.

Raman spectroscopy [4-6], infrared spectroscopy [7] and solid-state nuclear magnetic resonance (NMR) [8] have been used to study the change in boron environment and the change in boron-oxygen superstructural units in alkali borate glasses. Alkali oxide (R_2O) has been introduced into B_2O_3, providing glass of composition $xR_2O{\cdot}(1\text{-}x)B_2O_3$. A change occurs in the boron-oxygen medium range environment from the boroxol ring, which consists of only trigonal [BO_3] units, to more complex superstructural units, where tetrahedral $[BO_4]^{-}$ units are also present [9]. All boron-oxygen superstructural units, for example tetraborate, pentaborate and diborate, were depicted in **Chapter 2**. The structure of borate glasses and their relation to crystals of the same stoichiometry are reviewed by Wright [10]. Various models, which could explain the changes in short and medium-range structural units as x changes, have also been proposed [10]. In alkali borate glasses, two [BO_3] units are converted to two

$[BO_4]^-$ units when each unit of alkali oxide (R_2O) is introduced into the glass, as a result, the N_4 value, which represents the proportion of $[BO_4]^-$, increases as R_2O content increases.

N_4 values of glass could be predicted using the model proposed by Krogh-Moe [11] as $N_4 = x/(1-x)$. The N_4 values of alkali borates [12-14] follow this relationship closely until $x = 0.30$, where N_4 deviates from the model as high energy configurations involving adjacent $[BO_4]^-$ would be required [10]. Then $[BO_3]$ units with one non-bridging oxygen atom (NBO) are formed instead of $[BO_4]^-$ units in order to reduce the energy in the system, and the N_4 values start to decrease.

Unusual N_4 values of thallium borate glasses have been reported by Baugher and Bray [15] using wide-line, continuous-wave, solid-state ^{11}B NMR. In contrast to alkali borate or silver borate glasses [12-14, 16], N_4 values are well above the x/(1-x) model until $x > 0.4$. The rate of conversion of $[BO_4]^-$ from $[BO_3]$ was higher than two in $x < 0.20$ thallium borate glass. The reason proposed to explain this behaviour is the formation of 3-coordinated oxygen atoms, which are very unusual in alkali borate or other borate glasses.

X-ray diffraction studies have shown $Tl^+ \ldots Tl^+$ pairing in both borate [17] and silicate [18-20] glasses, with their separation being ~3.9 Å for samples of composition 16.1, 22.75 and 34.5 mol% Tl_2O [20]. Panek [18] suggested that Tl-O-Tl bonding or Tl…Tl pairing in thallium silicate glass was evidenced by the large exchange interaction broadening observed in ^{205}Tl NMR spectra.

As mentioned above, it is interesting to investigate the change of boron-oxygen environment as thallium content in glass increases in order to understand the effect of the lone pair of electrons of Tl^+. The interplay between Tl polyhedra and the coordination number of boron is also of interest. The results from various techniques, i.e. Raman spectroscopy, neutron diffraction and solid-state NMR spectroscopy, are discussed. Moreover, densities and molar volumes of glass are also presented.

7.2 Experimental details

7.2.1 Sample preparation

Thallium borate glasses were prepared by traditional melting and quenching from a mixture of thallium carbonate (Tl_2CO_3) and boron oxide glass (v-B_2O_3). Boron oxide powder was premelted to form a glass before mixing with Tl_2CO_3 in order to

reduce the moisture content in the B_2O_3. The batches, containing 5 to 50 mol% of thallium oxide (Tl_2O), were mixed and melted for 15 minutes in a Pt/Rh crucible at 100 °C above the liquidus obtained from the Tl_2O-B_2O_3 phase diagram [21] shown in **Chapter 6**. The melts were then cooled by splat-quenching between two cast iron plates, which is necessary to prevent the partial crystallisation of the samples, especially in high thallium content glasses. The splat-quenching is also used in order to control the cooling rate to be very close to that used in the thallium germanate glasses preparation. Weight change during the melting process was monitored to measure possible volatilisation of thallium oxides. Due to the slightly hygroscopic nature of the samples, they were then kept in desiccators until required for measurements.

99.62 % ^{11}B enriched B_2O_3 was used as a replacement for natural abundance B_2O_3 for neutron diffraction experiments in order to reduce the neutron absorption by the ^{10}B isotope. Samples of composition x = 0.05 – 0.40 were made for neutron diffraction experiments. The x = 0.45 and 0.50 samples were not used due to possible contamination of the samples, which may contain some crystalline phase or Tl^{3+} and Tl metal from the disproportionation reaction.

7.2.2 Density and molar volume

The density of each sample was measured using a Micrometritics AccuPyc 1330 gas pycnometer using helium. The molar volumes of the samples were then calculated using the nominal compositions.

7.2.3 Thallium solid-state nuclear magnetic resonance

^{205}Tl static NMR was performed on a 4.7 T Chemagnetics Infinity 200 MHz spectrometer using a 6mm Varian probe tuned to 115.7 MHz. A static echo pulse sequence was used with 1.5 μsec and 3 μsec pulse widths corresponding to 90° and 180° pulses, respectively with a pulse separation of 40 μsec, and 10 seconds pulse delay. Thallium nitrate ($TlNO_3$) solution was used as the reference. The whole echo FID obtained from the glass samples was Fourier transformed to get the NMR spectrum.

The spin-spin relaxation times (T_2) of the samples containing pure crystalline phase were measured by monitoring the changes in the area of the spectrum as the echo time, tau, was increased as described in **Chapter 3**.

7.2.4 Boron solid-state NMR

^{11}B NMR was performed on a 14.1T Bruker Avance II+ 600 MHz spectrometer using a 4mm Varian probe tuned to 192.5 MHz. The MAS frequency was 12.5 kHz and the samples were mixed with MgO powder to reduce the total mass of the packed rotor in order to safely achieve this spinning speed. A single pulse experiment was used with a 1.5 μsec pulse width, corresponding to one-third of the solid 90° pulse length measured using BPO_4 standard compound, and 8 seconds pulse delay. BPO_4 was used as a secondary reference at -3.3 ppm with respect to the primary reference boron trifluoride ether ($BF_3 \cdot Et_2O$). The N_4 values of the glass samples have been calculated using the method described in **Chapter 6**.

7.2.5 Raman spectroscopy

A Jasco NRS-3100 laser Raman Microscope (Coe College, Iowa, USA) with a 785 nm laser was used to examine powder samples of thallium germanate glasses over the range 1800 cm^{-1} to 100 cm^{-1}. Several areas were examined in each case and various exposure times were used to ensure that the spectra were reproducible.

7.2.6 Neutron diffraction

Neutron diffraction data from samples with composition x = 0.05 to 0.40 were obtained using the GEM diffractometer at the ISIS pulsed neutron source, Rutherford Appleton Laboratory, UK. Glass fragments were held in 8.3 mm diameter cylindrical cans made of 25 μm vanadium foil to minimise corrections due to the container. The differential cross-section $\frac{d\sigma}{d\Omega} = I(Q) = I^s(Q) + i(Q)$ was measured in order to obtain the distinct scattering $i(Q)$, where Q is the magnitude of the scattering vector.

7.3 Results and discussion

7.3.1 Glass composition and glass formation

The weight losses of the samples were largely as expected from the decomposition of Tl_2CO_3. However, some excess weight loss due to the evaporation of Tl_2O ($\lesssim$ 1 mole % was observed in $0.05 \leq x \leq 0.40$ glasses). The thallium loss in the higher thallium content glasses was higher and reached $\lesssim$ 5 mole % in x = 0.50 glass. There was no thallium metal inclusion and the Tl NMR spectra showed no Tl^{3+}

contribution, so that disproportionation or oxidation did not occur in thallium borate glass at the studied compositions, whereas it is present in thallium germanate glass (**Chapter 5**).

7.3.2 Density and molar volume

Glass densities are compared with the values given in the literature reported in the Sciglass database [22] in **Figure 7.1a** showing that the values are consistent with the literature. It was found that densities of glasses are largely dominated by the density of Tl_2O (~9.5 g/cm^3), which is about 4.5 times denser than B_2O_3 glass (~1.83 g/cm^3 [23]). and molar volumes, which were calculated using nominal compositions, are plotted in **Figure 7.1a**.

The borate anomaly was barely observable from the densities of the glasses, although the plot of molar volumes (**Figure 7.1b**), which was calculated from the densities of the glass, shows the minimum of the molar volumes at x ~ 0.28. This is in good agreement with the composition in the alkali borate glasses where N_4 values deviate from x=1/(1-x). However, the molar volumes of thallium borate glasses behave differently from alkali borate glasses, e.g. lithium borate glass [24] as shown in **Figure 7.2**, where there is no minimum.

7.3.3 Raman spectroscopy

Raman spectra of thallium borate glasses, presented in **Figure 7.3**, show the changes in borate superstructural units as Tl_2O increases. It is believed that the peaks appearing at low wave-numbers correspond to the vibrations of the thallium environment, and the intensity of these peaks increases as Tl_2O increases, although the interpretation of the Tl environment from Raman spectroscopy is not possible, due to the limitation of the spectrometer cut-off. **Table 7.1** summarises the observed peaks corresponding to the borate superstructural units from Raman spectroscopy study of alkali borate glasses [5]. These reported peaks are used as the reference to indentify the borate superstructural units present in thallium borate glasses, which are also listed in **Table 7.1**.

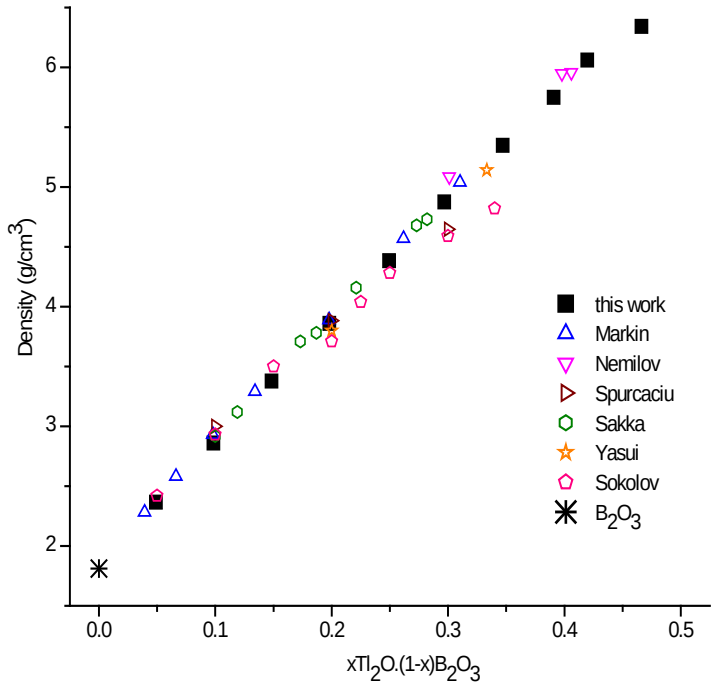

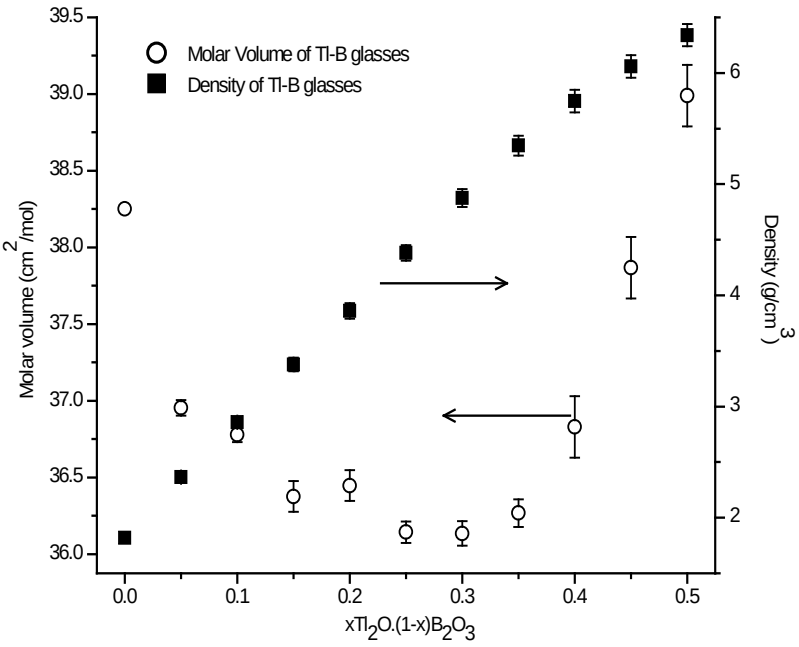

Figure7.1 (a) *Change in glass density with composition from the current study compared with literature values [22]* ***(b)****Molar volume calculated from measured density and nominal compositions.*

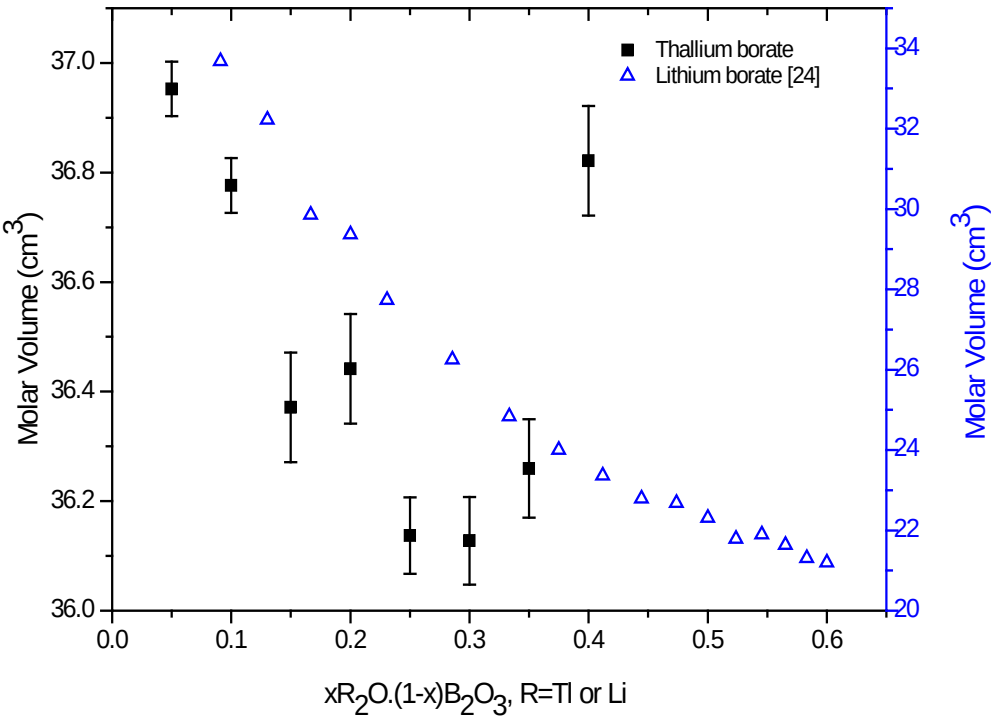

Figure 7.2 *Comparison of molar volumes changes against mole fraction (x) of Tl_2O and Li_2O in borate glasses [24].*

Table 7.1 *Borate superstructural units present in $xTl_2O{\cdot}(1\text{-}x)B_2O_3$ glasses.*

Peak (in Figure 7.3)	**Structural units**	**Frequency range (cm^{-1})**	**Thallium content where observed**
1	Boroxol ring	806 sharp	$0 \leq x \leq 0.20$
2	Triborate	450 broad and 770 sharp	$0 < x \leq 0.35$
3	Pentaborate	450 broad and 770 sharp	$0 < x \leq 0.35$
4	Metaborate (chain-type)	720	$0.25 \leq x \leq 0.50$
5	Metaborate (ring-type)	630	$0.30 \leq x \leq 0.50$
6	Diborate	1100 broad	$0.25 \leq x \leq 0.50$
7	Non-bridging oxygen (NBO)	1400 broad	$0.05 \leq x \leq 0.50$

The characteristic sharp peak at ~ 806 cm^{-1} representing the boroxol ring is replaced by the triborate and pentaborate peaks and eventually by ring and chain metaborate units at the composition x ~ 0.25. The boron-NBO vibration is also observed in the

glasses. The changes in borate superstructural units as Tl_2O increases are very similar to those observed in alkali borate glasses, indicating that Tl^+ has little effect on the change of borate superstructural units. It should be noted that the B-OH vibration at ~ 884 cm^{-1} [25, 26] is observed in the x = 0.05 sample. This is due to moisture contamination of the glass during the measurement. The effect of moisture contamination could be more harmful in solid-state NMR measurement as the samples have been ground to a fine powder to enable rotor stability and to increase the packing density and signal to noise ratio.

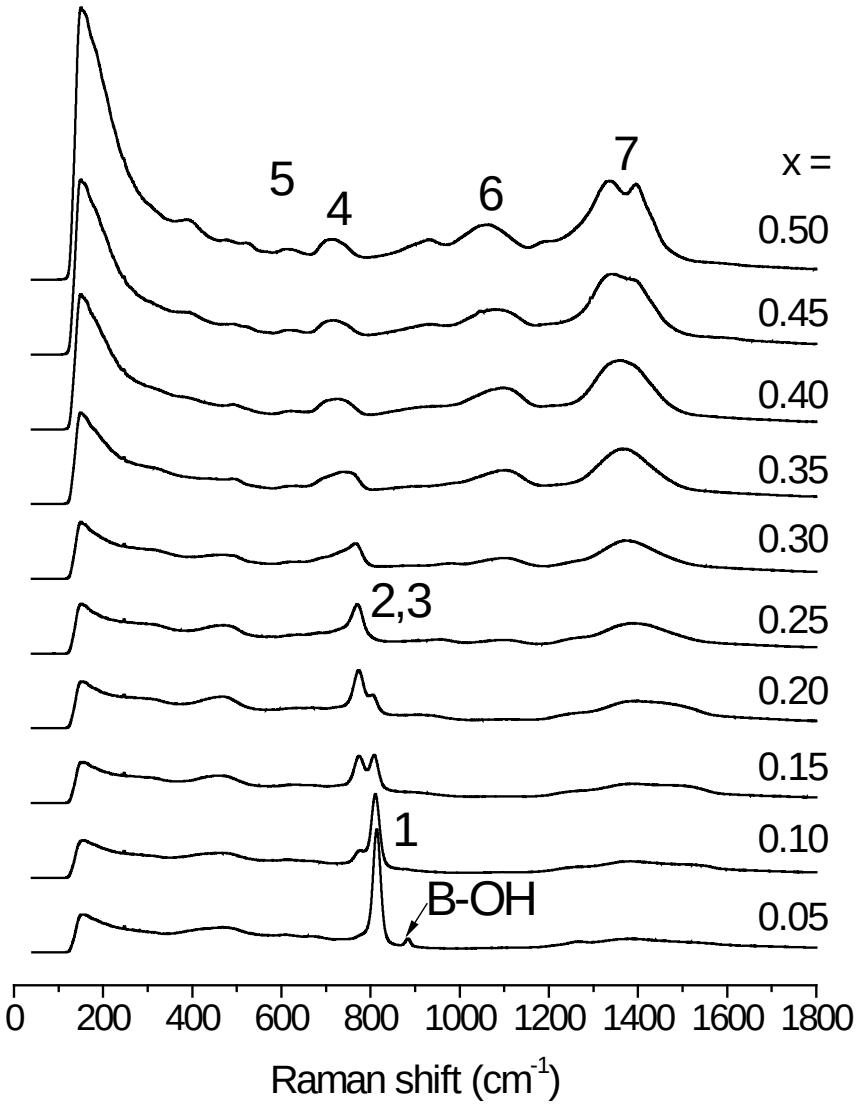

Figure 7.3 *Raman spectra of $xTl_2O\cdot(1-x)B_2O_3$ glasses.*

7.3.4 Neutron diffraction

The distinct scattering, *i(Q)*, which was reduced and corrected using Gudrun and Atlas software [27], is presented in **Figure 7.4** and reveals the presence of a prepeak at ~ 1.08 $Å^{-1}$, which is shifted to ~ 0.95 $Å^{-1}$ and sharpens in higher thallium content glasses as thallium content increases. The first diffraction peak at ~ 1.67 $Å^{-1}$, obtained from the x = 0.05 sample, shifts to ~ 2.01 $Å^{-1}$ in x = 0.40, reflecting changes in the medium-range order in the borate network. A quadratic of the form $A + BQ^2$ was fitted to *i(Q)* at low *Q* to extrapolate the data to $Q = 0$ before being Fourier transformed using the Lorch modification function with a maximum momentum transfer, Q_{max}, of 40 $Å^{-1}$ to reduce termination ripples [28]. The resulting correlation function, $T(r)$, is shown in **Figure 7.5** It is a weighted sum of all of the possible partial correlation functions, $t_{ll'}(r)$

$$T(r) = \sum_{ll'} c_l \, \overline{b_l} \overline{b_{l'}} t_{ll'}(r) \qquad \textbf{(7.1)}$$

and each correlation between two atoms, l and l', gives rise to a peak in $T(r)$ from which the coordination number $n_{ll'}$ can be calculated according to

$$n_{ll'} = \frac{r_{ll'} A_{ll'}}{(2-\delta_{ll'}) c_l \overline{b_l} \overline{b_{l'}}} \qquad \textbf{(7.2)}$$

where $A_{ll'}$ is the area of the peak, $r_{ll'}$ is its position, c_l is the atomic fraction of the species whose coordination number is required, $\overline{b_l}$ and $\overline{b_{l'}}$ are the coherent neutron scattering lengths and $\delta_{ll'}$ is the Kronecker delta.

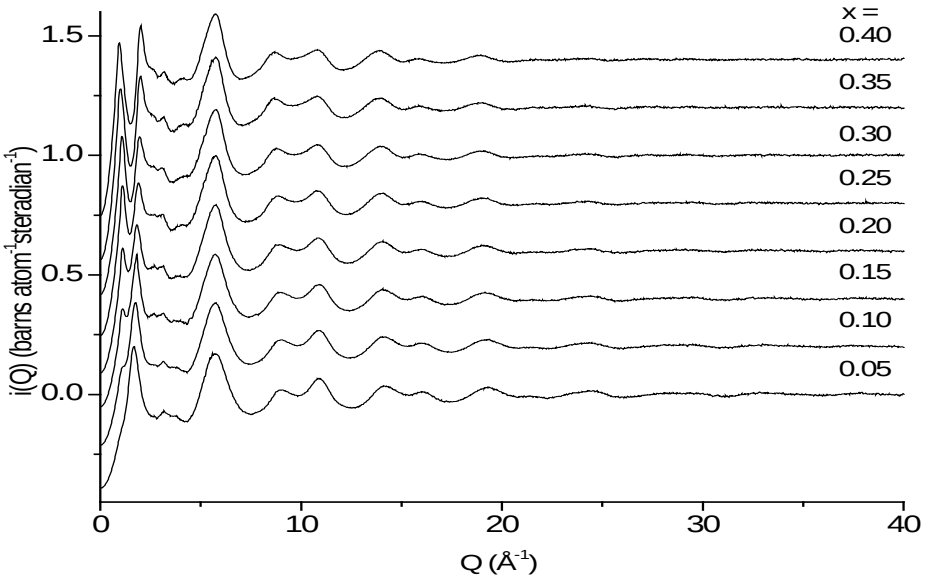

Figure 7.4 *Distinct scattering, i(Q), for the thallium borate glasses. Data are shown with vertical offsets of 0.2 for clarity.*

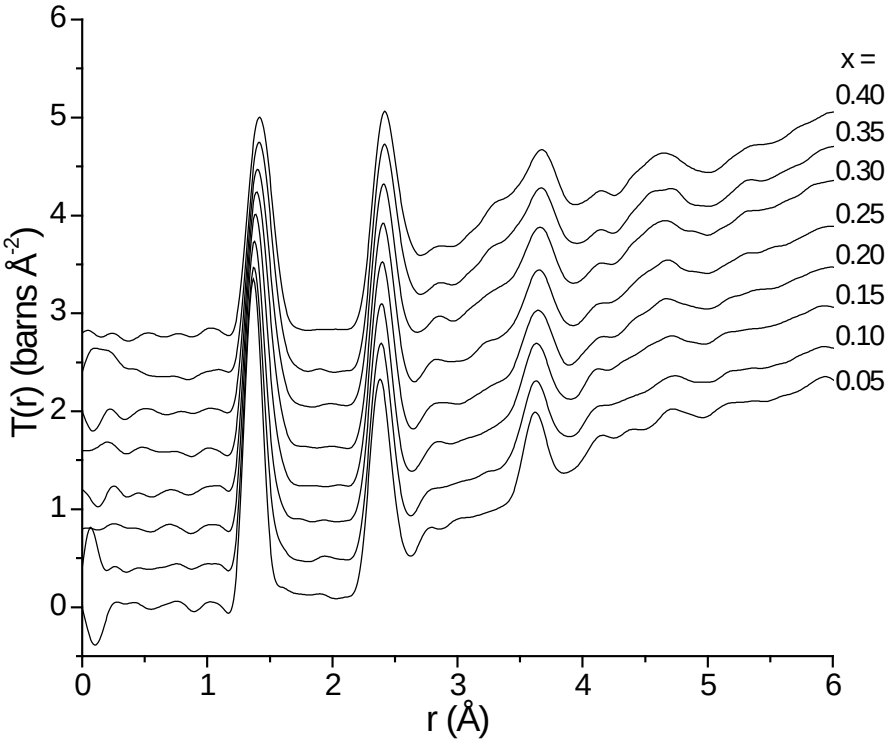

Figure 7.5 *Total scattering, T(r), for the thallium borate glasses. Data are shown with vertical offsets of 0.2 for clarity.*

Figure 7.6 expands *T(r)* of x = 0.05, 0.25 and 0.40 samples in order to visualise the changes of the peaks as Tl_2O content increases. The first *T(r)* peak at ~ 1.3 to 1.5 Å correlates to the B-O distances, where the contribution from different boron environments, i.e. $[BO_3]$ and $[BO_4]^-$, can be extracted. The intensity of the shoulder on the high *r* side of the peak increases as x increases showing the change in the boron environment from $[BO_3]$ to $[BO_4]^-$. The B-O peak was then fitted with two Gaussian contributions from each boron environment. The positions of these two contributions were fixed at the values predicted from bond-valence theory [29], i.e. 1.371 and 1.477 Å for $[BO_3]$ and $[BO_4]^-$, respectively. An example of the fit for x = 0.30 is given in **Figure 7.7**. Thus, the N_4 values could be calculated from the areas obtained from the integration of the $[BO_3]$ and $[BO_4]^-$ fits and the changes in N_4 values with increasing x are plotted in **Figure 7.9** and compared with the values obtained from ^{11}B NMR, showing good agreement.

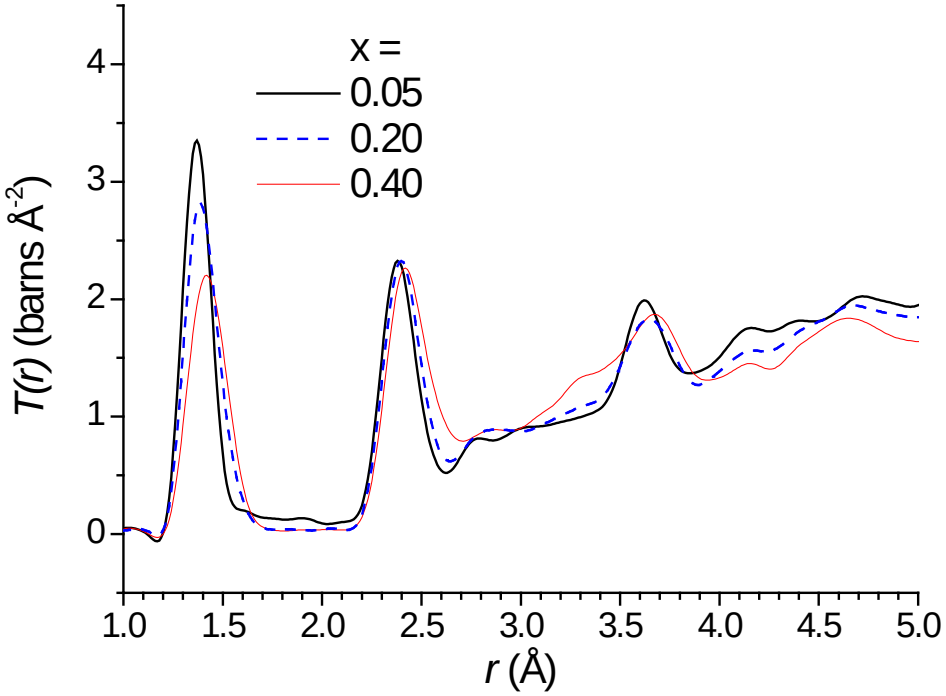

Figure 7.6 *Expanded, superposed T(r) plots for x = 0.05, 0.20 and 0.40 illustrating changes in correlations with composition.*

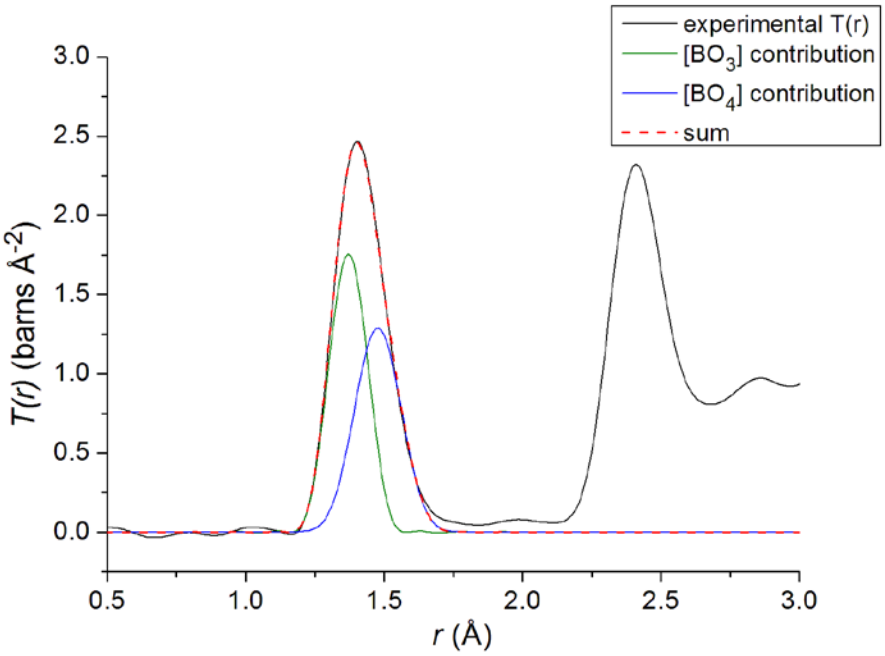

Figure 7.7 *Fit of the first B-O peak in the T(r) from the x = 0.30 sample to contributions from [BO_3] and* $[BO_4]^-$.

The second *T(r)* peak is due to O...O contribution from the distances between neighbouring oxygen atoms in $[BO_3]$ and $[BO_4]^-$ units, for which the peak positions can be calculated as 2.375 and 2.413 Å respectively. This is consistent with the observed O-O peak in this study, which shifted from ~ 2.380 to ~2.408 Å as x increases. From the bond-valence theory [29], the Tl-O correlation of the low coordinated thallium, $[TlO_3]$ or $[TlO_4]$ unit, is expected to arise at 2.578 to 2.685 Å, whereas the high coordinated thallium, $[TlO_6]$ or $[TlO_7]$ units, appears at 2.835 to 2.892 Å. Thus, the peak which arises at ~ 2.6 Å as x increases (**Figure 7.5** and **7.6**) is believed to be the Tl-O correlation of the low coordinated thallium, where its lone pair of electrons is sterically active. The B...B correlations are expected to contribute to the second peak, although it seems not to be responsible for the shoulder at ~ 2.6 Å, because the contribution from B-B correlations should decrease with increasing x. However, the contribution due to high coordinated Tl could not be easily observed.

A peak arising at ~ 3.3 Å as Tl_2O increases, could be due to Tl...Tl pairs, which are more favoured in higher thallium content glasses, e.g. thallium germanate glasses in **Chapter 5**. The reported Tl...Tl distances in the related crystal structures are longer (e.g. 3.52 or 3.46 Å in Tl_2O and $Tl_2B_4O_7$, respectively) but it should be noted that the thallium site in these crystalline phases is $[TlO_4]$, whereas it appears to be $[TlO_3]$ in glass. Therefore, the 3.3 Å peak is possibly due to the contribution from the O...O distance in $[TlO_3]$ units.

A peak at ~ 3.63 to ~3.67 Å is contributed from a typical boroxol ring structure, consistent with the distance between a ring boron and non-ring oxygen on the next boron in the same ring [30]. This peak broadens with increased x, as more ring structures form and contribute, but is still significant at x = 0.4.

7.3.5 ^{11}B solid-state NMR

Examples of ^{11}B solid-state NMR spectra of thallium borate glasses at x = 0.1, 0.2, 0.3, 0.4 and 0.5 are compared with the B_2O_3 glass in **Figure 7.8**. The peaks at 10-15 ppm and 0 ppm correspond to the resonances of $[BO_3]$ and $[BO_4]^-$ units, respectively. The fraction of $[BO_4]^-$ units obviously increases as x increases. N_4 values were calculated from the ratio between the area of the $[BO_4]^-$ peak and the total area of the boron spectrum, which were obtained by integrating under the two peaks and applying a

4% correction to the [BO_3] peak. This correction is necessary to compensate for the loss, under MAS, of central (+½ ↔ –½) transition intensity into the sidebands for the [BO_3] site with its large quadrupolar interaction [31].

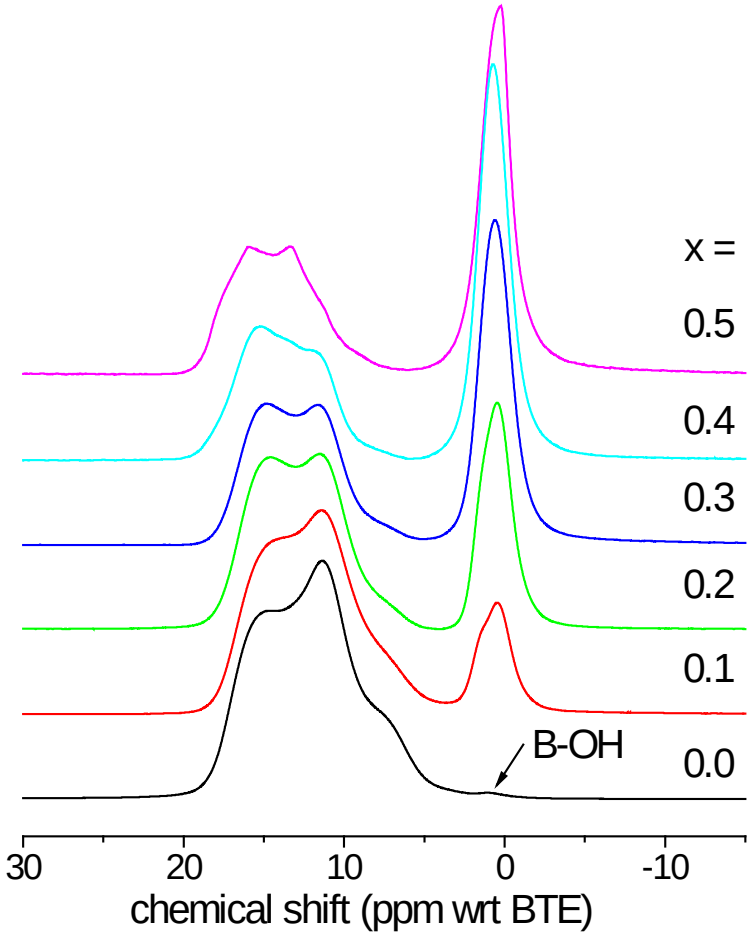

Figure 7.8 *^{11}B MAS NMR spectra of $xTl_2O•(1-x)B_2O_3$ glasses.*

The [BO_4]$^-$ peak from the samples with x ≤ 0.2 is similar to that observed in larger alkali ion (K^+, Rb^+, Cs^+) borate glasses by Kroeker *et al.* [32], as the peak at ~0 ppm could be resolved into two [BO_4]$^-$ sites. Though the two peaks are observable as high as x = 0.4 in large alkali ion containing borate glasses. It is suggested that these two sites correspond to different types of [BO_4]$^-$ superstructural environments, ones where the [BO_4]$^-$ unit occupies a single ring, and ones where the unit bridges two rings [32].

As x increases, the N_4 values increase, then start to deviate at x = 0.3 and are almost constant at x ≥ 0.40. The results from the current study agree within error for three repeated sample preparations and the values plotted in **Figure 7.9** are the average values. The values are also compared with those observed by Baugher and Bray [15] and also with values from lithium, caesium and rubidium borate glasses [32].

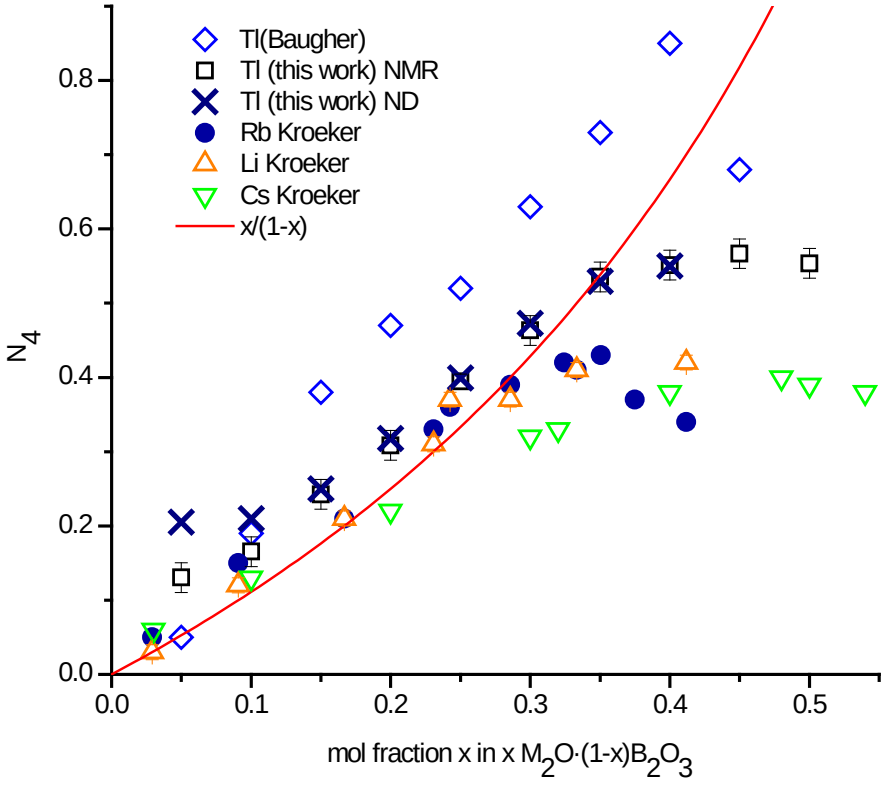

Figure 7.9 *N_4 values of $xTl_2O•(1-x)B_2O_3$ glasses obtained using NMR and also ND compared with literature values from NMR for borate glasses containing different amounts of M_2O, where M is Tl, Li, Cs or Rb.*

The deviation of N_4 values from x/(1-x) relationship is related to the stability of $[BO_4]^-$ units. Kroeker *et al.* [32] reported that this depends on the type of alkali ions. N_4 maintains higher values for Li^+ and Na^+ when x > 0.3 than is the case for K^+, Rb^+ and Cs^+ [32]. The approximate constancy of N_4 values of thallium borate glass in the range x = 0.35 to 0.50 cannot be due to the same reason as in the alkali systems since Tl^+ is very large (the Pauling ionic radius of thallium is close to rubidium at 1.44 Å and 1.48 Å, respectively [14]). As discussed for thallium germanate glasses (**Chapter 5**), this

difference in behaviour can be reconciled with the associated change in the coordination environment of the thallium ion, which will be discussed later.

The N_4 values are noticeably higher than the theoretical x/(1-x) line, although the deviation is much smaller than that reported by Baugher and Bray [15]. However, the NMR N_4 values of some alkali borates reported by Kroeker *et al.* are also higher than the x/(1-x) line, although they are not as high as those for thallium borate glasses. A possible source of extra $[BO_4]^-$ could be due to the presence of water in the glass [25, 26]. It is true for the x = 0.05 sample where there is evidence of a B-OH vibration at ~884 cm^{-1} in the Raman spectrum. Because finely ground powder samples are used for the ^{11}B NMR, the water attack problem could be more extensive - note that a small B-OH peak (at ~1 ppm) is observable in the ^{11}B NMR spectrum from B_2O_3 in **Figure 7.8**. The equivalent peak in samples containing higher concentrations of Tl_2O would be masked by the $[BO_4]^-$ peak produced by Tl^+ inclusion, though the Raman spectra (**Figure 7.3**) would suggest that B-OH formation is a significant problem only for the x=0.05 sample which does indeed show the greatest deviation from the x/(1-x) model.

One possible reason why the N_4 values presented here are closer to the x/(1-x) model than those reported by Baugher and Bray [15] is the difficulty in analysing their continuous-wave, static spectra compared to the high-field, high MAS frequency, pulsed NMR, which is used for ^{11}B NMR study on modern spectrometers. The N_4 values observed in this study are still higher than the x/(1-x) line, which is the case with some of the values reported by *Kroeker et al*. shown in **Figure 7.9**. The possible explanations of this might be compositional error, including water attack; loss of $[BO_3]$ peak intensity into the sidebands; insufficiently long relaxation delays (T_1 is usually shorter for $[BO_4]^-$ than $[BO_3]$; and difficulty in optimising acquisition conditions for the resonances from both the $[BO_3]$ and $[BO_4]^-$ sites simultaneously. However, the N_4 values obtained from neutron diffraction agree with the NMR. The errors in the case of neutron diffraction could arise from the data treatment, which is sensitive to inaccuracies in density and/or chemical composition; absorption or inelastic scattering (as can arise from ^{10}B and ^{1}H) and problems in merging data from the various detector banks. However, good, well-corrected data from modern, high-resolution diffractometers such as GEM can now produce coordination numbers from the first peak in *T(r)* which are very accurate. For example, Hannon *et al.* reported a value for

n_{BO} of 2·934(8) for B_2O_3 [33]. The very close agreement in N_4 values obtained from both NMR and neutron diffraction therefore confirms that the values higher than the predicted x/(1-x) line are indeed the correct values for these samples. This leaves the possibilities of either compositional deviation or some stabilising factor for $[BO_4]^-$. The greatest deviations are at low x and would be consistent with the presence of some water attack on the samples. Oxidation of Tl^+ to Tl^{3+} would increase the number of $[BO_4]^-$ (though disproportionation would not) but there is no indication of the higher oxidation state in the ^{205}Tl NMR.

7.3.6 ^{205}Tl solid-state NMR

Broad ^{205}Tl solid-state NMR spectra of thallium borate glass are shown in **Figure 7.10**, which shows the increase in spectrum width from ~ 400 ppm to 1000 ppm with increasing x. In **Figure 7.11**, the static ^{205}Tl NMR spectra of the glasses (x=0.05, 0.25 and 0.45) were also compared with the spectra of the crystalline phases discussed in **Chapter 6**, which are TlB_5O_8 (x=0.17) and TlB_3O_5 (x=0.25) containing samples. It is obvious that the spectrum of the glass, even in low thallium content is significantly broader than the crystalline spectra. However, increasing spectrum width with thallium content is consistent with the crystalline spectra. **Figure 7.12** shows the plots of full-width at half-maximum height (FWHM) values and the position of the peak maximum versus the Tl_2O content, with values increasing dramatically as x increases. The symmetry of the spectra changes from asymmetric line shape to symmetric line shape as x increases. This suggests the presence of more than one thallium site in the glass. The glass spectra are fitted with two contributions using DM2010 software [31]. The line shape of the crystalline compounds also changes significantly, as discussed in **Chapter 6**, which is due to the changes in thallium environment from spherically symmetric high-coordinated to axially symmetric low-coordinated.

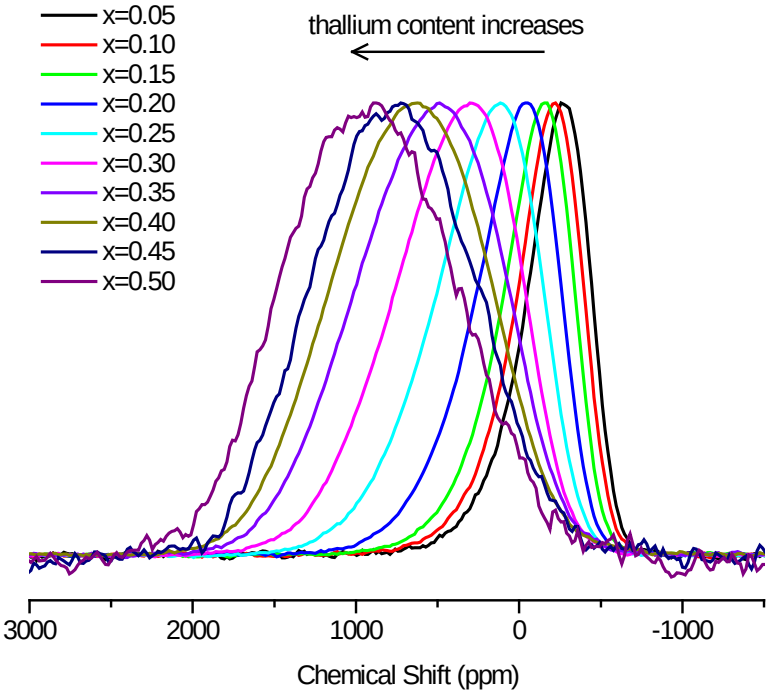

Figure 7.10 *^{205}Tl static NMR spectra of $xTl_2O{\cdot}(1\text{-}x)B_2O_3$ glasses.*

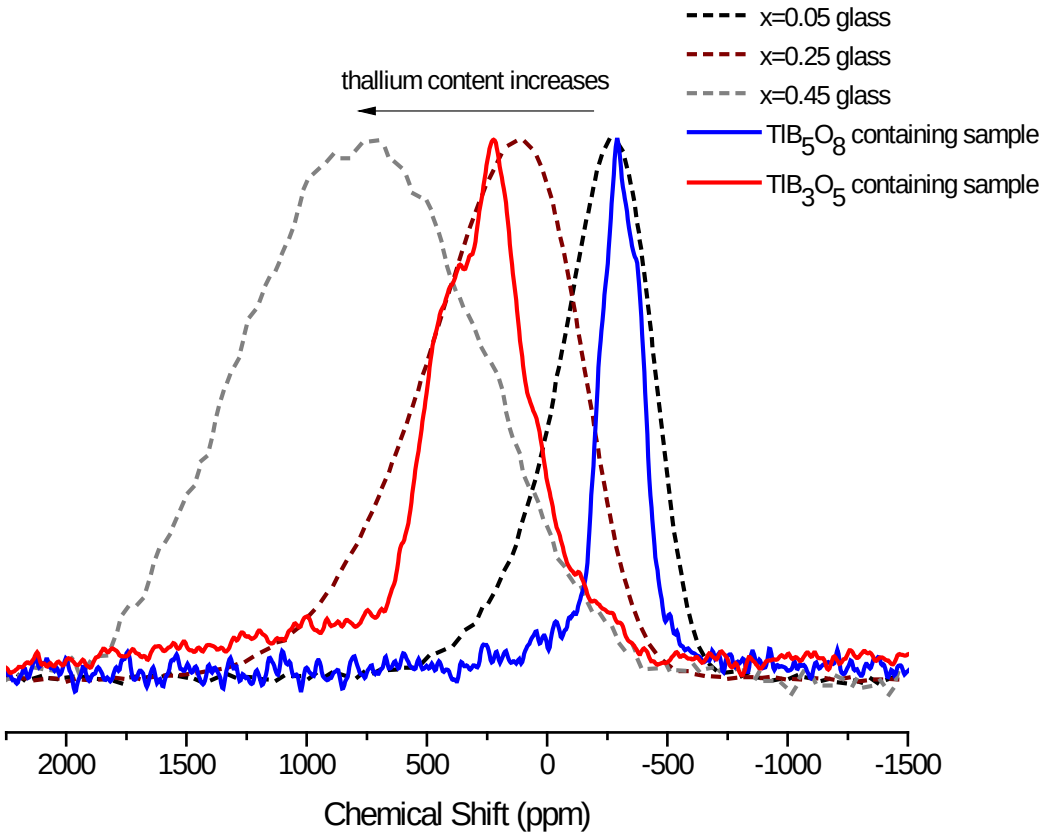

Figure 7.11 *^{205}Tl NMR spectra of $xTl_2O{\cdot}(1\text{-}x)B_2O_3$ glasses (x=0.05, 0.25 and 0.45), TlB_5O_8 compound and TlB_3O_5 compound (**Glasses – dash lines, crystalline compounds – solid line**).*

Thallium has two isotopes ^{203}Tl and ^{205}Tl, with nuclear spin, I, equal to 1/2 for both isotopes. There are several interactions between thallium nuclei which affect the line shape and line broadening in thallium NMR spectrum, for example the *dipolar interaction*, which is proportional to $\gamma_a\gamma_b/r^3$ where r is the internuclear separation and γ is the gyromagnetic ratio of each isotope; *chemical shift anisotropy (CSA)*, which depends on the symmetry of the chemical environments of the nuclei; *chemical shift dispersion* which depends on the distribution of environments; and *the exchange interaction*, which occurs where there is overlap of the electronic wave functions of thallium nuclei when the distance between ^{203}Tl and ^{205}Tl is sufficiently small [34, 35].

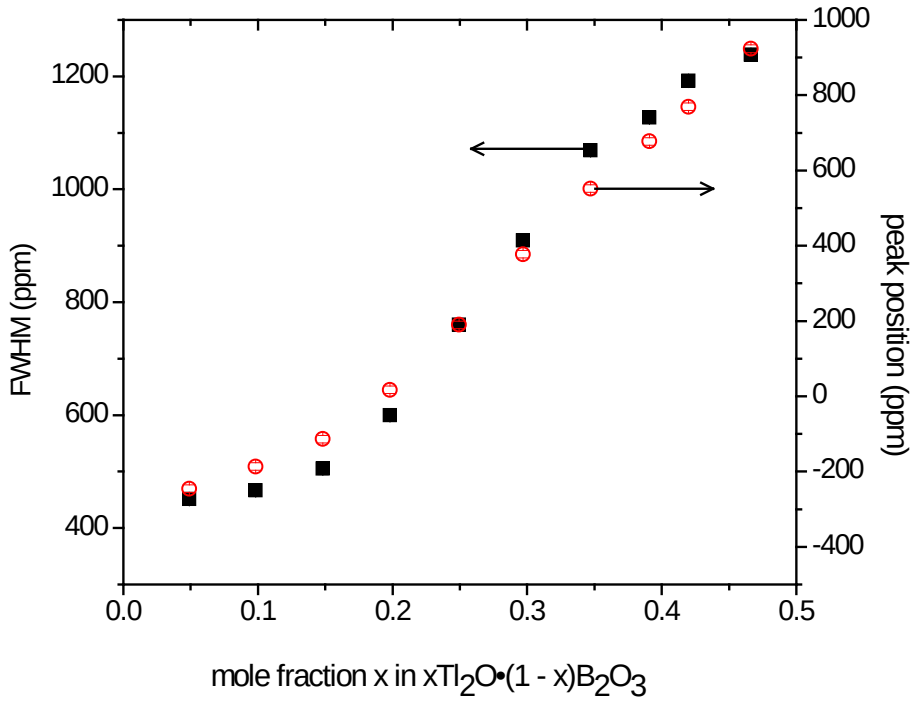

Figure 7.12 *Changes in ^{205}Tl NMR peak position and full-width at half-maximum height (FWHM) with glass composition.*

Some understanding of the changes occurring can be obtained by studying the corresponding crystalline samples, thus the ^{205}Tl NMR spectra from x = 0.15 and x = 0.25 glasses are compared with the one from the crystalline sample obtained by devitrifcation from x = 0.20 glass in **Figure 7.13.** As discussed in **Chapter 6**, the crystalline sample contains two crystal phases, TlB_3O_5 [36] (x = 0.25) and TlB_5O_8 [37]

(x = 0.17) plus some residual glass. Thus there are two peaks in the static ^{205}Tl NMR spectrum at -250 ppm and 300 ppm (**Figure 7.13**), respectively, arising from the single Tl sites in each crystal phase. It is assumed that these two chemical shifts represent two possible thallium environments in the glass samples. These two thallium sites are depicted in **Figure 7.14a** and **7.14b**. The highly distorted asymmetric, low coordinated and covalent thallium site; [TlO_4], in which the lone pair of electrons are sterically active, sp^3d is shown in **Figure 7.14a**. This is similar in symmetry to the [TlO_3] sp^3 site indicated by the neutron diffraction results. The crystalline TlB_5O_8 has more symmetric, high coordinated and ionic thallium environment, where the lone pair of electrons is sterically inert, $6s^2$ (**Figure 7.14b**). The coordination consists of 3 Tl-O distances between 2.90 and 2.97 Å, 4 between 3.07 and 3.09 Å and 2 at 3.17 and 3.28 Å. This can be considered either as a [TlO_9] site or (as done here) a [TlO_7] site. Thus, the two thallium sites, [TlO_3] and [TlO_7] are used as starting models in the NMR spectrum fit. A [TlO_3] site, which contributes an axially symmetric CSA component with broadening, increases in intensity, as x increases. In addition, a [TlO_7] site, which contributes an approximately symmetric static CSA component, decreases in intensity with increasing x and is represented by a Gaussian at all concentrations. The application of broadening parameters to the axially symmetric CSA and the Gaussian line shape used in the fitting of NMR spectra indicates that there is a large distribution in bond lengths in the glasses. Examples of the fitting of samples with x = 0.05, 0.15, 0.25, 0.30, 0.40 and 0.45 are shown in **Figures 7.15a to 7.15e**, respectively. It is clear that the Gaussian contribution, which appears at more negative chemical shift reduces in intensity, whereas the CSA lineshape increases in intensity as x increases. Unfortunately, the neutron diffraction data do not provide an average thallium-oxygen coordination number, $n_{Tl\text{-}O}$, otherwise this could be used to constrain the relative contributions of the two sites to obtain an unambiguous fit. In the glass containing more than 0.40 mol fraction of Tl_2O, the spectra can be fitted with a single Gaussian shape, shown in **Figure 7.15(e)**, and, as a result, there is only one thallium site as a 100 % of low coordinated thallium site is given in **Figure 7.16**. The amount of each thallium environment at various x is shown in **Figure 7.16**, and reveals rapid changes in the proportions of the different thallium environments in the composition range around x = 0.20 to 0.25 as is also found in the molar volume plot (**Figure 7.1b**) and the line width and shift plot (**Figure 7.12**).

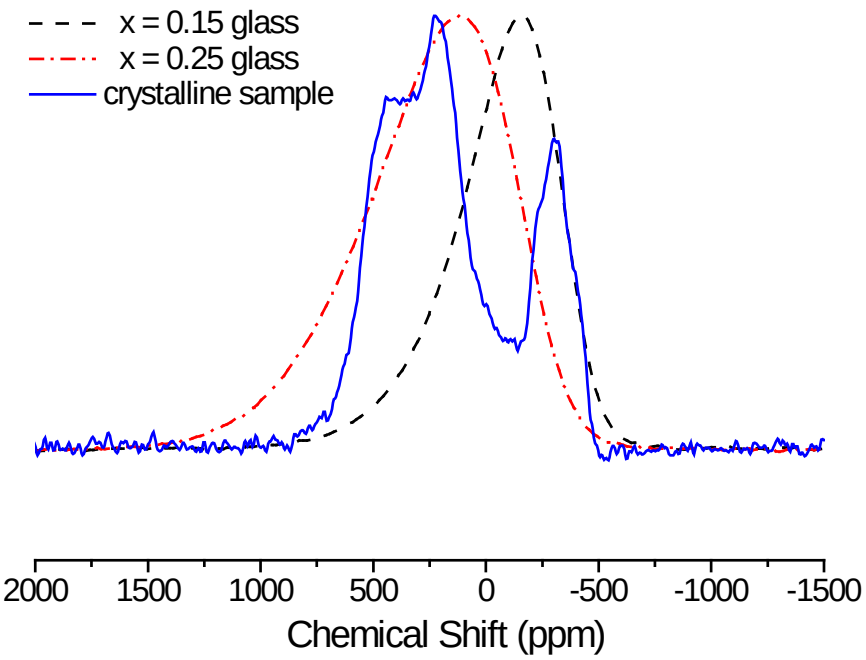

Figure 7.13 *^{205}Tl Static solid-state NMR spectra of crystalline phases devitrified from the $0.20Tl_2O{\cdot}0.80B_2O_3$ glass compared with spectra from the glasses nearest to the compositions of the crystal phases formed.*

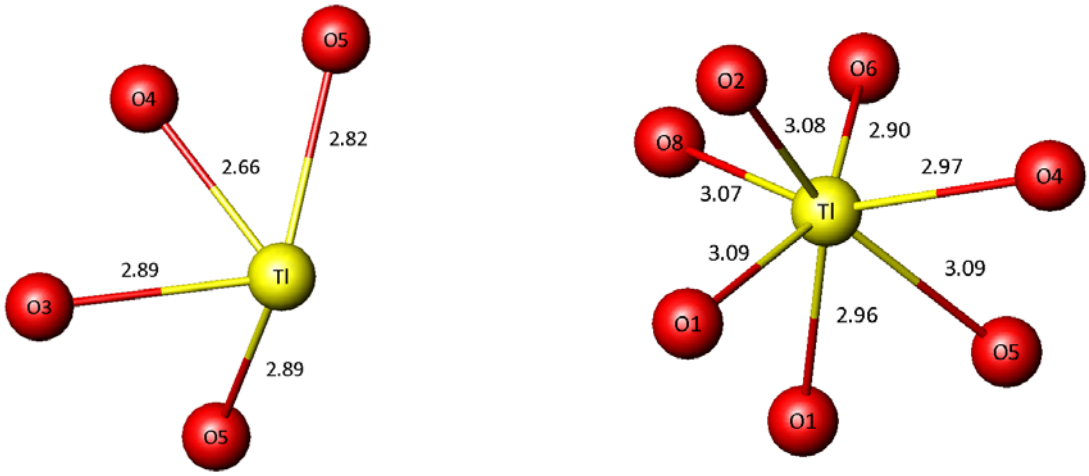

Figure 7.14 *The two crystalline thallium sites, (a) TlO_4 in TlB_3O_5 and (b) TlO_9 in TlB_5O_8 which are proposed as the basis for the dominant environments in the $xTl_2O{\bullet}(1\text{-}x)B_2O_3$ glasses. (Bond lengths are in Å)*

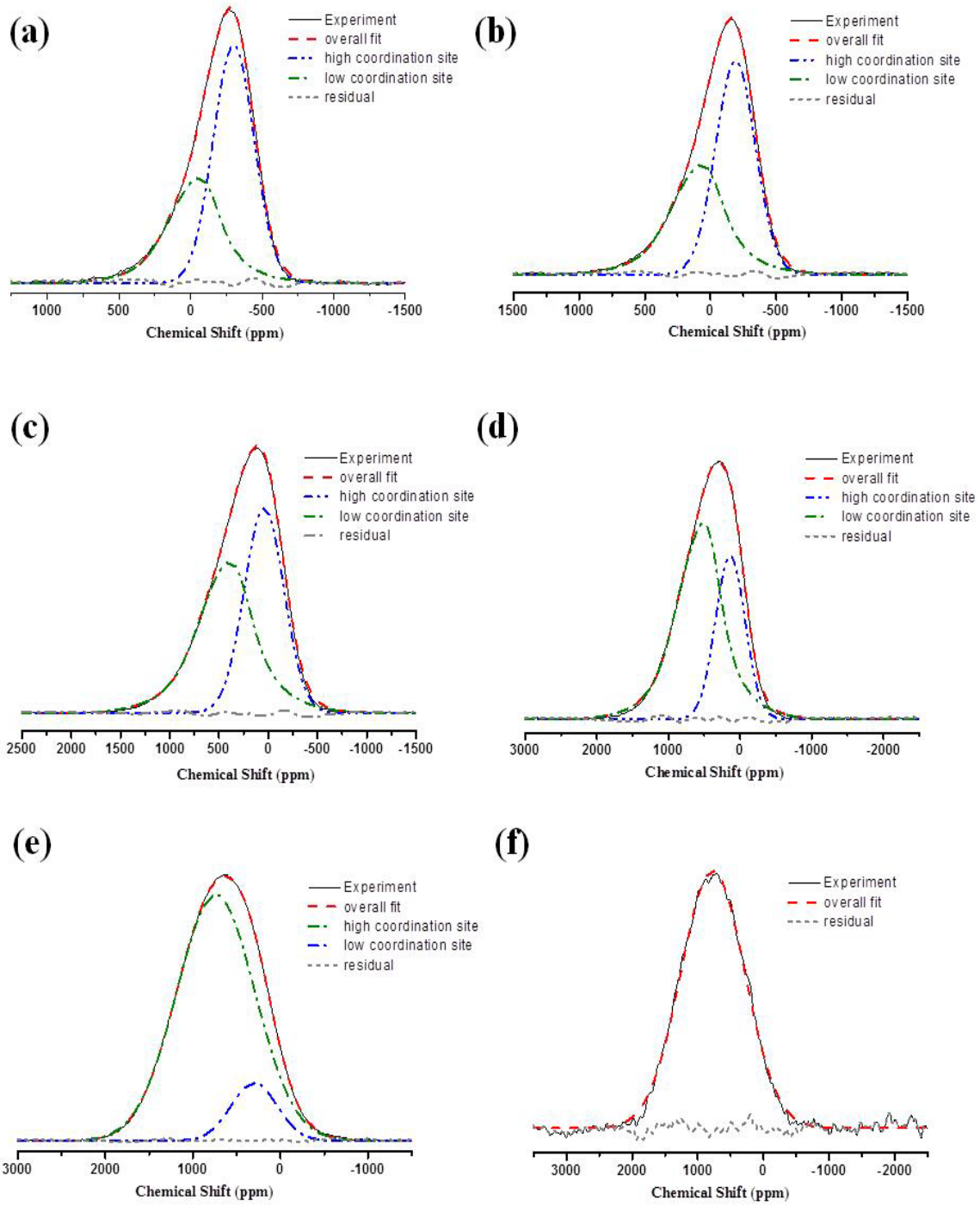

Figure 7.15 *Fits to the ^{205}Tl static NMR spectra of $xTl_2O•(1-x)B_2O_3$ glasses of composition: (a) x = 0.05, (b) x = 0.15, (c) x = 0.25, (d) x = 0.30, (e) x = 0.40 and (f) x = 0.45 using DM2010* [3].

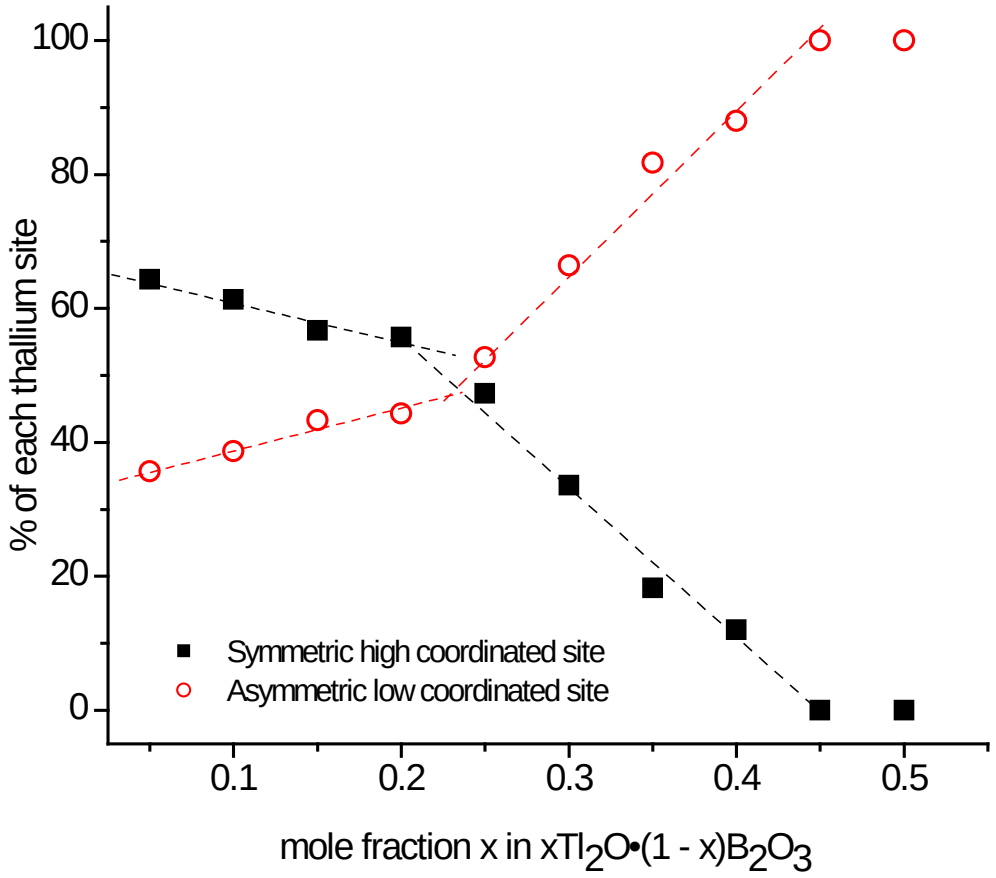

Figure 7.16 *Amount of each thallium site as a function of composition. The symmetric high coordinated site and the asymmetric low coordinated site contribute to the Gaussian and CSA line shapes respectively in* ***Figure 7.14****. Lines are drawn to guide the eye and error bars are smaller than the symbols used.*

The spin-spin relaxation time, T_2, has been measured by pulse echo experiment by varying the time between pulses. The T_2 values of all glass samples are presented in **Figure 7.17** showing the T_2 reduction versus the calculated Tl...Tl distances assuming that all thallium atoms are homogeneously distributed. The reduction in T_2 is proportional to the third power of the Tl...Tl distances. As mentioned in **Chapter 5,** T_2 is inversely proportion to the square root of the second moment, which is inversely proportion to the sixth power of the distances between thallium; $r_{Tl\text{-}Tl}$. As a result, the T_2 should follow the third power relationship if there are interactions contributing to the second moment. This indicates that the dipolar interaction and exchange interaction [38,

39], which contribute to the second moment, are present in all samples. This will broaden the ^{205}Tl spectrum together with the chemical shift dispersion due to the large distribution in bond length. This behaviour is different from what has been observed in thallium germanate glasses, where the dipole-dipole interaction and exchange interaction dominate only in high thallium content glass. This may suggest the presence of Tl-O-Tl bonds throughout the range of thallium composition investigated in this study as proposed in thallium germanate glasses [3].

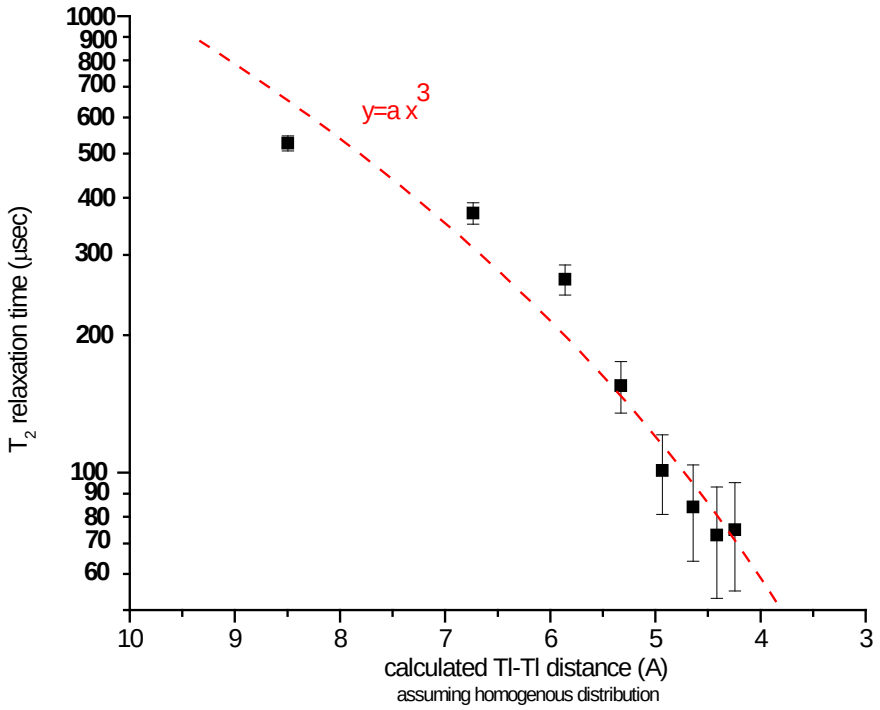

Figure 7.17 *Spin-spin relaxation time T_2 against the Tl...Tl distances calculated assuming a homogeneous distribution of Tl in the glass.*

7.3.7 Electrostatic bond strength calculation

The ^{11}B and ^{205}Tl NMR spectra indicate the presence of: $[BO_3]$ and $[BO_4]^-$ units in the form of superstructural units; a low-coordinated thallium species, probably $[TlO_3]$; and a high coordinated thallium species, probably $[TlO_7]$, in these glasses. The plot of N_4 values in **Figure 7.9** shows a consistently higher value of N_4 at higher Tl_2O content compared to the alkali borate glasses. This could indicate the stabilising of $[BO_4]^-$ units by $[TlO_3]$ units in thallium borate glasses. Electrostatic bond strength

(EBS) calculations, as previously performed for thallium germanate glasses [3] and in **Chapter 5**, are a useful tool to give an idea of how structural units are accommodated in the glass structure. **Figure 7.18** shows the proposed structures for low (**Figures 7.18a, b and c**) and high (**Figures 7.18d, e and f**) thallium content glasses. **Figures 7.18 (a)**, **(b)** and **(c)** show possible thallium coordinations to a ^{III}B-O-^{IV}B oxygen, where ^{III}B and ^{IV}B are three and four coordinated boron, respectively, which give acceptable values of EBS. A range of thallium environment could be bonded to the ^{III}B-O-^{IV}B oxygen, i.e. single high or single low coordinated thallium, or pairs of high coordinated thallium in **Figures 7.18 (a)**, **(b)** and **(c)**, respectively. At higher thallium content, ^{IV}B-O-^{IV}B bonds are unavoidable, as a result oxygen is significantly underbonded (<< 2.0). Raising the sum of EBS to 2.0 would require far more high-coordinated Tl^{+} than is feasible (oxygen coordination will not exceed 4 which includes the two boron atoms). Thus, bonding of the ^{IV}B-O-^{IV}B oxygen to low-coordinated thallium (**Figure 7.18d**) or a pair of low-coordinated thallium (**Figure 7.18e**) is necessary to achieve the sum that is close to the value of 2.0. Thus, the [BO_4] units could be stabilised by bonding to [TlO_3]. **Figures 7.18c** and **7.18e** also show that Tl-O-Tl bonds are possible in both low and high thallium content glasses, which enable the broadening of Tl NMR line shape by Tl-Tl exchange interaction or dipolar interaction. The unavoidable NBO, which is formed in high thallium content glass, possibly coordinates to low-coordinated thallium as shown in **Figure 7.18f**. It should be noted that changing the coordinations of thallium to [TlO_4] and [TlO_9] will change the EBS values but not the general argument.

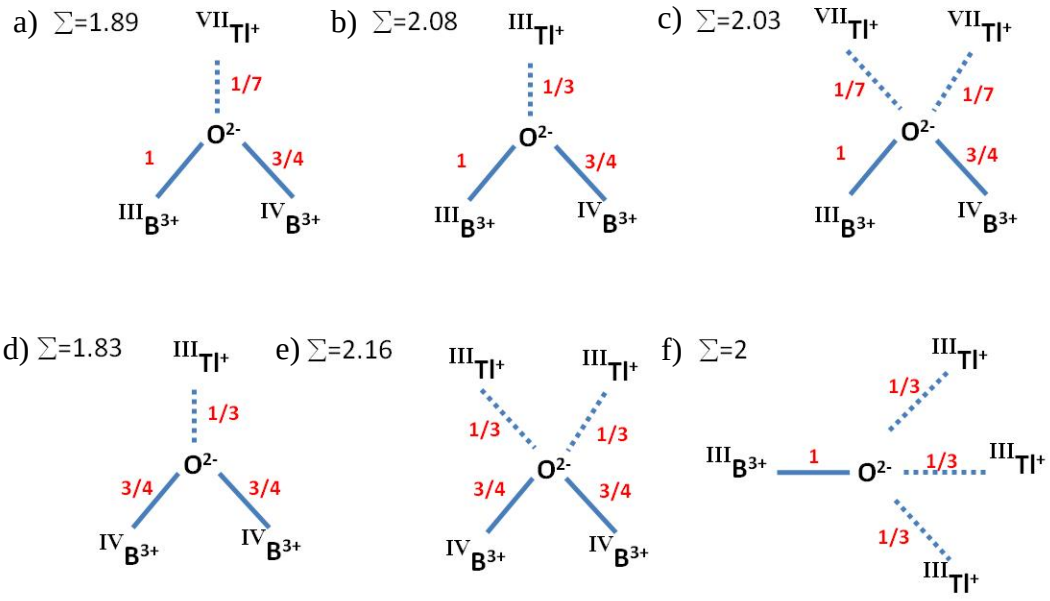

Figure 7.18 *Proposed thallium borate glass structure base on electrostatic bond strength; (a), (b), (c) for low thallium oxide glasses; (d), (e) and (f) for high thallium oxide glasses.*

7.4 Conclusions

A borate anomaly is present in thallium borate glass with a minimum value of molar volume suggesting significant structural change due to the addition of thallium oxide modifier. Thallium oxide affects the glass structure in terms of both boron and thallium environments. Neutron diffraction and solid-state NMR spectroscopy confirm the change in the coordination number of boron to oxygen atoms from $[BO_3]$ to $[BO_4]^-$. N_4 values, which indicate the change in boron environment as thallium oxide content increases, obtained from both techniques are very close. The N_4 values are larger than found for alkali borate glasses, indicating the stabilisation of $[BO_4]^-$ by the formation of low coordinated thallium $[TlO_3]$. Values at low x which are in excess of the x/(1-x) model may be explained by water contamination in the samples, though there is direct evidence in only the x = 0.05 sample. Raman spectroscopy also reveals the changes in boron-oxygen superstructural units. ^{205}Tl solid-state NMR suggests that at least two thallium sites are present in the glass. High coordinated thallium site $[TlO_7]$ with an inert lone pair of electrons is favourable in low thallium content glass. The amount of low coordinated thallium $[TlO_3]$ increases as Tl_2O increases. Tl-NMR spectra are broad and shifted mainly due to the chemical shift dispersion and chemical shift anisotropy

interaction, respectively. T_2 measurement, which ignores the chemical shift mechanism, confirmed that dipole-dipole and exchange interactions occur in glasses throughout the range of studied compositions. These mechanisms also broaden the Tl-NMR spectrum. Electrostatic bond strength (EBS) calculation is used to suggest a tentative thallium borate glass structure, where the change in thallium coordination number could stabilise high coordinated boron, $[BO_4]^-$, rather than formation of non-bridging oxygen. Moreover, the Tl-O-Tl bond is explained using EBS calculation, supporting the presence of exchange interaction in the Tl-NMR study of thallium borate glasses.

7.5 References

[1] C. Spurcaciu, T.P. Negreanu, *Journal of Non-Crystalline Solids*, **84** (1986) 105.

[2] E.R. Barney, A.C. Hannon, N. Laorodphan, R. Dupree, D. Holland, *Journal of Non-Crystalline Solids*, **356** (2010) 44.

[3] E.R. Barney, A.C. Hannon, N. Laorodphan, D. Holland, *The Journal of Physical Chemistry C*, **30** (2011) 14997.

[4] B.N. Meera, J. Ramakrishna, *Journal of Non-Crystalline Solids*, **159** (1993) 1.

[5] E.I. Kamitsos, M.A. Karakassides, *Physics and Chemistry of glasses*, **30** (1989) 19.

[6] B.P. Dwivedi, M.H. Rahman, Y. Kumar, B.N. Khanna, *Journal Physics and Chemistry of Solids*, **54** (1993) 621.

[7] E.I. Kamitsos, A.P. Patsis, M.A. Karakassides, G.D. Chryssikos, *Journal of Non-Crystalline Solids*, **126** (1990) 52.

[8] P.J. Bray, *Journal of Non-Crystalline Solids*, **73** (1985) 19.

[9] W.L. Konijnendijk, J.M. Stevels, *Journal of Non-Crystalline Solids*, **18** (1975) 307.

[10] A.C. Wright, *Physics and Chemistry of Glasses-European Journal of Glass Science and Technology Part B*, **51** (2010) 1.

[11] J. Krogh-Moe, *Physics and Chemistry of Glasses*, **1** (1960) 26.

[12] J.R. Berryman, S.A. Feller, M. Affatigato, M. Kodama, B.M. Meyer, S.W. Martin, F. Borsa, S. Kroeker, *Journal of Non-Crystalline Solids*, **293-295** (2001) 483.

[13] J. Zhong, P.J. Bray, *Journal of Non-Crystalline Solids*, **111** (1989) 67.

[14] R.E. Youngman, J.W. Swansiger, *Journal of the American Chemical Society*, **117** (1995) 1397.

[15] J.F. Baugher, P.J. Bray, *Physics and Chemistry of Glasses*, **10** (1969) 77.

[16] C. Spurcaciu, T.P. Negreanu, *Journal of Non-Crystalline Solids*, **84** (1986) 105.

[17] J. Krogh-Moe, H. Jürine, *Physics and Chemistry of Glasses*, **6** (1965) 30.

[18] L.W. Panek, *Nuclear Magnetic Resonance Studies of 203Tl, 205Tl, and 17O in Oxide Glasses*, Ph.D. thesis, Brown University (1977).

[19] K. Otto, M.E. Milberg, *Journal of the American Ceramic Society*, **50** (1967) 513.

[20] M.E. Milberg, C.R. Peter, *Physics and Chemistry of Glasses*, **10** (1969) 46.

[21] N. Penin, L. Seguin, B. Gerand, M. Touboul, G. Nowogrocki, *Journal of Solid State Chemistry*, **160** (2001) 139.

[22] SciMatics, *SciGlass - Glass Property Information System*, Computer software (2011).

[23] O.V. Mazurin, M.V. Streltsina, T.P. Shvaiko-Shvaikovskaya, *Handbook of Glass Data*, Elsevier (1985).

[24] H.A. Feller, A.R. Betzen, M. Affatigato, S.A. Feller, *Physics and Chemistry of Glasses-European Journal of Glass Science and Technology Part B*, **41** (2000) 341.

[25] S.Z. Smirnov, V.G. Thomas, S.F. Demin, V.A. Drebushchak, *Chemical Geology*, **223** (2005) 16.

[26] L. Xiaoping, G. Shiyang, X. Shuping, *Spectrochimica Acta A*, **60** (2004) 2725.

[27] A.C. Hannon, W.S. Howells, A.K. Soper, *Institute of Physics Conference Series*, (1990) 193.

[28] E. Lorch, *Journal of Physics C*, **2** (1969) 229.

[29] N.E. Brese, M. O'Keeffe, *Acta Crystallogr B*, **47** (1991) 192.

[30] A.C. Hannon, D.I. Grimley, R.A. Hulme, A.C. Wright, R.N. Sinclair, *Journal of Non-Crystalline Solids*, **177** (1994) 299.

[31] D. Massiot, F. Fayon, M. Capron, I. King, S. Le Calvé, B. Alongso, J.O. Durand, B. Bujoli, Z. Gan, G. Hoatson, *Magnetic Resonance in Chemistry*, **40** (2002) 70.

[32] S. Kroeker, P.M. Aguiar, A. Cerquiera, J. Okoro, W. Clarida, J. Doerr, M. Olesiuk, G. Ongie, M. Affatigato, S.A. Feller, *Physics and Chemistry of Glasses-European Journal of Glass Science and Technology Part B*, **47** (2006) 393.

[33] A.C. Hannon, E.R. Barney, D. Holland, *Physics and Chemistry of Glasses-European Journal of Glass Science and Technology Part B*, **50** (2009) 271.

[34] J.F. Hinton, K.R. Metz, R.W. Briggs, *Progress in Nuclear Magnetic Resonance Spectroscopy*, **20** (1988) 423.

[35] J.F. Hinton, *Bulletin of Magnetic Resonance*, **13** (1992) 90.

[36] M. Touboul, E. Betourne, G. Nowogrocki, *Journal of Solid State Chemistry*, **131** (1997) 370.

[37] M. Touboul, G. Nowogrocki, *Journal of Solid State Chemistry*, **136** (1998) 216.

[38] H.S. Gutowsky, B.R. McGarvey, *Physical Review*, **91** (1953) 81.

[39] N. Bloembergen, T.J. Rowland, *Physical Review*, **97** (1955) 1679.

Chapter 8

Conclusions and Future Work

8.1 Introduction

This chapter summarise all the work that has been presented in **Chapter 4** to **Chapter 7**, which can be divided into two systems, i.e. thallium germanate and thallium borate. It also includes suggestions as to future work in order to extend this study.

8.2 Structure of thallium germanate crystalline phases and glasses

The devitrified thallium germanate samples containing molar fractions of thallium oxide (Tl_2O) as 0.125, 0.143, 0.20 and 0.33 were made via heat treatment of the corresponding glasses at crystallisation temperatures obtained from thermal analysis. There are two crystallisation temperatures in all samples. X-ray diffraction of the samples heat-treated at lower crystallisation tempetature revealed that metastable phases were crystallised from the glasses. At higher temperature, the corresponding stoichiometric compounds were obtained with the presence of one or more second phases. The densities and molar volumes of the samples obtained from high-temperature heat treatment differ slightly from the values reported by Touboul and Feutelais [1]. ^{205}Tl NMR spectra confirmed that there are more than one thallium environments in all devitrified samples. The chemical shifts of each thallium environment are very similar in samples containing 0.125, 0.143 and 0.20 Tl_2O, whereas the high temperature heat-treated sample containing 0.33 Tl_2O has three thallium environments covering a range of chemical shifts from 700 to 2700 ppm. Magic angle spinning ^{203}Tl NMR an enriched sample containing $Tl_2Ge_4O_9$ phase, whose crystal structure is known, showing that there is only one thallium site, which is in consistent with the structure reported [1]. Raman spectroscopy revealed that there is no peak corresponding to the presence of non-bridging oxygen. In the samples containing $Tl_2Ge_7O_{15}$, $Tl_2Ge_6O_{13}$ and $Tl_2Ge_4O_9$, there are peaks corresponding to a $[Ge_3O_9]$ ring structure.

In thallium germanate glasses, 10 samples containing the molar fraction of Tl_2O from 0.05 to 0.50 were made by melting and qunching method. Densities and molar

volumes of glasses are consistent with the values reported in the literature [2-4], which confirmed that the Tl_2O content in the glass is very close to the nominal composition. The minimum of molar volume and change in density slope at about 0.15 Tl_2O content glass showed that there is anomalous behaviour in these glasses, which is due to the change in coordination number of germanium oxide network from [GeO_4] to [$GeO_{5\ or\ 6}$]. Neutron diffraction, from glasses containing 0.05 to 0.40 Tl_2O, has been performed. Peaks in total correlation function, T(r), obtained from the Fourier transform of the neutron distinct scattering data, correspond to the distances between pairs of atoms, i.e. the peaks at ~1.75, ~2.5 and 3.5-3.7 Å correspond to Ge-O, Tl-O and Tl-Tl distances, respectively. The broadening of the Ge-O peak with increasing addition of Tl_2O is presumed to be due to change of coordination number of germanium from 4 to 5 or 6 and possible formation of non-bridging oxygens. At low thallium content (0.05 to 0.15) glasses, the coordination number of thallium to oxygen is high and relatively symmetric, which is similar to the alkali germanate glasses. A feature due to low-coordinated thallium, i.e. [TlO_3], at ~ 2.527 Å in T(r), is visible in higher thallium content glasses. ^{205}Tl NMR spectra, which are very broad and with large chemical shift range, showed the presence of at least two thallium environments in thallium germanate glasses, which are high-coordinated with sterically inert lone pair of electrons, e.g. [TlO_7] or [TlO_9] [5] and low coordinated with sterically active lone pair of electrons e.g. [TlO_3] [6] or [TlO_4] [7]. Information on both thallium environments was extracted from the spectra using the DM2010 program [8] revealing that [Tl_{low}] increases and [Tl_{high}] decreases as Tl_2O increases. Tl^{3+} was believed to present in 0.40 to 0.50 $T_{l2}O$ glasses as detected in ^{205}Tl NMR spectra at the position ~ 2570 ppm. NMR transverse relaxation time T_2 measurement of the samples showed that chemical shift dispersion and chemical shift anisotropy contribute to the ^{205}Tl NMR spectra at low thallium content (0.05 to 0.25 Tl_2O). The extra contributions to peak width from dipole-dipole interaction and exchange interaction are apparent in higher Tl_2O content glasses. The ^{203}Tl NMR study on ^{203}Tl enriched $0.20Tl_2O{\cdot}0.80GeO_2$ glass showed that the contribution from the exchange interaction broadened the NMR spectrum by ~ 10 kHz. The change from [GeO_4] to [GeO_6] was also confirmed by Raman spectroscopy.

8.3 Structure of thallium borate crystalline phases and glasses

Five devitrified thallium borate samples were made from 0.10, 0.167, 0.20, 0.25 and 0.33 Tl_2O content glasses by heat-treatment of the corresponding glasses at their crystallisation temperatures obtained from thermal analysis. TlB_5O_8, TlB_3O_5 and $Tl_2B_4O_7$ are only the three crystalline phases formed from the glasses, either singly or in combination with each other. Density data, X-ray diffraction patterns and solid-state NMR results of the three phases formed support what structural information exists in the literature [5, 7, 9]. ^{205}Tl NMR spectra showed that the width of the peaks, correspond to TlB_5O_8, TlB_3O_5 and $Tl_2B_4O_7$, increases. The broadening and lineshape of the TlB_5O_8 and TlB_3O_5 spectra are due to the chemical shift anisotropy interaction, whose chemical shift anisotropy parameters were obtained. On the other hand in the very broad $Tl_2B_4O_9$ spectrum, the broadening and lineshape is not only due to the chemical shift anisotropy and dipolar interactions but also by the Tl…Tl exchange interaction. The chemical shift anisotropy parameters of TlB_5O_8 and TlB_3O_5 are presented. N_4 values, obtained from integration of ^{11}B NMR peaks, showed agreement with the values calculated from the X-ray crystal structure presented in the literature [5, 7, 9]. The Raman spectra of the samples have been obtained and compared with the caesium borate crystalline compound presented in [10]. Pentaborate units and triborate units are present in TlB_5O_8 and TlB_3O_5 as expected. The spectrum from $Tl_2B_4O_7$ has many overlapping peaks in this region because of the complexity of the medium range structure i.e. $(B_5O_{12})^{3-}$, $(B_7O_{15})^{3-}$ and also the presence of six Tl sites.

Ten thallium borate glasses with 0.05 to 0.50 Tl_2O content were made. Densities and molar volumes of these glasses have been measured and found to be consistent with the reported values in the literature in the Sciglass database [11]. The minimum in the molar volumes at ~ 0.28 Tl_2O content confirmed the presence of the borate anomaly as also found in the N_4 values of the glasses, obtained from ^{11}B NMR spectra, which deviate at the same composition. Raman spectroscopy showed the presence of boroxol ring, triborate, pentaborate, chain- and ring- type metaborate and diborate in the glasses at various compositions. Two distinct peaks in the neutron *T(r)* at ~ 1.3 to 1.5 Å and 2.3 to 2.5 Å correlate to the B-O and O...O distances, respectively. The first peak becomes broader as Tl_2O increases, which is due to the presence of the $[BO_4]$ units B-O correlation peak at ~1.477 Å. The N_4 values of glasses were calculate from the fit of the first peak at ~ 1.3 to 1.5 Å with two Gaussian peaks representing the $[BO_3]$ and $[BO_4]$

units. The N_4 values obtained from neutron diffraction and ^{11}B NMR are very similar and are consistenctly slightly above the x/(1-x) model. The peak in *T(r)* at ~3.3 Å could be due to Tl...Tl pairs n glasses at high Tl_2O content, although this peak overlaps with the O...O distance in [TlO_3] units. Broad ^{205}Tl solid-state NMR spectra of thallium borate glasses were obtained with large chemical shift range. The broadening mechanism in thallium borate glass is due to chemical shift anisotropy, chemical shift dispersion, dipolar interaction and exchange interaction throughout the range of the composition studied. The spectra were fitted with two Gaussian peaks contributed from low and high coordinated thallium, as found in thallium germanate glasses, using DM2010 [8]. As thallium increases, the highly ionic low coordinated thallium environment with a sterically active lone pair of electrons, increases and *vice versa* for high coordinated thallium environment.

8.4 Effect of lone pair electrons of thallium

The behaviour of borate and germanate anomalies in thallium containing glasses is different from what has been reported in alkali borate and germanate glasses due to the persistence of high coordinated network former, i.e. [BO_4] and [GeO_6] units to higher thallium contents. In alkali containing glasses, these high coordinated network former units are energetically less favourable than the formation of the low-coordinated units with non-bridging oxygens. The ability of thallium to lower its coordination number by changing the steric role of its lone pair of electrons, i.e. from average symmetrical, covalently, high-coordinated thallium site with sterically inert lone pair of electron ([TlO_7] or [TlO_9] [5]) to axially symmetrical, ionic, low-coordinated thallium site with sterically active lone pair of electrons ([TlO_3] [6] or [TlO_4] [7]), could stabilised the high coordinated network former units, thus the number of [BO_4] and [GeO_6] are formed at higher thallium content than in alkali containing glasses. The electrostatic bond strength calculations were used to demonstrate this stabilisation. They also suggest the presence of Tl-O-Tl bonds in the glasses.

8.5 Future Work

1) In the thallium germanate and thallium borate crystallisation studies, the crystalline phases devitrified from the glasses are not single phase. Study of the nucleation and crystallisation processes, in order to control and understand phase formation, would be necessary to be able to synthesis samples containing single phases, which could be helpful to get the precise information about thallium sites and network former site.

2) There is a problem in extracting the Tl-O distances from the thallium borate glasses due to the overlapping of the peak with the O...O correlation peak and also in obtaining the coordination number of thallium in thallium borate glass. Using multiple techniques, e.g. electron diffraction and x-ray diffraction, would be very helpful to obtain this important information.

3) The diffraction study of crystalline phase presented in the phase diagram, in the case where the single crystalline phases can be formed, would be able to provide useful information on local environments that can be used to understand the glass structure.

4) Simulation of the total correlation function, T(r), of the reported crystalline compounds with some constraints might be a good idea to compare with the glasses at the corresponding compositions, i.e. the TlB_5O_8, TlB_3O_5 and $Tl_2B_4O_7$ compounds.

8.6 References

[1] M. Touboul, Y. Feutelais, *Journal of Solid State Chemistry*, **32** (1980) 167.

[2] F.F. Riebling, *Journal of Chemical Physics*, **55** (1971) 804-&.

[3] K. Nassau, D.L. Chadwick, *Materials Research Bulletin*, **17** (1982) 715.

[4] K. Nassau, D.L. Chadwick, *Journal of the American Ceramic Society*, **65** (1982) 197.

[5] M. Touboul, G. Nowogrocki, *Journal of Solid State Chemistry*, **136** (1998) 216.

[6] M. Touboul, Y. Feutelais, *Acta Crystallographica Section B-Structural Science*, **35** (1979) 810.

[7] N. Penin, L. Seguin, B. Gerand, M. Touboul, G. Nowogrocki, *Journal of Solid State Chemistry*, **160** (2001) 139.

[8] D. Massiot, F. Fayon, M. Capron, I. King, S. Le Calve, B. Alonso, J.O. Durand, B. Bujoli, Z.H. Gan, G. Hoatson, *Magnetic Resonance in Chemistry*, **40** (2002) 70.

[9] M. Touboul, E. Betourne, G. Nowogrocki, *Journal of Solid State Chemistry*, **131** (1997) 370.

[10] R.N. Sinclair, R. Haworth, A.C. Wright, B.G. Parkinson, D. Holland, J.W. Taylor, N.M. Vedishcheva, I.G. Polyakova, B.A. Shakhmatkin, S.A. Feller, B. Rijal, T. Edwards, *Physics and Chemistry of Glasses-European Journal of Glass Science and Technology Part B*, **47** (2006) 405.

[11] SciMatics, *SciGlass - Glass Property Information System*, Computer software, 2011.